

**The role of volcanic ash in the global dispersion of the  
aerosol cloud from major tropical eruptions**

Sarah Elizabeth Shallcross

Submitted in accordance with the requirements for the degree of  
Doctor of Philosophy

The University of Leeds  
School of Earth and Environment

August 2020



## Declaration of authorship

The candidate confirms that the work submitted is her own and that appropriate credit has been given where reference has been made to the work of others. The candidate also confirms that she used the method for the backscatter to extinction conversion outlined in Chapter 3 was as part of the jointly authored paper:

**Dhomse, S. S., Mann, G. W., Antuña Marrero, J. C., Shallcross, S. E., Chipperfield, M. P., Carslaw, K. S., Marshall, L., Abraham, N. L., and Johnson, C. E. (2020): Evaluating the simulated radiative forcings, aerosol properties, and stratospheric warmings from the 1963 Mt Agung, 1982 El Chichón, and 1991 Mt Pinatubo volcanic aerosol clouds, *Atmospheric Chemistry and Physics*, 20, 13627–13654.**

This copy has been supplied on the understanding that it is copyright material and that no quotation from the thesis may be published without proper acknowledgement.

The right of Sarah Elizabeth Shallcross to be identified as Author of this work has been asserted by her in accordance with the Copyright, Designs and Patents Act 1988.

## Acknowledgements

I would like to thank my supervisors, Graham Mann, Anja Schmidt and Ryan Neely for their help, guidance and feedback throughout my PhD, particularly during the pandemic. Thank you to Graham for the implementation of the ash mode in order to make the ash work possible. Additional thanks go to Jim Haywood, Andy Jones and Ben Johnson at the Met Office for their help and encouragement. I would also like to thank Lauren Marshall for all her modelling advice and general support throughout.

This research was made possible by the Copernicus Atmosphere Monitoring Service, CAMS43 project and the University of Leeds joint scholarship, for which I am extremely grateful. Funding from the Met Office to attend workshops and meet with supervisors has helped me gain confidence and have useful discussions that have helped develop this thesis.

Model simulations in this thesis were run using high performance computing facility ARCHER, with data processing and analysis carried out using ARCHER, JASMIN and the Faculty of Environment computer systems. I am grateful for the support from Centre for Environmental Modelling and Computation (CEMAC), specifically from Mark Richardson and Richard Rigby. Thanks to the Shut Up and Write community also for all the productive and motivational writing sessions.

It has been wonderful having the added support and guidance from the aerosol research group at Leeds and from the ICAS community in general. Special thanks go to my 10.126 friends Laura, Tom, Chris, Rachel, Felicity and Joey for keeping me sane in the office. Added thanks go to Charlotte, Nicola and Gen for being with me through it all and to Anya, Anne, Josie, Laura, Charlotte and the countless others who have helped me over the past few years.

Words cannot express my gratitude to my family and friends throughout this process and to Madeleine for her continued support. Mark and Mandy thank you for feeding and generally looking after me in the last few weeks of writing up! Sam, there are frankly not enough words for how much you have helped me, I genuinely do not know what I would have done without you and I could not have asked for a better desk companion during our lockdown situation.

My final thanks go to the lady who came to my school when I was 4 and talked about pyroclastic flows on Montserrat, my love for volcanoes has grown ever since!

## Abstract

Explosive volcanic eruptions can inject huge quantities of ash and sulfur dioxide (SO<sub>2</sub>) into the stratosphere, which can significantly enhance the stratospheric aerosol layer leading to complex effects on the Earth's climate. One key effect is the oxidation of SO<sub>2</sub> into highly scattering sulfate aerosol, which can cool the Earth's surface globally.

The 1991 Mount Pinatubo eruption is the largest of the past century with many aspects of the aerosol cloud not understood. This eruption is an important case study for understanding the climate impacts of eruptions, especially in aerosol-climate models. Injection height, the erupted mass of SO<sub>2</sub> and the phase of the quasi-biennial oscillation (QBO) are all important factors that impact the subsequent dispersion and climate impact of a volcanic aerosol cloud. However, the importance of these factors, as well as their associated values, is disputed across the aerosol modelling community. Ash particles are usually disregarded in climate modelling studies, assumed to fall out within days of the eruption, however recent studies have found that they may impact the global dispersion of major volcanic eruptions.

The aim of this thesis is to investigate the initial dispersion of the Mount Pinatubo eruption cloud, focusing on the vertical extinction profiles from ground-based lidars to analyse the vertical dispersion of the volcanic aerosol cloud. Using an interactive stratospheric aerosol model, the impact of varying initial conditions is assessed, also differing injection heights and initial mass of SO<sub>2</sub> for a simulated Mount Pinatubo eruption. Finally, this thesis aims to analyse the role of ultra-fine ash in the stratosphere following the Mount Pinatubo eruption.

The results demonstrate the vertical profile of extinction is strongly dependent on the QBO-phase, with an injection height of 21-23 km producing the closest variation in extinction with time to observations. Injection height has a significant impact on the vertical dispersion of extinction, stratospheric aerosol optical depth (SAOD) and sulfate burden, with an injection height of 18-20 km preferentially removing aerosol from the cloud. An injection height of 21-23 agrees best with vertical extinction, sulfur burden and SAOD observations. An injection of 10-14 Tg SO<sub>2</sub> is, found to produce the best comparison to observations, with modelled SAOD values for 10 Tg and sulfate burdens of 14 Tg aligning best with observations. Ultra-fine ash is found to decrease tropical sulfate burdens up to 0.6 Tg and decrease tropical SAOD up to 0.06, due to increased dispersion to the northern hemisphere from increased heating and then lofting of aerosol out of the tropics into the northern hemisphere.

## Table of Contents

<b>Acknowledgements.....</b>	<b>ii</b>
<b>Abstract.....</b>	<b>iii</b>
<b>Table of Contents .....</b>	<b>iv</b>
<b>List of Figures.....</b>	<b>viii</b>
<b>List of Tables .....</b>	<b>xv</b>
<b>Abbreviations .....</b>	<b>xvi</b>
<b>Chapter 1 Introduction.....</b>	<b>19</b>
1.1 Motivation .....	19
1.2 Research rationale and thesis aims .....	24
1.3 Thesis aims .....	25
<b>Chapter 2 Background and literature review .....</b>	<b>27</b>
2.1 Vertical structure of the atmosphere .....	27
2.2 Stratospheric aerosol layer .....	28
2.2.1 Sulfate aerosol formation and microphysics.....	29
2.2.2 Stratospheric sulfur chemistry .....	30
2.2.3 Stratospheric circulation and transport .....	33
2.2.4 Ash in the stratosphere.....	35
2.2.4.1 Ash core particles.....	35
2.2.5 Residence time and aerosol size modes.....	36
2.2.6 Aerosol extinction and optical depth .....	39
2.3 Mount Pinatubo 1991 .....	40
2.3.1 Measurements.....	40
2.3.2 Mount Pinatubo model simulations - SO <sub>2</sub> emission and injection height 44	
2.3.3 Observations and model simulations of volcanic ash.....	47
2.4 Summary .....	48
<b>Chapter 3 Data and Methods.....</b>	<b>50</b>
3.1 Introduction .....	50
3.2 UM-UKCA model description .....	51
3.3 GLOMAP-mode .....	52
3.3.1 Introduction.....	52
3.3.2 Stratospheric chemistry scheme .....	55
3.3.3 Fine ash mode .....	55
3.3.4 Ash specifics – density, optical properties and size .....	57

3.4 Radiation scheme RADAER .....	57
3.5 Model configurations and eruption source parameters .....	58
3.6 Lidar measurements.....	60
3.6.1 Zubov shipborne lidar data .....	63
3.6.2 Layer analysis algorithm description.....	64
3.6.3 Backscatter ratio to extinction .....	65
3.6.4 Uncertainties within lidar data.....	67
<b>Chapter 4 Initial dispersion of the 1991 Mount Pinatubo aerosol cloud – a ground-based lidar and interactive composition climate model comparison</b> .....	<b>69</b>
4.1 Introduction .....	69
4.2 Data and Methods.....	73
4.3 Results and Discussion.....	75
4.3.1 Tropical lidar signal – Phases of the cloud dispersion and comparison of ground-based and ship-borne lidar with model simulations.....	76
4.3.2 MLO backscatter to extinction comparison to Zubov shipborne lidar data.....	79
4.3.3 Northern hemisphere mid-latitude lidar measurements.....	81
4.3.4 Model comparison to MLO, TAB, TOR and OHP.....	83
4.3.5 Wind profiles for June 1991 .....	90
4.3.6 Volcanic cloud depth .....	91
4.3.7 Regression analysis.....	92
4.3.8 Aerosol induced heating .....	96
4.3.9 Model simulated global-mean stratospheric aerosol optical depth (SAOD).....	97
4.4 Discussion and Conclusions .....	98
<b>Chapter 5 Exploring varying eruption source parameters: a Pinatubo case study</b> .....	<b>101</b>
5.1 Introduction .....	101
5.2 Methods .....	104
5.2.1 Model setup.....	104
5.2.1.1 Hypothetical lidar site .....	104
5.3 Results .....	105
5.3.1 Vertical structure of the volcanic cloud .....	105
5.3.2 Tropical radiative heating .....	108
5.3.3 Sulfate burden.....	111
5.3.4 Stratospheric aerosol optical depth (SAOD) .....	113
5.3.5 Aerosol effective radius .....	117

5.4 Hypothetical lidar site near the centre of the tropical reservoir .....	119
5.5 Discussion .....	121
5.6 Conclusions .....	126
<b>Chapter 6 The role of ultra-fine ash in the global dispersion of the 1991 Mount Pinatubo aerosol cloud .....</b>	<b>129</b>
6.1 Introduction .....	129
6.2 Data and methods .....	133
6.3 Stratospheric residence time of fine ash (super-micron).....	135
6.4 Stratospheric residence time and vertical distribution of ultra-fine ash (sub-micron).....	136
6.4.1 Ultra-fine ash burden for June 1991 - February 1992 .....	138
6.5 Impact of ultra-fine ash on optical depth from the Mount Pinatubo cloud .	141
6.5.1 Tropical SAOD variation.....	142
6.5.2 Mid-latitude SAOD variation .....	146
6.5.2.1 Northern and southern hemisphere midlatitudes SAOD variation .....	149
6.6 Sulfur burden.....	154
6.6.1 Tropical sulfur burden .....	154
6.6.2 Global sulfur burden .....	156
6.7 Vertical profile of aerosol extinction.....	159
6.7.1 Aberystwyth depolarisation and model data comparison .....	164
6.8 Ash-core sulfate particles .....	165
6.9 Discussion .....	166
6.10 Conclusions .....	171
<b>Chapter 7 Conclusions and Future Work.....</b>	<b>173</b>
7.1 Initial dispersion of the 1991 Mount Pinatubo aerosol cloud – a ground-based lidar and interactive composition climate model comparison .....	174
7.1.1 Main conclusions .....	174
7.1.2 Future work.....	176
7.2 Exploring varying eruption source parameters: a Pinatubo case study .....	176
7.2.1 Main conclusions .....	177
7.2.2 Future work.....	178
7.3 The role of ash in the initial dispersion of the 1991 Mount Pinatubo aerosol cloud.....	178
7.3.1 Main conclusions .....	178
7.3.2 Future work.....	179

<b>References .....</b>	<b>181</b>
<b>Appendix A Method for layer finding algorithm and conversion factors for BSR-EXT .....</b>	<b>206</b>
A.1 Layer finding algorithm explanation .....	206
A.2 Conversion factors for converting between 694 nm and 532 nm. These values are spilt for 3 monthly intervals and 5 km altitude resolution. ....	207
A.3 Conversion exponents for converting backscatter ratio to extinction. These values are spilt for 3 monthly intervals and 5 km altitude resolution. Obtained from Juan Carlos Antuña Marrera from Jager and Deshler (2005). 208	
<b>Appendix B Varying conversion factors vs blanket conversion of 40 .....</b>	<b>209</b>
<b>Appendix C Chapter 5 Northern and southern hemisphere sulfate burden and SAOD .....</b>	<b>214</b>
<b>Appendix D Chapter 6 sulfate and ash burden profiles .....</b>	<b>217</b>
<b>Appendix E Chapter 6 vertical extinction profiles for all lidar sites.....</b>	<b>219</b>

## List of Figures

- Figure 1-1** Updated from Robock (2000), a schematic diagram of quiescent and explosive volcanic effects on the radiative balance of the Earth (Fischer et al., 2006). ..... 20
- Figure 2-1** Schematic of the thermal structure of the atmosphere from Brasseur and Solomon (2005). ..... 28
- Figure 2-2** Simplified schematic of the cycle of ClO<sub>x</sub> ozone depletion. .... 32
- Figure 2-3** Schematic of stratospheric circulation for a Northern hemisphere summer, adapted from Bönisch et al. (2011) and Holton et al. (1995). The solid blue line denotes the tropopause. The dotted black line marks the 380 K potential temperature, above which is entirely stratospheric. Arrows indicate overall transport with arrow widths corresponding to relative circulation strength. Lines either side of the tropics and in the winter hemisphere show the tropical pipe and the edge of the polar vortex, respectively. Green arrows indicate lower stratospheric transport below the tropical pipe and wiggly red arrows denote isentropic transport. .... 34
- Figure 2-4** Aerosol size distribution and modes for atmospheric aerosol particles, adapted from Durant et al. (2010). ..... 37
- Figure 2-5** Fall speeds between the surface and 40 km for particles ranging in size from 0.003 and 10  $\mu\text{m}$  with density a) 1000  $\text{kg m}^{-3}$  (Kasten et al. (1968)) and b) 2000  $\text{kg m}^{-3}$  (Junge et al. (1961)). Figures are recreations of Figure 1 from Kasten et al. (1968) and Figure 2 from Junge et al. (1961), respectively. .... 38
- Figure 2-6** Size distributions from Langmann (2014) of modelled aerosol modes for the 1991 Mount Hudson eruption for a) without ash and b) with ash. Line represent modes, nucleation (red), Aitken (yellow), accumulation (green) and coarse (brown). .... 39
- Figure 3-1** Map locations for each lidar site location (yellow dots) and Mount Pinatubo for reference (red triangle). ..... 62
- Figure 3-2** Map of the course taken by the Professor Zubov ship from the 11<sup>th</sup> July to the 21<sup>st</sup> September 1991, as outlined in Avdyushin et al. (1993). Red dots show the direction the ship took southwards, with the majority of the journey spent around 20°N (purple) then progressing towards the equator and then back towards Spain past the west coast of Africa (blue dots). ..... 64
- Figure 3-3** Schematic for the layer finding algorithm with backscatter ratio against altitude. Red dots show the points where it would find the top and bottom of a layer, delta shows where the data must exceed above the first peak point to avoid areas of noise that may be picked out as layers. .... 65
- Figure 4-1** Schematic for how the regression analysis is performed. Orange cloud depicts the aerosol cloud pattern noted at MLO, red arrows indicate each slope analysed. .... 75
- Figure 4-2** Ground-based lidar backscatter ratio at MLO, initial layers are denoted with red arrows and different phases with greyed boxes. .... 77

- Figure 4-3 - Extinction values for (A) Zubov shipborne lidar and (B) MLO (expansion of Figure 4-2) from 12th July - 21st September 1991..... 80**
- Figure 4-4 Ground based lidar backscatter ratio plots for a) MLO, b) TAB, c) TOR and d) OHP from June 1991 - February 1992. Blue diamonds at 30 km show measurement dates. Red triangle shows eruption date and red arrows show layer duration. .... 82**
- Figure 4-5 Extinction (/km) values for Mauna Loa (MLO) from June 1991 - February 1992. a) Lidar with varying BSR-EXT values over time, b) Model simulation with approximate-QBO, c) Model simulation with pre-nudged conditions, black diamonds in (a) show days when measurements were taken..... 86**
- Figure 4-6 Extinction (/km) values for Table Mountain (TAB) from June 1991 - February 1992. a) Lidar with varying BSR-EXT values over time, b) Model simulation with approximate-QBO, c) Model simulation with pre-nudged conditions, black diamonds in (a) show days when measurements were taken..... 87**
- Figure 4-7 Extinction (/km) values for Toronto (TOR) from June 1991 - February 1992. a) Lidar with varying BSR-EXT values over time, b) Model simulation with approximate-QBO, c) Model simulation with pre-nudged conditions, black diamonds in (a) show days when measurements were taken..... 88**
- Figure 4-8 Extinction (/km) values for Haute Provence (OHP) from June 1991 - February 1992. a) Lidar with varying BSR-EXT values over time, b) Model simulation with approximate-QBO, c) Model simulation with pre-nudged conditions, black diamonds in (a) show days when measurements were taken..... 89**
- Figure 4-9 u-wind (m/s) profile comparison over the period 16-30th June, for a) ERA-interim, b) The pre-nudged UM-UKCA simulation and c) The approximate-QBO simulation..... 90**
- Figure 4-10 Cloud depth plots for Observations (left), approximate-QBO simulations (middle) and pre-nudged simulations (right) for June - September 1991 at MLO. Each line represents the depth of the cloud, as calculated using the layer finding algorithm. .... 91**
- Figure 4-11 Cloud depth plots for Observations (left), approximate-QBO simulations (middle) and pre-nudged simulations (right) for October 1991 - March 1992 at MLO. Each line represents the depth of the cloud, as calculated using the layer finding algorithm. .... 91**
- Figure 4-12 Tropical (20°S-20°N) radiative heating difference for the period June 1991-February 1992 between (a) modelled (14 Tg SO<sub>2</sub>, injected 21-23 km) and control (no eruption) and (b) ERA-interim reanalysis temperature anomalies. .... 96**
- Figure 4-13 Modelled a) Monthly averaged 550 nm SAOD from June 1991 to February 1992 b) Zonally averaged monthly mean for the pre-nudged QBO simulation..... 97**

- Figure 5-1 Extinction profiles for MLO lidar observations (top) and the 14 Tg SO<sub>2</sub>, 18-20 km injection height model simulation (bottom). Black dots represent the top and bottom of the sulfate aerosol cloud, calculated by the layer finding algorithm..... 106**
- Figure 5-2 Extinction profiles for MLO lidar observations (top) and the 14 Tg SO<sub>2</sub>, 18-25 km injection height model simulation (bottom). ..... 107**
- Figure 5-3 Extinction profiles for MLO lidar observations (top) and the 14 Tg SO<sub>2</sub>, 21-23 km injection height model simulation (bottom). ..... 108**
- Figure 5-4 Tropical (20°S-20°N) aerosol-induced stratospheric heating anomalies for model simulations (a-c) with injection height 21-23 km for June 1991 – February 1992, a) 10 Tg, b) 14 Tg and c) 20 Tg SO<sub>2</sub>. (d) ERA-interim tropical (20°S-20°N) stratospheric temperature anomalies for June 1991–February 1992. .... 109**
- Figure 5-5 Tropical (20°S-20°N) aerosol-induced stratospheric heating anomalies for model simulations (a-c) with injection height 18-20 km for June 1991 – February 1992, a) 10 Tg, b) 14 Tg and c) 20 Tg SO<sub>2</sub>. (d) ERA-interim tropical (20°S-20°N) stratospheric temperature anomalies for June 1991–February 1992. .... 110**
- Figure 5-6 Tropical (20°S-20°N) aerosol-induced stratospheric heating anomalies for model simulations (a-c) with injection height 18-25 km for June 1991 – February 1992, a) 10 Tg, b) 14 Tg and c) 20 Tg SO<sub>2</sub>. (d) ERA-interim tropical (20°S-20°N) stratospheric temperature anomalies for June 1991–February 1992. .... 110**
- Figure 5-7 Tropical (20°N-20°S) sulfur burden (Tg) for SO<sub>2</sub> (left) and SO<sub>4</sub> (right) for all model simulations. Black lines indicate observations with 10% error bars..... 112**
- Figure 5-8 Global sulfur burden (Tg) for SO<sub>2</sub> (left) and SO<sub>4</sub> (right) for all model simulations. Black lines indicate observations with 10% error bars. .... 113**
- Figure 5-9 Tropical (20°S-20°N) optical depth for all simulations, compared to AVHRR and GloSSAC. Different colours denote different amounts of SO<sub>2</sub> and linestyles denote different injection heights. .... 115**
- Figure 5-10 Global (80°S-80°N) optical depth for all simulations, compared to AVHRR and GloSSAC measurements. Different colours denote different amounts of SO<sub>2</sub> and linestyles denote different injection heights..... 116**
- Figure 5-11 Model effective radius (R<sub>eff</sub>) for each model simulation for the period June 1991 - February 1992. Line colour indicates mass of SO<sub>2</sub> injected and linestyle denotes injection height. .... 118**
- Figure 5-12 Comparison of model simulated R<sub>eff</sub> values (averaged for 14-30km) against in-situ measurements and previously modelled R<sub>eff</sub> for Wyoming, Laramie for June 1991 to February 1992. .... 119**
- Figure 5-13 Model-simulated extinction (550 nm) values for (A) 10°N, (B) the equator and (C) 10°S from June 1991 - March 1992..... 120**
- Figure 5-14 Absolute difference in extinction at 550 nm between the equator and 10°N (top) and the equator and 10°S. Red values indicate areas where the equator values are higher, blue indicate where equator values are lower..... 121**

<b>Figure 6-1 Percentage mass of ash over a one-week period following the eruption for 1, 3.16 and 10 <math>\mu\text{m}</math> ash sizes. ....</b>	<b>136</b>
<b>Figure 6-2 Percentage mass of ash in the first 3 months following the 1991 Mount Pinatubo eruption, for 3 different ash sizes (0.1, 0.316 and 1 <math>\mu\text{m}</math>) for 0.05 and 0.5 Tg of ash injected. Straight lines denote 0.05 Tg, dashed denote 0.5 Tg ash.....</b>	<b>137</b>
<b>Figure 6-3 Ash burden percentages for model simulation with 10, 14 and 20 Tg of <math>\text{SO}_2</math> and 18-20, 21-23 and 18-25 km injection heights. ....</b>	<b>139</b>
<b>Figure 6-4 Monthly average ash (red) and sulfate (blue) burden for the tropics (<math>20^\circ\text{S}</math>-<math>20^\circ\text{N}</math>) for a 14 Tg <math>\text{SO}_2</math> and 0.05 Tg ash injection mass at 18-20 km (solid lines), 21-23 km (dashed lines) and 18-25 km (dot-dashed line)....</b>	<b>141</b>
<b>Figure 6-5 SAOD for the tropics in all injection height scenarios for (left) 10 Tg, (middle) 14 Tg and (right) 20 Tg. Solid lines are ash simulations and dashed are non-ash simulations, note the difference in scale on the y-axis. ....</b>	<b>144</b>
<b>Figure 6-6 SAOD for the midlatitudes (inclusive of the tropics) (<math>60^\circ\text{S}</math>-<math>60^\circ\text{N}</math>) in all injection height scenarios for a) 10 Tg, b) 14 Tg and c) 20 Tg. Solid lines are ash simulations and dashed are non-ash simulations, note the difference in scale on the y-axis. ....</b>	<b>148</b>
<b>Figure 6-7 SAOD for the northern hemisphere midlatitudes (<math>20</math>-<math>60^\circ\text{N}</math>) in all injection height scenarios for a) 10 Tg, b) 14 Tg and c) 20 Tg. Solid lines are ash simulations and dashed are non-ash simulations, note the difference in scale on the y-axis. ....</b>	<b>152</b>
<b>Figure 6-8 SAOD for the southern hemisphere midlatitudes (<math>20</math>-<math>60^\circ\text{S}</math>) in all injection height scenarios for a) 10 Tg, b) 14 Tg and c) 20 Tg. Solid lines are ash simulations and dashed are non-ash simulations, note the difference in scale on the y-axis. ....</b>	<b>153</b>
<b>Figure 6-9 Tropical (Left) <math>\text{SO}_2</math> burden and (Right) <math>\text{SO}_4</math> burden for 10 Tg ash (solid line) and non-ash (dashed) simulations. ....</b>	<b>155</b>
<b>Figure 6-10 Tropical (Left) <math>\text{SO}_2</math> burden and (Right) <math>\text{SO}_4</math> burden for 14 Tg ash (solid line) and non-ash (dashed) simulations. ....</b>	<b>155</b>
<b>Figure 6-11 Tropical (Left) <math>\text{SO}_2</math> burden and (Right) <math>\text{SO}_4</math> burden for 20 Tg ash (solid line) and non-ash (dashed) simulations. ....</b>	<b>156</b>
<b>Figure 6-12 Global sulfur burden for (left) <math>\text{SO}_2</math> gas-phase sulfur and (right) sulfate aerosol for 10 Tg injected <math>\text{SO}_2</math> at all injection heights comparing with and without ash.....</b>	<b>158</b>
<b>Figure 6-13 Global sulfur burden for (left) <math>\text{SO}_2</math> gas-phase sulfur and (right) sulfate aerosol for 14 Tg injected <math>\text{SO}_2</math> at all injection heights comparing with and without ash.....</b>	<b>158</b>
<b>Figure 6-14 Global sulfur burden for (left) <math>\text{SO}_2</math> gas-phase sulfur and (right) sulfate aerosol for 20 Tg injected <math>\text{SO}_2</math> at all injection heights comparing with and without ash.....</b>	<b>159</b>

- Figure 6-15 Extinction plots for MLO with 14 Tg SO<sub>2</sub> and 21-23 km injection height. Plots show observations (top), no ash (middle) and with ash (bottom). Black dots denote where layers are picked out from the layer finding algorithm. .... 160**
- Figure 6-16 Extinction plots for MLO with 14 Tg SO<sub>2</sub> and 18-20 km injection height. Plots show observations (top), no ash (middle) and with ash (bottom). Black dots denote where layers are picked out from the layer finding algorithm. .... 161**
- Figure 6-17 Extinction plots for MLO with 14 Tg SO<sub>2</sub> and 18-25 km injection height. Plots show observations (top), no ash (middle) and with ash (bottom). Black dots denote where layers are picked out from the layer finding algorithm. .... 161**
- Figure 6-18 Extinction plots for TAB with 14 Tg SO<sub>2</sub> and 21-23 km injection height. Plots show observations (top), no ash (middle) and with ash (bottom)..... 162**
- Figure 6-19 Extinction plots for OHP with 14 Tg SO<sub>2</sub> and 21-23 km injection height. Plots show observations (top), no ash (middle) and with ash (bottom)..... 163**
- Figure 6-20 (Top) Contour plots of backscatter ratio and depolarisation data from Aberystwyth compared to ash ratio model data in 2 scenarios, (bottom) depth of cloud from the layer finding algorithm for observations and the same 2 model scenarios from the top row..... 165**
- Figure 6-21 Mass of sulfate aerosol condensed onto ash from June 1992 to October 1991 for all amounts of injected SO<sub>2</sub> and injection height. .... 166**
- Figure B-1 Extinction (/km) values for Mauna Loa (MLO) from June 1991 - February 1992. a) Lidar with varying BSR-EXT values over time, b) Lidar values with BSR-EXT value of 40, c) Model simulation with approximate-QBO, d) Model simulation with pre-nudged conditions. .. 210**
- Figure B-2 Extinction (/km) values for Table Mountain (TAB) from June 1991 - February 1992. a) Lidar with varying BSR-EXT values over time, b) Lidar values with BSR-EXT value of 40, c) Model simulation with approximate-QBO, d) Model simulation with pre-nudged conditions ... 211**
- Figure B-3 Extinction (/km) values for Toronto (TOR) from June 1991 - February 1992. a) Lidar with varying BSR-EXT values over time, b) Lidar values with BSR-EXT value of 40, c) Model simulation with approximate-QBO, d) Model simulation with pre-nudged conditions. .. 212**
- Figure B-4 Extinction (/km) values for Haute Provence (OHP) from June 1991 - February 1992. a) Lidar with varying BSR-EXT values over time, b) Lidar values with BSR-EXT value of 40, c) Model simulation with approximate-QBO, d) Model simulation with pre-nudged conditions. .. 213**
- Figure C-1 Northern hemisphere (left) SO<sub>2</sub> sulfur burden and (right) SO<sub>4</sub> sulfur burden for each injection height and mass of SO<sub>2</sub>..... 214**
- Figure C-2 Southern hemisphere (left) SO<sub>2</sub> sulfur burden and (right) SO<sub>4</sub> sulfur burden for each injection height and mass of SO<sub>2</sub>..... 214**

<b>Figure C-3 SAOD values for the northern hemisphere for each different injection height and mass of SO<sub>2</sub>. Red lines are 10 Tg, green lines are 14 Tg and blue lines are 20 Tg with different linestyles for each injection height.</b> .....	<b>215</b>
<b>Figure C-4 SAOD values for the southern hemisphere for each different injection height and mass of SO<sub>2</sub>. Red lines are 10 Tg, green lines are 14 Tg and blue lines are 20 Tg with different linestyles for each injection height.</b> .....	<b>216</b>
<b>Figure D-1 Monthly average ash (red) and sulfate (blue) burden for the northern mid-latitudes (20-60°N) for a 14 Tg SO<sub>2</sub> and 0.05 Tg ash injection mass at 18-20 km (solid lines), 21-23 km (dashed lines) and 18-25 km (dot-dashed line).</b> .....	<b>217</b>
<b>Figure D-2 Monthly average ash (red) and sulfate (blue) burden for the northern mid-latitudes (20-60°S) for a 14 Tg SO<sub>2</sub> and 0.05 Tg ash injection mass at 18-20 km (solid lines), 21-23 km (dashed lines) and 18-25 km (dot-dashed line).</b> .....	<b>218</b>
<b>Figure E-1 Extinction plots for MLO with 10 Tg SO<sub>2</sub> and 18-20 km injection height. Plots show observations (top), no ash (middle) and with ash (bottom). Black dots denote where layers.</b> .....	<b>219</b>
<b>Figure E-2 Extinction plots for MLO with 10 Tg SO<sub>2</sub> and 21-23 km injection height. Plots show observations (top), no ash (middle) and with ash (bottom). Black dots denote layers.</b> .....	<b>219</b>
<b>Figure E-3 Extinction plots for MLO with 10 Tg SO<sub>2</sub> and 18-25 km injection height. Plots show observations (top), no ash (middle) and with ash (bottom). Black dots denote layers.</b> .....	<b>220</b>
<b>Figure E-4 Extinction plots for TAB with 10 Tg SO<sub>2</sub> and 18-20 km injection height. Plots show observations (top), no ash (middle) and with ash (bottom).</b> .....	<b>220</b>
<b>Figure E-5 Extinction plots for TAB with 10 Tg SO<sub>2</sub> and 21-23 km injection height. Plots show observations (top), no ash (middle) and with ash (bottom).</b> .....	<b>221</b>
<b>Figure E-6 Extinction plots for TAB with 10 Tg SO<sub>2</sub> and 18-25 km injection height. Plots show observations (top), no ash (middle) and with ash (bottom).</b> .....	<b>221</b>
<b>Figure E-7 Extinction plots for TOR with 10 Tg SO<sub>2</sub> and 18-20 km injection height. Plots show observations (top), no ash (middle) and with ash (bottom).</b> .....	<b>222</b>
<b>Figure E-8 Extinction plots for TOR with 10 Tg SO<sub>2</sub> and 21-23 km injection height. Plots show observations (top), no ash (middle) and with ash (bottom).</b> .....	<b>222</b>
<b>Figure E-9 Extinction plots for TOR with 10 Tg SO<sub>2</sub> and 18-25 km injection height. Plots show observations (top), no ash (middle) and with ash (bottom).</b> .....	<b>223</b>

- Figure E-10 Extinction plots for OHP with 10 Tg SO<sub>2</sub> and 18-20 km injection height. Plots show observations (top), no ash (middle) and with ash (bottom). Black dots denote where layers are picked out from the layer finding algorithm. .... 223**
- Figure E-11 Extinction plots for OHP with 10 Tg SO<sub>2</sub> and 21-23 km injection height. Plots show observations (top), no ash (middle) and with ash (bottom)..... 224**
- Figure E-12 Extinction plots for OHP with 10 Tg SO<sub>2</sub> and 18-25 km injection height. Plots show observations (top), no ash (middle) and with ash (bottom)..... 224**

**List of Tables**

**Table 2-1 Eruption source parameters (mass of SO<sub>2</sub> and injection height) as inferred based on observations and as used in climate modelling studies of the 1991 Mount Pinatubo eruption. .... 45**

**Table 3-1 Each mode within GLOMAP-mode with associated size range, composition, solubility and mode width..... 52**

**Table 3-2 Sulfur chemistry reactions in UM-UKCA for stratospheric aerosol. Table modified from Dhomse et al. (2014), W = Weisenstein et al. (1997); S = Sander et al. (2006); K = Kreidenweis et al. (2003). .... 55**

**Table 3-3 Model parameter setup for approximate-QBO and pre-nudged Mount Pinatubo simulations. .... 59**

**Table 3-4 Details about the lidar locations, types, operational times and references to measurements. .... 62**

**Table 4-1 - MLO layer comparison between lidar and model, model altitude range in brackets denotes pre-nudged model run ..... 85**

**Table 4-2 Regression analysis of the depth of the volcanic cloud and cloud top height for the lidar and model simulations with pre-nudged and approximate-QBO at MLO..... 95**

**Table 5-1 Peak tropical sulfate burden values (Tg) as observed (Baran and Foot, 1994) and simulated. .... 112**

**Table 6-1 List of performed experiments, with "\_ash" indicating model simulations with ash injected and "non-ash equivalent" outlined in Chapter 5. .... 134**

**Table 6-2 Reduction in peak SAOD between ash and non-ash simulations. ... 145**

**Table 6-3 Maximum differences in Tg of sulfur in the tropical and global sulfate burden between non-ash and ash simulations in order of highest to lowest difference ..... 157**

## Abbreviations

AERONET	<b>Aerosol Robotic Network</b>
AVHRR	<b>Advanced Very High-Resolution Radiometer</b>
BDC	<b>Brewer-Dobson Circulation</b>
BSR	<b>Backscatter ratio</b>
CALIOP	<b>Cloud Aerosol Lidar with Orthogonal Polarisation</b>
CALIPSO	<b>Cloud-Aerosol Lidar and Infrared Pathfinder Satellite Observations</b>
CCN	<b>Cloud Condensation Nuclei</b>
CheST	<b>Chemistry of the Stratosphere and Troposphere</b>
CLAES	<b>Cryogenic Limb Array Etalon Spectrometer</b>
CMIP5/6	<b>Coupled Model Intercomparison Project phase 5/6</b>
DMS	<b>Dimethyl Sulfide</b>
ERBS	<b>Earth Radiation Budget Satellite</b>
GHG	<b>Greenhouse Gas</b>
GLOMAP	<b>GLOBAL Model of Aerosol Processes</b>
GloSSAC	<b>Global Space-based Stratospheric Aerosol Climatology</b>
HadGEM-3	<b>Hadley Centre Global Environment Model version 3</b>
HErSEA	<b>The Historical Eruptions SO<sub>2</sub> Emission Assessment</b>
HIRS	<b>High-resolution Infrared Radiation Sounder</b>
ISA-MIP	<b>Interactive Stratospheric Aerosol Model Intercomparison Project</b>
ITCZ	<b>Inter Tropical Convergence Zone</b>
LALINET	<b>Latin America Lidar Network</b>
Lidar	<b>Light Detection and Ranging</b>
LW	<b>Longwave</b>
MLO	<b>Mauna Loa</b>
MSP	<b>Meteoritic Smoke Particle</b>

NDACC	<b>N</b> etwork for the <b>D</b> etection of <b>A</b> tmospheric <b>C</b> omposition <b>C</b> hange
NOAA	<b>N</b> ational <b>O</b> ceanic <b>A</b> tmospheric <b>A</b> dministration
OCS	Carbonyl Sulfide
OHP	<b>O</b> bservatoire d' <b>H</b> aute <b>P</b> rovence
QBO	<b>Q</b> uasi- <b>B</b> iennial <b>O</b> scillation
$R_{\text{eff}}$	<b>E</b> ffective radius
SAGE II	<b>S</b> tratospheric <b>A</b> erosol and <b>G</b> as <b>E</b> xperiment <b>II</b>
SAOD	<b>S</b> tratospheric <b>A</b> erosol <b>O</b> ptical <b>D</b> epth
SPARC	<b>S</b> tratosphere-Troposphere <b>P</b> rocesses <b>A</b> nd their <b>R</b> ole in <b>C</b> limate
SW	<b>S</b> hortwave
TAB	<b>T</b> able Mountain
TIROS	<b>T</b> elevision <b>I</b> nfrared <b>O</b> bservation <b>S</b> atellite
TOA	<b>T</b> op of the <b>A</b> tmosphere
TOMS	<b>T</b> otal <b>O</b> zone <b>M</b> apping <b>S</b> pectrometer
TOR	<b>T</b> oronto
TOVS	<b>TIROS</b> <b>O</b> perational <b>V</b> ertical <b>S</b> ounder
UKCA	<b>U</b> nited <b>K</b> ingdom <b>C</b> hemistry and <b>A</b> erosols
UM	<b>U</b> nified <b>M</b> odel
VAAC	<b>V</b> olcanic <b>A</b> sh <b>A</b> dvisory <b>C</b> entre
VEI	<b>V</b> olcanic <b>E</b> xplosivity <b>I</b> ndex
VolMIP	<b>M</b> odel <b>I</b> ntercomparison <b>P</b> roject on the climatic response to <b>V</b> olcanic forcing



# Chapter 1 Introduction

## 1.1 Motivation

Explosive volcanic eruptions are capable of injecting huge quantities (10s of teragrams) of sulfur dioxide (SO<sub>2</sub>) and ash into the stratosphere, which can cause significant enhancement to the stratospheric aerosol layer and have complex effects on Earth's climate (**Figure 1-1**) (Robock, 2000; Kremser et al., 2016). Volcanic material has a longer residence time in the stratosphere than in the troposphere, lasting ~2-3 years for major eruptions in the tropics, compared to 1-3 weeks residence time for tropospheric aerosol (Robock, 2000). One primary effect of increased SO<sub>2</sub> and a longer residence time is the ability for SO<sub>2</sub> to oxidise into sulfuric acid (H<sub>2</sub>SO<sub>4</sub>) vapour that then condenses onto existing particles, such as ash particles, or nucleates, creating highly scattering sulfate aerosol particles in the stratosphere (Hamill et al., 1997). Ash particles were confirmed to be present in the stratosphere 3 months after the 2014 Kelud eruption (Vernier et al., 2016), with ash particles coated in sulfuric acid observed up to 9 months following the 1991 Mount Pinatubo eruption (Pueschel et al., 1994). These ash-sulfuric particles may act as a removal pathway for both ash and sulfate aerosol following major volcanic eruptions (Turco et al., 1983; Kremser et al., 2016; Deshler, 2016) potentially reducing the overall climate impact of an eruption.

Sulfate aerosols can have a significant impact on the Earth's radiation budget as they are highly efficient at scattering incoming shortwave radiation (SW) and also absorb outgoing longwave radiation (LW) (Labitzke and McCormick, 1992). The solar, near infra-red (LW) heating is most relevant in the stratosphere as there is substantial heating in the tropics which increases the temperature gradient between the poles and the equator, particularly in winter, strengthening the polar vortex and leading to warmer northern hemisphere winters (Robock, 2000). The more dominant scattering of sulfate aerosols leads to a net surface cooling effect, as occurred around a year after the June 1991 Mount Pinatubo eruption, estimated to have been around -0.4 to -0.6 °C globally (McCormick et al., 1995; Hansen et al., 1996). Internal climate variability, arising primarily from the El Nino Southern Oscillation (ENSO), means observed surface temperature anomalies are not a direct constraint for surface cooling following a major volcanic eruption and the magnitude of the climate impact of a volcanic eruption is

usually communicated by its net radiative forcing. Satellite measurements show that 2 years after the Mount Pinatubo eruption an additional  $2.5 \text{ Wm}^{-2}$  of the  $341 \text{ Wm}^{-2}$  incoming solar radiation was reflected back to space (Wielicki et al, 1995). The magnitude of this volcanic forcing for other major eruption clouds is determined primarily by the mass of  $\text{SO}_2$  reaching the stratosphere (Robock, 2000; Niemeier et al., 2009), the latitude and the injection height of the eruption determining the timescale for decay (Dyer, 1974; Marshall et al., 2019) and season also affecting the subsequent dispersion of the cloud (Toohey et al., 2011). The global volcanic cloud from major tropical eruptions also cause a strong and abrupt increase in aerosol surface area, which cause substantial perturbation to stratospheric chemistry, most importantly the depletion of polar ozone due to activation of chlorine on sulfate aerosol surfaces (Tie and Brasseur, 1995; Tabazadeh et al., 2002; Dhomse et al., 2015; Solomon et al., 2016) (discussed further in section 2.2.2).

There is a significant variation in the size of aerosols throughout the atmosphere (Seinfeld and Pandis, 2006) and the degree of scattering and absorbing of different aerosol types depends on the aerosol size distribution (Lacis et al., 1992).

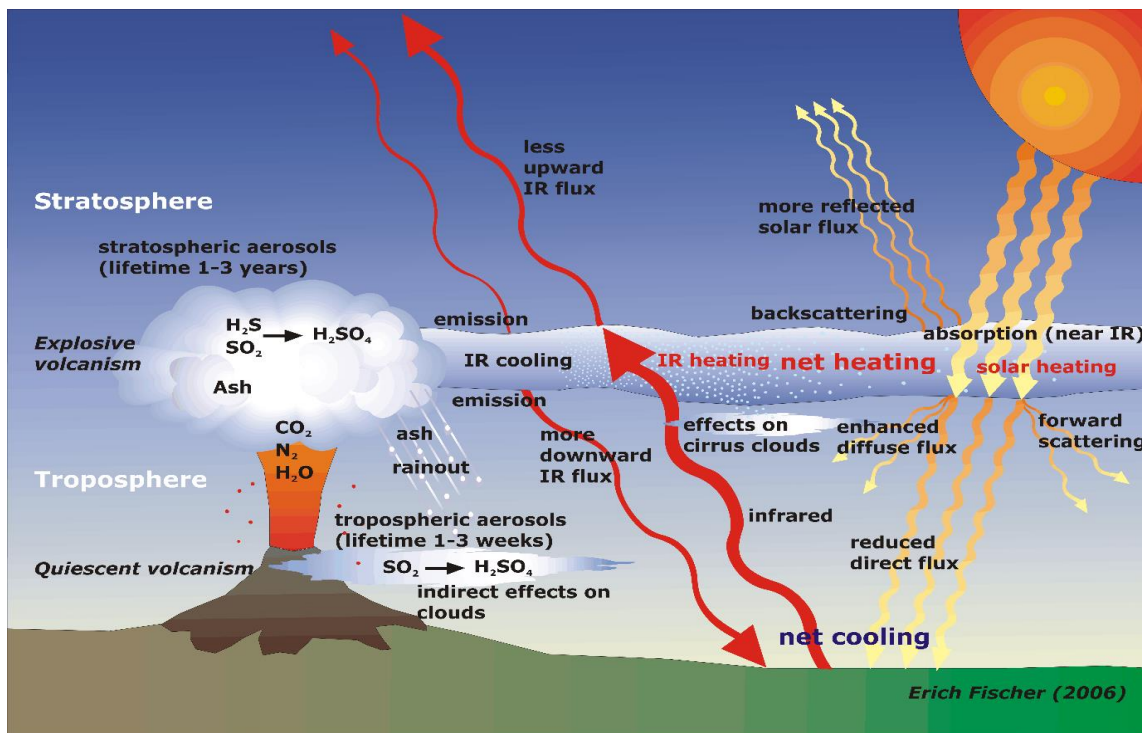


Figure 1-1 Updated from Robock (2000), a schematic diagram of quiescent and explosive volcanic effects on the radiative balance of the Earth (Fischer et al., 2006).

Gravitational sorting of different sized aerosol particles occurs within the volcanic cloud, for example particles growing to larger sizes then descend towards the tropopause and are removed from the stratosphere more readily than smaller particles (Pinto et al., 1989).

The residence time and scattering efficiency of volcanic aerosol particles are strongly size-dependent. Coagulation and condensation grow particles from nanometre sizes to hundreds of nanometres, these microphysical processes strongly influencing the climate impact of a volcanic cloud (Lacis et al, 1992; Timmreck, 2012).

Large injections of SO<sub>2</sub> can also lead to self-limiting chemical effects, as the larger the mass of SO<sub>2</sub> emitted, the slower it oxidises to sulfate aerosol (Pinto et al., 1989). This occurs because in the stratosphere SO<sub>2</sub> is oxidised in the gas-phase by hydroxyl radicals (OH) and OH can become depleted if a large mass of SO<sub>2</sub> is emitted by an eruption, therefore slowing the production of sulfate aerosol (Bekki, 1995; Bekki et al., 1996).

The climate impact of an explosive volcanic eruption is dependent on a number of factors. As already mentioned, injection into the stratosphere means aerosols have a much longer residence time than in the troposphere, prolonging the climate impact.

Volcanic aerosol clouds also absorb outgoing LW radiation from the Earth, causing a heating of the stratosphere (Angell, 1993), which further lofts the aerosol in altitude and can increase lifetime and resultant transport timescales (Young et al., 1994; Graf and Kirchner, 1999; Niemeier et al., 2009; Aquila et al., 2012; Timmreck, 2012). The displacement of a volcanic cloud can sometimes result in greater transport through the lower branch of the Brewer-Dobson Circulation (BDC), therefore decreasing the lifetime of the aerosol cloud with more transport to either hemisphere (Young et al., 1994; Aquila et al., 2012; Marshall et al., 2019). The quasi-biennial oscillation (QBO) phase, which defines easterly or westerly tropical zonal winds in the stratosphere (Baldwin et al., 2001), also has important impacts on the dispersal and climate effects from a major eruption cloud (Trepte and Hitchman, 1993). Mid-latitude to high-latitude eruptions mostly result in aerosol dispersed within the hemisphere of the eruption (Jones et al., 2017), whereas volcanic aerosol from tropical eruptions can disperse to both hemispheres, with stronger transport towards the winter pole (Holton et al., 1995). An easterly QBO phase, such as that at the time of the June 1991 Mount Pinatubo eruption (Hitchman et al., 1994; Punge et al., 2009), acted to confine the Mount Pinatubo cloud to the tropical reservoir, delaying its subsequent transport to the

midlatitudes (Trepte and Hitchman, 1992). These effects are discussed in more detail in Section 2.2.2.

Other indirect consequences for extremely large major eruptions, such as 1815 Tambora, are environmental and subsequent socioeconomic impacts, such as crop failure, famine and pandemics (Sigl et al., 2015; Puma et al., 2015; Toohey et al., 2016). If the eruption is confined to one hemisphere, the eruption may influence the position of the Intertropical Convergence Zone (ITCZ) (Haywood et al., 2013; Iles and Hegerl, 2014). Surface cooling can reduce Asian monsoons (Zambri et al., 2017) and precipitation has been found to decrease on a global scale (Schneider et al., 2009; Iles and Hegerl, 2014).

With recent increases in research into geoengineering as a possible way to mitigate the consequences of climate change due to increasing anthropogenic greenhouse gases (GHGs) (Crutzen, 2006; Irvine et al., 2016; Jones et al., 2017), understanding how large increases in sulfate aerosol disperse and affect our climate is important, for which large explosive eruptions are a natural analogue.

As with SO<sub>2</sub>, ash can have a longer residence time (months to years) in the atmosphere if injected into the stratosphere, as opposed to being rapidly washed out in the troposphere (Niemeier et al., 2009). Ash is usually disregarded in climate model studies of volcanic eruptions, due to the assumption that particles are large and therefore sediment out of the atmosphere within a few days of the eruption, therefore not residing in the atmosphere long enough to have an impact on climate (Pinto et al., 1989; Niemeier et al., 2009; Vernier et al., 2016). However, ash is an important product of an eruption as it can impact on aviation and geochemical cycles (Niemeier et al., 2009; Langmann, 2014). A modelling study using a coupled aerosol-climate model found that including ash in simulations of the 1991 Mount Pinatubo eruption can have a localised heating effect, lofting ash and surrounding aerosol to higher altitudes (Niemeier et al., 2009), therefore increasing the lifetime of both ash and sulfate aerosol particles. Niemeier et al. (2009) found that ash particles 1-15 µm in radius were short-lived. Nevertheless, the inclusion of ash induced lofting of surrounding aerosol and enhanced subsequent dispersion of volcanic aerosol to the northern hemisphere. Studies of more recent eruptions, such as Kelud in 2014, have also shown that ash with a radius of 0.3 µm can persist in the atmosphere for 3 months and account for optical depth (AOD) by up to 28% (Vernier et al., 2016). Vernier et al. (2016) assessed radiative forcing values

calculated for sulfate alone and for sulfate and ash and found that including ash increased the cooling effect by ~20%. The effects of longer lasting <1  $\mu\text{m}$  sized ash within the 1991 Mount Pinatubo eruption have not been investigated and are therefore examined in this thesis.

The 1991 Mount Pinatubo eruption, though well studied, is still the largest, explosive eruption in recent history, with a range of observations including evidence for volcanic ash persisting for up to 9 months after the eruption (Deshler et al., 1992; Vaughan et al., 1994; Pueschel et al., 1994; Deshler, 2016), discussed further in Section 2.3.3. The eruption is therefore an excellent case study for investigating the role of fine ash and input parameters such as QBO phase, injection height and mass of  $\text{SO}_2$  in how these parameters impact vertical dispersion of extinction, AOD, sulfate burden and anomalous heating.

Climate modelling studies of the 1991 Mount Pinatubo eruption have large variations in values used for injection height and initial mass of  $\text{SO}_2$ . Values for the mass of  $\text{SO}_2$  injected from the eruption are usually based around the 14-23 Tg suggested by Guo et al. (2004) based on satellite observations, however, other observational studies suggest 20-30 Tg of  $\text{SO}_2$  (McCormick and Veiga, 1992; McCormick et al., 1995). Model simulations of the Mount Pinatubo eruption generally vary values of injected  $\text{SO}_2$  between 10-20 Tg (Aquila et al., 2012; Dhomse et al., 2014; Sukhodolov et al., 2018).

As mentioned previously, depletion of OH with increased levels of  $\text{SO}_2$  in the stratosphere can lead to self-limiting effects, outlining the importance of representing both chemical and aerosol microphysical processes in climate models for studies of the climate effects of volcanic eruptions. Model estimates of the climatic impact of a volcanic eruption may be considerably overestimated when aerosol microphysics is not included. For example, for the Toba eruption ~74,000 years ago, the surface cooling is estimated at over three times as large for a model without microphysics (Zielinski et al., 1996) than with microphysics (Timmreck et al., 2010). Understanding how variations in injection height and mass of  $\text{SO}_2$  (and subsequently ash) with a coupled aerosol-climate model, affect the vertical distribution of volcanic aerosol, sulfate burden and SAOD is, therefore, necessary in order to understand and infer any resultant dispersion and climatic impact from a major eruption. Assessing how uncertainty in these parameters affects, for instance, sulfate aerosol properties may also enable us to put further constraints on the eruption source parameters of the 1991 Mount Pinatubo

eruption as well as aiding our understanding of future explosive eruptions and possible impacts of geoengineering.

The next section outlines the research rationale for this thesis and thesis aims (Section 1.2 and 1.3) and the following chapters henceforth are as follows: Methodologies used throughout this thesis and a description of UM-UKCA and GLOMAP-mode are described in Chapter 2. Results related to the thesis aims below are discussed in Chapters 3, 4 and 5. Lastly, Chapter 6 outlines conclusions and potential future work.

## **1.2 Research rationale and thesis aims**

Major volcanic eruptions that inject  $\text{SO}_2$  and ash into the stratosphere can have a dramatic impact on the atmosphere and climate (Robock, 2000). These impacts are dependent on many factors including QBO phase, latitude, injection height and the amount of  $\text{SO}_2$  injected (e.g. Marshall et al., 2019).

In the last 10 years, many national climate modelling centres have developed interactive stratospheric aerosol models (Timmreck et al., 2018). The international Stratospheric Sulfur and its Role in Climate activity (SSiRC), is coordinating research towards the next generation of climate models that will apply aerosol schemes to interactively simulate aerosol in the stratosphere as well as the troposphere. The UK composition-climate model was adapted for stratosphere-troposphere aerosol by Dhomse et al. (2014), the resulting interactive stratospheric aerosol configuration of UM-UKCA model validated to accurately represent the 1991 Mount Pinatubo eruption cloud. The model was developed to enact the effects of radiative heating on the global dispersion of the volcanic cloud from Mount Pinatubo (Mann et al., 2015). One important finding from the Dhomse et al. (2014) study was that the Mount Pinatubo case studies achieve agreement with stratospheric aerosol measurements when using the lowermost end of the observed 14-23 Tg range for  $\text{SO}_2$ . This was also found to be the case for several other interactive stratospheric aerosol model simulations of the Mount Pinatubo eruption (Sheng et al., 2015; Mills et al., 2016; Kleinschmitt et al., 2017). These results have indicated that the models do not currently represent an important loss pathway for the  $\text{SO}_2$  and resultant sulfate aerosol in the initial weeks and months after the eruption. The most plausible mechanism suggested, was that of uptake of sulfate aerosol onto ash

acting to scavenge sulfate aerosol, causing that fraction of the cloud to be removed more effectively.

The overall aim of the research conducted in this thesis is to understand the dispersion of volcanic sulfate aerosol and ash following the 1991 Mount Pinatubo eruption and evaluate the use of different initial QBO conditions and the role of injection height, mass of SO<sub>2</sub> and the role of fine ash (super micron, 1-10 µm diameter) and ultra-fine ash (sub-micron, <1 µm diameter). This work uses the Met Office Unified Model (UM) coupled with the United Kingdom Chemistry and Aerosol sub-model (UKCA).

### 1.3 Thesis aims

1. The first research aim of this thesis is to investigate the initial dispersion (June 1991 – February 1992) of the Mount Pinatubo volcanic sulfate aerosol cloud using lidar data and comparing to UM-UKCA simulations. The following questions are addressed:
  - a) What do lidar sites at the time of the Mount Pinatubo eruption tell us about the timing of the initial dispersion of the volcanic cloud?
  - b) How well does the global aerosol-climate model reproduce the vertical distribution of extinction seen in the lidar observations?
  - c) How does varying initial QBO conditions in the model impact comparisons to observations?
2. The second research aim of this thesis is to investigate how varying injection height and SO<sub>2</sub> emission impacts the vertical dispersion of sulfate aerosol, the optical depth and the sulfate burden. The following questions are addressed:
  - a) How does varying SO<sub>2</sub> mass and injection height alter the vertical dispersion and overall height of the eruption cloud?
  - b) Which injection height scenario recreates the closest match to vertical extinction profiles seen in lidar observations?
  - c) How does varying SO<sub>2</sub> mass and injection height increase or reduce resultant sulfate burden and SAOD?
3. The third and final research aim in this thesis is to investigate the role of fine ash during the Mount Pinatubo eruption, following development of the model to include fine ash. The following research questions are addressed:

- a) What is the lifetime of fine ash sizes in the atmosphere in UM-UKCA?
- b) What is the lifetime of ultra-fine ash ( $<0.1 \mu\text{m}$ ) sizes in the atmosphere in UM-UKCA?
- c) How does the inclusion of ash impact on the vertical dispersion of sulfate aerosol and how does this compare to depolarisation data from Aberystwyth?
- d) Does ash alter the results for variations in injection height and mass of  $\text{SO}_2$  for a purely sulfate aerosol cloud?
- e) Does including ash decrease aerosol optical depth and sulfate burden compared to when ash is not included?

## **Chapter 2 Background and literature review**

This chapter provides background information on the stratospheric aerosol layer, including sulfate aerosol and ash, outlining relevant chemical and microphysical processes. The second half of this chapter discusses measurements and modelling studies for the 1991 Mount Pinatubo eruption.

The following sections are: The vertical structure of the atmosphere (Section 2.1); an in-depth description of the stratospheric aerosol layer (Section 2.2) including the formation of sulfate (Section 2.2.1); stratospheric chemistry (Section 2.2.2) and transport (Section 2.2.3); ash in the stratosphere (Section 2.2.4) and a detailed description of our knowledge of the Mount Pinatubo eruption to date, for both observations and modelling studies relevant to this thesis (Section 2.3).

### **2.1 Vertical structure of the atmosphere**

The different layers of the atmosphere are usually explained through their thermal characteristics (Figure 2-1). The troposphere is defined through decreasing temperatures with height up to a minimum point, defined as the tropopause, which varies depending on latitude and season (Brasseur and Solomon, 2005). The stratosphere is located above the tropopause and varies between 8-16 km depending on latitude, up to ~50 km (Brasseur and Solomon, 2005).

The stratosphere is an area of the atmosphere where temperature increases with height due to absorption of ultraviolet radiation from the sun by chemical species, such as ozone, which is abundant in the stratosphere (e.g. Brusseau et al., 2019). The stratosphere is a highly stable area of the atmosphere in terms of the layers of air, due to this increase in temperature with height, meaning vertical mixing is slow in this layer.

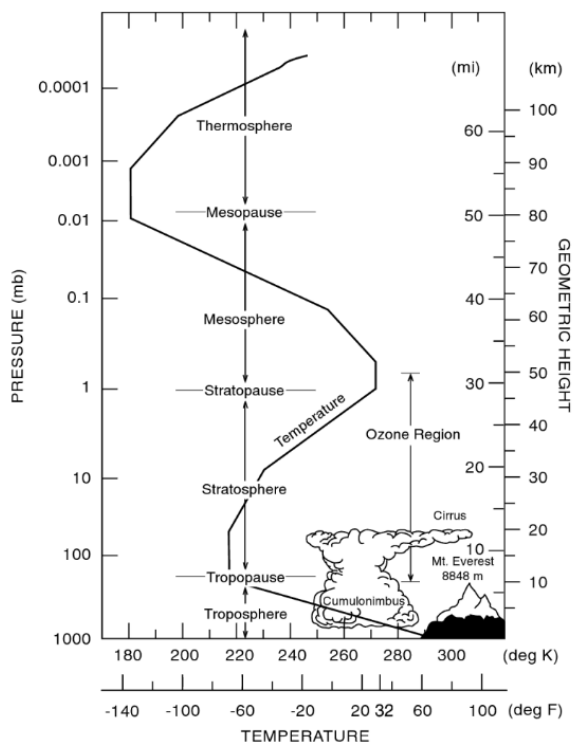


**Figure 2-1 Schematic of the thermal structure of the atmosphere from Brasseur and Solomon (2005).**

## 2.2 Stratospheric aerosol layer

Aerosols in the atmosphere are defined as solid or liquid particles suspended in the air and vary greatly in size from nanometres to  $\sim 100 \mu\text{m}$  (Whitby, 1978; Seinfeld and Pandis, 2006), discussed further in Section 2.2.5. Sources of aerosol are both natural (e.g. volcanic aerosol and dust) and anthropogenic, (e.g. sulfate and soot particles from pollutants) in origin.

The stratosphere has a distinct layer of aerosol particles, often referred to as the ‘Junge’ layer after Christian Junge, whose high-altitude balloon observations in the late 1950s demonstrated the existence of the layer, composed of predominantly liquid sulfate particles (Junge et al., 1961). This layer is more commonly referred to as the stratospheric sulfate layer, which plays an important role in the radiation and chemical balance of the atmosphere, primarily the abrupt increase in the optical thickness of the layer following major eruptions (McCormick et al., 1995) and impacts on the ozone layer (e.g. Solomon, 1999).

The primary sources of sulfur in the volcanically quiescent stratosphere are carbonyl sulfide (OCS), tropospheric  $\text{SO}_2$  and dimethyl sulfide (DMS) from the ocean, which

enter the stratosphere via the tropical tropopause (SPARC, 2006; Kremser et al., 2016). Background levels of sulfur in the stratosphere are 115-130 Gg (Sheng et al., 2015) and can increase by up to 60 times following a major volcanic eruption (Dhomse et al., 2014; Kremser et al., 2016).

Research into the sulfate aerosol layer has helped to further our understanding of the circulation patterns in the stratosphere, as well as the sources of sulfate and their chemical and microphysical processes, along with their ultimate removal from the stratosphere (Kremser et al., 2016). An important distinction from gas-phase species in the stratosphere is that aerosol particles are continually sedimenting out of their host air masses, and so their chemical and microphysical processes play a first-order role in determining the rate of their ultimate removal from the stratosphere (Kremser et al., 2016).

The vertical distribution of stratospheric particles is controlled by the complex interplay of chemical reactions, global circulation and the associated growth by condensation and coagulation, microphysical processes being a key determinant for sedimentation rate (SPARC, 2006; Kremser et al., 2016). Therefore, to have an understanding of sulfate aerosol in the stratosphere we need to understand the formation processes, microphysics and the general circulation of the stratosphere, discussed in the following sections.

### **2.2.1 Sulfate aerosol formation and microphysics**

The main source of aerosol particles in the stratosphere is their formation in the upper troposphere via binary homogenous nucleation of sulfuric acid and water (Kulmala et al., 1998). Binary homogenous nucleation occurs when the equilibrium vapour pressure is exceeded (supersaturated) (Kulmala et al., 1998; Vehkamäki et al., 2002). With the slow, but continual, source of SO<sub>2</sub> from OCS, the vapour partial pressure of H<sub>2</sub>SO<sub>4</sub> is usually supersaturated and the condensation of H<sub>2</sub>SO<sub>4</sub> steadily provides additional mass to existing particles (Seinfeld and Pandis, 2006; Kremser et al., 2016). The primary regions for nucleation are in the tropical tropopause layer (TTL), which are then transported upwards into the stratosphere (Brock et al., 1995) and can also form seasonally at high-latitudes in late winter into early spring (Campbell et al., 2014).

An increasingly recognised stratospheric particle formation pathway, in addition to homogenous nucleation, is heterogenous nucleation, which forms sulfate aerosol particles by co-condensation of H<sub>2</sub>SO<sub>4</sub> vapour and H<sub>2</sub>O vapour onto existing non-sulfate

particles such as meteoritic smoke particles or ash (Pueschel et al., 1994; Langmann, 2014; Kremser et al., 2016).

Newly forming particles grow rapidly from an initial nm size up to ~30-50 nm in diameter in a few hours via condensation and coagulation with particles of a similar size (Seinfeld and Pandis, 2006). Coagulation of these newly formed particles also occurs through the collision with particles of larger sizes, which may vary in size and composition, to form larger, single particles, also acting as a sink of these newly formed particles by sticking to larger particles (Jacob, 1999). As particles grow larger to ~50-100 nm, the (Brownian) collision rate reduces, and the contribution coagulation makes to the overall particle is reduced (Seinfeld and Pandis, 2006). Nucleation and coagulation processes occur rapidly at high number concentrations, such as following a large volcanic eruption (Deshler, 2008). Condensational, growth and evaporative processes occur throughout the lifetime of stratospheric aerosol and are more dependent on concentrations of  $\text{H}_2\text{SO}_4$  (Kremser et al., 2016).

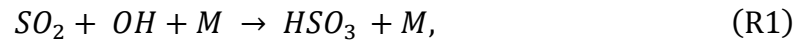
Sulfate aerosol particles transported within the stratospheric circulation may either be lost through transport across the tropopause (including the sedimentation effect) or by evaporation if transported to higher altitudes within the stratosphere. Whilst evaporation removes sulfate to the gas-phase between 32-35 km in altitude (Turco et al., 1979; Weisenstein et al., 1997), heterogeneously nucleated particles will remain at the size of their involatile core, whereas homogeneously nucleated pure sulfuric particles will evaporate completely. The gas-phase sulfuric acid that results from evaporation may be re-condensed onto other particles or form new particles at higher latitudes (Hofmann et al., 1985; Mills et al., 2005; Campbell and Deshler, 2014), whereas sedimentation removes aerosol permanently from the stratosphere, as it is moved downwards through the tropopause.

### **2.2.2 Stratospheric sulfur chemistry**

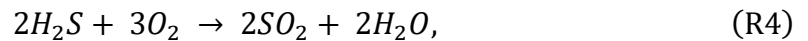
Explosive volcanic eruptions are the largest source of  $\text{SO}_2$  to the stratosphere (SPARC, 2006; Kremser et al., 2016). Volcanic sulfate aerosols are both primary (found near the vent) and secondary volcanic products (Allen et al., 2002), formed when the  $\text{SO}_2$  emitted from the volcano is oxidised to gas phase sulfuric acid ( $\text{H}_2\text{SO}_4$ ) (Seinfeld and Pandis, 2006). Oxidation to sulfate aerosols occurs with an e-folding time (time for the cloud to decrease to 1/e of its original mass) of roughly one-month (Bluth and Rose, 2004; Timmreck, 2012). The abrupt increase in  $\text{H}_2\text{SO}_4$  vapour due to explosive

volcanic eruptions creates new sulfate aerosol particles (nucleation) which can then condense onto particles, such as ash and existing stratospheric aerosol (Korhonen et al., 2003), growing them to larger sizes (e.g. Hamill et al., 1997), as described in Section 1.2.1.

The main sulfur chemistry reaction-set producing the sulfuric acid vapour that drives these particle changes is shown below (Seinfeld and Pandis, 2006):



An additional, smaller volcanic source of  $SO_2$  is from the oxidation of hydrogen sulfide ( $H_2S$ ). There is also a continual background source of  $SO_2$  from the photo-dissociation of carbonyl sulfide (OCS) (Crutzen, 1976; Brühl et al., 2012). In both cases, the additional source of stratospheric  $SO_2$  subsequently oxidises to form stratospheric sulfate aerosol:



At altitudes  $>35$  km, where the equilibrium vapour pressure of sulfuric acid becomes sufficiently high, meaning that condensation and nucleation cannot occur (Hamill et al., 1997; Seinfeld and Pandis, 2006), an important sink of  $H_2SO_4$  vapour is its subsequent photodissociation to sulfur trioxide:



The source of sulfur trioxide from the  $H_2SO_4$  photolysis is then further photolyzed to reform  $SO_2$ , with this process occurring particularly in the downwelling branch of the BDC (Mills et al., 2005).

The presence of a major volcanic aerosol cloud in the stratosphere greatly perturbs a range of different trace gases, both via heterogenous chemistry on particles and also from circulation-driven changes from tropical stratospheric heating. For example, hydrolysis of di-nitrogen pentoxide ( $N_2O_5$ ) to nitric acid ( $HNO_3$ ) occurs on stratospheric sulfate particles, volcanic clouds thereby reducing  $NO_x$  within the overall reactive

nitrogen family ( $\text{NO}_y$ ) (Fahey et al., 1993; Aquila et al., 2013). The reaction of dinitrogen pentoxide to nitric acid is:



On the surface of sulfate aerosols, reaction R8 is assumed to occur with rate constant:

$$k_{\text{R8}} = \frac{\gamma}{4} \left( \frac{8kT}{\pi m_{\text{N}_2\text{O}_5}} \right)^{1/2} A_p$$

Where  $\gamma$  is reaction efficiency,  $m_{\text{N}_2\text{O}_5}$  is the molecular mass of  $\text{N}_2\text{O}_5$ ,  $(8kT/\pi m_{\text{N}_2\text{O}_5})^{1/2}$  is the mean molecular speed of an  $\text{N}_2\text{O}_5$  molecule and  $A_p$  is the surface area per unit volume ( $\text{cm}^2 \text{cm}^{-3}$ ) of the aerosol (Seinfeld and Pandis, 2006).

Activation of chlorine nitrate ( $\text{ClONO}_2$ ) on volcanic aerosol particles leads to ozone destruction, as observed following the 1982 El Chichón eruption (Hofmann and Solomon, 1989), outlined by the following reaction and schematic (Figure 2-2):

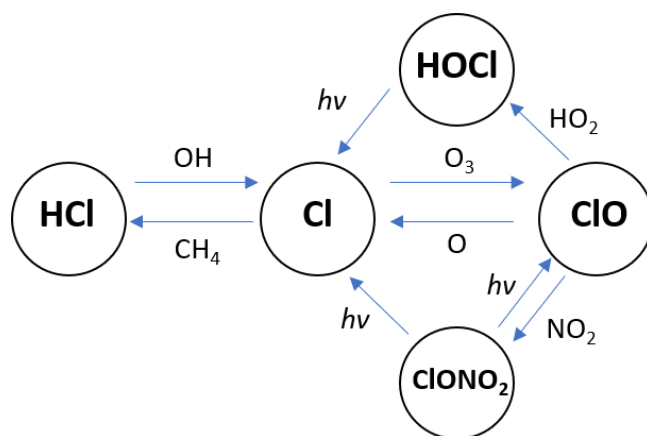


**Figure 2-2 Simplified schematic of the cycle of ClOx ozone depletion.**

The rates of these heterogeneous reactions are roughly proportional to the aerosol surface area, with a saturation effect observed from the  $\text{N}_2\text{O}_5$  hydrolysis following the 1991 Mount Pinatubo eruption (Fahey et al., 1993). Also in the Mount Pinatubo case, ozone decreased during 1992 by 5-10%, observed by the Total Ozone Mapping Spectrometer (TOMS) in the northern hemisphere, whilst increased ozone was detected at southern mid to high latitudes (Zerefos et al., 1994; Randel et al., 1995). The effects on trace

gases by circulation are largely due to the heating of the tropical stratosphere after major tropical eruption, with a tropical ozone decrease occurring as a result of increased upwelling bringing ozone-poor air up into the stratosphere (Kinne et al., 1992) and strengthened circulation then causing greater transport to mid-latitudes (e.g. Dhomse et al., 2015).

### **2.2.3 Stratospheric circulation and transport**

Aerosol is able to spread globally in latitude within weeks due to the presence of strong zonal winds ( $\sim 35$  m/s) in the stratosphere (Bluth et al., 1992). The large-scale transport of aerosol in the stratosphere is dominated by the BDC (Figure 2-3), which is a wave-driven circulation that involves tropical upwelling, transport through the mid-latitudes and downwelling at the poles (Brewer, 1949; Holton et al., 1995; Bönisch et al., 2011; Butchart, 2014). The BDC is driven by breaking Rossby waves and, to a lesser extent, gravity waves with preferential transport of aerosol to the winter hemisphere creating a strong poleward downwelling (Holton et al., 1995). Mixing and transport within the stratospheric midlatitudes also occurs most prominently in the winter hemisphere, through isentropic surfaces (Figure 2-3) (Holton et al., 1995; Butchart, 2014).

A “tropical pipe” exists in the stratosphere at  $\sim 21$ -30 km which weakens mixing between the tropics and the midlatitudes (Trepte and Hitchman, 1992; Plumb, 1996). A restriction in mixing allows stratospheric aerosol to build up and form a “tropical aerosol reservoir” following tropical and near-tropical eruptions (Trepte and Hitchman, 1992; Grant et al., 1996). In volcanically quiescent periods, the tropical tropopause is the main source of material to the tropical aerosol reservoir (Brewer, 1949; Grant et al., 1996). Material is transported to midlatitudes sporadically during events such as hurricanes, which can disturb the tropopause region (Trepte and Hitchman, 1992; Trepte et al., 1993; Grant et al., 1996).

Another phenomenon that exists in the stratosphere is the QBO which is an oscillation of downward propagating winds in the stratosphere that vary between easterly and westerly roughly every 28 months (Baldwin et al., 2001).

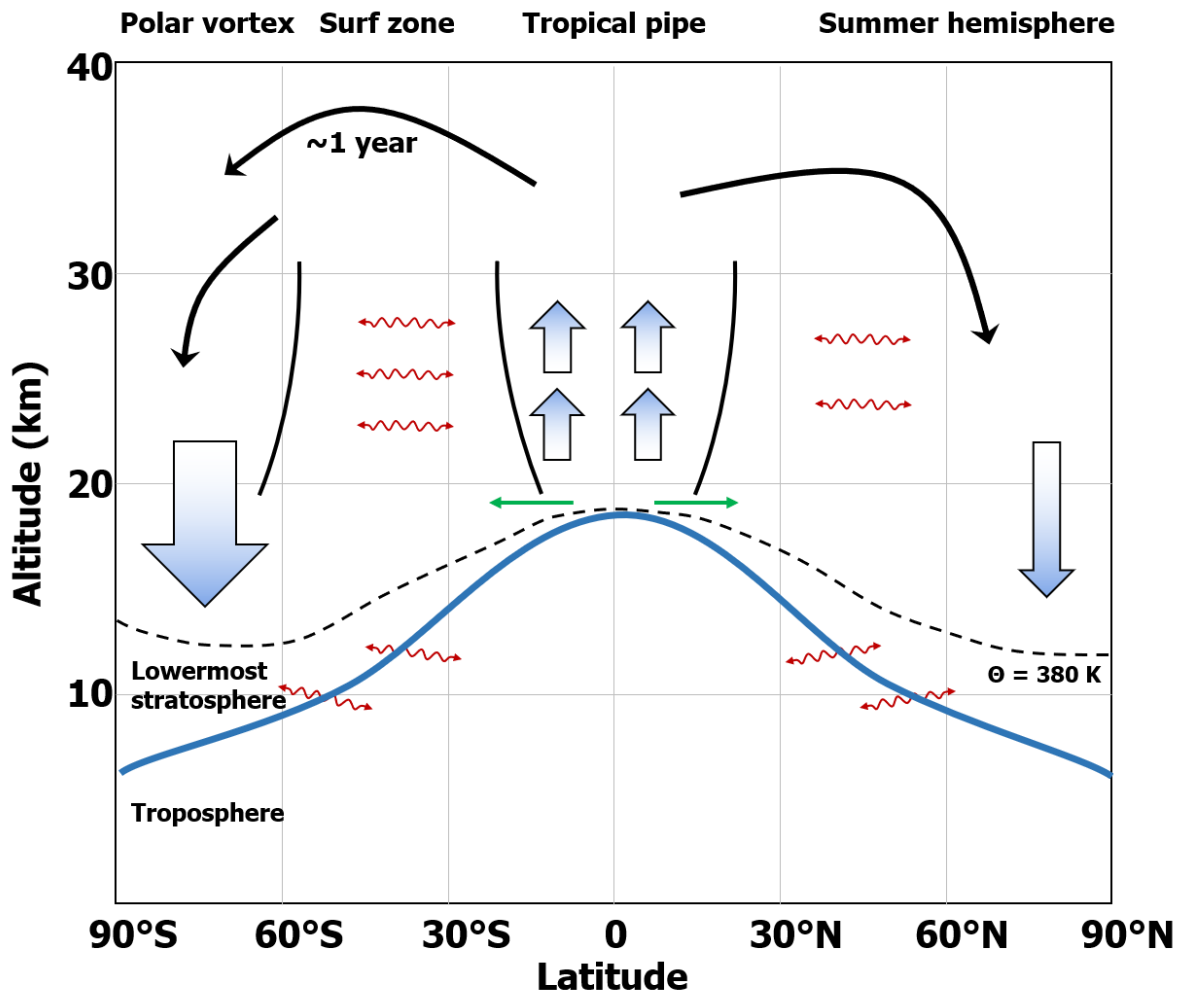


Figure 2-3 Schematic of stratospheric circulation for a Northern hemisphere summer, adapted from Bönisch et al. (2011) and Holton et al. (1995). The solid blue line denotes the tropopause. The dotted black line marks the 380 K potential temperature, above which is entirely stratospheric. Arrows indicate overall transport with arrow widths corresponding to relative circulation strength. Lines either side of the tropics and in the winter hemisphere show the tropical pipe and the edge of the polar vortex, respectively. Green arrows indicate lower stratospheric transport below the tropical pipe and wiggly red arrows denote isentropic transport.

During the westerly QBO phase, the tropical pipe is wider than in the easterly phase, allowing aerosol ~15-22 km in altitude to be more readily transported to the poles (Trepte et al., 1993; Grant et al., 1996), whereas during the easterly phase transport is inhibited as the tropical pipe is narrower (Hitchman et al., 1994; Punge et al., 2009) and material above ~22 km is confined to the tropics (Trepte et al., 1993). The width of the tropical pipe can also be found to vary seasonally, as Grant et al. (1996) found when analysing satellite and airborne lidar data following the Mount Pinatubo eruption. They observed a narrower tropical pipe (~1° latitude in width) in the winter hemisphere and wider (up to 20° in width) in the summer hemisphere during an easterly QBO. The

phase of the QBO, therefore, has a large effect on the meridional transport of aerosol from a tropical eruption and the movement of aerosol out of the tropical reservoir. Largest areas of circulation occur through and out of the tropical pipe, however, shallower branches below the tropical pipe at approximately 20 km allows year-round transport of aerosol to both hemispheres.

Aerosol can be removed through tropopause folds (Shapiro, 1980), areas where stratospheric air intrudes into the troposphere, inducing rapid mixing and rapid poleward movement (e.g. Kremser et al., 2016) and understood to be the dominant process for stratospheric aerosol removal (SPARC, 2006). Aerosol confined within the tropical pipe and moved through the larger, overarching branches of the BDC, however, may stay in the stratosphere for a number of years and be transported around the globe.

#### **2.2.4 Ash in the stratosphere**

Ash is defined as very small ejected rock particles (<2 mm), with very fine ash expressed as particles <30  $\mu\text{m}$  in diameter, and sub-classes classified as super-micron (>1  $\mu\text{m}$  in diameter) and sub-micron (<1  $\mu\text{m}$  in diameter) (Rose and Durant, 2009). Volcanic ash is primarily formed due to explosive eruptions, measured as >4 on the Volcanic Explosivity Index (VEI), but can be found from more effusive eruptions (Newhall and Self, 1982). As magma rises, bubbles form where dissolved volatiles (e.g.  $\text{H}_2\text{O}$  and  $\text{SO}_2$ ) become separated from the magma under decompression. The faster the decompression, the less time bubbles have to be released resulting in more fragmentation of the magma and surrounding rock and, therefore, smaller rock fragments (e.g. Cashman and Scheu, 2015).

Ash particles are heavier and typically larger than sulfuric acid droplets, with coarse ash (larger than 1  $\mu\text{m}$ ) sedimenting out of the plume during the first week post-eruption (Bluth and Rose, 2004). Nevertheless, due to the nature of these particles, they absorb solar radiation and thus heat their surroundings on a short-term, localised scale (up to 20 K/day) (Niemeier et al., 2009). This local heating adds to the long-wave absorption from sulfuric acid particles (1.5-2 K/day) (R.E. Young et al., 1994; Niemeier et al., 2009; Jones et al., 2016).

##### **2.2.4.1 Ash core particles**

Ash-core particles occur when the co-existence of ash and  $\text{SO}_2$  causes some ash particles to become coated in sulfuric material, consequently becoming a sulfate particle

with a fine-ash inclusion (Deshler, 2016). These particles have been observed for up to 3 months after the Kelud 2014 eruption (Vernier et al., 2016), but may potentially persist for longer in the atmosphere for an explosive eruption such as Mount Pinatubo 1991 (Pueschel et al., 1994; Deshler, 2016).

A recent re-examination of balloon measurements after the 1991 Mount Pinatubo eruption (discussed in Section 2.3.3) shows that the finest ash particles (smaller than 1  $\mu\text{m}$  diameter) were measured in the atmosphere up to a year following the eruption as ash-core sulfuric particles, which are larger and sediment faster than typical non-ash included sulfuric particles (Deshler, 2016).

### 2.2.5 Residence time and aerosol size modes

When volcanoes inject ash and  $\text{SO}_2$  into the stratosphere, the abrupt enhancement to the stratospheric sulfate aerosol layer can remain elevated for several years due to the long (1-3 years) residence time of air masses within the stratosphere (Kremser et al., 2016). Residence time is also related to particle size, as discussed here and outlined in Pinto et al. (1989).

Aerosol size distributions vary from 0.001 to 2000  $\mu\text{m}$  size particles, spanning aerosols of varying size, composition and number concentrations (Seinfeld and Pandis, 2006). Size distributions are typically represented by “modes” with log-normal distributions (Figure 2-4).

*Nucleation* mode is the first stage of aerosol growth and is defined as the smallest particle diameter mode, with aerosols forming at 1-10 nm in diameter (e.g. Kulmala et al., 2004). Once formed, they can be categorised into other modes depending on their size. Fine particles can be categorised under *Aitken* and *Accumulation* mode, with *Aitken* mode ranging from particles 0.001 – 0.1  $\mu\text{m}$  (1-100 nm) in diameter and *Accumulation* mode ranging from 0.1 - 1  $\mu\text{m}$  (100-1000 nm) in diameter (Willeke and Whitby, 1975; Kulmala et al., 2004; Seinfeld and Pandis, 2006). During volcanically perturbed periods, growth from *Nucleation* and *Aitken* modes occurs much faster, leading to *Accumulation* mode particles becoming abundant in the stratosphere (e.g. Timmreck, 2012; Kremser et al., 2016).

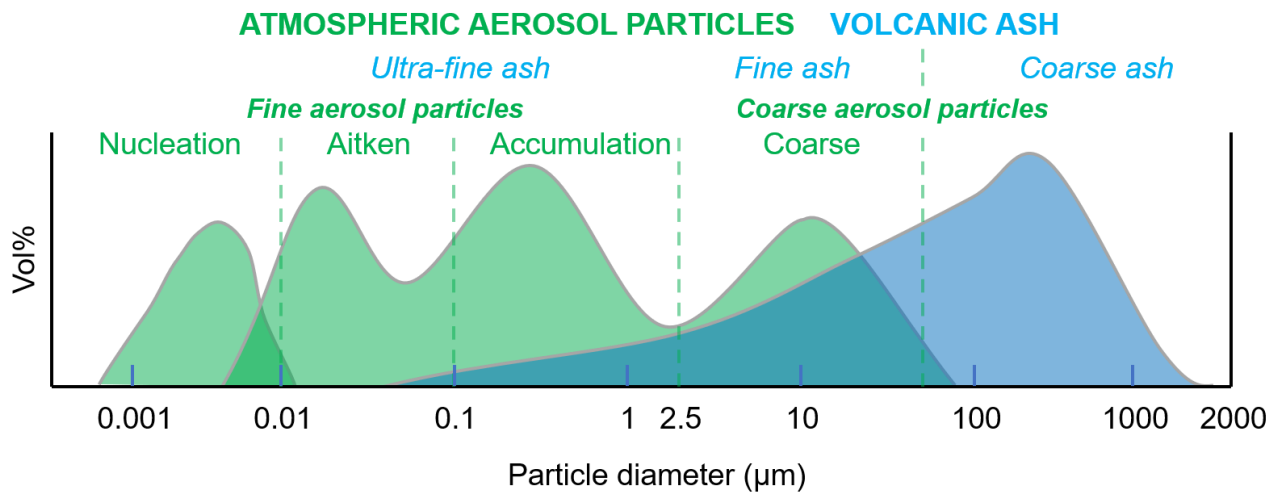


**Figure 2-4** Aerosol size distribution and modes for atmospheric aerosol particles, adapted from Durant et al. (2010).

*Coagulation* and *Condensation* are the main mechanisms by which aerosol particles grow and move between size modes (e.g. English et al., 2013). Condensational growth is based on water and  $\text{H}_2\text{SO}_4$  uptake, and hence is mostly controlled by temperature and the thermodynamic elements of  $\text{H}_2\text{SO}_4$ .

Larger particles at  $\sim 1 - 100 \mu\text{m}$  in diameter are defined as *Coarse* particles, primarily consisting of sea salt, volcanic ash particles, dust and plant particles. Directly emitted fine ash is the main source of coarse mode particles in the stratosphere, as sulfuric particles sediment out before growing into the coarse size range.

Aerosols are removed through the processes of wet and dry deposition. Wet deposition, also referred to as “washout”, occurs when aerosols condense onto cloud condensation nuclei (CCN) and are rained out in clouds. Dry deposition usually occurs when particles grow large enough and sediment out of the atmosphere due to gravity (Bluth and Rose, 2004). Bluth and Rose (2004) outline the effect of size on fallout rates for particles from 1-50  $\mu\text{m}$  in diameter from an altitude of 10 km, indicating that  $<1 \mu\text{m}$  particles can persist for years in the atmosphere.

Fall speeds increase in the stratosphere, with spherical 0.1  $\mu\text{m}$  in radius (0.2  $\mu\text{m}$  in diameter) size particles of density  $1000 \text{ kg m}^{-3}$  increasing in speed from  $\sim 10^{-4} \text{ cm s}^{-1}$  at the surface to  $\sim 10^{-2} \text{ cm s}^{-1}$  at 30 km (Junge et al., 1961; Kasten, 1968). Figure 2-5 outlines the differences between fall speeds for different sized particles with densities of 1000 and 2000  $\text{kg m}^{-3}$ , respectively.

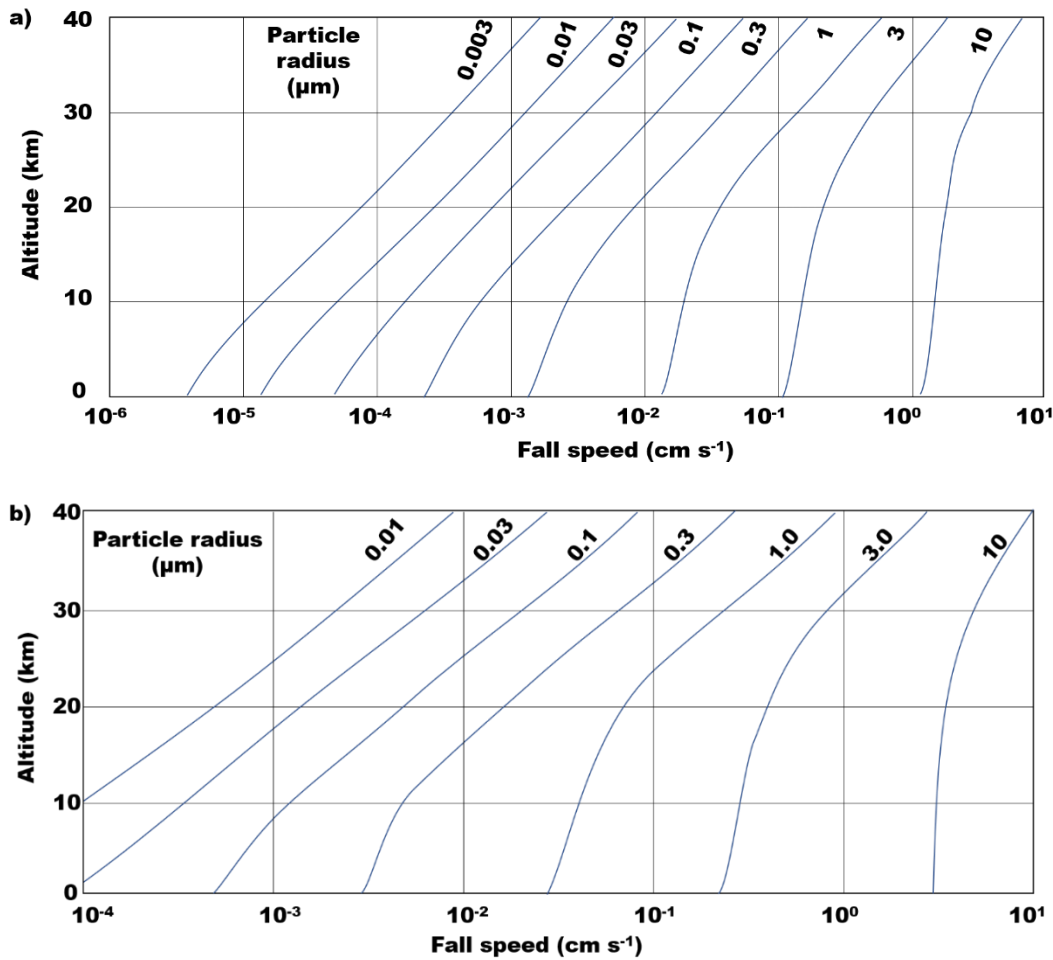


Figure 2-5 Fall speeds between the surface and 40 km for particles ranging in size from 0.003 and 10 μm with density a) 1000 kg m<sup>-3</sup> (Kasten et al. (1968)) and b) 2000 kg m<sup>-3</sup> (Junge et al. (1961)). Figures are recreations of Figure 1 from Kasten et al. (1968) and Figure 2 from Junge et al. (1961), respectively.

Ash sizes ~100 μm in diameter have densities closer to 1000 kg m<sup>-3</sup> and ash particles <10 μm in diameter have densities closer to 2000 kg m<sup>-3</sup> (2000-2700 kg m<sup>-3</sup>) (Beckett et al., 2015).

Langmann (2014) outlined how modelled ash particles (>1 μm in diameter) influence the microphysical evolution of sulfate aerosol for the 1991 Mount Hudson eruption. Without ash present, nucleation mode is dominant in the first day following the eruption, closely followed by the Aitken mode after 2 days and then the Accumulation mode ~6 days after the eruption (Figure 2-6a). When ash is present, the coarse mode is most dominant at first, diminishing

nucleation mode by ~20% (Figure 2-6b). Fast sedimentation of larger ash particles in as little as a few hours (Textor et al., 2003) means the Accumulation and Aitken modes take over in a comparable size distribution to the non-ash scenario.

Langmann (2014) does not account for sub-micron sized ash particles, however. Ash may influence climate through these sub-micron diameter sized particles (~100 nm) as an inclusion within sulfuric particles, as observed from aircraft (Pueschel et al., 1994) and balloon-measurements (Deshler, 2016) (Section 2.2.4.1).

These ash-core sulfuric particles are larger, with faster sedimentation which may cause a larger proportion of the emitted sulfur to be removed in the first few months after major eruptions, when ash is present. Therefore, climate models that do not account for volcanic ash may be creating an unrealistic size distribution in the first few weeks following an eruption and may be missing a crucial sulfur removal mechanism.

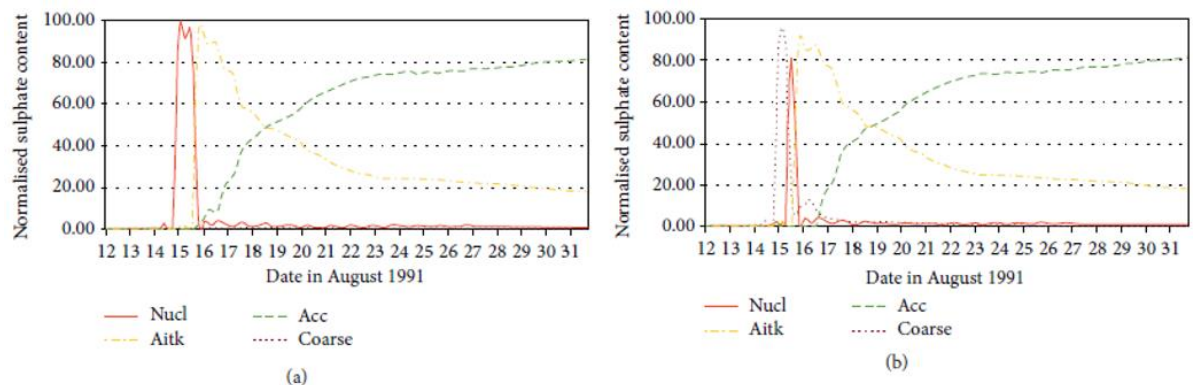


**Figure 2-6** Size distributions from Langmann (2014) of modelled aerosol modes for the 1991 Mount Hudson eruption for a) without ash and b) with ash. Line represent modes, nucleation (red), Aitken (yellow), accumulation (green) and coarse (brown).

## 2.2.6 Aerosol extinction and optical depth

Aerosols scatter and absorb radiation, depending on refractive index, particle size and the incident radiation wavelength (Seinfeld and Pandis, 2006). When aerosols are assumed spherical, Mie theory can be used to calculate aerosol scattering and absorption (Seinfeld and Pandis, 2006). Extinction is defined as the sum of the scattering and absorption of an aerosol and is most efficient when the wavelength of radiation is similar to the size of the atmospheric particle itself (Seinfeld and Pandis, 2006).

Aerosol optical depth (AOD) is the vertical sum of extinction and is a commonly used metric for determining the amount of aerosol in the atmosphere. Stratospheric aerosol

optical depth (SAOD) is commonly used in volcanic modelling studies to determine the optical depth associated with stratospheric aerosol (e.g. Schmidt et al., 2018). Both extinction and SAOD are used throughout the results chapters in this thesis.

## 2.3 Mount Pinatubo 1991

This thesis focuses on the 1991 Mount Pinatubo eruption, as it is still the largest explosive eruption in recent history and was the first major (VEI=6) explosive eruption to be recorded by multiple types of satellite instruments as well as ground-based lidar, balloon-borne particle counters and surface radiation instruments (Kremser et al., 2016; Jones et al., 2016).

Mount Pinatubo is situated at 15°N in the Philippines and on the 12-14<sup>th</sup> June 1991, a series of small eruptions were noted with associated pyroclastic flows before it erupted explosively on June 15<sup>th</sup> 1991 (Wolfe and Hoblitt, 1996). One eruption on 14<sup>th</sup> June reached ~21 km altitude before the most explosive eruption for more than 50 years occurred on 15<sup>th</sup> June with around 9 hours of continuous, explosive activity (Lynch and Stephens, 1996). Self et al. (1996) suggest an ash-related column above 17 km was observed using temperature measurements in the early hours of 16<sup>th</sup> June, along with ash layers ~ 11 km in altitude noted due to plane engine failures.

### 2.3.1 Measurements

The main eruption sent approximately 14-23 Tg of SO<sub>2</sub> (estimated 20 Tg (Guo et al., 2004)) into the atmosphere more than 25 km in altitude (Bluth et al., 1992; Hansen et al., 1992). These values were deduced by comparing the ultraviolet satellite data from TOMS instrument on board the Nimbus-7 satellite and infrared SO<sub>2</sub> data from the High-resolution Infrared Radiation Sounder/2 (HIRS) on board NOAA's Television Infrared Radiation Sounder (TIROS) Operational Vertical Sounder (TOVS). TOMS observes the whole Earth each day, crossing the equator at every 26 degrees of longitude. Guo et al. (2004) estimate 50 Tg of fine ash (1-15 μm) was emitted from the eruption, compared to just 3 Tg from Cerro Hudson which erupted in August of the same year, by comparing satellite measurements from TOVS and Advanced Very High Resolution Radiometer (AVHRR). The aerosol from this eruption circled the globe within 2 weeks, as shown by Bluth et al. (1992) using TOMS. The Stratospheric Aerosol and Gas Experiment II (SAGE II) satellite measurements suggested a peak in global aerosol mass burden of 30 Tg (McCormick and Veiga, 1992), including sulfuric acid and water,

with the enhanced aerosol residing between 20 and 27 km in altitude, mean tropical altitude of 22 km (McCormick et al., 1995). The SAGE II measurements have large errors associated with the initial months following the eruption, as instrument ranges were exceeded in the tropics during June-August 1991 (e.g. Antuña et al., 2002) with no other truly tropical measurements in June 1991 (Thomason et al., 2018).

Considering the transport of the Mount Pinatubo cloud, although the volcano is situated at 15°N, SAGE II and AVHRR (on board the NOAA-11 satellite) measurements suggest the large volume of injected material initially moved south during its longitudinal transport over the first few weeks, centred at around 10°S, with little meridional transport, leading to the cloud being confined to 20°S to 30°N for the first month (McCormick and Veiga, 1992; Long and Stowe, 1994). The initial phase of southward transport, and the subsequent transport to both hemispheres was unusual, with previous major tropical eruptions seen to disperse mostly within their original hemisphere (McCormick et al., 1995). SAGE II measurements indicated maximum AOD of 0.2 at 10°S, with tropospheric weather systems, the QBO and localised heating causing enhanced upwelling or “self-lofting” of the plume caused by the absorption of infrared radiation by the aerosol (Trepte et al., 1993; R.E. Young et al., 1994; McCormick et al., 1995).

Trepte et al. (1993) outline two atmospheric regimes seen to have occurred during the 10 months after Mount Pinatubo erupted. The first “lower regime” occurring just above the tropopause sending aerosol to lower altitudes and polewards and the second “upper regime” transporting aerosol out of the aerosol reservoir (20°S-30°N) through planetary wave activity, particularly when winter circulation became more prominent.

The initial southward transport in the first phase is thought to be due to anticyclonic tropospheric weather circulation. However, during the second phase, Mount Pinatubo was also unusual with much more southern hemisphere transport than following the 1982 El Chichón eruption, despite their similar latitudes (Trepte and Hitchman, 1992). This second phase effect of southern hemisphere transport is thought to be due to stronger westerly winds in the tropics during 1982 (westerly QBO phase) encouraging northward transport compared to the easterlies which occurred during 1991 (Trepte and Hitchman, 1992; Jones et al., 2016).

The radiative effects of Mount Pinatubo were measured by the Earth Radiation Budget Satellite (ERBS) instrument (Minnis et al., 1993; Wong et al., 2006) and clearly indicate

the short-wave cooling effect. A peak of  $8 \text{ W m}^{-2}$  higher tropical-mean ( $20^{\circ}\text{S}$ - $20^{\circ}\text{N}$ ) outgoing short-wave flux at the top of the atmosphere (TOA) was measured (Wong et al., 2006) and a global radiative flux anomaly of  $-3 \text{ W m}^{-2}$  (Minnis et al., 1993), compared to the 1985-1989 mean.

The Mount Pinatubo eruption impacted stratospheric ozone (Solomon, 1999) with unprecedented reductions in stratospheric ozone measured in mid-latitudes such as a 25% reduction in winter 1992-1993 (Hofmann et al., 1994). 6-8% ozone reduction at the equator was also noted and was dynamically driven, as a result of the heated aerosol layer bringing lower-ozone air from below (McCormick et al., 1995). The effect offsets some of the temperature increase in the tropical stratosphere (McCormick et al., 1995) and also lifted ozone-rich air to mid-latitudes (Kinne et al., 1992; Dhomse et al., 2015).

The 1991 Mount Pinatubo eruption is the best characterised VEI 6 eruption to date, as a result of the increased volume of measurements available from that time compared to the other large eruptions such as El Chichón (1982) and Mount Agung (1963) (Arfeuille et al., 2013a). The aerosol cloud was observed by SAGE II and AVHRR, although the eruption was so intense that some measurements, such as SAGE II, could not receive signals as the eruption cloud had values greater than the upper signal range of the instruments (Antuña et al., 2002). Antuña et al. (2002) discuss the use of lidar measurements from Mauna Loa, Hawaii and Hampton, Virginia to fill the data gaps, which they found to agree relatively well, with the gap-fill now used to compare with model simulations, such as in Dhomse et al. (2014).

From June-October 1991, the Japanese lidar network ( $26$ - $45^{\circ}\text{N}$ ) noted the Mount Pinatubo cloud signal with a slight increase (background is  $\sim 1$ ) in backscatter ratio of 2 as early as June 28<sup>th</sup> 1991, then observing the signal above 20 km with a cloud depth of 2 km on July 15<sup>th</sup> 1991 (Akiyoshi et al., 1993). The volcanic cloud was not seen again until August 6<sup>th</sup> 1991 and subsequently rapidly increased in backscatter ratio value to a peak of 12.9, with a deeper cloud of 7 km, coincident with the change to a westerly QBO (Akiyoshi et al., 1993). Winker and Osborne (1992a) outline NASA Electra lidar observations showing layering that occurred in the stratosphere shortly after the 1991 Mount Pinatubo eruption between 17 and 26 km in altitude. These observations showed that 3-4 weeks after the eruption the cloud was spatially inhomogeneous and well layered. Winker and Osborn (1992b) also show depolarisation over 10% at 23.5 km, indicative of non-spherical particles or differing chemistry in particles within the layer.

Ship-borne lidar data covering latitudes of 8°S-60°N from July 1991 – April 1992 show AOD values up to 0.2, with maximum extinction values of 0.08/km at 18°N (Avdyushin et al., 1993). Ansmann et al. (1997) observed similar AOD values of 0.25 in Spring 1992 with a calculated 1.9 km/year decrease in aerosol and increase from 0.2  $\mu\text{m}$  effective radius particles in August 1991 to 0.5  $\mu\text{m}$  in October 1991 - February 1992. At a latitude of 52°N, Vaughan et al. (1994) noted an increase in AOD of 0.02 to 0.2 between August 1991 and March 1992, values which concur with those seen in Ansmann et al. (1997) and Avdyushin et al. (1993).

Investigations into stratospheric aerosols have become increasingly prominent over recent years, with enhanced observational and modelling capability allowing more in-depth knowledge of our atmosphere and the processes that occur within it (Kremser et al., 2016). Much of the observational data before 1980 consisted of estimates taken from volcanic evidence (1850-1882), solar irradiance at northern mid latitudes (1883-1959), solar eclipse and direct solar radiation measurements in both hemispheres (1960-1978) (Sato et al., 1993). The first in-situ measurements were in the form of balloon-borne measurements (e.g. Junge and Manson (1961)) and before 1960 only ground-based remote sensing observations were available.

Satellite observations that can specifically measure volcanic gas species are more prominent today, with 19 currently in use (Carn et al., 2016), however, before 1980 there were only three (Carn et al., 2016). Global vertical profiles of stratospheric aerosol can now be measured using comparisons and combinations of different observational data, for example space-borne lidar, such as Cloud Aerosol Lidar with Orthogonal Polarisation (CALIOP) and solar occultation, such as SAGE II (Vernier et al., 2011). Aerosol Robotic Network (AERONET) observations using ground-based sun photometer measurements (Ridley and Solomon, 2014) are another demonstration of the relatively recent expansion in atmospheric observational measurement capability, useful both for more recent observations and to help validate previous datasets.

The use of Light Detection and Ranging (lidar) for observing aerosol patterns in the atmosphere dates back to the 1960s, with Fiocco and Grams (1964) observing the previously sampled 20 km aerosol layer using lidar analysis. Lidar has since been a vital tool used to measure volcanic signals, observing the occurrences of eruptions and the transport of resulting clouds, as well as observing background conditions when not perturbed by eruptions (Jäger, 2005). Lidar instruments emit laser light and detect the

light backscattered by objects, such as atmospheric particles, towards the instrument. From these useful observations variables such as backscatter ratio (aerosol + molecular backscatter/molecular backscatter) can be calculated (e.g. DeFoor et al., 1992).

### **2.3.2 Mount Pinatubo model simulations - SO<sub>2</sub> emission and injection height**

Following the Stratospheric Processes And their Role in Climate (SPARC) report (SPARC, 2006), there have been large advances in and development of global stratospheric models. Interests in geoengineering and the climatic impact of volcanic eruptions increased these advances and over 15 aerosol-climate models with 3D stratospheric capabilities are currently active (Kremser et al., 2016). The models outlined in Kremser et al. (2016) vary depending on whether they use sectional or modal size distributions, are radiatively coupled and the stratospheric compounds included (e.g. just sulfate or sulfate, organics and meteoritic dust, for example.)

Climate modelling studies of large volcanic eruptions have previously used prescribed AOD values, such as in Jones et al. (2005) and in studies using CMIP5 data (e.g. Driscoll et al., 2012). That said, these studies have been found to be limited by a lack of aerosol microphysics, an example being a prediction of surface cooling from the super eruption of Toba around 74,000 years ago being 3 times smaller when aerosol microphysics were included in a model (Timmreck et al., 2010) compared to without (Jones et al., 2005).

While global-mean SAOD and its relationship with radiative forcing is used as a key parameter in deducing volcanic forcing (Sato et al., 1993; Schmidt et al., 2018), and deducing volcanic forcing from other climate-influencing factors (Hansen et al., 2005), it has been found that the same SAOD can be achieved from a variety of contrasting eruption source parameters (Marshall et al., 2019). Investigating the variation of extinction with altitude, which is consequently integrated to derive SAOD, can therefore give an indication of which eruption source parameters also closely match vertical profiles from, for example, ground-based lidar.

Eruption source parameters usually have fairly broad estimates, such as 14-32 Tg SO<sub>2</sub> by Guo et al. (2004) for the Mount Pinatubo eruption (Table 2-1). Using an interactive microphysical-climate model to investigate different variations on parameters and comparing to available observations can, potentially, help constrain the estimates.

As the Mount Pinatubo eruption was such a well observed, large eruption it has been widely used as a case study within the modelling community (Table 2-1). Estimates of SO<sub>2</sub> and its injection height are still uncertain, hence varying values for injection height and mass of SO<sub>2</sub> have been used or suggested across the modelling community.

**Table 2-1 Eruption source parameters (mass of SO<sub>2</sub> and injection height) as inferred based on observations and as used in climate modelling studies of the 1991 Mount Pinatubo eruption.**

Name	SO <sub>2</sub> injected (Tg)	Injection height (km)	Reference
<b>OBSERVATIONS</b>			
TOMS	18 ± 4	25	Guo et al. (2004)
			Bluth et al. (1992)
TOVS	19 ± 4		Guo et al. (2004)
SAGE II	30	20-27	McCormick and Veiga (1992)
<b>MODELLING</b>			
ECHAM4	17	20-27	Timmreck et al. (1999)
		(2/3 at 10 hPa, 1/3 at 50 hPa)	
GEOS-5	20	16-18	Aquila et al. (2012)
WACCM	10	15.1-28.5 (peak at 21)	English et al. (2013)
UM-UKCA	10, 20	19-27	Dhomse et al. (2014)
AER-2D	14	18-20	Sheng et al. (2015)
HadGEM2-CCS	14, 20	16-18, 19-27	Jones et al. (2016)
WACCM	10	18-20	Mills et al. (2016, 2017), Schmidt et al. (2018)
SOCOL-AER	12, 14	16-20 (peak 18-21)	Sukhodolov et al. (2018)

Values used are based on predictions from observations and sometimes to account for lacking removal of SO<sub>2</sub> on ash or ice (Mills et al., 2017) or resultant lofting from the aerosol cloud (Aquila et al., 2012). Sheng et al. (2015) for example, suggest optimum injection height is 18-20 km and mass of SO<sub>2</sub> is 14 Tg. Mills et al. (2016; 2017) and Schmidt et al. (2018) also agree with 18-20 km, but use 10 Tg of SO<sub>2</sub> to account for SO<sub>2</sub> removed on ash and ice in the first few days of the eruption. Aquila et al. (2012), however, inject 20 Tg over a lower injection height of 16-18 km, also testing a higher injection height of 17-27 km. English et al. (2013) use 10 Tg SO<sub>2</sub> and inject between 15.1 and 28.5 km, peaking at 21 km, whilst Dhomse et al. (2014) use 10 and 20 Tg and have an injection height of 19-27 km.

Modelling studies that have included aerosol microphysics have found self-limiting responses of explosive eruptions (Pinto et al., 1989; Timmreck et al., 2010; English et al., 2013; Arfeuille et al., 2014). As discussed in Section 1.1, there is a non-linear effect of increased SO<sub>2</sub> emission and resulting radiative forcing due to the effects of condensation and coagulation increasing particle size and, therefore, sedimentation. Metzner et al. (2014) furthered this research, finding that there is a linear relationship between mass of SO<sub>2</sub> injected and peak AOD for SO<sub>2</sub> masses < 5 Tg and non-linear above 5 Tg. Comparatively, English et al. (2013) found that global AOD was only 20 times larger for a value 100 times that of the Mount Pinatubo eruption (assuming 10 Tg for Mount Pinatubo). Scaling values for Metzner et al. (2014), an eruption of ~7 Tg compared to ~700 Tg produced AOD values of 0.09 and 2.37, respectively, meaning the 700 Tg SO<sub>2</sub> injection produced an AOD 26 times higher than the 7 Tg injection, similar to English et al. (2013). A study by Timmreck et al. (2010) using a similar 100 Tg SO<sub>2</sub> injection mass also found these self-limiting effects, yet, their maximum global AOD value is 4 in comparison to a value of 2.5 calculated by English et al. (2013). These two studies differed, as English et al. (2013) used a sectional scheme and included van der Waals forces which act to increase particle size, but did not include aerosol radiative heating, whereas Timmreck et al. (2010) use a modal scheme and include aerosol radiative heating. Sectional schemes divide aerosol sizes into discrete bins, whereas a modal scheme uses log-normal size distributions and fixed mode widths for each. The use of each of these types of schemes can affect resultant size distributions and its evolution during model simulations (e.g. Kokkola et al., 2009; Mann et al., 2012). Sectional schemes, although more complex, can be highly expensive computationally. Mann et al. (2012) for example, have shown that modal schemes are capable of matching aerosol results from sectional schemes and many Mount Pinatubo studies using modal schemes compare closely with observations (Niemeier et al., 2009; Dhomse et al., 2014; Mills et al., 2016; Mills et al., 2017; Schmidt et al., 2018).

Dhomse et al. (2014) outlined the first use of the composition-climate model (Unified-Model – United Kingdom Chemistry and Aerosol (UM-UKCA)) with interactive troposphere-stratosphere aerosol microphysics and chemistry in simulating the Mount Pinatubo eruption. Overall, using an injection of 10 Tg SO<sub>2</sub> is more comparable to observations than 20 Tg, as the aerosol mass burden is predicted to be twice as high with 20 Tg when compared to satellite measurements. Satellite measurements also indicate a large reduction in aerosol burden in the initial months following the eruption

that is not simulated in the model, possibly due to a lack of removal pathway by ash or ice that is not simulated.

Arfeuille et al. (2014) mention how small differences in injection height can lead to large differences in transport following tropical volcanic eruptions. Aquila et al. (2012) attempted different injection heights, identifying variations in vertical profiles of aerosol and finding overall that higher injection heights lead to longer lasting aerosol. Toohey et al. (2016) similarly find that a higher injection height of 24 km leads to aerosol persisting for longer in the stratosphere than heights of 13 or 16 km. The reason for longer lasting aerosol is the confinement of aerosol to the tropical pipe, as noted in Niemeier et al. (2011) and Niemeier and Timmreck (2015). Some modelling studies also suggest that above ~25 km there may be over spilling of aerosol into the mid-latitudes (Arfeuille et al., 2014; Stoffel et al., 2015) with these higher injection heights then leading to greater hemispheric asymmetry in aerosol transport and subsequent cooling (Stoffel et al., 2015). Furthermore, this effect of confined aerosol may act to reduce subsequent radiative effects, as aerosols may coagulate, grow and sediment more quickly, also indicating that a higher mass of SO<sub>2</sub> does not equate to a higher radiative forcing (Niemeier and Schmidt, 2017; Kleinschmitt et al., 2018; Tilmes et al., 2018).

Aquila et al. (2012) advise that radiative heating is required for successful aerosol lofting and suggest that the mass of SO<sub>2</sub> injected determines subsequent lofting. Additionally, Aquila et al. (2012) indicate that changes in QBO were more important in controlling aerosol distribution than meteorology, with their model simulating constant easterlies as opposed to a varying QBO throughout.

### **2.3.3 Observations and model simulations of volcanic ash**

The theory that sulfuric acid may condense onto ash particles was noted before the Mount Pinatubo eruption by Pinto et al. (1989), who used a 1D aerosol model to examine volcanic stratospheric clouds and specifically treat mixed particles of ash and sulfate. Turco et al. (1983) also found evidence for sulfuric acid coated ash particles following the 1980 Mount St Helens eruption, with 0.1-3 μm radius ash particles persisting for up to a month. Measurements of ash and sulfur aerosols with non-sulfurous cores in the stratosphere were taken as early as 1963 following the Mount Agung eruption up to 20 km (Mossop, 1964; Mossop, 1965). Ash particles were noted after the April 1982 El Chichón eruption from 16.8-19.2 km altitude as late as October of the same year, with some visibly in liquid droplets (Gooding et al., 1983).

Deshler (2016) shows measurements of balloon-borne particle counters at Laramie, Wyoming, indicating that ash-core particles existed following the Mount Pinatubo eruption, the ash accounted for ~20% of the particle mass and that these particles persisted for ~1 year. Impactor measurements also show evidence for ash particles coated in sulphuric acid as late as February 1992 (Pueschel et al., 1994), 8 months after the eruption. Additionally, lidar data from Aberystwyth (52°N) (Vaughan et al., 1994) show a depolarising layer at 19 km in October 1991. A higher depolarisation value indicates non-spherical particles, which are usually determined to be ash or ice (Prata et al., 2017). Vernier et al. (2016) further suggested the persistence of ash particles following the 2014 Kelud eruption, finding ash particles contributed ~24% of the volcanic cloud and persisted for 3 months after the eruption. These ash particles were also found to increase volcanic radiative forcing by 20% more than if calculated solely for sulfate, suggesting ash may have more of an impact on radiative forcing than previously thought and that further climate simulations should include ash (Vernier et al., 2016). Modelling by Niemeier et al. (2009) indicate that ash has a short-term, localised effect, but may affect local radiative heating and winds, impacting transport direction of volcanic aerosol.

Although a number of modelling studies have investigated the Mount Pinatubo eruption, these studies have tended to focus on global properties such as AOD and sulfur burden rather than more localised effects. The importance of aerosol microphysics, injection height, SO<sub>2</sub> magnitude, QBO and radiative heating have been noted, with many studies not including one, or a number of these. For example, Aquila et al. (2012) and Jones et al. (2017) do not include aerosol microphysics, English et al. (2013) do not generate a QBO and Arfeuille et al. (2014) do not include radiative heating. Almost all modelling studies have regarded ash as being sedimented too quickly to be important for climatically relevant eruptions, yet ash has been found to impact radiative heating and aerosol transport (Niemeier et al., 2009). No study has thus far investigated the longer lasting, sub-micron ash particles seen to persist for months following explosive eruptions (Vernier et al., 2016; Deshler, 2016).

## **2.4 Summary**

This chapter summarises background information on the stratospheric aerosol layer, the 1991 Mount Pinatubo eruption outlining associated measurements and modelling studies. The literature review has outlined the variation in eruption source parameters

between modelling studies of the 1991 Mount Pinatubo eruption and a lack of observations around the equator at the time of the eruption. Volcanic ash has also been observed up to 9 months following the Mount Pinatubo eruption, but largely ignored in modelling studies due to an assumption that ash is quickly removed from the atmosphere following an eruption.

The aims of this thesis are to: 1) Investigate the initial dispersion of the Mount Pinatubo eruption using ground-based lidar and UM-UKCA, 2) Examine how varying eruption source parameters affects the vertical profile of extinction as simulated in the model, SAOD and sulfate burden and 3) Assess how sensitive the results from (1) are to the inclusion of ultra-fine ash. Having summarised the background of the stratospheric aerosol layer and the 1991 Mount Pinatubo eruption, the next chapter (Chapter 3) will outline the methods used to address the aims of this thesis.

# Chapter 3 Data and Methods

## 3.1 Introduction

This thesis is aimed at understanding the stages in the formation and global dispersion of the volcanic aerosol cloud from major tropical eruptions. The research involves analysing observations of the 1991 Mount Pinatubo aerosol cloud and interactive stratospheric aerosol model experiments to explore how alternative representations of the volcanic cloud affect its progression. The main research tool for the volcanic aerosol experiments is the Unified Model (UM) coupled to the United Kingdom Chemistry and Aerosol (UKCA) sub-model (Brown et al., 2012; Abraham et al., 2012) (from here on described as UM-UKCA), as configured for interactive stratospheric aerosol (Dhomse et al., 2014). The UM-UKCA Mount Pinatubo aerosol cloud simulations are analysed in conjunction with ground-based lidar observations from the first 9 months after the 15<sup>th</sup> June 1991 Mount Pinatubo eruption. A detailed description of the model and the observations utilised are given in this chapter.

The Mount Pinatubo aerosol cloud observations analysed are mainly from ground-based lidar measurements from one near-tropical (Mauna Loa) and three northern hemisphere lidar sites (Table Mountain, Toronto and Haute Provence), with a recently recovered dataset from shipborne lidar (Avdyushin et al., 1993). Monthly global composite datasets from two satellite measurement datasets of the Mount Pinatubo cloud are also used, the Advanced Very-High-Resolution Radiometer (AVHRR) nadir-sounding instrument on the NOAA-11 satellite (Long and Stowe, 1994) and the Global Space-based Stratospheric Aerosol Climatology (GloSSAC) dataset (Thomason et al., 2018; Damadeo et al., 2018) which consists primarily of solar occultation measurements from the SAGE II instrument on the ERBS satellite (McCormick and Veiga, 1992; Thomason, 1992). Errors associated with the AVHRR AOD data are in the range 0.03-0.05 (Stowe et al., 1992). GloSSAC uncertainties for the lower stratosphere are <5% on average following the Mount Pinatubo eruption with other uncertainties primarily from the uncertainty of the combined measurements (Thomason et al., 2018).

Chapter 4 focuses on the lidar measurement analysis, exploring the initial progression of the Mount Pinatubo aerosol cloud and how the vertical structures seen within the data change with the continuing wind shear during the progression from a concentrated

volcanic plume to a well-mixed cloud throughout the tropical reservoir. The interactive stratospheric aerosol model experiments further explore how the volcanic cloud evolves using a “pre-nudging” to improve on “approximate-QBO” simulations in previous UM-UKCA studies (Dhomse et al., 2014; Dhomse et al., 2020). Free-running simulations then represent the QBO accurately and allow the progression of the aerosol cloud including radiative heating. Chapter 5 analyses how the Mount Pinatubo cloud would have evolved for different eruption source parameters, exploring how changing the injection height and injected mass of SO<sub>2</sub> influences the simulated vertical distribution and global dispersion of the volcanic cloud. Chapter 6 assesses how ultra-fine ash particles impact the dispersion of the volcanic cloud, applying a new configuration of the model adapted specifically to explore these effects.

### **3.2 UM-UKCA model description**

The model used throughout this thesis is version 8.4 of the interactive stratospheric aerosol configuration of the UM-UKCA composition-climate model. This is the UM general circulation model extended for stratosphere-troposphere chemistry (UKCA). The configuration of UM-UKCA used is Release job 4.0 of the UK community composition-climate model (Abraham, 2017), based around atmosphere-only simulations with the UM Global Atmosphere 4.0 (GA4.0) configuration (Walters et al., 2014). GA4.0 is an interim configuration of the atmospheric component of the Hadley Centre Global Environment Model version 3 (HadGEM3) climate model, but with interactive aerosol microphysics from the Global Model of Aerosol Processes (GLOMAP) mode aerosol scheme (Section 3.3) and whole-atmosphere chemistry (Mann et al., 2010). Tropospheric and stratospheric chemistry schemes are used, with extension for aerosol-precursor chemistry suitable for interactively simulating the stratospheric aerosol layer (Section 3.3.2).

The GLOMAP-mode module within UM-UKCA simulates aerosol mass and number within 7 lognormal modes (4 soluble and 3 insoluble) to track particle sizes, which contain sulfate (SU), black carbon (BC), organic carbon (OC), dust (DU) and sea salt (SS), a detailed description of which can be found in Mann et al. (2010) and is further discussed in Section 3.3. This model setup has also been used previously in Turnock et al. (2015) with adaptations for interactive stratospheric aerosol as in Dhomse et al. (2014), Marshall et al. (2018), Timmreck et al. (2018) and Marshall et al. (2019).

Davies et al. (2005) outline the dynamical core used in the GA4.0 atmosphere model, which is based on the atmospheric equations of motion using semi-implicit, semi-Lagrangian methods. The GA4.0 model was designed to have well-resolve stratospheric dynamics, with a model top at 85 km and 85 vertical hybrid height levels with a horizontal grid of  $1.875^\circ$  longitude by  $1.25^\circ$  latitude (N96 resolution) and the model can be run with an internally generated QBO (Morgenstern et al. 2009).

All simulations were free-running, atmosphere-only simulations with time-varying sea ice, sea surface temperature, greenhouse gases and ozone-depleting substance values set for the period 1991-1992, which is the timeframe of interest in this study. The default set-up of GLOMAP-mode is implemented for Chapters 4 and 5, but adapted for Chapter 6 to incorporate ash, the process for which is outlined in Section 3.3.

### 3.3 GLOMAP-mode

#### 3.3.1 Introduction

GLOMAP-mode is an aerosol microphysics module, developed specifically for the UM-UKCA composition climate model, to predict the particle size distribution interactively. The size-resolved aerosol properties simulated and tracked in GLOMAP-mode are 7 lognormal modes, soluble modes for nucleation, Aitken, accumulation sized aerosol, a coarse soluble mode for super-micron sea-salt aerosol, and insoluble modes to simulate carbonaceous and dust particles (Table 3-1). The following processes are simulated within GLOMAP-mode: new particle formation (i.e. nucleation), coagulation, condensation and cloud processing.

**Table 3-1 Each mode within GLOMAP-mode with associated size range, composition, solubility and mode width.**

Mode	Size range (nm)	Composition	Mode width ( $\sigma$ )
1 - Nucleation soluble	$R < 5$	SU, OC	1.59
2 - Aitken soluble	$5 < R < 50$	SU, BC, OC	1.59
3 - Accumulation soluble	$50 < R < 500$	SU, BC, OC, SS, DU	1.4
4 - Coarse soluble	$500 < R$	SU, BC, OC, SS, DU	2.0
5 - Aitken insoluble	$5 < R < 50$	BC, OC	1.59
6 - Accumulation insoluble	$50 < R < 500$	DU	1.59
7 - Coarse insoluble	$500 < R$	DU	2.0

The aerosol microphysics is mainly designed to simulate how particles grow during their residence time through condensation and coagulation and how they form from homogenous and heterogenous sulfate nucleation. The two-moment microphysics in GLOMAP-mode means it predicts particle mass and number as separate prognostic variables in each mode. This is important to enable the model to conserve particle number whilst increasing mass concentrations when particles grow (e.g. via condensation), and to decrease particle number whilst conserving total mass (during coagulation). GLOMAP-mode also simulates removal processes in a size-resolved manner, including sedimentation, dry deposition and wet removal from tropospheric clouds via nucleation scavenging (rainout) and impaction scavenging (washout).

The growth of particles larger than the upper range of the mode radius (see Table 3-1 size range for values) is resolved through mode-merging, whereby a proportion of the mass concentrations and the number concentration from the donor (grown) mode are transferred across to the adjacent mode of the next highest size, as described in (Mann et al., 2010). Note that this mode-merging process only needs to be applied for the soluble nucleation and Aitken modes, as growth becomes much slower in the accumulation mode and the process does not need to be applied for the insoluble modes. A process known as condensation-ageing was originally applied for all 3 of the insoluble modes, separating carbonaceous and dust particles either into uncoated insoluble particles or internally-mixed soluble modes. These internally mixed particles become soluble following condensation of  $\text{H}_2\text{SO}_4$  or organic vapours or from coagulation of soluble particles. However, to allow meteoritic smoke particles (MSPs) to heterogeneously nucleate sulfate aerosol particles in the stratosphere (Brooke et al., 2017), this condensation-ageing was de-activated for the accumulation insoluble mode and used instead to track condensed sulfate on the accumulation insoluble mode.

Sedimentation of aerosols occurs throughout the atmosphere and they are removed through wet and dry deposition. Wet deposition of aerosol occurs in UM-UKCA via both the convective and large-scale precipitation schemes (Kipling et al., 2013), based on the GLOMAP-mode schemes for below-cloud (impaction) and in-cloud (nucleation) scavenging (Pringle, 2006; Spracklen et al., 2007), also referred to as washout and rainout, respectively. Below-cloud scavenging occurs when raindrops collide with aerosols and is treated in the model using aerosol and raindrop collision efficiencies from Slinn (2004). In-cloud scavenging takes place when particles are activated to form

cloud droplets by acting as cloud condensation nuclei (CCN) and are eventually removed through rainout. For in-cloud scavenging through convective precipitation, the convective precipitation rate by Kipling et al. (2013) assumes all mass from soluble accumulation and coarse modes plus half of the soluble Aitken mode are assumed dissolved and therefore removed. In-cloud scavenging by large-scale precipitation uses the assumption from Spracklen et al. (2005) of the dissolution of soluble particles with  $> 103$  nm wet radius can be removed by precipitation depending on precipitation rate.

Dry deposition in GLOMAP-mode is described in Mann et al. (2010) with dry deposition velocity ( $V_d$ ), calculated for each mode based on Slinn (1982).  $V_d$  is dependent on aerodynamic and surface resistance, which depend on surface roughness, surface friction velocity and collection coefficients for Brownian diffusion, impaction and interception (Zhang et al., 2001). It is also dependent on gravitational settling velocity, which in turn depends on particle density, size, air viscosity and gravitational acceleration.

The formation of sulfate aerosol via binary homogenous nucleation of  $\text{H}_2\text{SO}_4\text{-H}_2\text{O}$  is represented using the parameterised from Vehkämäki et al. (2002), updated from Kulmala et al. (1998), to include nucleation rates in the upper tropical troposphere at  $\sim 200$  K. In-cloud formation of sulfate via oxidation of  $\text{SO}_2$  is also accounted for (Mann et al., 2010). Hygroscopic growth of particles is described in Mann et al. (2010), which was applicable for tropospheric conditions, but was later adapted for the stratosphere using calculations from Carslaw et al. (1995). Sulfuric acid aerosol particles have a composition of 74.5%  $\text{H}_2\text{SO}_4$  and 25.5%  $\text{H}_2\text{O}$  for 225 K and 101 hPa.  $\text{H}_2\text{SO}_4$  condensation and evaporation were also applicable to the troposphere in Mann et al. (2010), and depend on the vapour pressure and gas phase partial pressure of  $\text{H}_2\text{SO}_4$  (Dhomse et al., 2014), so that above  $\sim 35$  km evaporation of  $\text{H}_2\text{SO}_4$  droplets occurs rapidly whereas at  $\sim 25\text{-}30$  km increasing temperatures equally increase the significance of the  $\text{H}_2\text{SO}_4$  vapour pressure. The model also includes MSPs, which can also act as nucleation cores for heterogenous formation of sulfate particles (Brooke et al., 2017). As mentioned above, the amount of sulfate condensed onto MSPs is now tracked in the accumulation-insoluble mode, as with condensation-ageing to the accumulation-soluble is switched off (Brooke et al., 2017).

### 3.3.2 Stratospheric chemistry scheme

The Chemistry of the Stratosphere and Troposphere (CheST) scheme is used for atmospheric chemistry in the model, combining tropospheric (O'Connor et al., 2014) and stratospheric (Morgenstern et al., 2009) chemistry schemes. Added aerosol chemistry is included for GLOMAP-mode, which results in ~300 reactions between 86 species.

UM-UKCA was adapted to also simulate the stratospheric aerosol layer interactively in Dhomse et al. (2014), an sulfur chemistry was extended, based on the reactions shown in Table 3-2. In background (volcanically quiescent) conditions, the stratospheric aerosol layer is maintained primarily from sulfur from OCS, as outlined in Section 2.2.2 of Chapter 2, with minor contributions from tropospheric SO<sub>2</sub> and DMS. The key oxidation pathway for the production of sulfuric acid aerosol particles by SO<sub>2</sub> is with OH, with intermediate species SO<sub>3</sub> and H<sub>2</sub>SO<sub>4</sub> also important for the fate of particles evaporating during transport within the upper branch of the BDC.

**Table 3-2 Sulfur chemistry reactions in UM-UKCA for stratospheric aerosol. Table modified from Dhomse et al. (2014), W = Weisenstein et al. (1997); S = Sander et al. (2006); K = Kreidenweis et al. (2003).**

Reaction	Reference
DMS + O( <sup>3</sup> P) → SO <sub>2</sub>	W, S
DMS + OH → SO <sub>2</sub> + CH <sub>3</sub> O <sub>2</sub> + HCHO	W
DMS + OH → SO <sub>2</sub> + CH <sub>3</sub> O <sub>2</sub>	W
DMS + NO <sub>3</sub> → SO <sub>2</sub> + HNO <sub>3</sub> + CH <sub>3</sub> O <sub>2</sub> + HCHO	W
OCS + O( <sup>3</sup> P) → CO + SO <sub>2</sub>	W, S
OCS + OH → CO <sub>2</sub> + SO <sub>2</sub>	W, S
SO <sub>2</sub> + OH + M → SO <sub>3</sub> + HO <sub>2</sub> + M	W
SO <sub>2</sub> + O <sub>3</sub> → SO <sub>3</sub>	W, S
SO <sub>3</sub> + H <sub>2</sub> O → H <sub>2</sub> SO <sub>4</sub>	S
SO <sub>2</sub> + H <sub>2</sub> O <sub>2</sub> <sup>aq</sup> → SO <sub>4</sub>	K
OCS + <i>hν</i> → CO + SO <sub>2</sub>	W
H <sub>2</sub> SO <sub>4</sub> + <i>hν</i> → SO <sub>3</sub> + H <sub>2</sub> O	W
SO <sub>3</sub> + <i>hν</i> → SO <sub>2</sub> + O( <sup>3</sup> P)	W

### 3.3.3 Fine ash mode

To facilitate the simulation of volcanic ash particles in the model, GLOMAP-mode was adapted by Graham Mann to use mode 7 (coarse insoluble) as a “fine-ash” mode, as mode 7 contained only dust (Table 3-1). This process is outlined as follows:

The first change was to allow mode 7 to internally mix ash and sulfate, to allow sulfate particles to be removed via condensation of sulfate aerosol onto the ash particles. A similar process was used for adapting mode 6 for MSPs (Brooke et al., 2017).

The second change was to edit the volcanic SO<sub>2</sub> emissions routine to enable co-emissions of volcanic ash and SO<sub>2</sub>. The UKCA\_VOLCANIC\_SO2.F90 subroutine already does 3D emissions of SO<sub>2</sub> according to parameters “AEROS\_SO2KG\_VOLC”, “AEROS\_HHTOP\_VOLC” and “AEROS\_HTBOT\_VOLC”, accounting for the mass of SO<sub>2</sub> injected (kg), the upper injection height (m) and the lower injection height (m), respectively. Further details on the ash specifications are outlined in Section 3.3.4. Editing this file was necessary to input the amount of ash injected (kg) and the injection height top and bottom (m).

The final change was coding a logical on/off switch for the condensation of H<sub>2</sub>SO<sub>4</sub> onto the mode 7 mass mixing ratio for sulfate. The UKCA\_CONDEN.F90 subroutine already condenses H<sub>2</sub>SO<sub>4</sub> onto the other 6 modes, but for 5 (Aitken insoluble) and 7 (coarse insoluble) the subroutine condensation-ages condensed-H<sub>2</sub>SO<sub>4</sub> over to the respective soluble mode (e.g. coarse insoluble to coarse soluble) (Mann et al., 2010). Thus, sulfate in mode 5 and 7 were previously moved into modes 2 and 4, respectively. Prior to changes to mode 6 for MSPs, the accumulation insoluble mode also condensation-aged over to the accumulation soluble mode (mode 3), but this was recoded to instead track mixed MSP-sulfate to stay in mode 6 (accumulation insoluble mode). This is then the same for mode 7, so it will not age to mode 4 but will track mixed dust/ash-sulfate particles in mode 7, therefore tracking SO<sub>4</sub> mass mixing ratio and SO<sub>4</sub> in this mode.

As described in Section 3.2, mode 7 now allows condensed sulfate into the coarse soluble mode (mode 4) so that sulfate aerosol can condense onto volcanic ash particles. This step 3 is necessary, as studies such as Pueschel et al (1994) and Chuan and Woods (1984) have shown evidence for sulfate coated ash particles in the stratosphere up to a year after the 1991 Mount Pinatubo and 1982 El Chichón eruptions, respectively. Therefore, it is important to allow ash particles to be coated in H<sub>2</sub>SO<sub>4</sub> in the model simulations carried out in this study.

### 3.3.4 Ash specifics – density, optical properties and size

The density of the ash is  $2650 \text{ kg m}^{-3}$ , as this value applies to andesitic tephra, which represent the andesitic/dacitic chemical composition and thus density of the 1991 Mount Pinatubo ash well. A density of  $2650 \text{ kg m}^{-3}$  lies in the ranges outlined in Beckett et al. (2015) where densities of ash with similar chemical compositions ranged from 2300-2750  $\text{kg/m}^3$  in the size range of 1-10  $\mu\text{m}$ . An ash density of  $2650 \text{ kg m}^{-3}$  is also similar to Niemeier et al. (2009) who used a density of  $2400 \text{ kg m}^{-3}$  for their ash particles to simulate the 1991 Mount Pinatubo eruption. Beckett et al. (2015) also show that particle density decreases with particle size (particles 1-10  $\mu\text{m}$  diameter having densities 2300-2700  $\text{kg m}^{-3}$  and 100-1000  $\mu\text{m}$  diameter particles with densities  $\sim 400\text{-}1000 \text{ kg m}^{-3}$ ) indicating that the smaller size fractions have the higher densities, but this process is not accounted for in UM-UKCA. Ash mass concentrations and number concentrations are tracked within each size mode, as with the other components of the other 6 modes. At present the ash has the same optical properties as mineral dust.

With regards to sizes of particles, in Chapter 6, sizes between 0.1 – 10  $\mu\text{m}$  are tested, specifically looking at sizes with mean radius 0.1, 0.316, 1, 3.16 and 10  $\mu\text{m}$ . Initial simulations with 50 Tg of ash were performed for the larger size fractions, as this was the estimated mass of ash from the Mount Pinatubo eruption by satellites (S. Guo et al., 2004). As discussed in the Methods section of Chapter 6 (Section 6.2), a smaller mass of 0.05 Tg was injected to account for the smaller ash particles that remained after the initial fallout of larger ash particles. In all simulations ash was emitted equally across all injection height grid boxes at the same latitude, longitude and height levels as the  $\text{SO}_2$ . Dispersion models such as the Numerical Atmospheric-dispersion Modelling Environment (NAME) that is used by the Met Office Volcanic Ash Advisory Centre (VAAC), use a size range between 0.1 – 100  $\mu\text{m}$ , however, a sectional approach is used whereby differing amounts of each size fraction can be simulated.

### 3.4 Radiation scheme RADAER

The radiation scheme within the UM uses six shortwave and nine longwave wavebands, following the Edwards-Slingo scheme (Edwards and Slingo, 1996; Abraham et al., 2012). GLOMAP-mode interacts with radiation through UKCA\_RADAER, which is a specific routine within the UKCA code framework. Carrying out Mie calculations during runtime would be too computationally expensive, therefore, UKCA\_RADAER relies on pre-calculated look-up tables for optical properties. These look-up tables

contain scattering and extinction coefficients ( $\text{m}^{-1}$ ), volume fractions (dimensionless) and asymmetry parameters (dimensionless) of aerosols in each mode. Particle radius, complex refractive index and wavelength are used to calculate these optical properties. These values vary between the modes due to variation in composition and solubility. The offline Mie calculations performed for the lookup tables are monochromatic, therefore integration over each waveband, as well as over the size distribution, is needed for use by the radiation scheme (Bellouin et al., 2013). RADAER also calculates the first and second indirect effects of aerosols and the model allows calculation of all-sky and clear-sky radiative fluxes.

The RADAER module calculates optical properties for each of the modes (Bellouin et al., 2013). The ash is based on dust within the coarse-insoluble mode, therefore look-up table values for dust are used for calculating resultant refractive index (Johnson and Osborne, 2011), the optical properties for mineral dust from Balkanski et al. (2007).

### **3.5 Model configurations and eruption source parameters**

Volcanic aerosol simulations, including sulfate or sulfate and ash, can be carried out within interactive stratospheric composition-climate models either in free-running mode or with specified dynamics (nudged mode).

In nudged mode, the winds and temperatures simulated by UM-UKCA are “nudged” every 6 hours to follow best-estimate fields from ERA-interim meteorological re-analysis (Dee et al., 2011). Using the nudged mode, therefore “nudges” the winds in the model to observed winds values, however, other aspects such as aerosols cannot feedback via aerosol heating, for example. This nudged configuration of UM-UKCA was developed by Telford et al. (2008) and has been used for interactive tropospheric aerosol UM-UKCA simulations (e.g. Turnock et al. (2015); Butt et al.(2017)).

In Chapter 4 we compare free-running UM-UKCA mid-altitude, mid-SO<sub>2</sub> (Timmreck et al., 2018) “best-estimate Pinatubo” volcanic sulfate aerosol simulations with equivalent specified-dynamics runs. These specified-dynamics runs nudge the winds and temperature for the period prior to the 15<sup>th</sup> June 1991 Mount Pinatubo eruption in order to simulate the exact stratospheric winds that occurred at the time of the eruption. Although it is possible to nudge winds and temperature also during the eruption, this would suppress any dynamical changes induced by the aerosol heating, thus from 1<sup>st</sup> June onwards the simulations are run in a free-running configuration. However,

nudging to two months prior to the eruption allows accurate wind and temperature fields to be in place and allows a settling period prior to the eruption.

The model simulations used in Chapter 4 are henceforth described as “pre-nudged“ and “approximate QBO” and have respective start dates of a) 01/04/1991 and b) 01/02/1996. a) started with initial conditions that were nudged until 01/04/1991 and was then free-running in order to have an initial two month settling period before the eruption. b) has a start date of 01/02/1996 as this particular setup in the model simulates a QBO similar to the time of the Mount Pinatubo eruption. For the volcanically-perturbed Mount Pinatubo simulations in this chapter, the volcanic SO<sub>2</sub> injection occurred for 1 day with the model parameters for both simulations set out in Table 3-3.

14 Tg SO<sub>2</sub> was chosen according to middle SO<sub>2</sub> values from Timmreck et al. (2018) and in order to compare with recent Mount Pinatubo climate modelling studies (Dhomse et al., 2014; Sheng et al., 2015; Mills et al., 2016). 21-23 km was chosen as a median level altitude range as stated by Timmreck et al. (2018), as a range of observations show the initial cloud was located here (e.g. McCormick, 1992; Antuña et al., 2002). The injection across 12 grid boxes (5°S-15°N) was used to account for spatial distribution of the resultant volcanic cloud. As found in Dhomse et al (2014) it is necessary to spread the injection over multiple grid boxes in order to capture the spread of the eruption to the southern hemisphere, therefore the injection is between 15°N-5°S.

**Table 3-3 Model parameter setup for approximate-QBO and pre-nudged Mount Pinatubo simulations.**

<b>Model parameter</b>	<b>Value</b>
<b>Injection longitude</b>	120.5°
<b>Injection latitude</b>	14.375°
<b>Number of grid boxes spread across</b>	12
<b>Degrees spread across</b>	5°S - 15°N
<b>Injection magnitude (Tg)</b>	14
<b>Injection altitude (km)</b>	21-23

### 3.6 Lidar measurements

Ground-based lidar (light detection and ranging) measurements from the time of the Mount Pinatubo eruption are a valuable tool for understanding the vertical dispersion of the volcanic cloud (Russell et al., 1979). The lidar data used for this study were chosen based on the availability of observations during the first year following the Mount Pinatubo eruption, as the aim was to investigate the initial dispersion. Many more lidars were installed following the eruption, as they were found to be increasingly useful for observing potential injection heights of the cloud along with its vertical structure (Kremser et al., 2016). The Lauder, New Zealand lidar was installed in November 1992 (Sakai et al., 2016), allowing an assessment of the well-developed Mount Pinatubo cloud in the southern hemisphere. However, lidar data from Lauder is not used in this thesis, as this thesis is focussed on the early development of the aerosol cloud and data for this time for the southern hemisphere was not available. A description of the different lidars used in this thesis and their locations is below.

In general, lidars consist of a transmitter, receiver and detector (McCormick and Fuller, 1973). The transmitter pulses a laser of monochromatic light and the backscatter signals are then collected by a telescope within the receiver and these signals are counted by the detector (McGill, 2002; Ansmann and Müller, 2005). As the laser interacts with molecules and aerosols, some light is backscattered, with these signals indicating the amount of material in the atmosphere, with a higher signal suggesting a larger amount of material is present (Northam et al., 1974). This metric is important and extremely useful in the instance of a volcanic eruption and for tracking the stratospheric sulfate layer, as the position and relative amount of aerosol in the atmosphere can be detected using lidars (Fiocco and Grams, 1964; Fernald et al., 1972).

The Network for the Detection of Atmospheric Composition Change (NDACC, 2019) lidar working group is an international network of lidar research stations providing long term, standardised high-quality observational data. From as early as 1974 to present day this group has observed aerosols, stratospheric and tropospheric ozone, temperature and water vapour around the globe. All lidar backscatter ratio (BSR) data used here were obtained from NDACC (2019).

The BSR data from lidar stations used within this research are located at Mauna Loa, USA (MLO), Table Mountain, USA (TAB), Toronto, Canada (TOR) and Haute

Provence, France (OHP). Figure 3-1 is a map of these sites in relation to the location of Mount Pinatubo and

Table 3-4 has information on each of the lidar instruments at the time of the eruption.

Table 3-4 outlines the location of each lidar, where and when each lidar operated (or still operates), wavelength and altitudinal range. Each site has good altitudinal range for observing stratospheric aerosols (between 8 and 32 km), whereby they all measure backscatter from aerosols from the tropopause and into the stratosphere.

As each site's observations have variable start and end altitude and resolution, a standardised altitude range of 15-30 km with 300 m resolution was used in order to compare these sites directly and in order to assess changes within the stratosphere. A 15-30 km range was chosen as all lidars measured within this range and it includes the stratosphere, with a 300 m interval chosen as this was the altitudinal interval for all the lidar measurements.

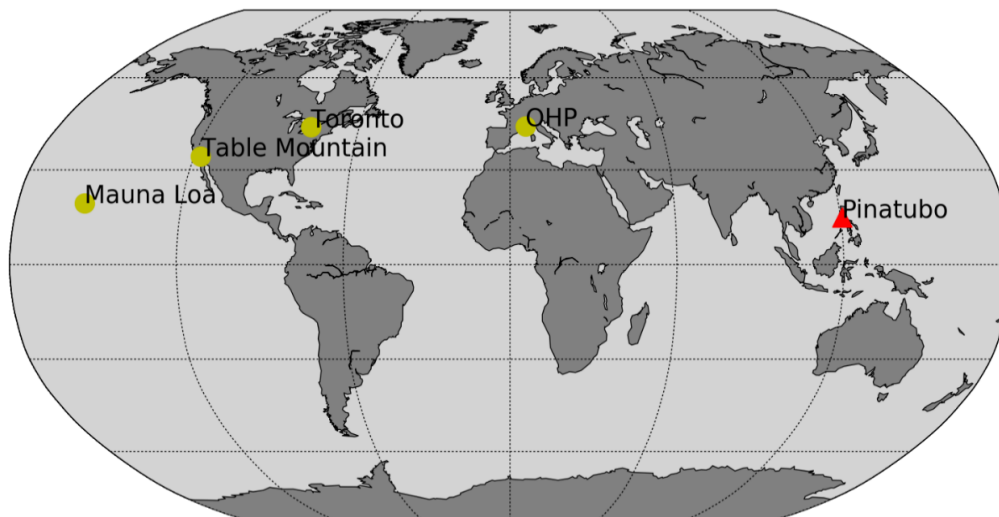


**Figure 3-1** Map locations for each lidar site location (yellow dots) and Mount Pinatubo for reference (red triangle).

**Table 3-4** Details about the lidar locations, types, operational times and references to measurements.

Site	Coordinates	Altitude range (km)	Wavelength (nm)	Operational time	References
MLO	19°N, 155°W	15-40	694	1974 - 1998	e.g. DeFoor and Robinson (1987), Barnes and Hofmann (1997)
TAB	34°N, 118°W	12-50	353	1989 - Present	Parrish et al. (1998)
TOR	44°N, 79°W	13-35	532	1991 - 1997	Donovan et al. (1996)
OHP	44°N, 6°E	8-32	532	1980 - Present	Chazette et al. (1995)

An initial qualitative analysis was performed to note when the aerosol was received at each site and any particular patterns in the data. In order to quantitatively compare cloud depth between the model and lidar data, an algorithm for picking out individual

layers within the MLO data was used (described in Section 3.6.2). A linear regression was then performed on each half of each layer to determine the change in slope within the layers. Using the layer-finding method and regression analysis, the cloud thickness, cloud top height and regression of the layers can be calculated. These metrics allow an analysis of the speed of the descent of the layers and of the aerosol cloud thickness through time to assess the progression of the aerosol cloud. In order to gain a further quantitative comparison, using methods outlined in Section a.a.i, the BSR was converted to 532 nm for all lidar sites and then converted to extinction in order to directly compare with extinction values from the model. BSRs from each of the sites were plotted against time for the period June 1991 – February 1992.

UM-UKCA extinction values are output on a daily timescale between 0-85 km, whereas the lidar measurements vary in altitude and time. It was therefore necessary to interpolate the model extinction onto the lidar measurements times and altitudes for the same lidar sites within the model for the same time period, in order to directly compare between the observations and model extinction. This was to enable a more direct comparison between the observational data collection days and those same days in the model data.

### **3.6.1 Zubov shipborne lidar data**

In Chapter 4, a comparison of the ground based lidar with shipborne lidar (Avdyushin et al., 1993) from July 11<sup>th</sup> – September 21<sup>st</sup> 1991 is made. The Zubov ship took measurements of extinction (539.5 nm) between 8-40°N, starting from the West coast of Spain, travelling towards Cuba, down towards the West coast of Africa and then back North towards Spain (Figure 3-2).

The timing and latitudes of this ship journey complement the study of the ground-based lidar well, as they cover the evolution of the aerosol in the tropical band in these first few months following the eruption.

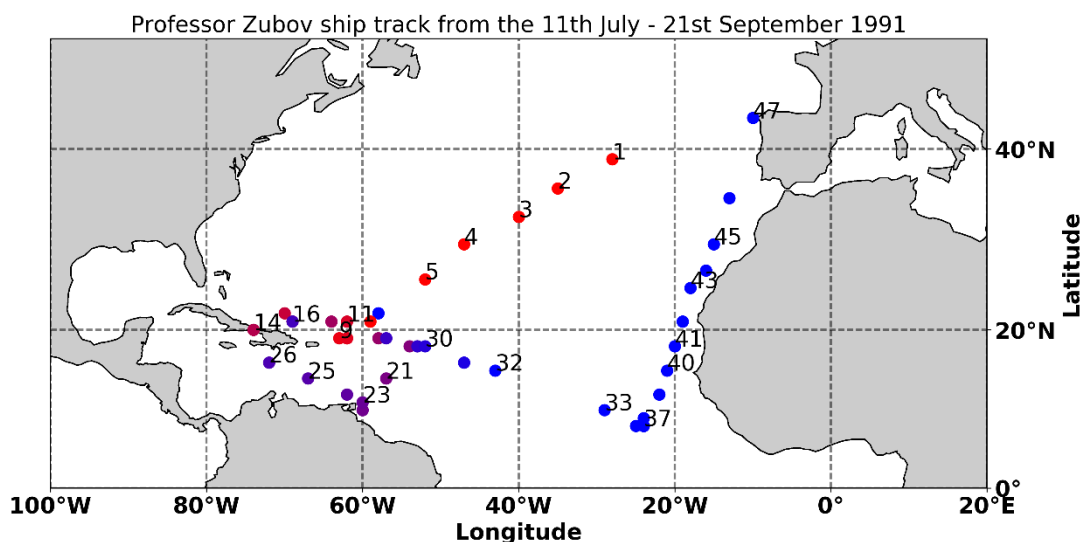


**Figure 3-2** Map of the course taken by the Professor Zubov ship from the 11<sup>th</sup> July to the 21<sup>st</sup> September 1991, as outlined in Avdyushin et al. (1993). Red dots show the direction the ship took southwards, with the majority of the journey spent around 20°N (purple) then progressing towards the equator and then back towards Spain past the west coast of Africa (blue dots).

### 3.6.2 Layer analysis algorithm description

As mentioned previously, the layer analysis algorithm picks out the top and bottom of the aerosol layer each day in order to assess the descent and depth of the aerosol cloud over time, to assess how the aerosol cloud is progressing. Figure 3-3 outlines the overall picture for how this is achieved, with the method outlined in Appendix A. The code works by finding the top and the bottom of the aerosol layer, accounting for any noise (i.e. small peaks above the BSR value for the top and bottom of the layer) using the ‘delta’ ( $\Delta$ ) value of 0.01 (dimensionless) and applying this in a loop for each day in the model and lidar data for MLO.  $\Delta = 0.01$  was chosen based on finding the average increase in BSR above background levels deemed to be noise as opposed to volcanic signal.

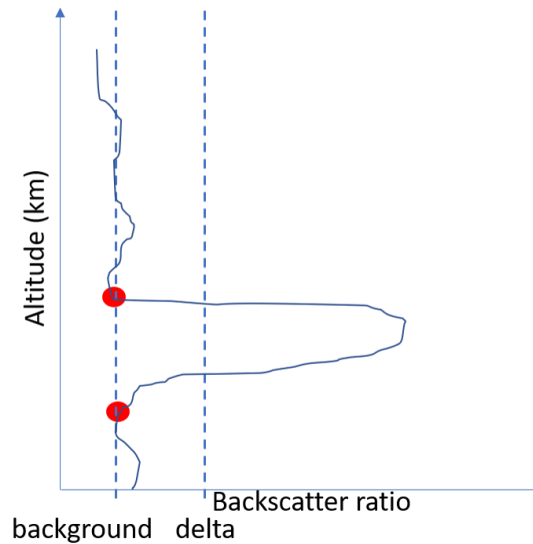


**Figure 3-3 Schematic for the layer finding algorithm with backscatter ratio against altitude. Red dots show the points where it would find the top and bottom of a layer, delta shows where the data must exceed above the first peak point to avoid areas of noise that may be picked out as layers.**

The use of the  $\Delta$  value accounts for small increases in the data above the background value that are not part of the main aerosol cloud (areas where there are small peaks above the “background” values in Figure 3-3). Systematic bias in the altitudes found for the top and bottom of the aerosol cloud are on the order of 300 m, i.e. the altitudinal interval, as the value for the top and the bottom of the layer correspond to the first point above the background level and the first point where the data goes below the background value.

### 3.6.3 Backscatter ratio to extinction

Molecular backscatter may be estimated (Vega and Antuña Marrero, 2017) as follows:

$$\beta_{Rayleigh}(\lambda, z, \theta = \pi) = 2.938 \times 10^{-32} \frac{P(z)}{T(z)} \cdot \frac{1}{\lambda^{4.0117}} (m^{-1}sr^{-1}), \quad (1)$$

where  $P$  is pressure (mbar),  $T$  is temperature (K),  $z$  is altitude (m),  $\lambda$  is wavelength (m), and  $\beta_{Rayleigh}$  is the backscatter coefficient (angular).

Backscatter ratio is defined (Ansmann and Müller, 2005) as:

$$backscatter\ ratio\ (BSR) = \frac{\beta_{mol} + \beta_{aer}}{\beta_{mol}}, \quad (2)$$

where  $\beta_{mol}$  is molecular backscatter and  $\beta_{aer}$  is aerosol backscatter. In order to quantitatively compare values between the lidar and the model, BSR needs to be converted to extinction. Conversion from BSR to extinction was chosen due to all

model data being measured in extinction and conversion factors from Jäger and Deshler (2002; 2003) tested for the period following the Mount Pinatubo eruption, accounting for variation in size distribution. The steps used to convert the lidar backscatter ratio to extinction are as follows.

Molecular backscatter is calculated for each lidar site using the  $\beta Rayleigh$  equation with values of pressure, temperature and altitude from the 12 UTC atmospheric soundings from the University of Wyoming soundings website (<http://weather.uwyo.edu/upperair/sounding.html>) for each of the measurement days.

Aerosol backscatter ( $\beta_{aer}$ ) is calculated using:

$$\beta_{aer\lambda} = (BSR - 1) \times \beta_{mol\lambda}, \quad (3)$$

where  $\beta_{aer\lambda}$  is aerosol backscatter at wavelength  $\lambda$ , BSR is backscatter ratio and  $\beta_{mol\lambda}$  is molecular backscatter at wavelength  $\lambda$ .

Wavelength conversion from X nm wavelength to 532 nm is calculated using:

$$\beta_{\lambda_1} = \left( \frac{\lambda_1}{\lambda_2} \right)^{wavelength\ exponent} \times \beta_{\lambda_2}, \quad (4)$$

where  $\lambda_1$  is the wavelength of the aerosol backscatter to convert to (i.e. the model wavelength) and  $\lambda_2$  is the wavelength of the aerosol backscatter to convert from.

Wavelength exponents to allow for conversion of extinction within wavelength range 355-1064 nm are obtained from Figure 4 in Jäger and Deshler (2002) (0).

Extinction at 532 nm is calculated using:

$$EXT_{532} = \beta_{aer532} \times aerosol\ extinction\ factor$$

where  $EXT_{532}$  is extinction at 532 nm and  $\beta_{aer532}$  is aerosol backscatter at 532 nm. The aerosol extinction factor, the coefficient calculated to convert from BSR to EXT, is taken from Figure 2 in Jäger and Deshler (2003) (0). The conversion factors used are calculated based on wavelength, particle radius, Mie extinction efficiency and particle size distribution, accounting for the change in size distribution during the time following the Mount Pinatubo eruption. Calculations were done for height ranges tropopause-15 km, 15-20 km, 20-25 km and 25-30 km, refractive indices between 1.4-1.45 and gravity values of 1.65-1.8. A single conversion factor (usually 40-50) is often used to convert between backscatter and extinction, however the conversion factors above vary based on size distribution, discussed further in Section 3.6.4. The

conversion of backscatter ratio to extinction was also used as part of the jointly authored paper by Dhomse et al. (2020).

### 3.6.4 Uncertainties within lidar data

Retrieval uncertainties primarily occur from the lidar signal due to photon counting, molecular density and the size distributions assumed (McGill, 2002). Uncertainty due to photon counting is the largest source of error in lidar analysis and can be explained due to the Poisson distribution that is applied to distinguish number of photons collected (McGill, 2002). As signal-to-noise ratio is defined as:

$$\frac{N}{\sqrt{N}} = \sqrt{N}$$

where N is number of photons, a larger number of photons will have a smaller amount of relative noise. This therefore shows that a larger photon count due to increased backscattering from volcanic material will have a smaller relative noise ratio.

Molecular density can have an error of 1% if measured from a radiosonde, increasing to ~3% if modelled or interpolated (Russell et al., 1979). If incorrectly interpolated or modelled larger errors can occur.

Size distributions and respective refractive indices within lidar analysis create uncertainty as they are often assumed. For non-volcanic conditions an assumed size distribution can be used, as in Russell et al. (1979). Large changes in size distributions and refractive indices caused by volcanic eruptions can, therefore, cause uncertainties in lidar analysis. Overall, however, total relative error decreases with increased aerosol loading, such as following a volcanic eruption (Russell et al., 1979).

The conversion varying technique used in Section 3.6.3 is seen as a more accurate technique as it accounts for size distribution variation over time, rather than assuming this constant conversion factor as applied by Vaughan et al. (1994), for example. Size distribution is an important factor to account for, as this can vary dramatically following a volcanic eruption, due to the increase in both smaller and much larger particle sizes (Jäger and Deshler, 2002). Conversion factors used and a comparison of using varying extinction conversion factors through time and a blanket conversion factor of 40 is discussed in 0.

Errors with BSR-EXT are acknowledged in Jäger and Deshler (2002) including particle counter error of ~10% and standard deviation from averaging within 5 km times in 4

monthly intervals which indicates both measurement error and variability associated with changing air masses. The impact of aerosol concentrations on the derived size distribution has a maximum error of 30%, though has an average error of less than 10% (Deshler et al., 1993). Error in aerosol concentration increases with decreasing number of particles (Deshler et al., 1993), however, this is not applicable to the period of time studied during this thesis due to the large number concentrations following the Mount Pinatubo eruption in the first 9 months.

In summary, the largest errors occur within the conversion of BSR to EXT, though the method by Jäger and Deshler (2002) is seen as more accurate than a blanket conversion factor of 40, as it accounts for varying size distribution following the Mount Pinatubo. Other errors include instrument error and incorrect photo counting, with overall total relative errors assumed to be decreased during this period due to increased aerosol loading following the Mount Pinatubo eruption.

## Chapter 4

# Initial dispersion of the 1991 Mount Pinatubo aerosol cloud – a ground-based lidar and interactive composition climate model comparison

### 4.1 Introduction

Volcanic eruptions are capable of injecting tens to hundreds of teragrams of ash, sulfur dioxide (SO<sub>2</sub>) and other chemical species into the atmosphere (e.g. McCormick et al., 1995; Stenchikov et al., 1998; Ramachandran et al., 2000; Timmreck, 2012). When explosive enough, eruptions can inject ash and SO<sub>2</sub> into the stratosphere and cause significant enhancement to the stratospheric aerosol layer (Deshler, 2008; Vernier et al., 2011). Scattering of solar radiation from the volcanically enhanced stratospheric aerosol layer cools the surface (~0.25°C for the 1991 Mount Pinatubo eruption (Hansen et al., 1992; Hansen et al., 1996; Stenchikov et al., 1998), and causes changes to circulation and other stratospheric trace species leading to complex indirect effects on Earth's climate (Stenchikov et al., 1998; Robock, 2000; Ramachandran et al., 2000; Timmreck, 2012; Kremser et al., 2016). For major tropical eruptions (defined as VEI >5, (Newhall and Self, 1982), the continued upwelling into the stratosphere causes a long-lived “tropical reservoir” of volcanic aerosol (e.g. Grant et al., 1996). The confinement of this reservoir results in slow dispersion to the mid-latitudes, which, in turn, leads to global dimming reducing below 1 Wm<sup>-2</sup> in the two years after the eruption (e.g. Hansen et al., 1996).

The dispersion of volcanic aerosol clouds from major tropical eruptions is linked to the initial confinement of aerosol within the tropical reservoir (e.g. Grant et al., 1996), determining, to a large extent, where volcanic aerosol is dispersed and over what timescale (Trepte and Hitchman, 1992). The more we understand about the initial dispersion of past eruption clouds, the better we can constrain interactive stratospheric aerosol models to fit observations and the more confidently climate models can then attribute the impacts from past eruptions. Future climate models with interactive

volcanic aerosol will be better equipped to predict the effects for a future eruption of a similar magnitude.

Mount Pinatubo is situated at 15°N in the Philippines and, after a series of smaller eruptions from 7-12<sup>th</sup> June, on June 15<sup>th</sup> 1991 it progressed to a cataclysmic eruption, injecting approximately 20 Tg of SO<sub>2</sub> (estimated 14-23 Tg (S Guo et al., 2004)) between 25-31 km into the atmosphere (Bluth et al., 1992; Hansen et al., 1992; Read et al., 1993). This eruption is still the only widely observed Volcanic Explosivity Index (VEI) 6 eruption with in-situ measurements from high-altitude aircraft (e.g. Pueschel et al., 1994) as well as satellite and ground-based lidar observations of SO<sub>2</sub>, sulfate aerosol particles and ash particles (e.g. McCormick et al., 1995; Arfeuille et al., 2013; Kremser et al., 2016). Additionally, this is the largest eruption observed to date with ground-based lidars located around the world (Ansmann et al., 1997; Antuña et al., 2002).

In the tropics, the volcanic sulfate aerosol particles were so reflective that space borne passive instruments, such as SAGE II, became saturated and were only able to measure the upper part of the aerosol cloud (e.g. Thomason and Osborn, 1992). Globally located ground-based lidar has been used for many years in atmospheric science (Wandinger, 2005) and at the time of the Mount Pinatubo eruption they were invaluable in observing the global dispersion of a thick cloud of stratospheric ash and sulfate aerosol. Ground-based lidar allows the stratospheric column to be observed at the same location over time, with the Mauna Loa observatory measuring both the 1982 El Chichón and 1991 Mount Pinatubo major volcanic aerosol clouds (Barnes and Hofmann, 1997).

In contrast to the SAGE-II measurements, the laser profiling lidar instrument penetrates the full depth of the Mount Pinatubo aerosol cloud (including both ash and sulfate aerosol particles) and provides detailed, high-resolution information on the progression of the tropical reservoir of volcanic aerosol after the eruption. Lidars provide an accurate vertical analysis with many extending up into the stratosphere. Analysing lidar measurements at different latitudes allows a constraint on model predictions of the volcanic cloud dispersion.

Although this means observations are only from one location, ground-based lidars are applied to observe the temporal development of clouds and other atmospheric structures. Ship-borne (Avdyushin et al., 1993; Stevens et al., 1994) and aircraft-borne lidar measurements (e.g. Winker and Osborn, 1992; Browell et al., 1993) of the Mount Pinatubo aerosol cloud were also made, measuring a broader latitude range of the

structure and spatial variability of the volcanic cloud. These were deployed only for limited time-periods (July 1991 and January-March 1992 for Winker and Osborn (1992a) and Browell et al. (1993), respectively), essentially sampling the volcanic cloud progression at different points.

While instruments such as SAGE II could not be used to examine the vertical distribution of much of the tropical aerosol cloud, it still provided observations of the spatial coverage of the upper extent of the Mount Pinatubo aerosol cloud and was able to measure the full extent of the cloud in mid-latitudes. The measurements show that the Mount Pinatubo cloud took three weeks to cross the equator and disperse globally (Bluth et al., 1992; McCormick and Veiga, 1992; Robock, 2000; Guo et al., 2004).

The 1991 Mount Pinatubo eruption has been studied extensively; however, most model studies have tended to focus on the long-term trends (a year or more) following the eruption (Ansmann et al., 1997; Stenchikov et al., 1998; Arfeuille et al., 2013b; Schmidt et al., 2018). This study focuses on the initial dispersion following the eruption, specifically June 1991-February 1992, in order to see how the tropical volcanic aerosol cloud evolved in the first nine months on a near-daily timescale. An assessment of the altitude and timing of the dispersion to mid-latitudes is also conducted, together with a comparison of ground-based and ship-borne lidar measurements to interactive stratospheric aerosol simulations with a coupled chemistry and aerosol model.

The Historical Eruptions SO<sub>2</sub> Emission Assessment (HErSEA) Pinatubo interactive stratospheric aerosol simulations are one of the co-ordinated multi-modelled experiments in the Interactive Stratospheric Aerosol Model Intercomparison Project (ISA-MIP) (Timmreck et al., 2018). This analysis tests the accuracy of the UM-UKCA mid-altitude (21-23 km), mid-SO<sub>2</sub> mass (14 Tg) HErSEA simulations. Moreover, the analysis will aid our understanding of the impact that nudging to meteorological re-analysis fields has on interactive volcanic aerosol simulations. The evaluation also relates to the UKCA aerosol module use in the European “IFS-GLOMAP” system, which has been applied to simulate other eruption clouds (Remy et al., 2018; Remy et al., 2019) and to understand similarities and differences between models that conducted in the Model Intercomparison Project on the climatic response to Volcanic forcing (VolMIP) multi-model interactive stratospheric aerosol Tambora experiment (Zanchettin et al., 2016; Marshall et al., 2018) which showed a large range in sulfate deposition, for example (Marshall et al., 2018).

Lidar observations from the Mauna Loa Observatory, USA (MLO), Table Mountain, CA, USA (TAB), Toronto, ON, Canada (TOR) and Observatoire de Haute Provence, France (OHP) are used to investigate the initial dispersion of the Mount Pinatubo sulfate and ash cloud in the stratosphere. Analysis of the initial dispersion allows us to see how the cloud evolves in the first weeks and months after the eruption. The progression of the volcanic cloud was significantly affected by the nature of the vertical wind shear in the tropics at this time. As explained in Section 2.2.3 the QBO represents a slowly descending quasi-periodic oscillation between easterly and westerly winds and is the leading mode of dynamic variability in the tropical stratosphere. Within the tropical upwelling inherent with the BDC (e.g. Butchart, 2014) the initial transport of volcanic aerosol from tropical eruptions is essentially driven by the prevailing phase of the QBO, which was transitioning into strongly easterly in June 1991 (Dee et al., 2011; Dhomse et al., 2014). This phase involved the easterly winds strengthening with altitude (easterly shear), causing the upper edge of the volcanic cloud to be transported fastest. As mentioned in Section 2.2.3, the easterly QBO phase tends to restrict meridional transport via its effects on the sub-tropical barrier, with the Mount Pinatubo cloud remaining confined in the tropical region until the seasonal cycle of the BDC shifts into predominantly northern hemisphere transport from September 1991 into early 1992.

Comparing the lidar measurements at MLO to those from northern mid-latitude sites (Table Mountain (TAB), Toronto (TOR), Haute Provence (OHP)) allows a detailed assessment of the temporal progression of the volcanic cloud, including both ash and sulfate aerosols, from a near-tropical site to northern mid-latitude sites. By comparing the observations to simulations from UM-UKCA it is possible to see how well the model (simulating just sulfate aerosols in this chapter) represents observations, both qualitatively and quantitatively. Comparisons within this chapter are of extinction ( $\text{km}^{-1}$ ) in the mid-visible (550 nm), the wavelength of maximum solar radiation, over time and altitude, in order to obtain a quantitative comparison between the lidar observations and the model simulations.

Another test for the model is to assess the impact of an approximate QBO, whereby the initial conditions of the model are set to a time when winds are close to reality and a pre-nudged QBO, where winds are nudged to 2 months before the eruption. Accurately producing the wind and temperature patterns for the initial conditions at the time of the Mount Pinatubo eruption is important, as these conditions have a large impact on the

progression of the volcanic aerosol cloud. Testing the impact of different initial conditions at the time of the Mount Pinatubo eruption allows an assessment of how different initial conditions may affect the progression of the volcanic aerosol cloud.

Overall the aims of this chapter are to:

- 1) Compare ground-based lidar observations from the near tropics and northern hemisphere sites against one another in order to understand when the volcanic cloud was observed at different locations around the globe.
- 2) Compare ground-based lidar observations to the UM-UKCA to understand how the specification of the QBO (approximate-QBO or pre-nudged) influences the volcanic sulfate cloud at these sites.

These comparisons allow for an improved understanding of the progression of the volcanic cloud from the initial sheared plume structure, when the cloud stretched from the Philippines to Caribbean at the end of June (S Guo et al., 2004) to then becoming a confined tropical reservoir of volcanic aerosol (Grant et al., 1996) and the stages of the subsequent transport of the aerosol cloud to the northern hemisphere mid-latitudes. In further analysing the Mount Pinatubo cloud from its transition from a concentrated plume through the stages of global dispersion (specifically June 1991-February 1992), the aim is to better understand how these major tropical eruptions ultimately impact on climate.

## 4.2 Data and Methods

As outlined in Section 3.6 this chapter focuses on the lidar sites at MLO, TAB, TOR and OHP with a comparison to model data from UM-UKCA. Shipborne extinction data from Avdyushin et al. (1993) is also investigated in this chapter, as this ship passed close to the equator ( $8^{\circ}\text{N}$ ) and through the near-tropics and mid-latitudes. The shipborne data is from the Russian lidar that was on board the “Professor Zubov” ship (herein referred to as “Zubov”). This lidar operated at a wavelength of 539.5 nm and took measurements between the 11<sup>th</sup> July 1991 and 21<sup>st</sup> September 1991 on 48 nights, traversing between latitudes of  $40^{\circ}\text{N}$  in the Atlantic Ocean down to the west coast of Africa before returning to the northwest of Spain, as shown in Chapter 3. The journey largely traversed an area within the latitudes of  $8\text{-}22^{\circ}\text{N}$ . The timing and the latitudes of this ship journey complement this study well, as they show the evolution of the aerosol in the tropical band following the eruption in these first few months.

As explained in Chapter 3, the modelling research tool used in this thesis is the interactive stratospheric aerosol configuration of the UM-UKCA composition-climate model (Dhomse et al., 2014; Mann et al., 2014; Marshall et al., 2018; Marshall et al., 2019), with comparisons to the lidar based on the aerosol extinction profiles at 550 nm diagnosed by the model. When comparing the model to observations, the backscatter ratio (BSR) measured by the lidars (ground-based and shipborne) is converted to extinction using the methods outlined in Section 3.6.3. In order to compare more directly between lidar measurements and model simulated extinction, model data is converted onto the same altitudinal range (15-30 km, 300 m resolution) and temporal range, i.e. the days when measurements were taken. As the model simulated extinction is interpolated onto the same time and altitude resolution as the lidar measurements, a direct comparison is possible.

As described in Chapter 3, the test cases for the model use the mid-range values of 14 Tg SO<sub>2</sub> and 21-23 km injection height from Timmreck et al. (2018). In order to investigate the importance of stratospheric winds on the dispersion of the cloud, the initial conditions were varied between an approximate-QBO and a pre-nudged QBO (outlined in Chapter 3).

The approximate-QBO simulation analysed here is one of 3 ensemble members in the Mount Pinatubo simulations shown in Dhomse et al. (2014), where all 3 runs are initialised from June 1st in different years within a 15-year control TimeSlice integration, the years selected to produce a similar wind pattern to the time of the Mount Pinatubo eruption. The ensemble member in this study has a start date of 01/02/1996 from the TimeSlice 2000 (TS2000) control, however, the TimeSlice run has repeating year-2000 conditions, hence the point of re-initialisation does not represent 1996 conditions. In contrast, in the pre-nudged QBO case, the initialisation continues from the free-running with an “interim nudged control run” for at least 2 years until 2 months prior to the eruption, allowing some time to progress into the free-running mode of the model. Both of the model simulations are free-running, which ensures that the transport of the aerosol cloud is fully consistent with the effects from the radiative heating from the aerosol.

Given the pattern noted in the observations at MLO (Section 4.3.1), a regression analysis is performed on the descending layers of aerosol that are found, both in the observations and in the model, to provide a further quantitative comparison between the

observations and the model. The regression is split between the first and second half of the descending pattern that is seen (

Figure 4-1), as they show a steep initial descent before flattening nearer the tropopause. A regression line is fitted for each slope (slope denoted as downward red arrows in Figure 4-1) in each descending layer, with the resulting value demonstrating the extent of the slope (where 0 = flat line, 1 or -1 = vertical line) to quantify the steepness in descent of the layers. The output of this regression is to determine changes in slope, with negative values indicating the downward trend of the data. Larger values indicate a steeper gradient on the layers with smaller values indicating a “trailing off” of the layers. The purpose of this analysis is to compare quantitatively the descent of the volcanic cloud between the observations and the model simulated vertical profiles, as an assessment of the cloud structure as it descends towards the tropopause.

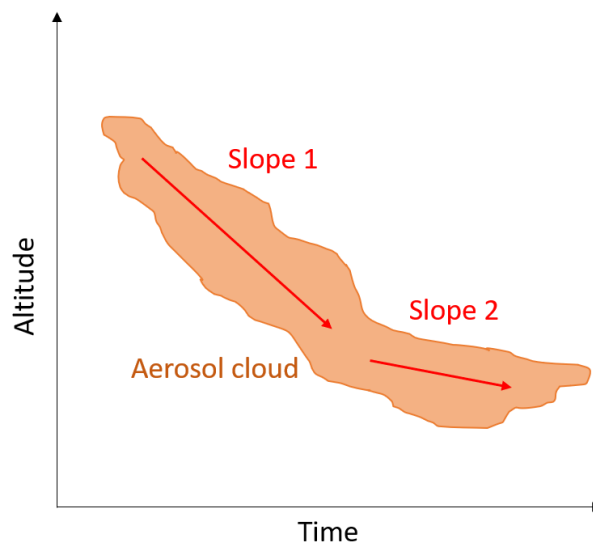


**Figure 4-1 Schematic for how the regression analysis is performed. Orange cloud depicts the aerosol cloud pattern noted at MLO, red arrows indicate each slope analysed.**

### 4.3 Results and Discussion

The results shown in this section begin with a description of how the Mount Pinatubo aerosol progressed in the tropics, comparing the signals in the near-tropical ground-based lidar data from Mauna Loa and ship-borne lidar data from the Zubov cruise through the North Atlantic (see Section 3.6.1). This comparison allows an assessment of early tropical measurements (Zubov) with a near-tropical site (MLO) to establish a more detailed analysis of the movement of volcanic aerosol out of the tropical reservoir.

This is followed by discussion regarding the detection of the volcanic cloud at each of the northern hemisphere sites, in relation to the timing of the dispersion from the tropical reservoir, providing a conceptual basis for comparisons to the model simulations. The model analysis is primarily focused on the differences between the approximate-QBO and the pre-nudged simulations.

#### **4.3.1 Tropical lidar signal – Phases of the cloud dispersion and comparison of ground-based and ship-borne lidar with model simulations**

Figure 4-2 shows the BSR profiles measured by the ground-based lidar at MLO from June 1991-February 1992. The volcanic aerosol cloud is first detected at MLO on July 1<sup>st</sup> 1991, travelling 16,140 km in two weeks. During the first 2 months after this initial signal of the cloud, the measurements show there are three descending structures, from here on described as “layer 1, 2 and 3” (outlined in Figure 4-2). Although the structure of each layer is descending, because of the steep vertical gradient in the easterly winds, the cloud is effectively being stretched, with air masses in the upper extent of the volcanic cloud transported faster than in the lower part of the cloud (see also discussion in Section 2.2.3). The regression analysis mentioned in Section 4.2 also allows an assessment of this cloud stretching. As part of this analysis, we define the period where these layers are apparent (July 1<sup>st</sup> – September 15<sup>th</sup> 1991) as the “first phase” of the global dispersion of the Mount Pinatubo cloud, where the structure is highly inhomogeneous.

The first of the 3 layers above MLO is detectable in the measurements for 24 days (1<sup>st</sup>-25<sup>th</sup> July 1991), beginning as a small 900 m deep signal between 22.3 and 23.2 km before increasing to ~3km deep from 21-25 km within 2 days of the initial signal being received. The upper portion from 23-24 km has the strongest signal, with extremely high backscatter ( $BSR > 10^2$ ) with the lower 21-23 km showing BSR values  $\sim 10^1$ . This trend of the highest signal being in the upper part continues for the duration of this first MLO layer detection, with values in the upper part staying above 20 ( $10^{1.3}$ ) throughout and lower part values staying around 10 ( $10^1$ ). When considering the full vertical extent of this first layer, the overall depth is 7.5 km (17.5-25 km), but with an average “layer-thickness” of 2.4 km.

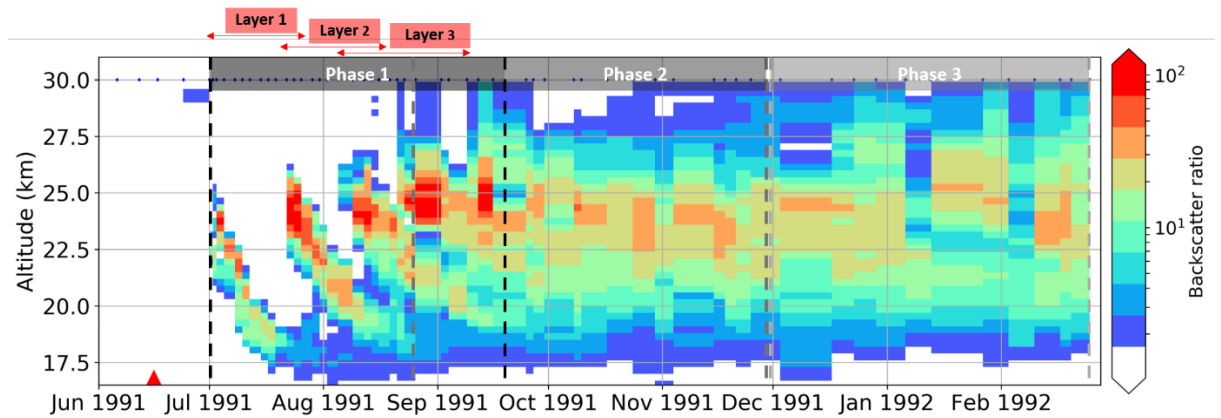


**Figure 4-2** Ground-based lidar backscatter ratio at MLO, initial layers are denoted with red arrows and different phases with greyed boxes.

The second MLO layer appears on 22<sup>nd</sup> July, whilst the lower extent of the first MLO layer is still present, again showing significant BSR values above 100 between 22-26 km. This second MLO layer ends on 25<sup>th</sup> August with a slightly deeper layer-thickness than the first layer (~4 km). The high BSR values are also more consistent throughout this second layer with a deeper extent of values  $> 25$  ( $10^{1.4}$ ) through the middle of the layer, whereas values in this mid-layer stay  $\sim 10$  ( $10^1$ ), as in layer 1. The overall depth of this second layer is 17.5-26.5 km, with the highest values again appearing at the beginning of the layer. The conversion of volcanic  $\text{SO}_2$  to sulfate aerosol taking 30-45 days and layer 2 having higher BSR values in the lower half of the cloud than seen in layer 1 may be due in part to the  $\text{SO}_2$  still being oxidised in July, when the first layer was detected over MLO. As discussed by Bluth et al. (1992), ~60% of the erupted  $\text{SO}_2$  still remained in the volcanic aerosol cloud by July 1<sup>st</sup> 1991, thus these higher values during layer 2 are likely areas of increased sulfate aerosol.

The third layer first appears on 9<sup>th</sup> August at 26.5 km with a similar initial thickness to layer 2 (4km) before deepening with an average depth of ~5 km in mid-August 1991. This gradual increase in layer thickness may be indicating the fall speed of the largest particles in the cloud slowly sedimenting whilst smaller particles remain at the upper extent of the layer. Note that a 100 nm particle sediments ~1 km in 6 months whilst a 500 nm particle sediments ~1 km in around 1 month (Junge et al., 1961 and Section 2.2.5). As with the other two layers, the initial, higher altitude values have the highest BSR values 64-100 ( $10^{1.8}$  -  $10^2$ ) with values lessening throughout the layer, but remaining mostly  $>10$  ( $10^1$ ), still at significantly high values. The period of these initial

three MLO layers is defined in Figure 4-1 as Phase 1, when the cloud still has BSR values in excess of 100 (red values) within the distinct, inhomogeneous layered structures.

Since there are still some similar areas of these very high BSR values ( $>10^2$ ) at 24.5-25.5 km in mid-September, this is defined as the end point for Phase 1 of the dispersion of the Mount Pinatubo cloud. After Phase 1 showing very defined layers begins Phase 2 of the volcanic cloud, when the cloud is becoming more homogenous and well-mixed. Phase 2 is a transition phase that is defined visually, beginning with a fourth layer that is noticeable within the MLO lidar profiles at the end of August 1991, showing the highest BSR values at the lower portion of the cloud. Potentially, this could indicate a further progression of the size distribution of the particles, with slow sedimentation, and the associated size-sorting effect gradually changing the vertical profile of the backscatter signal, from initially the highest values at the upper extent of the cloud, to then this decreasing profile in the 4<sup>th</sup> layer. The head of the 5<sup>th</sup> layer is then mixed with the middle and tail of the cloud, the stirring of the wind shear causing more cloud mixing with some periods of ~2 km deep regions of larger BSR values (orange, BSR $>$ 25). After mid-November 1991 there are only thinner regions of larger BSR values, defined in this study to be “Phase 3”, when the cloud is more uniform and well-mixed. Some variability can be seen in January-February 1992, though BSR values and altitudes are similar to values at the end of 1991.

The three phases following the eruption are shown in Figure 4-2 in the form of grey boxes. In summary, the first phase spans from July 1<sup>st</sup> – September 9<sup>th</sup> 1991 with the three descending layers in this phase that start at 25, 25.5 and 26 km, respectively, and descend to 18, 19 and 20 km, respectively. The second phase occurs from August 23<sup>rd</sup> – November 28<sup>th</sup> 1991, as the cloud is evolving into becoming a fully mixed aerosol cloud. Phase 2 shows some indication of a fourth layer, but much less distinct in both shape and gradient than the layers seen in Phase 1. Phase 2 then begins to become more homogeneous, a potential transitional phase between the highly inhomogeneous first phase and comparatively more homogeneous later phases. The third phase indicates when the volcanic aerosol is fully mixed within the tropical reservoir, with the lidar measurements showing a more homogeneous signal, no obvious layer structures and an altitudinal span that extends to an 8.5 km depth, between 18.5-27 km.

The phases seen in this analysis are primarily driven by the nature of the vertical wind shear, but may also be related to the microphysical sorting of the cloud itself, with different sized particles falling at different speeds, potentially impacted by volcanic ash. Phase 1 indicates the inhomogeneous stage in the cloud dispersion, when the cloud is still plume-like, becoming increasingly stretched by the wind shear. The signal appears disordered in the lidar signal, as the volcanic material is still circling the globe, with a composition which is likely to still contain sulfate and ash from the initial eruption. When comparing to the model simulated global SAOD plots (section 4.3.9) it is important to consider that whereas the easterly wind shear is the primary reason for the layered structure seen in the measurements, MLO is at 19°N, therefore on the edge of the tropical reservoir (Barnes and Hofmann, 1997). The location of MLO means the layers could potentially indicate in part filaments of the Mount Pinatubo cloud being exported towards the midlatitudes on the edge of the developing tropical reservoir (Trepte et al., (1993). The successive layers and phases of transition are occurring as the cloud is wrapped around the Earth, with the upper edge of each new layer becoming further ahead of the lower edge. In this analysis, the second phase is defined as the end of these layers and the start of the cloud becoming more homogeneous, plus the timing of the tropical reservoir spilling over into the northern hemisphere. The third and final phase by mid-late November 1991 is the stage at which the cloud begins to become homogeneous, the point at which the cloud stabilises into a fully mixed cloud of volcanic aerosol in the tropical reservoir of the stratosphere (e.g. Grant et al., 1996).

### **4.3.2 MLO backscatter to extinction comparison to Zubov shipborne lidar data**

This section explores the initial progression of the Mount Pinatubo cloud further, comparing the signal seen in the MLO observations with the shipborne lidar observations (section 4.2) that measured the tropical stratosphere above the Caribbean in July/August (Phase 1) and in a transect across the tropical North Atlantic in late August and early September (Phase 2).

Figure 4-3 shows a comparison between shipborne lidar data from the Zubov ship (Avdyushin et al., 1993) and the MLO ground-based lidar during the period spanning July 12<sup>th</sup> 1991 – September 20<sup>th</sup> 1991. The Zubov shipborne lidar data spans between 8-40°N, the majority of this period between 8-20°N. The initial phase in the 2<sup>nd</sup> half of July (17<sup>th</sup>-31<sup>st</sup> July) was towards Cuban waters (19-21°N, 58 to 74°W), with a wider

loop around the Caribbean in the first half of August (2<sup>nd</sup>-22<sup>nd</sup> August) a southward portion reaching 10-14°N on 9<sup>th</sup>-12<sup>th</sup> August, and a trans-Atlantic leg (25<sup>th</sup> August to 9<sup>th</sup> September) towards North Africa at 15-20°N in late August, progressing to measure in the core of the tropical reservoir (8-15°N) in early September.

The majority of these measurements are in the latitude range 18-22°N, with the observations from the Caribbean showing obvious similarities to layers noted in the first phase of the MLO measurements. However, the Zubov shipborne lidar had two periods that sampled the Mount Pinatubo volcanic cloud at ~10°N (first 9-12<sup>th</sup> August and then again in early September), giving an opportunity to understand how far into the tropical reservoir the layers observed at MLO progressed.

The first layer is not detected at all in these first days when the ship was at higher latitudes but the second is detected strongly when the ship reached latitudes closer to the equator (~19°N), suggesting this pattern was only detectable around the equator region.

The earliest Zubov measurements of the volcanic cloud (18<sup>th</sup> July) detected the trailing end of the first MLO layer at 16-18 km, then with the second and third MLO layers seen in the Zubov data slightly earlier as the ship began measuring on 12<sup>th</sup> July and did not reach 20°N until 18<sup>th</sup> July, but the second and third layers can be seen clearly in both.

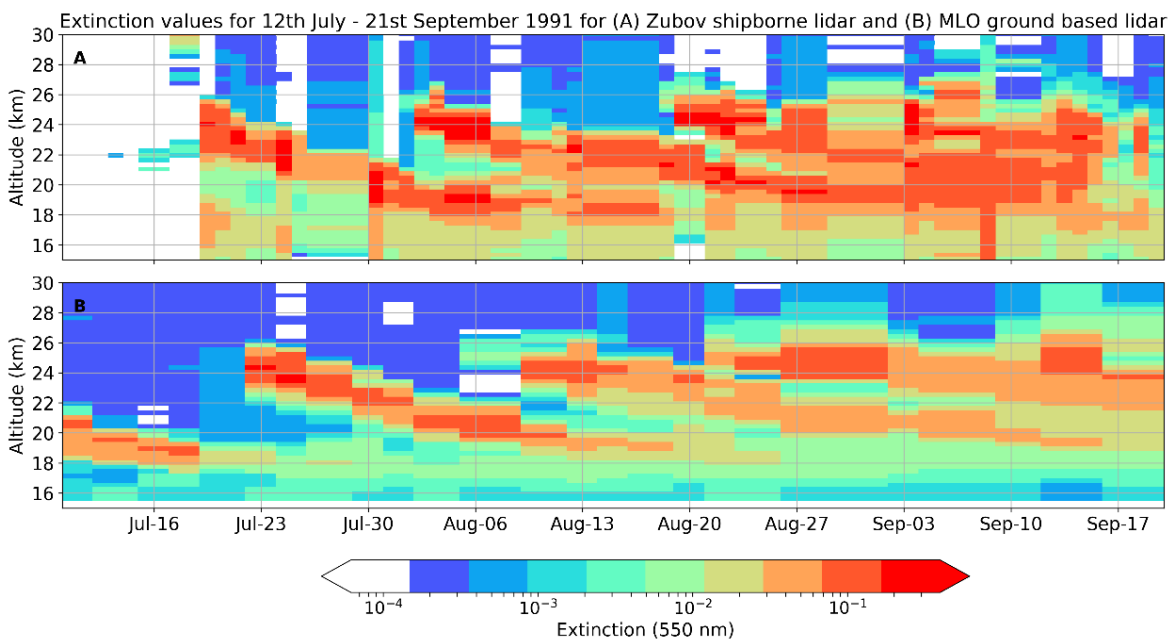


**Figure 4-3 - Extinction values for (A) Zubov shipborne lidar and (B) MLO (expansion of Figure 4-2) from 12th July - 21st September 1991.**

With the Zubov measuring from the North Atlantic, around 10,000 km to the west of MLO, the expected lag (based on the global circulation of the volcanic aerosol cloud) in detecting the cloud between the two datasets can be seen, with the Zubov data showing the second and third of these 3 and 7 days earlier than they are detected at MLO (detected from Zubov on 19<sup>th</sup> July and 2<sup>nd</sup> August and at MLO on 22<sup>nd</sup> July and 9<sup>th</sup> August, respectively). Both sets of measurements show detection of the second layer at 26 km descending to 19 km within a month (19<sup>th</sup> July – 18<sup>th</sup> September and 22<sup>nd</sup> July – 19<sup>th</sup> September, respectively).

The maximum extinction values for each observational dataset was at the leading edge of layer 3 for Zubov and the leading edge of layer 2 for MLO at 0.4 for Zubov and 0.2 for MLO on 2<sup>nd</sup> August and 24<sup>th</sup> July, respectively. The layer values for each site are similar. The layers themselves range from 0.08-0.13 with surrounding values of 0.001 and below, signifying a factor increase of 80-130 between background extinction values and the extinction values of the volcanic layers.

### **4.3.3 Northern hemisphere mid-latitude lidar measurements**

In this section, we explore the timing of the dispersion of the Mount Pinatubo cloud to the northern hemisphere mid-latitudes (Table Mountain (TAB), Toronto (TOR), Haute Provence (OHP)), and the nature and variability of the BSR profile of the volcanic cloud measured by lidar sites in Europe and North America. The purpose is to understand better the timing of the hemispheric dispersion in relation to the phases of the progression of the cloud in the tropics.

Figure 4-4 also shows BSR values for MLO, the 3 layers and phases defined in the previous section, alongside the TAB, TOR, OHP, mid-latitude lidar profiles. All three mid-latitude lidars show that during July to mid-August, when MLO had two very strong layers at  $BSR > 100$ , there was some early dispersion of the volcanic cloud in the lowermost stratosphere (15-17 km), with BSR enhanced by a factor of 2 to 3 over background ( $BSR \sim 2-3$ ), as discussed for example by Deshler et al. (1992) and Dhomse et al. (2014). The much higher BSR values ( $> 7$ , pale green) occurred later within deeper layers only two months after the eruption at TAB (21<sup>st</sup> August 1991), three months after at OHP (20<sup>th</sup> September 1991) and four and a half months after at TOR (29<sup>th</sup> October 1991) with values  $> 3$  ( $10^{0.5}$ ).

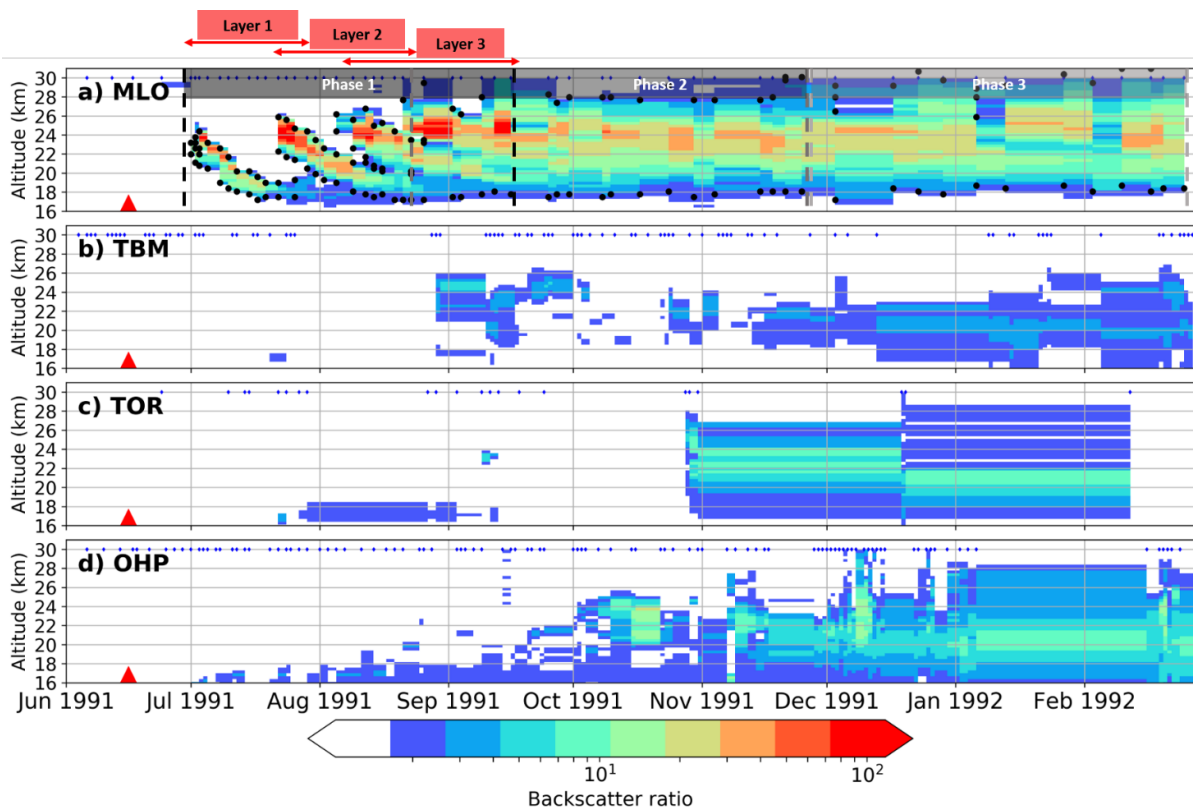


**Figure 4-4** Ground based lidar backscatter ratio plots for a) MLO, b) TAB, c) TOR and d) OHP from June 1991 - February 1992. Blue diamonds at 30 km show measurement dates. Red triangle shows eruption date and red arrows show layer duration.

Whereas the MLO signal was organised into distinct structures, the Mount Pinatubo signal at TAB and TOR is much more variable with the height of maximum BSR at 25 km on occasion, and other times at 20 or 22 km, particularly during September 1991. The higher frequency of the OHP data confirms this variability continued into October 1991 before a far more homogenous profile is evident in November, with BSR values above  $10^1$  confined between 20-22 km, descending to 18-20 km in January 1992. At TOR, there were only a limited number of measurements in November 1991 to February 1992, with only 12 soundings at TAB after November 1991. The initial strong variability in the detection of the volcanic cloud at the different lidar sites indicates the initial filamentary structure of the cloud as it dispersed globally.

This disordered structure in the mid-latitude ground based lidar observations are consistent with those observed at Garmisch (Germany) and Tsukuba (Japan) (Jager et al., 1995). Comparing to high latitude sites such as Thule (Greenland,  $76.5^\circ\text{N}$ , di Sarra et al., (1998)), there the cloud had a longer initial transport in a shallow and variable layer, a much deeper cloud transported in the spring. BSR values continuing to exceed

6 in April 1992 show that the polar stratosphere contained a large amount of volcanic aerosol only after the polar vortex broke up (di Sarra et al., 1998).

The mid-latitude BSR values are much lower than at MLO in the first months following the eruption, due to the structure of the tropical reservoir and related to the phase of the QBO. Issues such as instrument error are possible, however, so values should be considered with some caution, with exact errors difficult to quantify. At MLO, the maximum backscatter stayed at ~25 km throughout the 2<sup>nd</sup> and 3<sup>rd</sup> phase. This persisted as a result of tropical upwelling from the BDC, with aerosol heating also leading to stronger upwelling, promoting greater transport to higher northern hemisphere latitudes (Trepte et al., 1993). The initial detection seen at TAB at 25 km is indicative of a filament from this highest backscatter altitude, with the relative strength of the filaments at the different sites consistent with the BSR gradient in the tropical reservoir.

This analysis indicates how the volcanic aerosol from the Mount Pinatubo cloud progressed in the first 8 months following the eruption in both ground-based and ship-borne lidar observations. The pattern at MLO has been differentiated into three separate phases that occurred following the eruption, the first of which has distinct descending layer structures. The sites at mid-latitude show a significantly varied structure, as filaments of volcanic aerosol are transported at different altitudes from the tropical reservoir, with the relative strength of these filaments consistent with the BSR profile of the tropical reservoir.

#### **4.3.4 Model comparison to MLO, TAB, TOR and OHP**

The following section outlines a comparison between the modelled extinction values at 550 nm from UM-UKCA and the ground-based lidar measurements discussed in the previous sections. Conversion factors for converting between backscatter and extinction are varied through time to account for changes in size distribution, as in Jäger and Deshler (2003). The lidar in extinction (550 nm) is then compared with model simulated extinction from the two different initial condition methods.

The maximum extinction at MLO from the lidar, pre-nudged model run and approximate-QBO model run is 0.2, 0.11 and 0.18, respectively, with the observations and pre-nudged conditions showing maximum extinction values on July 21<sup>st</sup> 1991 and the approximate-QBO simulation 4 days prior to this date. With reference to the layers, Figure 4-5 shows that the model layers are thicker and less distinct with a higher cloud

top than the observations (by 2.5 km in layer 2 and 3) in both simulations.

Nevertheless, both the lidar and the model do show descending layer structures.

The shape and thickness of the layers and timings of the occurrence of the layers are closer to observations in the pre-nudged conditions simulation than in the approximate QBO simulation, with the second and third layers appearing a week before the observations in the approximate-QBO simulation. A closer match to observations suggests that the pre-nudged conditions allow accurate wind shear and, therefore, dispersion closer to what was seen in reality. Initially, the first layer matches well (Figure 4-5d), as it is the thinnest of the three (2 km thick). The layer top is marginally above 24 km and the bottom of the second and third layers are also between 18-19 km. The second and third layers thicken over time as in the observations, however, they appear thicker (4.6 and 6.3 km, respectively) than those in the observations (3.1 and 3.7 km, respectively) and their layer top is far higher (27.8 and 28.6 km in the model simulations, 23.2 and 25.6 in the observations). The timings of the phases in the pre-nudged model are more spread out than in the observations, though still showing a distinct Phase 1, less homogenous Phase 2 that develops into a more homogeneous Phase 3. The biggest differences are seen between the timing of cloud detection and height of the layers, outlined in Table 4-1.

At TAB (Figure 4-6) the lidar shows a stronger signal from the beginning of September 1991 onwards ( $10^{-2}$  and greater) whereas this is closer to  $10^{-3}$  in the model before having a stronger signal than the observations from mid-September onwards. The TAB data shows values around  $10^{-2}$  at 17 km resemble observations from Boulder, Colorado (Post et al., 1992) at the same latitude.

At TOR (Figure 4-7) the approximate-QBO model simulation corresponds with observations slightly better, though neither model run matches observations as closely as the other lidar sites. The sparseness of the data at this lidar site also means that the altitude and strength of the volcanic signal is difficult to distinguish. Observations indicate that the volcanic aerosol was seen at lower altitudes (15-17 km) at the end of July, although values  $>10^{-2}$  were not seen until November 1991.

The overall pattern seen at OHP (Figure 4-8) is similar between the observations and the model, notably a strong signal ( $10^{-2}$ ) ~20 km at the beginning of November that is fairly continuous until February 1992. There also appears to be a greater signal closer

to the tropopause (~15 km) at each of the northern hemisphere sites in the lidar extinction.

**Table 4-1 - MLO layer comparison between lidar and model, model altitude range in brackets denotes pre-nudged model run**

<b>Layer</b>	<b>Lidar period covered</b>	<b>Observed vertical extent of volcanic cloud (km)</b>	<b>Model period covered</b>	<b>Modelled vertical extent of volcanic cloud (km)</b>
1	July 1 <sup>st</sup> – July 25 <sup>th</sup> 1991	18-25	June 30 <sup>th</sup> – July 24 <sup>th</sup> 1991	17-24.5 (17-25)
2	July 22 <sup>nd</sup> – August 19 <sup>th</sup> 1991	18-25.5	July 15 <sup>th</sup> – August 13 <sup>th</sup> 1991	17.5-28 (17-27)
3	August 9 <sup>th</sup> – September 12 <sup>th</sup> 1991	19-26	July 28 <sup>th</sup> – August 30 <sup>th</sup> 1991	18-30 (19-28.5)

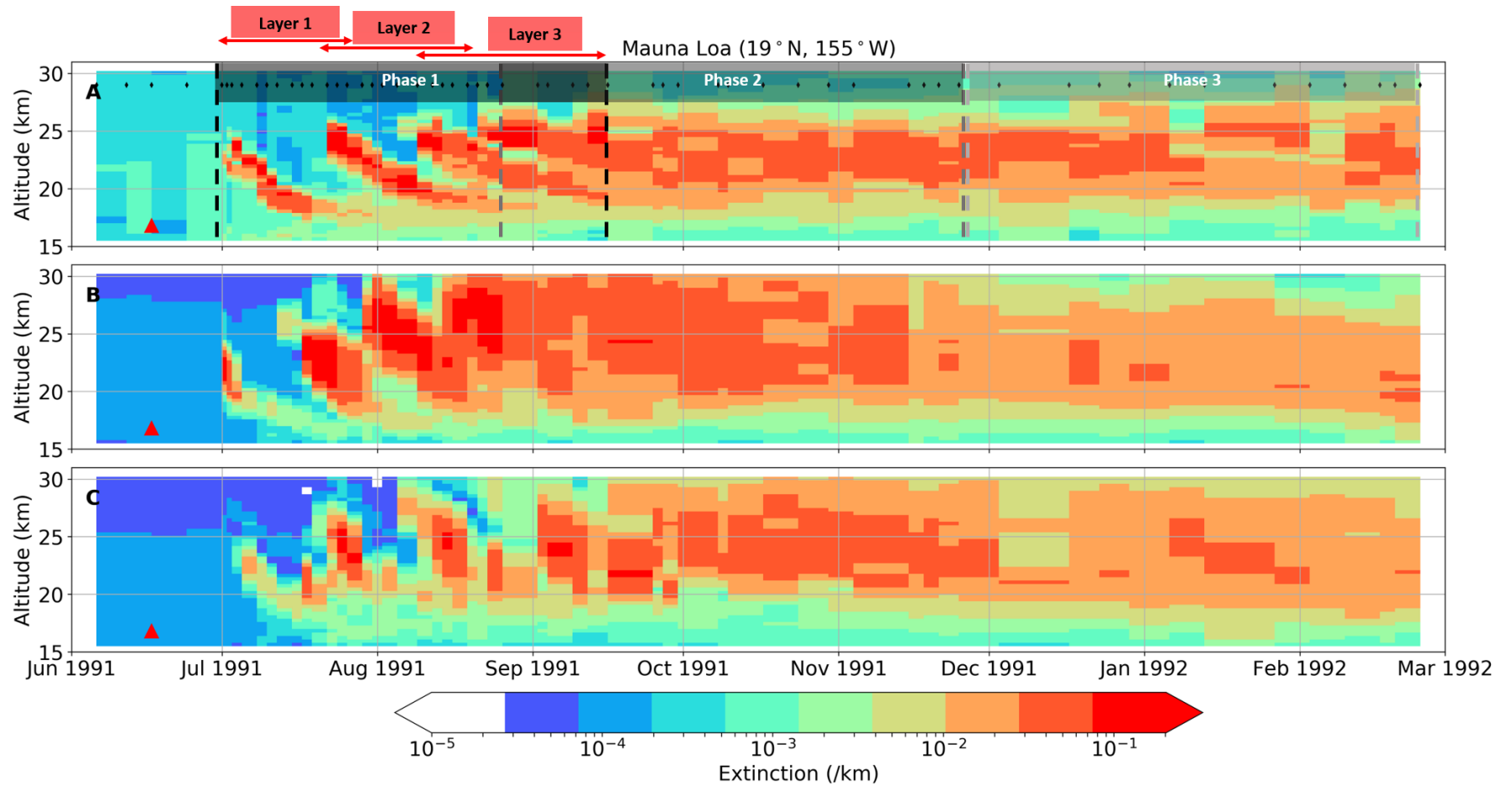
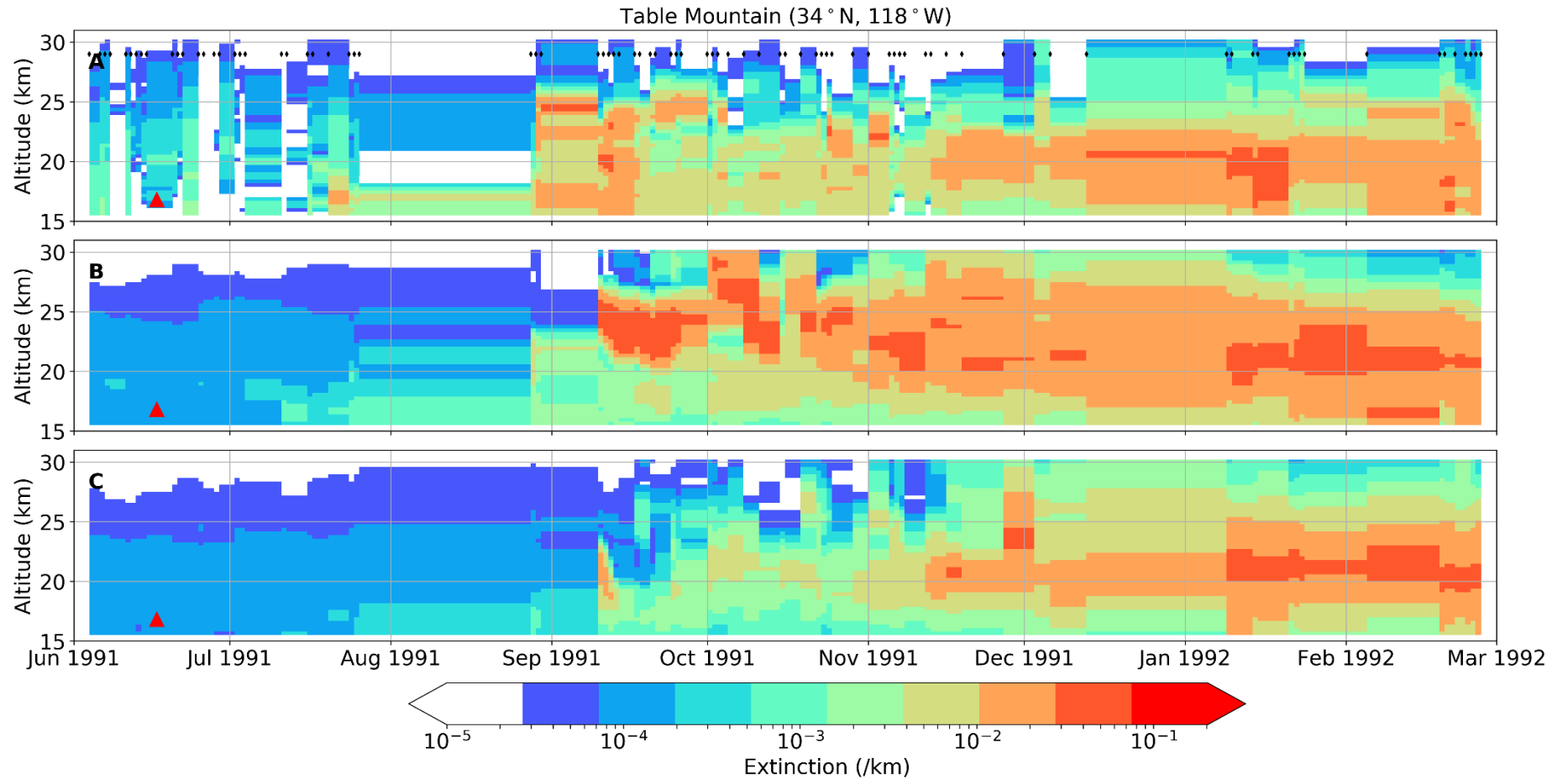
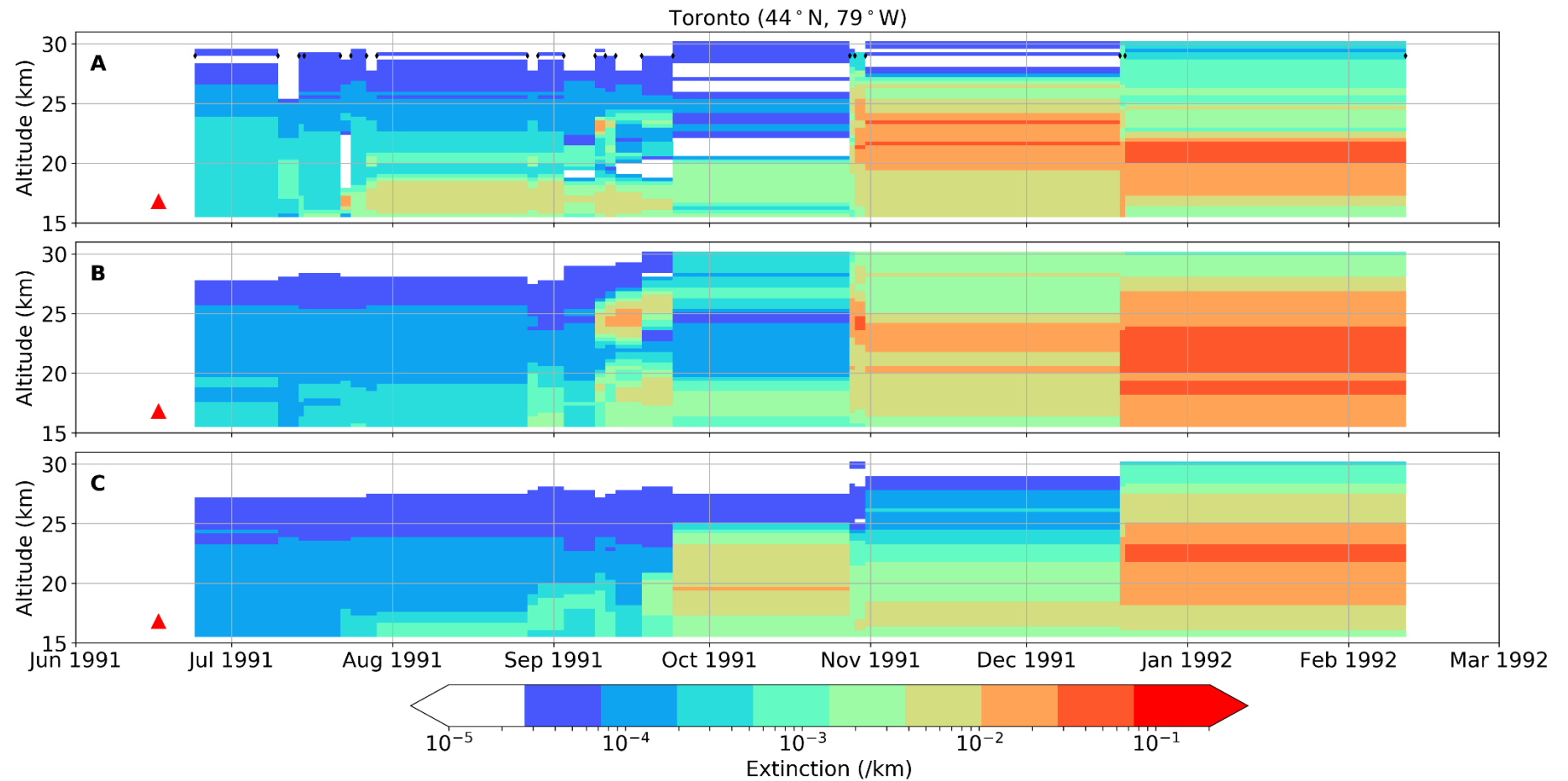


Figure 4-5 Extinction (/km) values for Mauna Loa (MLO) from June 1991 - February 1992. a) Lidar with varying BSR-EXT values over time, b) Model simulation with approximate-QBO, c) Model simulation with pre-nudged conditions, black diamonds in (a) show days when measurements were taken.



**Figure 4-6** Extinction ( $/\text{km}$ ) values for Table Mountain (TAB) from June 1991 - February 1992. a) Lidar with varying BSR-EXT values over time, b) Model simulation with approximate-QBO, c) Model simulation with pre-nudged conditions, black diamonds in (a) show days when measurements were taken.



**Figure 4-7 Extinction ( $/\text{km}$ ) values for Toronto (TOR) from June 1991 - February 1992. a) Lidar with varying BSR-EXT values over time, b) Model simulation with approximate-QBO, c) Model simulation with pre-nudged conditions, black diamonds in (a) show days when measurements were taken.**

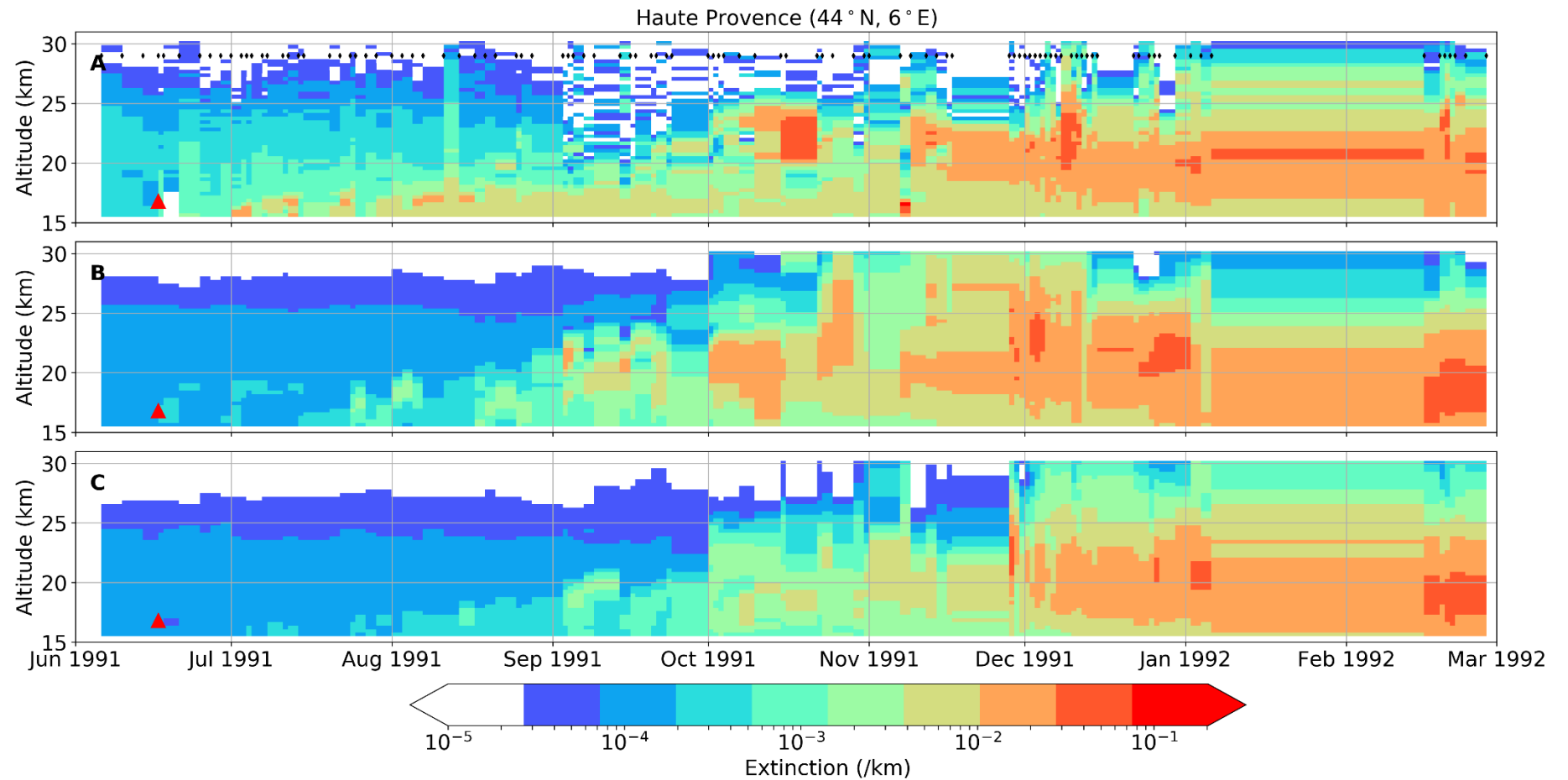


**Figure 4-8** Extinction (/km) values for Haute Provence (OHP) from June 1991 - February 1992. a) Lidar with varying BSR-EXT values over time, b) Model simulation with approximate-QBO, c) Model simulation with pre-nudged conditions, black diamonds in (a) show days when measurements were taken.

### 4.3.5 Wind profiles for June 1991

In order to justify the selection of the pre-nudged model simulation as the choice of initial conditions for this study and future chapters, Figure 4-9 shows a wind plot comparison between Trepte et al. (1993) and the pre-nudged and approximate-QBO model simulations. As this figure shows, there is a good spatial comparison between the observed meteorology and that in the model simulation using pre-nudged conditions, with the wind patterns in the two figures matching almost identically. The 10 m/s wind speeds are the same, around 15 km altitude for 30°N and S and areas of 0 m/s are broadly located in the same regions. The higher wind speed values of 60 m/s are located in the same locations in both figures at 30 km for 60°S. For the negative values, the -30 m/s values descend to around 26 km in the model compared to 27 km for Trepte et al. (1993), however -20 m/s values come down to 23 km in both cases.

In Figure 4-9c there is good agreement between the approximate-QBO simulation and the observations for the southern hemisphere, however, there are significant discrepancies from around 15°S into the equator and across the northern hemisphere latitudes. Values of -10 m/s at around 15°N and 10-20 m/s at 30-60°N in the approximate-QBO simulation are similar to observations, but otherwise the pre-nudged simulation (Figure 4-9b) matches much more closely with observations.

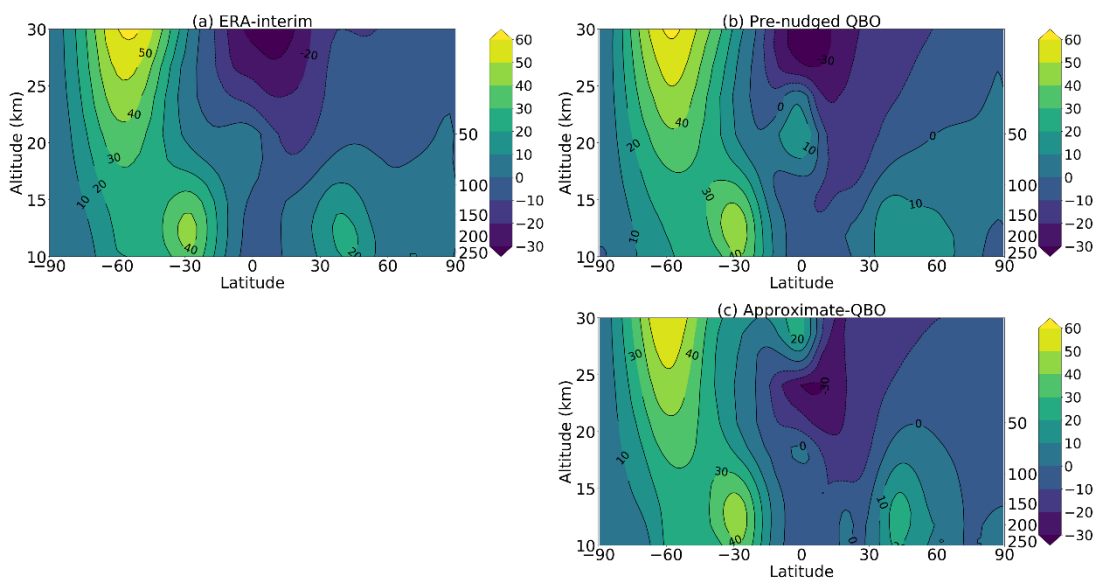


**Figure 4-9** u-wind (m/s) profile comparison over the period 16-30th June, for a) ERA-interim, b) The pre-nudged UM-UKCA simulation and c) The approximate-QBO simulation.

### 4.3.6 Volcanic cloud depth

The layer finding algorithm (Section 3.6.2) was employed in order to compare the layers detected by the MLO lidar (Figure 4-4) with those simulated in the model, thus identifying the upper and lower margins where the extinction reached above a representative background level. This technique is useful to identify where the top of the observed layers are, their timings and their general progression through time. Figure 4-10 shows that the observed layers are at 25, 26 and 26.5 km and begin on July 1<sup>st</sup>, progressing until the end of August. Figure 4-11 shows September onwards when the cloud appears more homogenous and confined between ~17.5 and 27 km until early 1992.

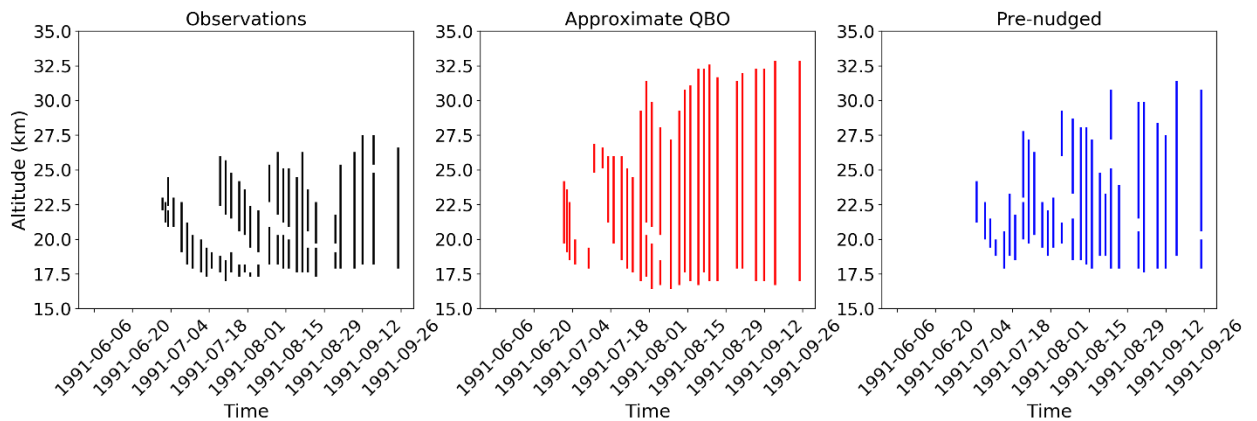


**Figure 4-10** Cloud depth plots for Observations (left), approximate-QBO simulations (middle) and pre-nudged simulations (right) for June - September 1991 at MLO. Each line represents the depth of the cloud, as calculated using the layer finding algorithm.

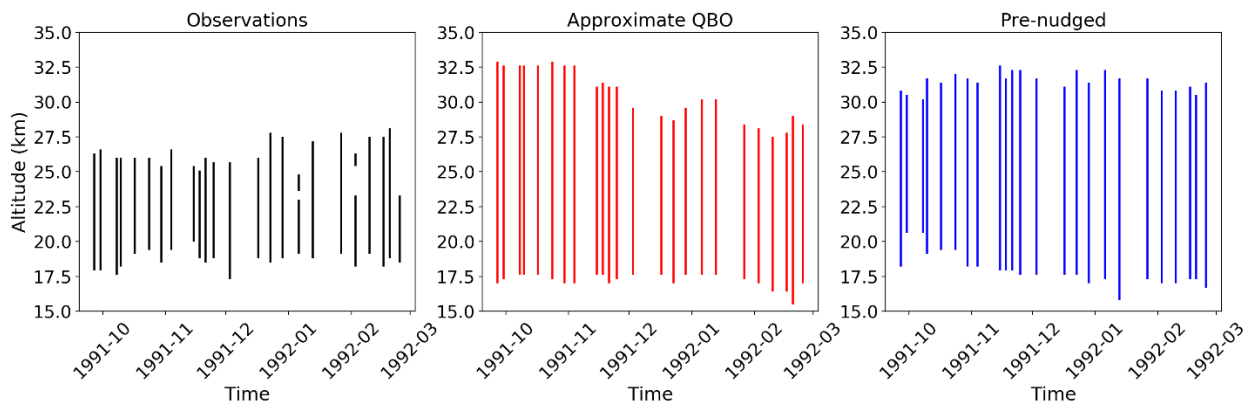


**Figure 4-11** Cloud depth plots for Observations (left), approximate-QBO simulations (middle) and pre-nudged simulations (right) for October 1991 - March 1992 at MLO. Each line represents the depth of the cloud, as calculated using the layer finding algorithm.

In the approximate-QBO case, the first layer is visible at the correct time, however, it is slightly too low (24 km) and lacks the distinct shape seen in the observations. The later layers are subsequently wider and lost by the beginning of August.

Furthermore, the cloud is far higher by 5 km in October, decreasing steadily towards the beginning of 1992 (Figure 4-11). In the pre-nudged case, three distinct layers are clearly visible with a more distinct shape similar to those seen in the observations. The upper layer cloud heights are still slightly lower for the first and too high for the others. During September 1991 the upper cloud limit is lower than in the approximate QBO case. The October 1991-February 1992 period is broadly similar in both model cases with fairly poor agreement with observations, closer in shape and height to observations in the pre-nudged case, yet still too deep and tall.

This analysis allows a more noticeable comparison between the layers produced during the approximate-QBO and pre-nudged simulations, clearly indicating the thinner (closer to observations) simulated layers by the pre-nudged simulation and the thicker overall cloud produced by the approximate QBO simulation. 26-27 km is noted as the peak altitude at MLO, which agrees with the 17-26 km and 17-28 km ranges noted by other lidar measurements (DeFoor et al., 1992; Jäger, 1992) and 26 km estimation from satellite measurements (Read et al., 1993). Thus, the higher altitudes reached in the model simulations can be more confidently attributed to excess heating by the aerosol in the model.

#### **4.3.7 Regression analysis**

Given the interesting signal noted in the observations at MLO with the descending layers and evolutionary phases of the volcanic aerosol cloud, it was decided to investigate further. An assessment was made, comparing average cloud depth, upper cloud extent and a regression analysis for the first, steeper and second, shallower half of the layers in the phases within the lidar and the model (Section 4.2, Figure 4-1).

Considering the descending nature of the volcanic signal seen in both the lidar and the model, the regression analysis here refers to the slope of these layers to assess how quickly they descend in the observations compared to the model. This analysis allows an assessment of the cloud descent in the model simulations and whether the model is potentially simulating wind shear that is too strong and/or strong sedimentation.

The pre-nudged simulation allows more accurate initial conditions than the approximate-QBO simulation, which will ultimately impact on the later progression of the cloud. Table 4-2 outlines the results for the cloud depth, upper extent and regression analysis performed on the layers within the first phase, as well as Phases 2 and 3 for MLO. In both the lidar and the model data, the average cloud depth increases over time between the layers, with differences of 0.6-0.7 km between layer 1-2 (July to mid-August 1991) and 2-3 (mid-August to mid-September 1991), respectively, in the lidar. An increase in cloud depth of 1.3 km (from 10.2-11.5 km) can also be seen between Phases 2-3. The model simulations, however, show much deeper layers, with the approximate-QBO case predicting layer depths three times as large as in the observations (layer 1 6.1 km depth compared to 2.44 km depth in observations), whereas the pre-nudged case predicts layers 1.5 to 2 times higher on average (3.11 km in the first layer).

For all of the layers in the observations, the upper extent of the cloud in both model cases is higher by 1.1 km for the first layer. In the observations, the upper extent of the cloud is at 25.6 km and 26.8 km for layers 2 and 3, respectively, whereas it is 2.2 km and 1.8 km higher in the pre-nudged case and 2.4 km and 4.5 km higher in the approximate-QBO case. During the regression analysis, it is worth noting that both the lidar and the pre-nudged model simulation showed a similar gradient for layer 1 (-0.38 and -0.44 respectively), yet the gradient is much steeper in layer 2 in the pre-nudged model (-0.55 vs -0.22) and steeper in layer 3 in the lidar (-0.39 vs -0.15). This suggests that more aerosol sediments out at higher altitudes within layer 2 than layer 3 in the pre-nudged model simulation. The overall values were steeper in the model simulations, showing a steeper descent of the layers within the model data, particularly in the approximate-QBO case. Furthermore, the differences in slope values suggest wind shear is stronger in the model between ~20-25 km during the progression of layer 2 and not as strong as reality in layer 3.

On the whole, the lidar and model simulation data show a similarly increasing upper cloud extent and two steeper layers, with the overall depth and gradient being higher within the model simulations. When comparing the observations to the model simulation, it is clear that UM-UKCA simulates the spatio-temporal pattern of dispersion well, including the layers and phases noted in the observations. The overall pattern of dispersion is consistent between the near-tropics and the northern hemisphere

mid-latitudes and the rate of descent between the layers. The model is, however, predicting an upper cloud extent that is higher than seen in observations by 1-2 km in the layers and up to 3 km in Phase 3, as well as simulating thicker (by ~1 km), less defined layers. This is possibly a result of too much radiative heating, known to have a strong impact on the behaviour of the cloud (Stenchikov et al., 1998; Aquila et al., 2012) and/or possibly a lack of ash acting as a sedimentation factor (e.g. Deshler, 2016) in the model, which will be investigated and discussed further in Section 4.3.8 and Chapter 6. When comparing the pre-nudged and approximate-QBO model simulations, the pre-nudged simulation shows cloud heights and depths closer to observations, plus a similar overall shape and regression values of the first layer similar to those obtained for the lidar measurements. The pre-nudged simulation allows more accurate initial conditions than the approximate-QBO simulation, which will ultimately impact on the later progression of the cloud.

**Table 4-2 Regression analysis of the depth of the volcanic cloud and cloud top height for the lidar and model simulations with pre-nudged and approximate-QBO at MLO.**

Phase/Layer	MLO Lidar				Model (pre-nudged)				Model (approximate-QBO)			
	Average depth of the cloud (km)	Upper extent of the cloud (km)	Upper half of layer	Lower half of layer	Average depth of the cloud (km)	Upper extent of the cloud (km)	Upper half of layer	Lower half of layer	Average depth of the cloud (km)	Upper extent of the cloud (km)	Upper half of layer	Lower half of layer
Phase 1 – Layer 1	2.44	23.19	-0.38	-0.04	3.11	24.27	-0.44	-0.03	6.10	24.27	-0.75	-0.1
Phase 1 – Layer 2	3.12	25.59	-0.22	-0.05	4.60	27.80	-0.55	-0.15	8.23	28.02	-0.37	-0.12
Phase 1 – Layer 3	3.70	26.79	-0.39	-0.06	6.28	28.60	-0.15	-0.39	7.68	31.30	-0.74	-0.29
Phase 2	10.16	30.00			12.51	32.90			16.06	35.19		
Phase 3	11.46	30.00			14.32	32.60			13.82	33.81		

### 4.3.8 Aerosol induced heating

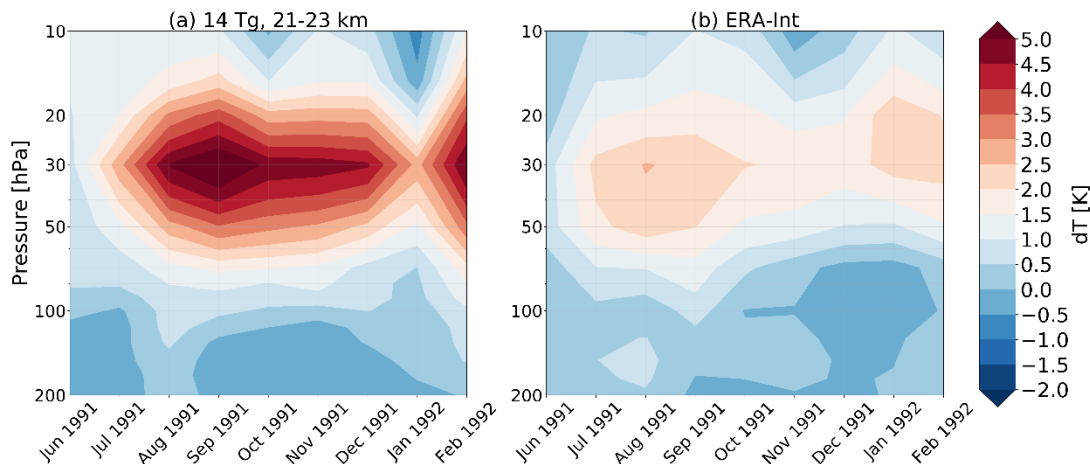


**Figure 4-12 Tropical (20°S-20°N) radiative heating difference for the period June 1991-February 1992 between (a) modelled (14 Tg SO<sub>2</sub>, injected 21-23 km) and control (no eruption) and (b) ERA-interim reanalysis temperature anomalies.**

It was important to assess whether high cloud top heights, as noted in the model, may have been a result of radiative heating. Figure 4-12 plots the simulated anomalous temperatures in comparison to ERA-interim reanalysis data, suggesting the model has a positive anomaly that is double that observed, however, the location and spatio-temporal spread of the increased temperature anomalies throughout 1991 is represented well in the model. A larger period of positive anomalies in August and September and at the beginning of 1992 characterised well, with slight negative values ( $\sim 0.5$  K) shown at  $\sim 100$  hPa in both the model and observations. It must be noted that ERA-interim temperature anomalies include changes related to shifts in the QBO phase during this period, for example (e.g. Dhomse et al., 2020) whereas the model anomalies do not. Also, comparisons of multiple models in the SPARC (2010) report show that most models produced temperature anomalies that were higher than observations, even with those comparisons being made with deviations from the mean of 5 years (as opposed to the simulation minus the control run shown here). Revell et al. (2017) also show that simulations using the aerosol dataset from SAGE-4 $\lambda$  found  $\sim 3$ K positive anomalies for the tropical stratospheric warming following the Mount Pinatubo eruption. Comparisons here provide a spatio-temporal constraint, with the pre-nudged simulation comparing well but exact temperature anomaly value comparisons should be assessed with caution.

### 4.3.9 Model simulated global-mean stratospheric aerosol optical depth (SAOD)

The following section is a brief analysis of the monthly global SAOD to illustrate the model simulated global dispersion of the volcanic sulfate aerosol cloud following the Mount Pinatubo eruption from June 1991-February 1992.

Figure 4-13a shows monthly mean model SAOD between June 1991 and February 1992 for the pre-nudged model simulation. Low SAOD values  $\sim 0.1$  are seen in June dispersing in a band from 0-15°N.

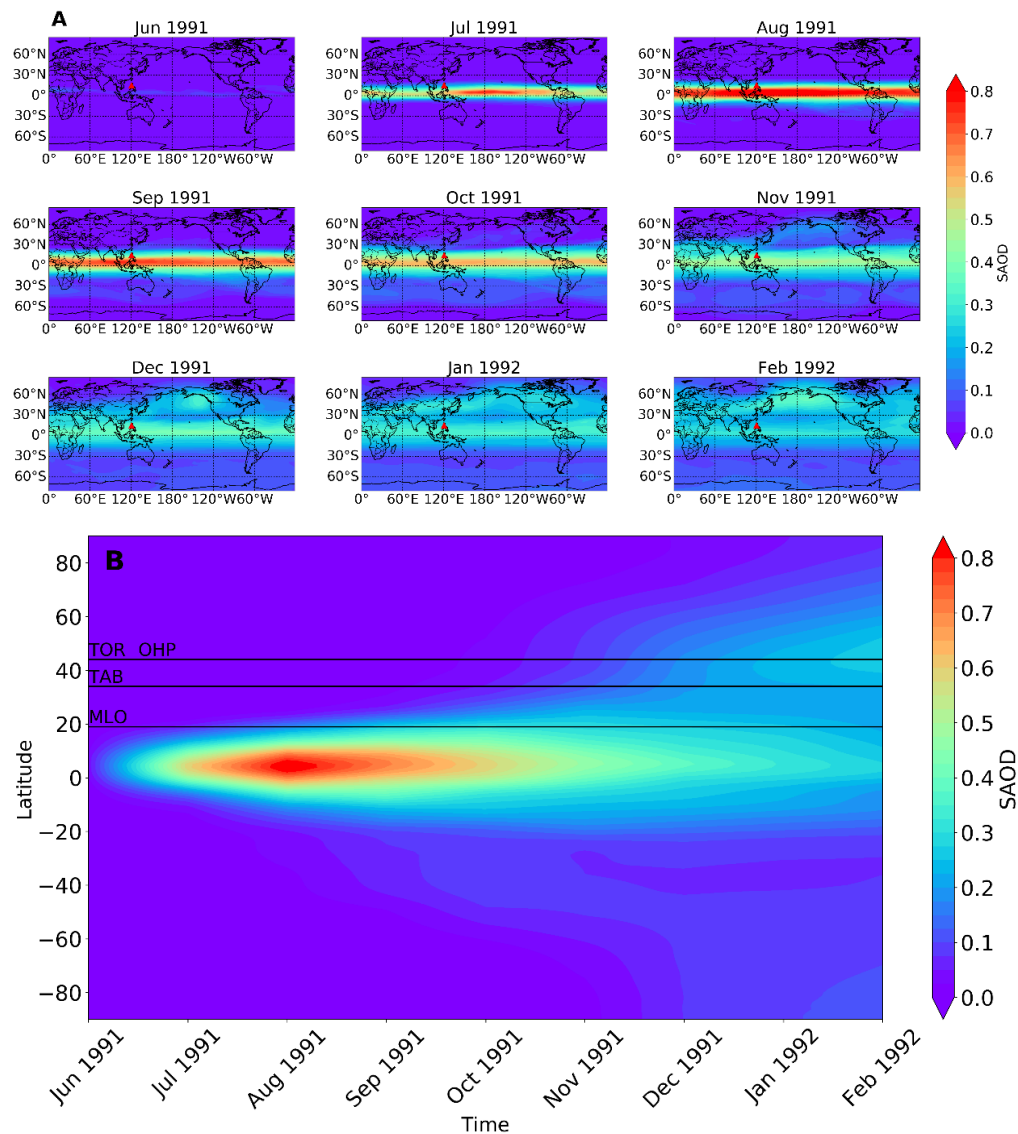


**Figure 4-13 Modelled a) Monthly averaged 550 nm SAOD from June 1991 to February 1992 b) Zonally averaged monthly mean for the pre-nudged QBO simulation.**

Values increase up to 0.65 in July when a zonal band around the equator is clearly visible, remaining so until November 1991. In July this band of higher SAOD values is tightly confined to 5°S-5°N with the highest values appearing over the Pacific Ocean. The highest SAOD values between 0.725 and 1 are noticeable from July-September 1991, with peak values between 0-10°N in August.

The first dispersion to the Southern hemisphere below 30°S is seen between mid-August - September 1991, steadily spreading to higher latitudes in both hemispheres in October and November. Trepte et al. (1993) found increased extinction levels ~30-50°S by the end of July 1991, suggesting dispersion to the southern hemisphere is weaker than reality in UM-UKCA. SAOD values up to 0.5 are visible from 10°S - 70°N between December 1991 and February 1992. Figure 4-13b highlights these patterns, showing this tropical band and eventual dispersion to either hemisphere with high SAOD values lasting to the end of 1991.

The SAOD plots highlight that MLO is on the edge of the tropical reservoir of volcanic aerosol that was formed by the eruption. This tropical reservoir is filled when an eruption at lower latitudes creates a reservoir of volcanic aerosol that tends to stay confined to the tropics in a tropical pipe before the Brewer-Dobson Circulation (BDC) transports aerosol towards the winter pole (e.g. Plumb, 1996; Grant et al., 1996). Hence, MLO was in, or at least on the edge of, this tropical reservoir before winds in the higher branches of the BDC transported aerosol into the northern hemisphere mid-latitudes and reached the other lidar sites.

#### **4.4 Discussion and Conclusions**

Ground-based lidars are a useful tool to investigate the evolving vertical structure during the progression of a major volcanic aerosol cloud. For the Mount Pinatubo aerosol cloud, the Mauna Loa lidar at 19°N was the only tropical ground-based lidar that measured the volcanic aerosol throughout the different stages of its progression in the first 6 months after the eruption. The MLO and Reunion Island (21°S) lidars provide improved ground-based coverage of the edge of the tropics than was the case after the Mount Pinatubo eruption (NDACC, 2020), with the Reunion Island lidar operating since March 1994 (Bencherif et al., 1997). Since 2006, the Cloud-Aerosol Lidar with Orthogonal Polarization (CALIOP) lidar on the Cloud-Aerosol Lidar and Infrared Pathfinder Satellite Observations (CALIPSO) satellite (e.g. Winker et al.,

2007) provides global coverage and, in the event of a major eruption, would also be monitored by SAGE III (e.g. Bourassa et al., 2019). Several other initiatives have also expanded lidar sites across Latin America (Antuña et al., 2017). In addition to greater coverage in a zonal direction, the substantial variation in wind shear (Section 4.3.5) within the tropical reservoir shows the value of having a continuous record from ground-based lidar at additional locations. One recommendation from this thesis is to suggest the international VolRes activity develop a co-ordinated plan for deploying further lidars at several additional sites within the tropical band 20°S-20°N. This is assessed further in Chapter 5.

The analysis of lidar measurements from Mauna Loa and the 3 mid-latitude sites confirms that the majority of the volcanic aerosol cloud from Mount Pinatubo remained confined to the tropical aerosol reservoir between 20°N and 20°S for the first 3 months after the eruption. Although the lower portion of the cloud was dispersed to both latitudes earlier, it was only after September 1991 that the mid-latitude sites measured the full depth of the dispersed cloud observed at Mauna Loa. Although Mauna Loa was on the edge of the tropical reservoir, the lidar observations are able to profile the full depth of the Mount Pinatubo cloud, and provide a unique record of the progression of the cloud, the increasing easterly winds shearing the cloud as it circled the globe. These measurements also provide additional data to the measurements from SAGE II which could only profile the upper portion of the cloud (McCormick and Veiga, 1992).

The analysis of this thesis has identified three stages in the record from Mauna Loa, progressing from the highly heterogeneous cloud into a dispersed tropical reservoir of volcanic aerosol. Analysis of the northern hemisphere mid-latitudes has given additional insight into the likely progression of the cloud within the tropical reservoir after a future major tropical eruption and the likely timings for when it might reach the northern hemisphere (Trepte et al., 1993). After the Mount Pinatubo eruption, the northern hemisphere sites showed increased aerosol only in the 15-20 km altitude region between June - August 1991, followed later by increased aerosol ~25 km from mid-August onwards, consistent with SAGE II data presented in Trepte et al. (1993). Mauna Loa is a useful observational site for examining the vertical profile through the atmosphere at the edge of the tropical reservoir (Antuña et al., 2002). The layers seen at Mauna Loa in the first few months after the 1991 Mount Pinatubo eruption illustrate how relatively minor differences in the horizontal wind structure, within the same

phase of the QBO, would have a significant effect on the subsequent progression of the volcanic aerosol cloud. Furthermore, the layers clearly show the inhomogeneous stage of the volcanic aerosol cloud (Antuña et al., 2002), when the cloud was beginning to disperse globally following the Mount Pinatubo eruption and had not yet spread a band of volcanic aerosol around the globe.

The analysis confirms UM-UKCA can represent the timing of the phases detected at MLO and the northern hemisphere mid-latitudes well, both with an approximate-QBO and pre-nudged initialisation. The main differences seen between the observations and the model simulations are the thickness (1-2 km thicker than observations) and height of the volcanic layer (~1-3 km higher) and the steeper descent, -0.55 compared to -0.22 for layer 2 in the pre-nudged simulation and observations, respectively. This is potentially a result of not including ash in the model which could act to remove aerosol from the cloud, reducing the height of the cloud. This may also allow sedimentation of aerosol particles from the lower altitudes, reducing the steepness of the descent of the layers. When comparing extinction values, the lidar values are higher overall at all sites compared to modelled values, possibly indicating a larger mass of SO<sub>2</sub> was injected at the time of the eruption than the 14 Tg tested in this chapter.

This study finds that a model run pre-nudged to the conditions before the eruption and allowed to relax into free-running mode 2 months prior to the eruption gives a closer spatio-temporal match to observations than an approximate-QBO simulation. Although UM-UKCA has an internally generated QBO, Dhomse et al. (2014) found that the QBO has easterlies lasting slightly longer than ERA-interim reanalysis for 1991, prolonging QBO in the model than is seen in reality. Using these pre-nudged conditions allows the initial conditions to be closer to reality and, therefore, enables the model to simulate a more accurate dispersion of the Mount Pinatubo aerosol cloud on a scale closer to reality. Consequently, this model configuration is used for further analysis in the next two results chapters (Chapters 5 and 6).

## Chapter 5

# Exploring varying eruption source parameters: a Pinatubo case study

### 5.1 Introduction

In the previous chapter, ground-based lidar measurements from Mauna Loa (MLO) were shown to be an effective tool to understand the progression of the vertical dispersion of the 1991 Mount Pinatubo volcanic aerosol cloud in the tropics, and a good test case for the model. The layered structures of each detection of the Mount Pinatubo cloud seen at MLO were explained to be primarily caused by wind shear, with additional disturbance from convective upwelling near the tropopause. The stages of this initial dispersion of the Mount Pinatubo cloud were also outlined, with three distinct phases identified as the cloud progressed from the initial sheared plume structure into a dispersed tropical reservoir, and its subsequent transport to mid-latitudes.

Interactive stratospheric aerosol simulations with the UM-UKCA model were shown to represent the timing of these layers and phases well, with some minor differences being the cloud top altitude with the first 3 MLO layers being 1.0, 2.2 and 1.8 km higher, respectively, than in the measurements, and with extinction values biased slightly low. A new technique to “pre-nudge” interactive stratospheric aerosol simulations was shown to retain the benefits of free-running simulations whilst better matching the particular QBO transition from 1991. The timing of the MLO layers then matched more closely with observations than in the approximate-QBO free-running simulations.

In this chapter, the MLO-layer analysis from Section 3.6.2 is applied to additional interactive stratospheric aerosol simulations of the Mount Pinatubo sulfate aerosol cloud, assessing the effects of varying the mass of SO<sub>2</sub> and the injection heights (from here on referred to as “eruption source parameters”). Specifically, the model experiments use the eruption source parameter values specified for the 1991 Mount Pinatubo experiment with the coordinated “Historical Eruptions SO<sub>2</sub> Emission Assessment” (HerSEA) activity within the international multi-model International Stratospheric Aerosol Model Intercomparison Project (ISA-MIP) activity (Timmreck et

al., 2018). The analysis presented in this chapter explores how the Mount Pinatubo aerosol cloud would have dispersed differently had the volcano injected SO<sub>2</sub> closer to the tropopause, also assessing the impacts of assumptions about the spread of the injection over a deeper altitude range, (i.e. to ensure the model captures well the depth of the progressed cloud) in order to assess the effect of these parameters on the vertical cloud distribution. The analysis is an important first step towards understanding more generally how varying the SO<sub>2</sub> mass and injection height changes the dispersion and microphysical evolution of the cloud.

Interactive stratospheric aerosol model studies of the 1991 Mount Pinatubo aerosol cloud vary widely in their eruption source parameters (Aquila et al., 2012; English et al., 2013; Dhomse et al., 2014; Jones et al., 2016; Mills et al., 2016) and primarily focus on ensuring the model simulations capture the total aerosol extinction through the full depth of the cloud (i.e. the stratospheric AOD (SAOD)), compared with satellite observations from SAGE II and AVHRR. Using the GEOS-5 model (coupled to the GOCART aerosol transport module), Aquila et al. (2012) illustrated the importance of injection height differences with radiatively coupled simulations, showing that various injection heights between 17-27 km led to aerosol being lofted too high and that an injection height of 16-18 km in their model agreed best with observations. Using the UM-UKCA v7.3 model, Dhomse et al. (2014) found a deeper injection height of 19-27 km was required for radiatively uncoupled simulations to match SAGE II and AVHRR SAOD observations. Sheng et al. (2015) explored a broad range of injection height simulations in the ETH-Zurich 2D-AER model, comparing initial simulations in the 3D SOCOL-AER model. Sukhodolov et al. (2018) specify the same injection heights in a series of SOCOL-AER Mount Pinatubo simulations, with their injection heights between 16-30 km and the majority of the SO<sub>2</sub> injected between 18-21 km.

In addition to exploring variations in injection height, and co-variations in the SO<sub>2</sub> mass, UM-UKCA is applied here to explore how the observations of the Mount Pinatubo cloud at MLO, at the northern edge of the tropical reservoir, compare to the morphology of the cloud closer to the equator. Although a lidar was operating at Bandung, Indonesia (6°S) at the time of the Mount Pinatubo eruption (NDACC, 2020), the measurements there were exceptionally hindered by extreme wet weather conditions, and although the Camaguey lidar in Cuba (21°N) began measuring in January 1992 (Antuña, 1996), there were no ground-based lidars making stratospheric observations between 23°S-19°N at that time (Antuña et al., 2002).

The analysis here uses the HErSEA Mount Pinatubo eruption source parameters in UM-UKCA to assess the daily progression of the initial phase of the Mount Pinatubo cloud, exploring whether the sheared-plume structure observed at MLO is also seen within the core of the tropical reservoir. The analysis also seeks to understand the progression of aerosols from this tropical volcanic eruption as simulated with an interactive stratospheric model, in relation to how a hypothetical tropical lidar station would have observed the Mount Pinatubo volcanic aerosol cloud. This allows for a further assessment of the evolution of the volcanic aerosol cloud in the tropical reservoir and provides more detail on its dispersion.

Interactive stratospheric aerosol modelling groups tend to use the Mount Pinatubo case study as their test for validating their model predictions. However, whilst the models are all able to achieve good comparisons to observations, for example comparing simulated SAOD with AVHRR and SAGE II data for the Mount Pinatubo case (Niemeier et al., 2009; Aquila et al., 2012; Dhomse et al., 2014), the differences in the specified injection heights suggests there are important structural differences among the models. Also, although the models achieve good comparisons to global variation in SAOD, the simulations may not be producing the correct vertical dispersion. The residence time of a tropical volcanic aerosol cloud is strongly dependent on the height of SO<sub>2</sub> injection as well as season and QBO phase (Thomas et al., 2009; Timmreck, 2012; Marshall et al., 2019). Understanding how perturbing these eruption source parameters impacts the initial progression of the Mount Pinatubo volcanic aerosol cloud is, therefore, important for understanding the subsequent global dispersion and climatic impacts from a major tropical eruption. Although not a key aim of this chapter, assessing these different parameters will also potentially help constrain the actual eruption parameters for the 1991 eruption of Mount Pinatubo and present a test case for other aerosol-climate models in future studies. In summary, the key aim of this chapter is to understand how co-varying eruption source parameters affects the vertical profile of extinction, SAOD and sulfate burden following the Mount Pinatubo eruption.

This chapter is structured as follows: The model experiments are described in Section 5.2. The results of the model experiments to vary injection height and mass of SO<sub>2</sub> on vertical dispersion are described in Section 5.3.1, with sulfur burden and SAOD analysis outlined in Sections 5.3.2 and 5.3.4. The analysis of a hypothetical tropical lidar is described in Section 5.4. A discussion of the results is in Section 5.3 and conclusions in Section 5.6.

## 5.2 Methods

### 5.2.1 Model setup

The initial conditions in each simulation were the same as those outlined in Chapter 4 with either mass of SO<sub>2</sub> or injection height changed. These parameters are 10, 14 and 20 Tg of SO<sub>2</sub> and injections heights of 18-20, 21-23 and 18-25 km, denoted as the SO<sub>2</sub> mass and “lowalt”, “midalt”, or “deepalt” (e.g. “10\_lowalt” for 10 Tg SO<sub>2</sub> injected at 18-20 km).

The eruption source parameters for these experiments were chosen based on Timmreck et al. (2018). The upper value (20 Tg) for SO<sub>2</sub> mass emitted is based on TOMS/TOVS observations (S Guo et al., 2004). The mid (14 Tg) and low (10 Tg) values are based on recent climate model studies of the Mount Pinatubo eruption (Dhomse et al., 2014; Sheng et al., 2015; Mills et al., 2016; Sukhodolov et al., 2018) where lower estimates of SO<sub>2</sub> emission agreed with HIRS/ISAMS peak sulfate burden values (Baran and Foot, 1994). The injection heights are based on Timmreck et al. (2018) and Antuña et al. (2002) with the idea of a lower, shallow injection (18-20 km), a middle level, shallow injection height (21-23 km) and a deep injection height (18-25 km).

Model simulated sulfate burden is compared to measurements from Baran and Foot (1994) in this chapter (Section 5.3.3) with an error of 10% associated with these measurements (Baran and Foot, 1994). Stratospheric aerosol optical depth (SAOD) (550 nm), is used to evaluate the interactive Mount Pinatubo aerosol simulations in this chapter (Section 5.3.4). The two datasets for SAOD following the eruption are the GloSSAC dataset (Thomason et al., 2018) and AVHRR (Long and Stowe, 1994). SAOD from GloSSAC (Thomason et al., 2018), incorporates the latest version 7.0 SAGE II dataset (Damadeo et al., 2018). The sulfate burden and AVHRR observational measurements are widely used in the modelling community for simulating the Mount Pinatubo eruption, with the GloSSAC data providing a more up-to-date dataset of the SAGE II data (Dhomse et al., 2020) that was super-saturated at the time of the Mount Pinatubo eruption (e.g. Antuña et al., 2002).

#### 5.2.1.1 Hypothetical lidar site

Observational measurements were either saturated or highly uncertain for the tropics following the eruption of Mount Pinatubo (e.g. Antuña et al., 2002) and no genuinely tropical observational data was available following the eruption (Thomason et al.,

2018), therefore the model can be used to indicate the progression of the tropical reservoir.

Model output from the simulations described in Chapter 4 was analysed at hypothetical lidar sites (10°S, equator and 10°N) in order to investigate the model simulated progression of aerosol from the tropical reservoir. 14 Tg of SO<sub>2</sub> was emitted on 15<sup>th</sup> June 1991 at an injection height between 21-23 km. Hypothetical lidar sites at 10°N, the equator and 10°S, can be represented by the model and the vertical dispersion of these locations are assessed for the same June 1991 – February 1992 period as the other simulations.

## 5.3 Results

### 5.3.1 Vertical structure of the volcanic cloud

As outlined in Chapter 4, there are distinct layers noticeable in the MLO lidar data in the vertical profile of extinction (Figure 4-5). The first of these begins on July 1<sup>st</sup> 1991, the second on July 22<sup>nd</sup> and the third on August 9<sup>th</sup>. These layers are key structures in the observations and the model captures these relatively well in the simulations performed in Chapter 4, however, the altitude of the simulated aerosol layer is too high at these sites, reaching up to 30 km, where the observations show cloud top maximum height of 26 km (Figure 4-5). Although satellite observations show a cloud top height up to 30 km elsewhere (S Guo et al., 2004), this is not the case in these lidar observations. In order to attempt to understand and rectify this discrepancy, mass of SO<sub>2</sub> and injection height are varied.

Overall, the largest effect on the vertical extinction profile results from varying the injection height of SO<sub>2</sub> as expected. An injection of 18-20 km in all simulations keeps the aerosol confined to a region between 15-25 km with no noticeable layers or structure (Figure 5-1).

The appearance of the aerosol cloud at MLO is 2 days later in the 18-20 km case than in the observations. The overall height of the aerosol layer is reduced with this injection height, however over time the aerosol cloud reaches higher altitudes than the lidar observations suggest, for example at the end of November 1991 the cloud is ~28 km whereas the observations are closer to 26 km (Figure 5-1). The highest extinction value occurs for the 20\_lowalt simulation (0.181), which is the closest to observations

(0.202). Values for 10\_low alt and 14\_lowalt are 0.109 and 0.161, respectively, therefore doubling the injection of SO<sub>2</sub> does not double the resulting extinction value.

Injecting SO<sub>2</sub> between 18 – 25 km creates some form of layers; however, the second and third layers appear slightly too early, they are all too steep and their top height is too high (25 km, 29 km and 30.5 km, respectively) when compared to observations (Figure 5-2). A lower section of aerosol between 15 – 22 km is also created in these cases, similarly to the 18 – 20 km simulations. The maximum values of extinction are again lower than those from the observations with values of 0.093, 0.126 and 0.135 for 10, 14 and 20 Tg, respectively. As mentioned in Chapter 3, errors associated with the conversion of BSR to EXT are <10%, with higher aerosol loads decreasing this error, suggesting that the maximum values for the observations at MLO are distinctly higher than those seen in the model.

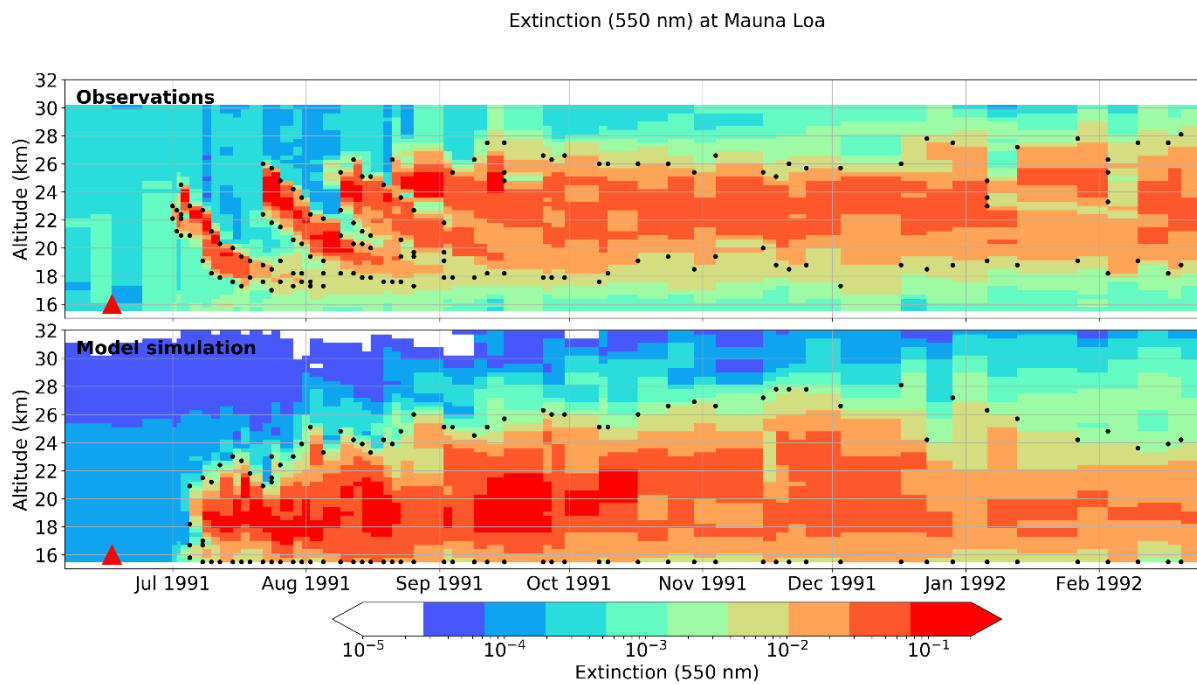


**Figure 5-1** Extinction profiles for MLO lidar observations (top) and the 14 Tg SO<sub>2</sub>, 18-20 km injection height model simulation (bottom). Black dots represent the top and bottom of the sulfate aerosol cloud, calculated by the layer finding algorithm.

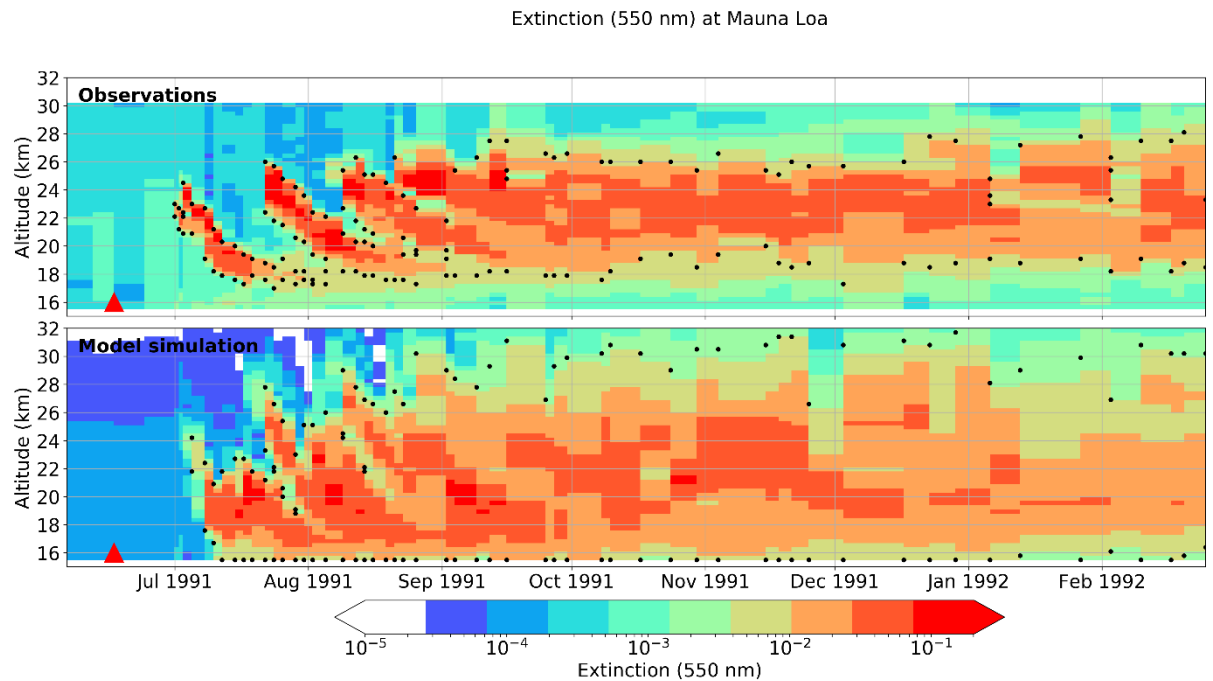


**Figure 5-2** Extinction profiles for MLO lidar observations (top) and the 14 Tg SO<sub>2</sub>, 18-25 km injection height model simulation (bottom).

Figure 5-3 shows the closest matching injection height for these simulations is the 21-23 km case, with the 14\_midalt simulation giving the correct layer timing. Model layer heights of the second and third layers (28 and 30 km, respectively) along with the subsequent evolution of the cloud with time are still higher than those seen in observations and the descent of the cloud much steeper than seen in the observations.

In all the simulations the peak extinction values are all too low relative to values seen in the observations at all sites with the 10 Tg model simulations being a factor of 2 lower on average. The closest match of model-simulated and observed extinction values is achieved with the 20\_lowalt simulation, which has a maximum extinction of 0.18 compared to 0.20 in the observations.

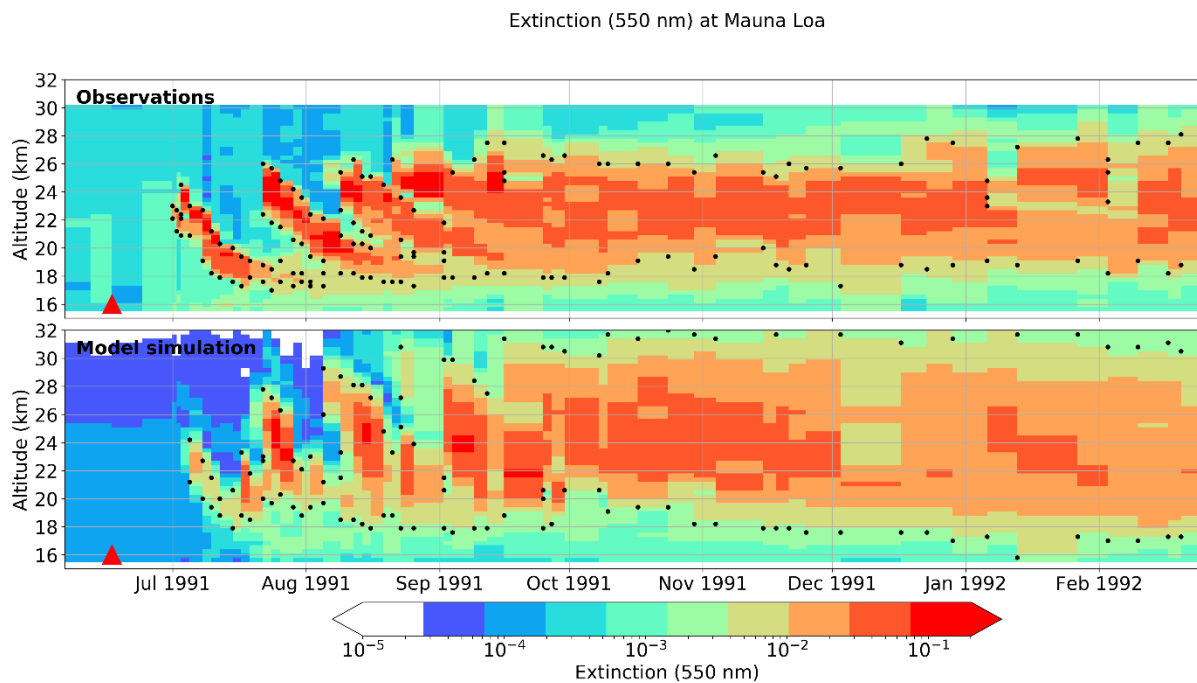


**Figure 5-3** Extinction profiles for MLO lidar observations (top) and the 14 Tg SO<sub>2</sub>, 21-23 km injection height model simulation (bottom).

Increasing the mass of SO<sub>2</sub> emitted for the 18-20 km simulations leads to maximum extinction values of 0.109, 0.161 and 0.181 for 10, 14 and 20 Tg, respectively. Across all model simulations the maximum extinction values are highest for the 18-20 km simulations, followed by the 18-25 km and then the 21-23 km simulations. Extinction values at the leading edges of the observational layers are always greater than 0.1 km<sup>-1</sup>, whereas these values are only reached in the second layer in the model (Figure 5-3). First layer values are ~0.01 km<sup>-1</sup> in both the 14 Tg and 20 Tg 21 – 23 km simulations, suggesting the observational values are not due to differences in SO<sub>2</sub> mass.

### 5.3.2 Tropical radiative heating

The following section assesses how differing eruption source parameters affects the radiative heating in the stratosphere following the 1991 Mount Pinatubo eruption. This section allows another set of independent observations to be used to assess which eruption source parameters best represent the Mount Pinatubo eruption. ERA-interim temperature anomalies are composed of tropical radiosonde measurements (Dee et al., 2011) and can be compared to model simulated tropical radiative heating as an independent test. Uncertainties with this comparison are primarily due to ERA-interim data including temperature fluxes from all dynamical and chemical changes (e.g. shifts

in QBO phase). The model will not account for QBO changes, for example as temperature anomalies are calculated by removing the control run from the volcanic simulations, removing any QBO influences.

Figure 5-4 to Figure 5-6 show the model simulated tropical stratospheric warming anomaly induced by the Mount Pinatubo volcanic sulfate aerosol cloud and a comparison to the ERA-interim temperature-anomaly. The purpose of this analysis is to assess the levels of radiative heating in the model caused by the sulfate aerosol cloud in response to differing the SO<sub>2</sub> injection mass and injection height. The 21-23 km simulations (Figure 5-4) show a similar vertical pattern to the observations, with the main region of positive temperatures seen around 10-100 hPa (0 to >5 K) and a second region with negative temperature anomalies (-2 to 0 K) below 100 hPa. The 14\_midalt simulation (Figure 5-4b) shows the closest match to the ERA-interim data, with positive anomalies noted in July to September 1991, before a small region of positive values (~2 K in ERA-interim and 4 K in the model simulation) emerges from October to December 1991. Further positive values are then seen at the beginning of 1992 of ~3 K in the observations and up to 5 K in the model simulation. The 20\_deepalt simulation (Figure 5-6c) shows a similar spatial distribution to ERA-interim, however, also showing the highest differences, up to 7.2 K.

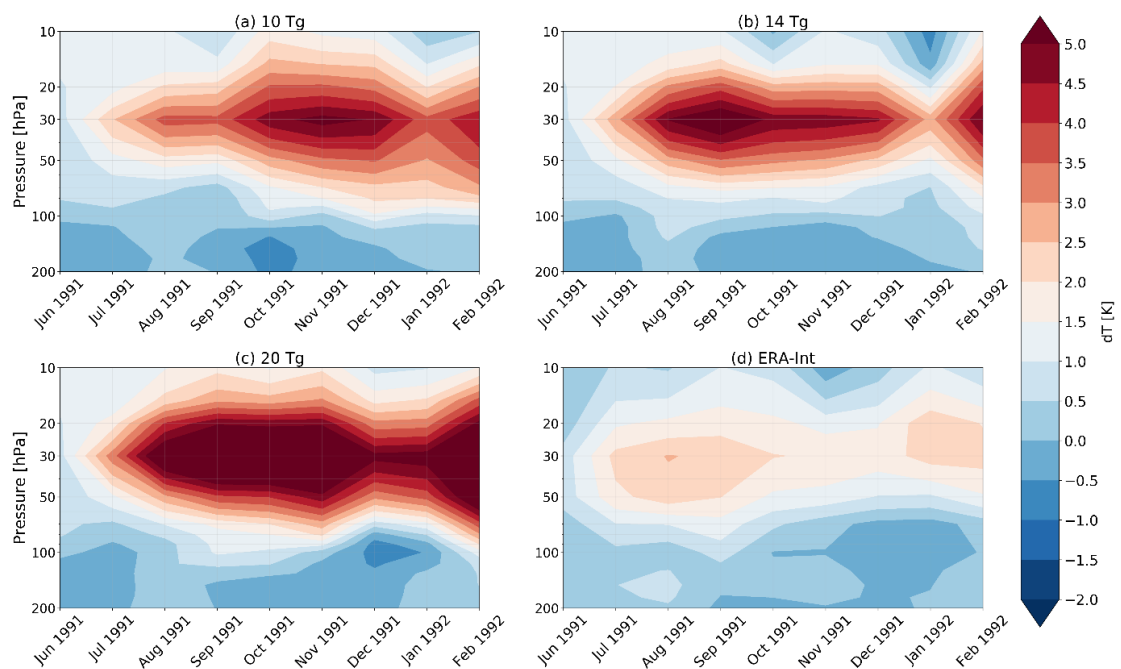


**Figure 5-4 Tropical (20°S-20°N) aerosol-induced stratospheric heating anomalies for model simulations (a-c) with injection height 21-23 km for June 1991 – February 1992, a) 10 Tg, b) 14 Tg and c) 20 Tg SO<sub>2</sub>. (d) ERA-interim tropical (20°S-20°N) stratospheric temperature anomalies for June 1991–February 1992.**

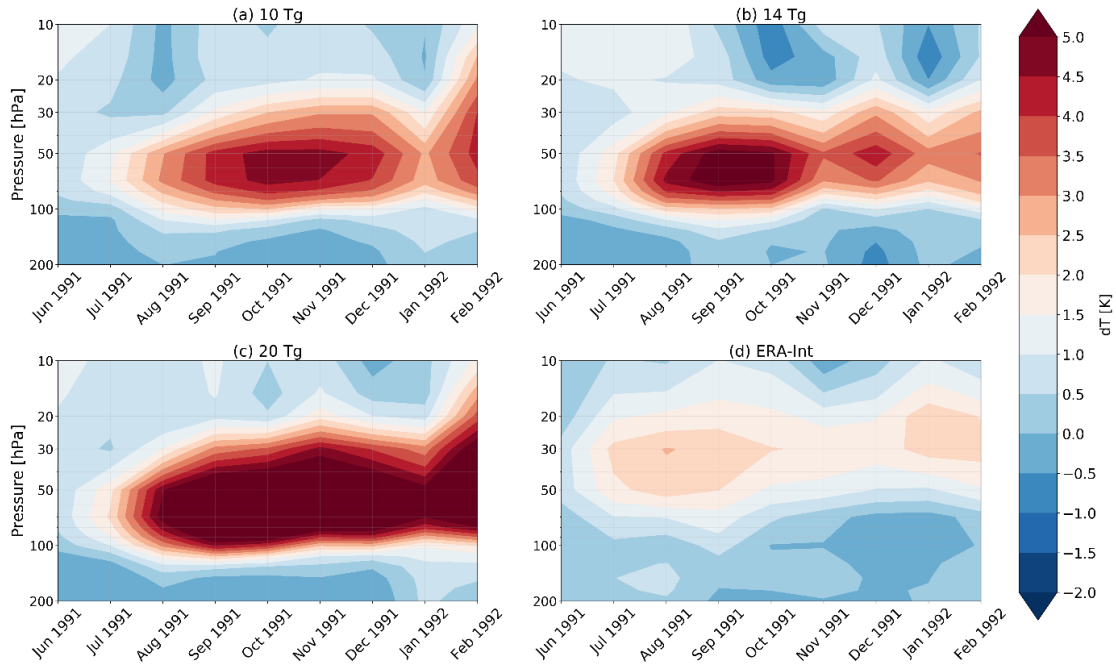


**Figure 5-5** Tropical ( $20^{\circ}\text{S}$ - $20^{\circ}\text{N}$ ) aerosol-induced stratospheric heating anomalies for model simulations (a-c) with injection height 18-20 km for June 1991 – February 1992, a) 10 Tg, b) 14 Tg and c) 20 Tg  $\text{SO}_2$ . (d) ERA-interim tropical ( $20^{\circ}\text{S}$ - $20^{\circ}\text{N}$ ) stratospheric temperature anomalies for June 1991–February 1992.

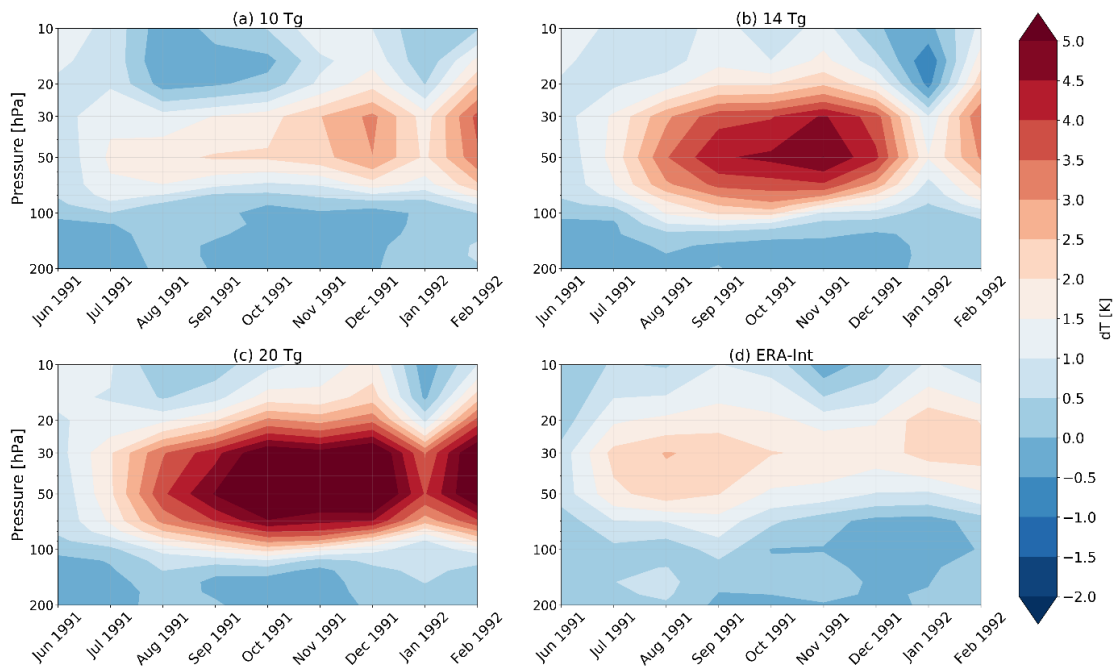


**Figure 5-6** Tropical ( $20^{\circ}\text{S}$ - $20^{\circ}\text{N}$ ) aerosol-induced stratospheric heating anomalies for model simulations (a-c) with injection height 18-25 km for June 1991 – February 1992, a) 10 Tg, b) 14 Tg and c) 20 Tg  $\text{SO}_2$ . (d) ERA-interim tropical ( $20^{\circ}\text{S}$ - $20^{\circ}\text{N}$ ) stratospheric temperature anomalies for June 1991–February 1992.

The 10\_midalt simulation (Figure 5-4a) is the weakest match with observations spatio-temporally, reaching largest differences (2K and 5 K differences between ERA-interim and the model simulation, respectively) in the October to December 1991 period.

All other model simulations also show positive temperature anomalies than suggested by the re-analysis data, with the model showing values a factor of 2 higher than the ERA-interim temperature anomalies. Both 18-20 km (Figure 5-5) and 18-25 km (Figure 5-6) simulations show the highest anomalously high values, 3 times that of ERA-interim at altitudes ~10 hPa lower than the ERA-interim data in the 18-20 km simulation. The 10\_deepalt simulation (Figure 5-6a) shows values closest values to observations (maximum 3.6 K). Although confidence in the magnitude of stratospheric heating following major volcanic eruptions has increased, uncertainties associated with observational data remain, particularly there is a lack of as high-quality data from the tropics for the 1991 Mount Pinatubo eruption (Dee et al., 2011).

### 5.3.3 Sulfate burden

The following section explores the evolution of sulfate burden between June 1991 and February 1992, assessing the differences for the different eruption source parameters. The first part of this analysis focuses on changes seen in the tropics (20°S-20°N) where the majority of the aerosol initially resided, with the second part focussing on the global changes and differences in sulfate burden (80°S-80°N). This analysis explores how differing these injection parameters impacts on sulfate burden, the main climatically significant product following a volcanic eruption.

Comparing the evolution of the tropical aerosol sulfate burden for these model simulations reveals a number of interesting features. Firstly, the 21-23 km simulation consistently shows the highest sulfate burden of the three simulations within each SO<sub>2</sub> injection, followed by the 18-25 km injection and then the 18-20 km injection height (Figure 5-7). The evolution over time of the modelled sulfate burden compares very well to HIRS satellite measurements of sulfuric acid shown in Baran and Foot (1994), with a similar increase in sulfate burden between June and July to the 14 Tg simulations (Figure 5-7). The observations match closely to the 14\_deepalt model simulation until December 1991 where the 14\_midalt simulation matches best (Figure 5-7), although both 14\_deepalt and 14\_midalt both lie within the observational error. 20\_lowalt also fits within the observational error in July 1991 and into 1992. All the simulations and

the observations show a peak in September 1991 before the tropical sulfate burden begins to decrease. These peak values are outlined in Table 5-1.

The observations show a less rapid decrease in sulfate burden at the beginning of 1992, with an e-folding time of 9.9 months. The model simulations have an average e-folding time of 7.3 months, with 21-23 km injection height simulations showing the highest e-folding times for an injection of 10, 14 and 20 Tg (7.9, 7.6 and 8.5 months, respectively).

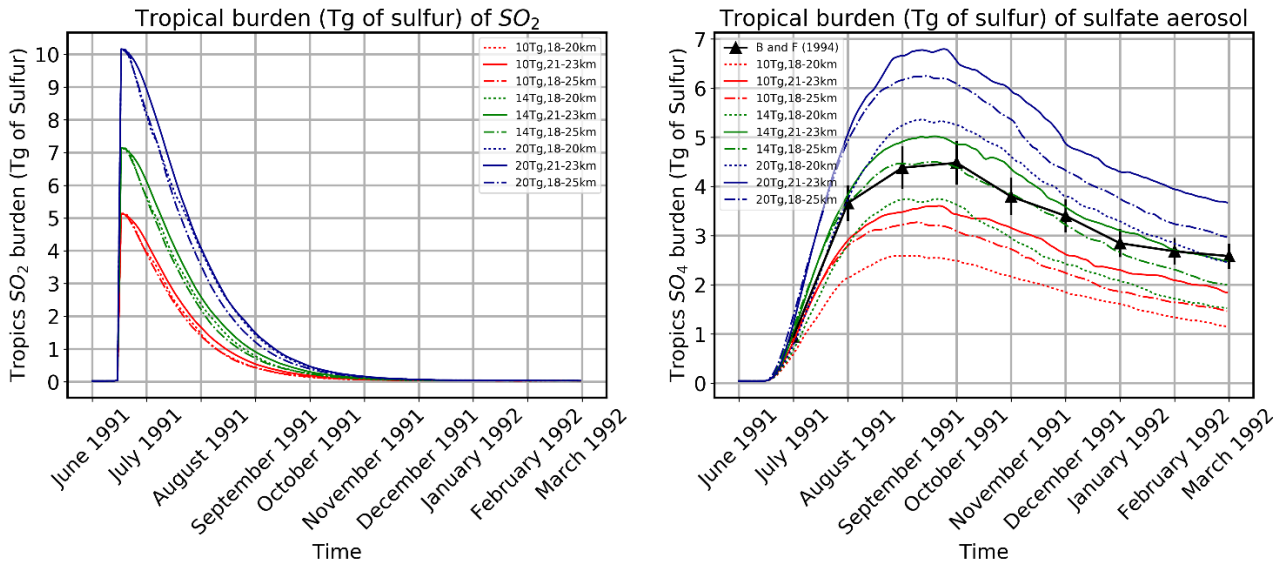


**Figure 5-7** Tropical (20°N-20°S) sulfur burden (Tg) for SO<sub>2</sub> (left) and SO<sub>4</sub> (right) for all model simulations. Black lines indicate observations with 10% error bars.

**Table 5-1** Peak tropical sulfate burden values (Tg) as observed (Baran and Foot, 1994) and simulated.

Name	Peak tropical sulfate burden (Tg)
Baran and Foot (1994)	4.48
10_lowalt	2.59
10_midalt	3.61
10_deepalt	3.27
14_lowalt	3.75
14_midalt	5.02
14_deepalt	4.50
20_lowalt	5.37
20_midalt	6.80
20_deepalt	6.25

The global comparison of model-simulated sulfate burden with Baran and Foot (1994) shows a relatively good agreement with the time evolution of sulfate over time (Figure 5-8). The model shows a much smoother curve in all simulations, whereas the observations fluctuate around August and September.

The observations appear to fall between the 14 and 20 Tg model simulation values with a close match in September 1991 and January-February 1992 with the 14\_midalt simulation. The global sulfate burden in the 20 Tg simulations closely match observed values in July and August 1991, however, values in September 1991 are 5.3 Tg sulfur in the observations which matches within the range of all 14 Tg simulations.

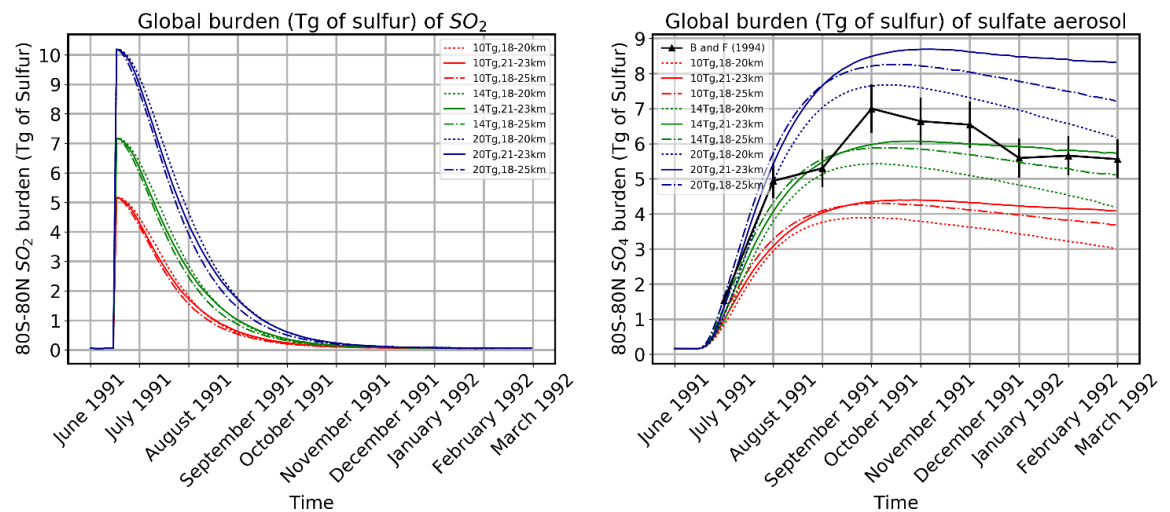


**Figure 5-8 Global sulfur burden (Tg) for SO<sub>2</sub> (left) and SO<sub>4</sub> (right) for all model simulations. Black lines indicate observations with 10% error bars.**

### 5.3.4 Stratospheric aerosol optical depth (SAOD)

The following section outlines the daily-mean SAOD values for all injection heights and SO<sub>2</sub> masses for the period June 1991-February 1992 for the tropics and globally, with a comparison to GloSSAC and AVHRR measurements.

In the tropics, the model data for all simulations show the characteristic signature of initial production up to the maximum SAOD, followed by a decay phase. It is clear that the model has approximately the same timescale decay as in the AVHRR observations, with the GloSSAC dataset having a different temporal variation. The peak SAOD depends primarily on the magnitude of the injected mass of SO<sub>2</sub> (Figure 6-5), with 0.27-0.34, 0.39-0.45 and 0.55-0.62 for the 10 Tg, 14 Tg and 20 Tg simulations, respectively. To quantify the decay timescale difference apparent in the model simulations, and the

GloSSAC and AVHRR datasets, an e-folding time is derived based on the period after the peak SAOD.

The GloSSAC data peaks and decays more smoothly in the tropics than AVHRR, with an e-folding time of 20.2 months. The GloSSAC data has lower values than AVHRR until December 1991-March 1992, with AVHRR showing a peak AOD value of 0.32 and GloSSAC peaking at 0.17. From September 1991 to March 1992 GloSSAC SAOD values decrease from 0.17 to 0.14 and AVHRR values decrease from 0.32 to 0.15.

In comparison to the sulfate burden, the 18-20 km simulations also consistently show the lowest optical depths of the different injection heights across all latitude comparisons. 20 Tg has the highest SAOD values, followed by 14 Tg and 10 Tg, respectively.

AVHRR has peak values of 0.32 in September 1991 in the tropics, peaking in September 1991 (Figure 5-9). The GloSSAC data peaks in October 1991 at 0.17, almost half that of the AVHRR peak. The GloSSAC SAOD values are lower than all model simulated SAOD values, except for in February 1992 when GloSSAC SAOD 0.14 match with 10\_lowalt. Highest values of SAOD in the model are 0.62 in the tropics compared with 0.32 for AVHRR and 0.17 for GloSSAC. All model simulations show the shape of the AVHRR measurements with 10 Tg simulations lying closest to AVHRR values. In the tropics (Figure 5-9) the 18-20 km simulations have consistently lower SAOD values than their 21-23 and 18-25 km equivalents for each amount of SO<sub>2</sub> injected. The 10\_midalt and 10\_deepalt simulations are both in good agreement with the AVHRR measurement values.

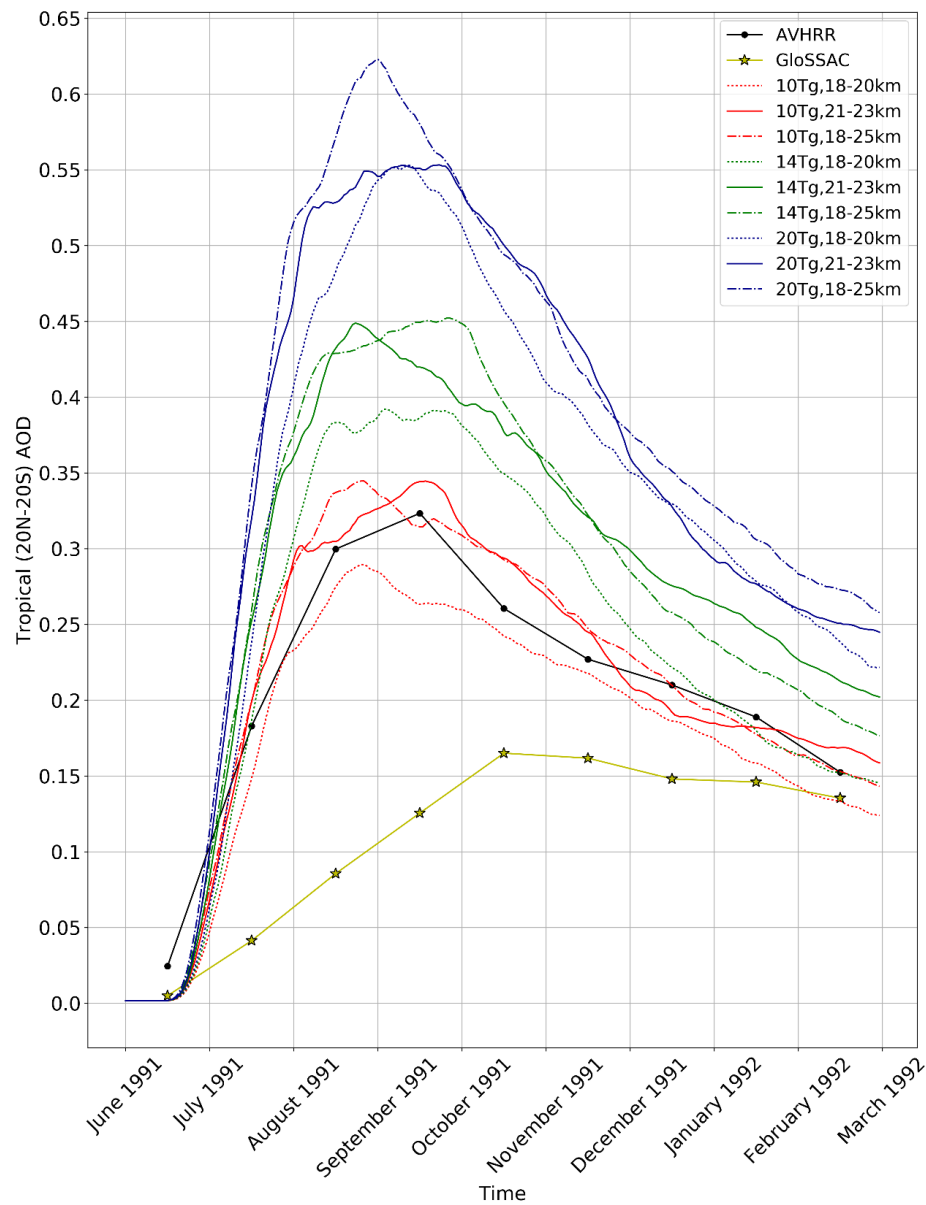


**Figure 5-9 Tropical (20°S-20°N) optical depth for all simulations, compared to AVHRR and GloSSAC. Different colours denote different amounts of SO<sub>2</sub> and linestyles denote different injection heights.**

The 21-23 km and 18-25 km simulations show fairly similar peak values of SAOD for each mass of SO<sub>2</sub>, except for the 20 Tg case where the 20\_deepalt shows a much higher peak of 0.63, where the 20\_midalt simulation has an SAOD of 0.55.

The 80°S – 80°N SAOD comparison to AVHRR indicates a peak period in mid-August to mid-September 1991 that compares best with 10\_deepalt and 14\_midalt (Figure 5-10).

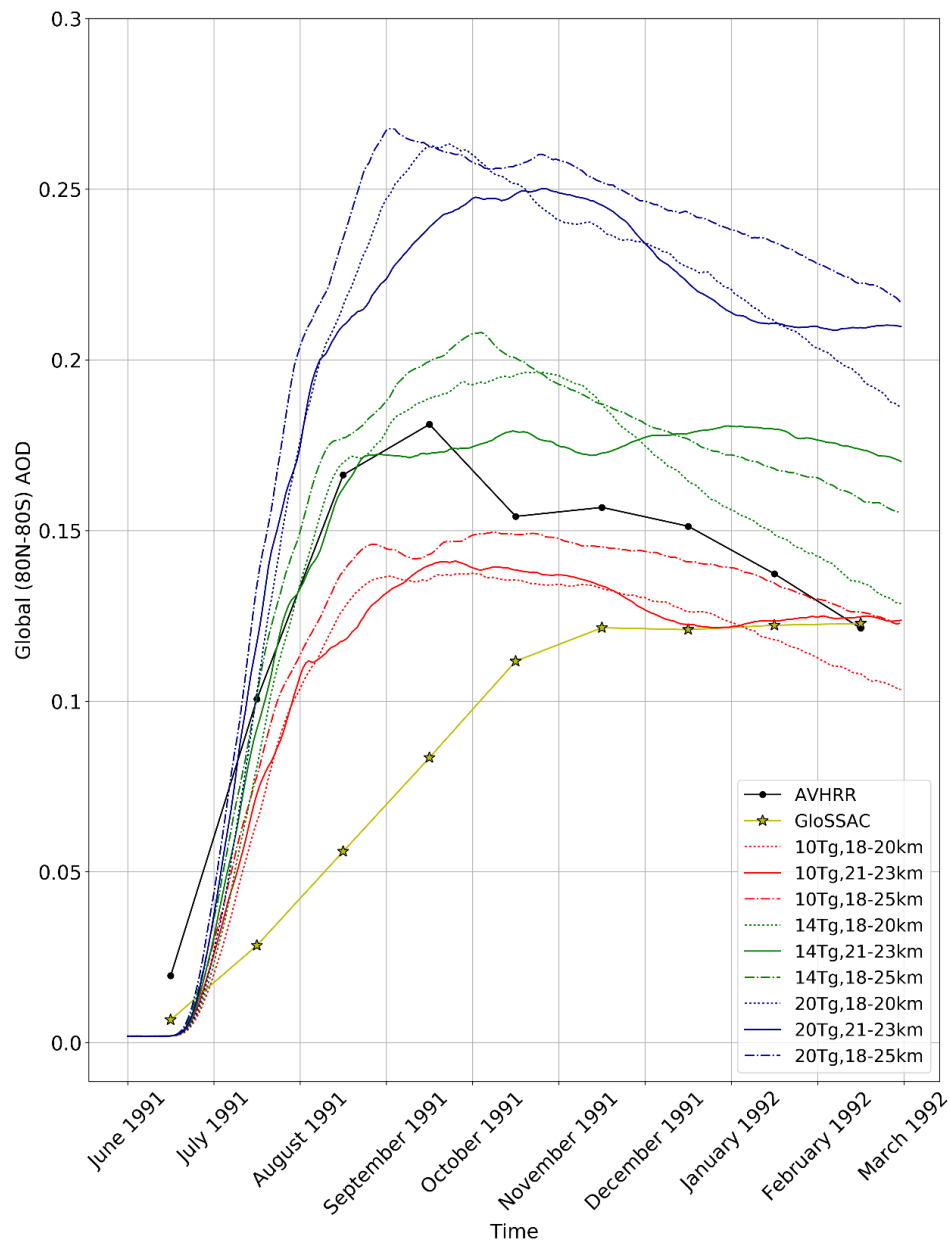


**Figure 5-10 Global (80°S-80°N) optical depth for all simulations, compared to AVHRR and GloSSAC measurements. Different colours denote different amounts of SO<sub>2</sub> and linestyles denote different injection heights.**

The 10 Tg simulations then compare well with AVHRR from October 1991, matching closest with 10\_deepalt (Figure 5-10). The shape of all the model SAOD matches well with the AVHRR data, however. The GloSSAC data is again lower than AVHRR and model simulated SAOD in all simulations until December 1991. 10\_midalt SAOD values align with GloSSAC SAOD from December 1991-February 1992 with values ~0.12.

In comparison to the tropics, where the 18-20 km simulations had the lowest SAOD values, the 21-23 km simulations show the lowest SAOD values on average when looking at the global pattern (Figure 5-10). All 21-23 km simulations change in pattern from December 1991 onwards, however, showing highest SAOD values from this point in the 14 Tg simulations and increasing in the 10 Tg simulations. All simulations show a trend closer to the AVHRR measurements than the GloSSAC measurements.

Results for the northern and southern mid-latitudes (0) show a less obvious pattern for the SO<sub>2</sub> injections, however, still broadly show 10 Tg simulations producing the lowest SAOD values on average, followed by 14 and then 20 Tg. In the northern hemisphere, the 21-23 km simulations produce the lowest SAOD values for each amount of SO<sub>2</sub> and it takes until November 1991 before the 21-23 km simulations overtake the 18-20 and 18-25 km simulations. The southern hemisphere shows the opposite trend, whereby the 21-23 km simulations produce the highest SAOD values for each injected SO<sub>2</sub> mass. All model simulations show SAOD values <0.1 apart from the 20\_midalt simulation.

### 5.3.5 Aerosol effective radius

Aerosol effective radii ( $R_{\text{eff}}$ ) are calculated for each model simulation in order to understand the temporal evolution of the size of aerosol particles in each simulation. This is important in order to establish any periods of distinctly increased aerosol sizes, which would suggest relative differences in coagulation rates between the simulations. A comparison to measurements (Deshler, 2008) and a SOCOL-AER Mount Pinatubo study (Sukhodolov et al., 2018) also allow an assessment of how UM-UKCA compares to observations and another modelling study. Sukhodolov et al. (2018) use a stratospheric aerosol-climate model with key differences in their study being the use of nudged QBO conditions and a bin-resolved aerosol scheme, as well as an injection height between 16 and 30 km, centred around 18-21 km.

Figure 5-11 shows that effective radius increases over the period June 1991 to February 1992 as expected, with maximum values of 314 nm, 348 nm and 395 nm for 10 Tg, 14 Tg and 20 Tg, respectively, indicating a slight increase in particle size with injected SO<sub>2</sub> magnitude. Injection height variations also affect  $R_{\text{eff}}$  but to a lesser extent than variations in SO<sub>2</sub> mass, with an injection height of 18-20 km showing the lowest particle sizes (263 nm, 295 nm and 334 nm, respectively for each mass of SO<sub>2</sub> injected), followed by 18-25 km (278 nm, 314 nm

and 354 nm, respectively for each mass of SO<sub>2</sub> injected) and the highest values seen with an injection height of 21-23 km (maximum values mentioned previously).

In order to assess the accuracy of the model simulated Reff values, a comparison to in-situ measurements (Deshler, 2008) and previously modelled values for a 14 Tg injection with and without radiative heating (Sukhodolov\_14Tg and Sukhodolov\_14Tg\_NORAD, respectively) (Sukhodolov et al., 2018) at Laramie, Wyoming are presented (Figure 5-12). All UM-UKCA simulations lie within the error of the observations, except for August 1991 when there is a spike in the observational dataset (which is, however, associated with large errors  $\pm 110$  nm compared to an average error of  $\pm 50$  nm). Broadly, all simulations agree with the Sukhodolov et al. (2018) data from October 1991 onwards, with initial UM-UKCA values indicating a bias by  $\sim 100$  nm towards smaller particles between June and October 1991.

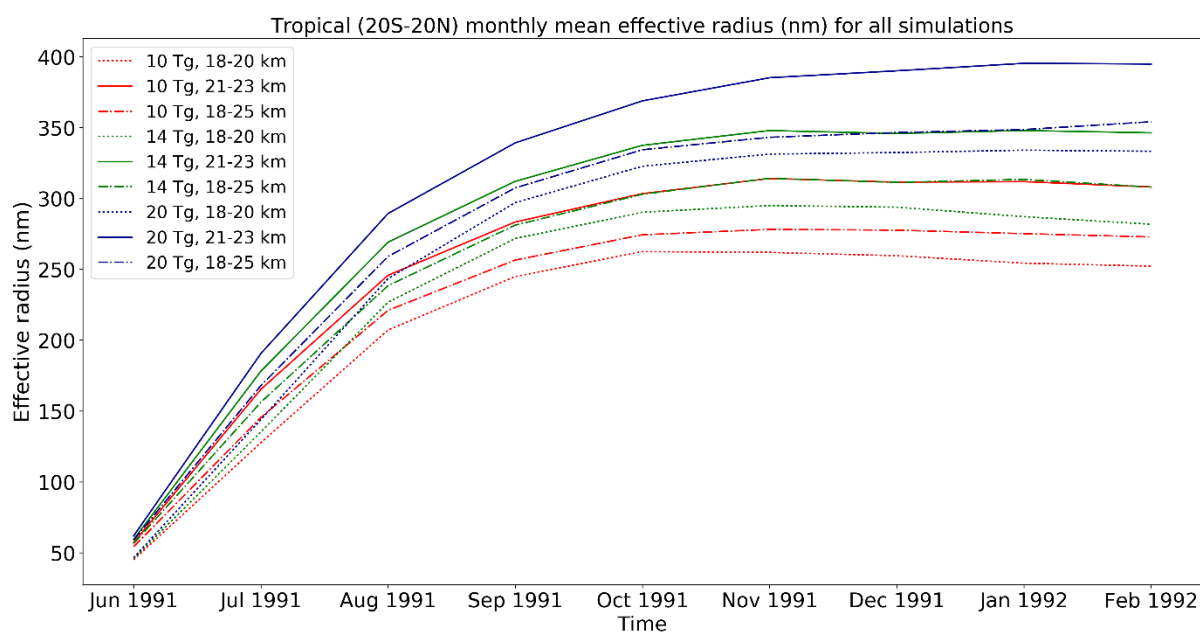


**Figure 5-11 Model effective radius (Reff) for each model simulation for the period June 1991 - February 1992. Line colour indicates mass of SO<sub>2</sub> injected and linestyle denotes injection height.**

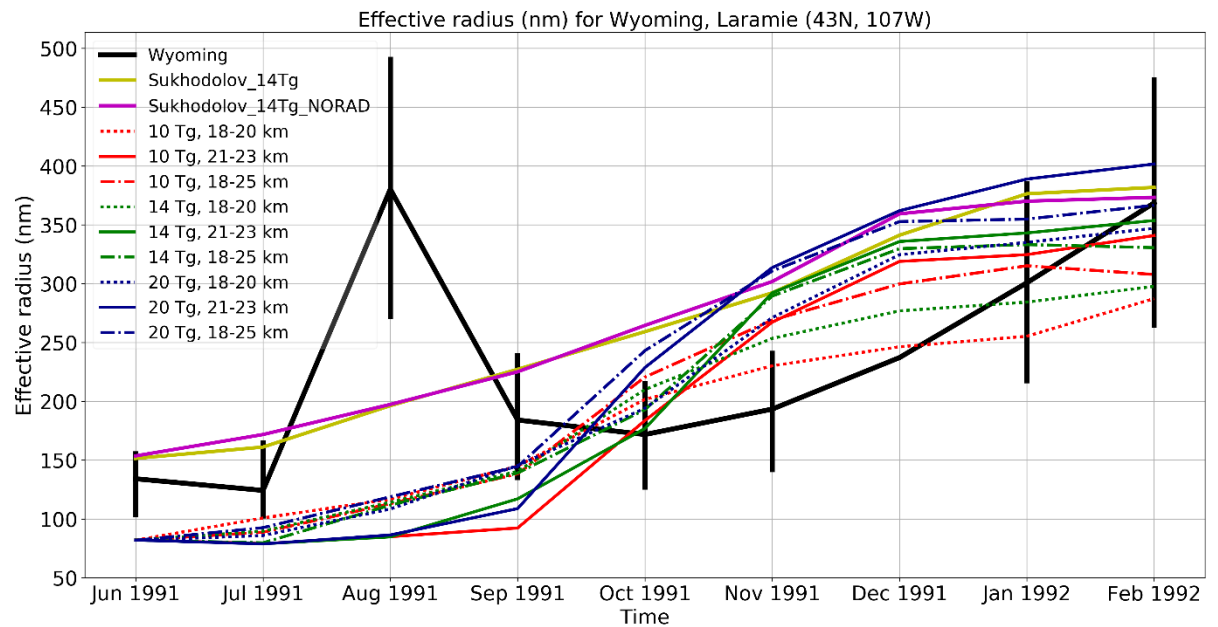


**Figure 5-12 Comparison of model simulated  $R_{\text{eff}}$  values (averaged for 14-30km) against in-situ measurements and previously modelled  $R_{\text{eff}}$  for Wyoming, Laramie for June 1991 to February 1992.**

#### 5.4 Hypothetical lidar site near the centre of the tropical reservoir

Figure 5-13 shows a daily comparison of extinction at 550 nm at 10°N, the equator and 10°S as simulated in the model. The purpose of exploring the equator and 10° in latitude north and south of the equator is to show what a tropical lidar may have observed and explore the value of, and need for, a tropical lidar station. The most striking feature when looking at this figure is what additional information on the dispersion a tropical lidar could reveal, as well as how MLO ties into the dispersion from the tropical reservoir. At 10°N (Figure 5-13a) detection of the cloud is 2 days sooner than was seen at MLO on June 28th 1991. The cloud appears to have descending layer structures at the beginning, middle and end of July in the upper altitudes (27, 30 and 31 km, respectively). The 10°N plot shows the highest extinction value is 0.20, close to the observed value at MLO (0.22). Exploring these sites within the model allows a closer assessment of how the Mount Pinatubo aerosol cloud may have developed out of the tropical reservoir that was not visible with observations.

The hypothetical equatorial lidar site (Figure 5-13b) captures the aerosol cloud first at 24 km on June 20th 1991 with extinction values steadily increasing into July 1991. At this site, the cloud is fairly homogenous increasing from 4 km thick initially to 12 km thick by September 1991. Both the 10°N and equatorial lidar sites show extinction

values beginning to decrease around October 1991, though high extinction values are seen throughout this time period.

The site at 10°S (Figure 5-13c) indicates the volcanic cloud reaching the southern hemisphere around the same time as at 10°N, just before July when it is noted at MLO. The cloud here resides at higher altitudes between 23 and 30 km throughout this time period.

In showing the differences between the equator and 10°N and the equator and 10°S (Figure 5-14), it is possible to understand more about how the cloud may have developed from the tropical reservoir. Figure 5-14 shows that the values at higher altitudes, between 22.5 and 30 km are higher in the equator than in the northern extra-tropics (10°N), but values at lower altitudes around 20 to 22.5 km are higher in at 10°N. There are three noticeable small areas (in blue) above the higher equator values (in red) at ~26, 27.5 and 29 km showing values of higher extinction at 10°N than at the equator.

In the case of comparing to 10°S (Figure 5-14), it is clear that the values of extinction at the equator are higher, almost consistently throughout this period. A few areas around 25 km in August and September are noticeable, although on a much smaller scale than seen in the comparison to 10°N.

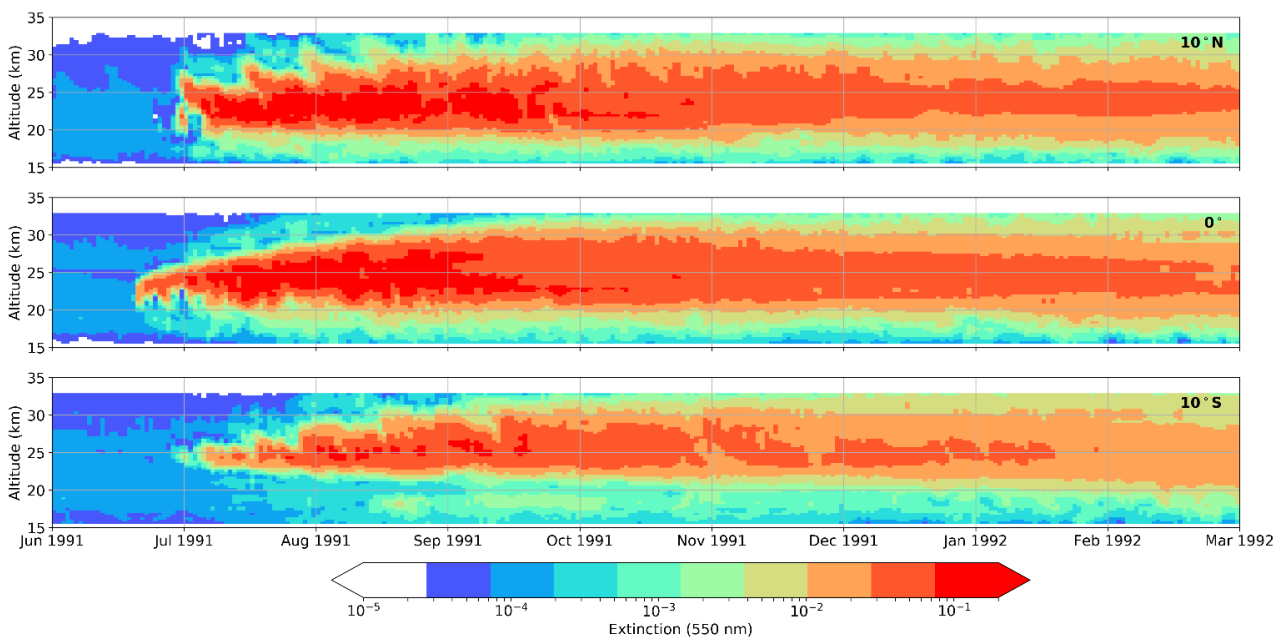


**Figure 5-13** Model-simulated extinction (550 nm) values for (A) 10°N, (B) the equator and (C) 10°S from June 1991 - March 1992.

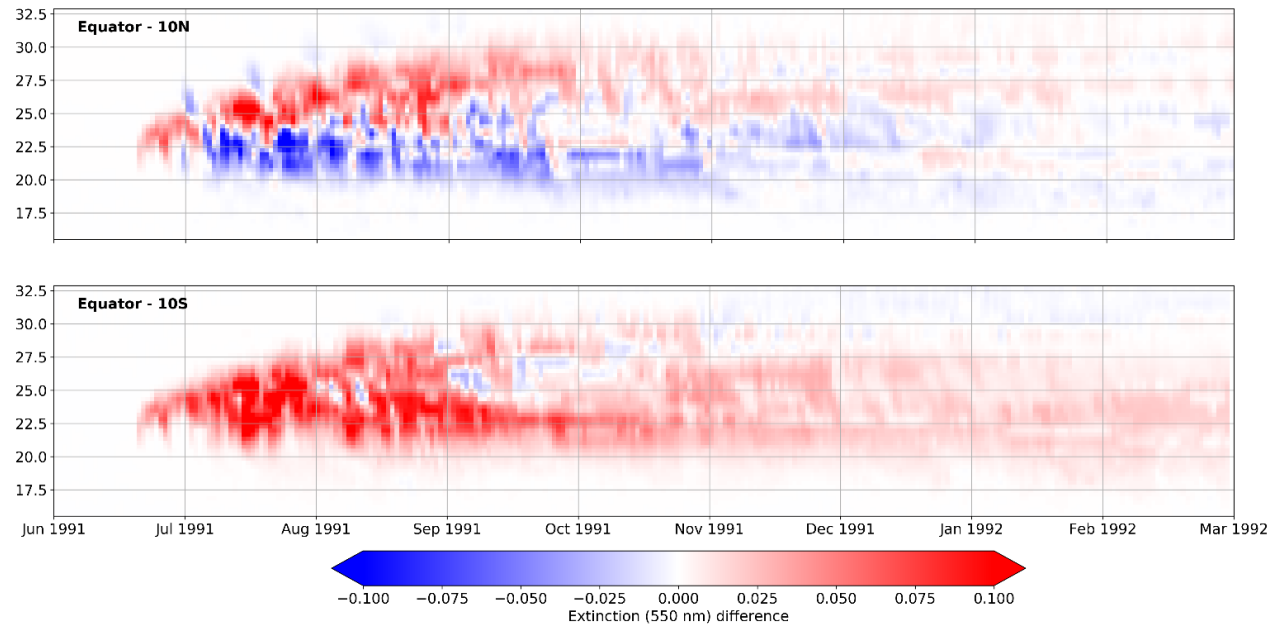


**Figure 5-14 Absolute difference in extinction at 550 nm between the equator and 10°N (top) and the equator and 10°S. Red values indicate areas where the equator values are higher, blue indicate where equator values are lower.**

## 5.5 Discussion

As stated in Section 5.3.1, the injection height has the largest effect on the vertical profile of extinction, with 18-20 km, out of those considered, showing the most obvious difference qualitatively and highest extinction values for all SO<sub>2</sub> mass injections. These large extinction values are likely due to the aerosol being confined to this layer resulting in more numerous particles in close proximity. This in turn results in maximum extinction values in regions with large clusters of aerosol. Relating this to SAOD, the 18-20 km simulations have the lowest SAOD values in the tropics, but exceed the 21-23 km injection height values on the global (80°S-80°N) scale before rapidly decreasing from November 1991 onwards. Sulfate burden is lowest in all SO<sub>2</sub> mass injection scenarios for an 18-20 km injection height for the tropics (2.6, 3.7 and 5.4 Tg, respectively) and globally (3.9, 5.4, 7.7 Tg, respectively). As the eruption occurred at 15°N, this appears to be consistent with findings of Marshall et al. (2018), whereby injection height has a larger effect on peak SAOD for tropical eruptions than those at higher latitudes.

The faster decrease of the 18-20 km SAOD and sulfate burden values (e-folding time of 5.9 months for 14 Tg of SO<sub>2</sub>) are potentially due to the regional confinement of the aerosol seen in the vertical profiles causing more coagulation, therefore, growing sulfate

aerosol to larger sizes and sedimenting out faster than for the other injection heights where the aerosol is more spread out and thus coagulation rates are reduced. Per unit mass, larger-sized particles have a smaller optical depth than a large number of smaller-sized particles (Pinto et al., 1989; Laciš et al., 1992), therefore the 18-20 km simulations may show lower SAOD values in the tropics due to these larger-sized (i.e. due to coagulation) particles, which also explains the lower sulfate burden values as particles sediment out faster. Monthly-mean effective radii values for each of the model simulations indicate that the largest-sized particles occur in the 21-23 km simulations with no significant difference seen when the injection height is varied, therefore suggesting that the aerosol closer to the tropopause is being removed more efficiently in the 18-20 km and 18-25 km simulations, as opposed to coagulation driving this process. Injecting SO<sub>2</sub> at around 18 km altitude in UM-UKCA, therefore leads to increased transport out of the lower branches of the BDC (discussed in Section 2.2.3) illustrating the effects of stratospheric dynamics on the longevity and properties of the volcanic aerosol cloud. Initially higher values of global SAOD for the 18-20 km and 18-25 km simulations are likely a result of this lower branch, as aerosol is preferentially transported to the midlatitudes (Holton et al., 1995; Marshall et al., 2019). Peak global SAOD values for the 18-20 km simulations occur before the peak SAOD in the 21-23 km simulations, suggesting that the majority of the volcanic aerosol in the 21-23 km simulation is confined in the tropics for longer before spreading to the mid-latitudes.

The faster decreasing SAOD values along with the fact that maximum extinction for 10 Tg SO<sub>2</sub> is not half that of 20 Tg SO<sub>2</sub> is likely linked to the self-limiting effects created as the amount of SO<sub>2</sub> emitted increases, as particles grow to larger sizes (e.g. Pinto et al., 1989; Timmreck et al., 2009). Another reason for the self-limiting effects is the effect of an increase in SO<sub>2</sub> leading to a decrease in OH, as OH levels are decreased by gas-phase reactions of SO<sub>2</sub> with OH (Bekki, 1995; Bekki et al., 1996). As these 18-20 km injection height simulations do not indicate that rapid coagulation is occurring and decreasing the mass of aerosol in the stratosphere by sedimentation, the impact of decreased OH by SO<sub>2</sub> scavenging is seemingly having more of an impact as SO<sub>2</sub> emission increases than the effects of coagulation.

There is a distinct difference between the sulfate burden and SAOD when varying the initial injection of SO<sub>2</sub>. For SAOD values, the 10 Tg SO<sub>2</sub> injection matches most closely with AVHRR measurements, whereas sulfate burden values for 14 Tg SO<sub>2</sub> most closely match the HIRS observations. A possible reason for the observed SAOD

matching the 10 Tg simulation and sulfate burden observations matching 14 Tg simulation is the differences in the observations. The HIRS observations (Baran and Foot, 1994) for global and tropical sulfate burden were taken at 0.8  $\mu\text{m}$  wavelength and therefore are likely to be underestimating the sulfate burden from smaller particles, potentially meaning the observations are actually closer to the 20 Tg injection or between 14 and 20 Tg. Sukhodolov et al. (2018) found a similar result, whereby their 14 Tg injection of  $\text{SO}_2$  matched well with HIRS data initially, but later agreed with other observations such as SAGE 3 $\lambda$ , suggesting that the HIRS data is more reliable in this first year following the eruption than in later years. They assume their 14 Tg simulation is a good estimate for their model but comment that their vertical distribution may be preferentially shifted to lower altitudes. Given that their injection height is preferentially set between 18-21 km, this indicates that injection heights around 18 km for the Mount Pinatubo eruption may be too low with preferential removal of aerosol from these lower altitudes. Some uncertainties also lie in the AVHRR and GloSSAC data, found similarly in Sukhodolov et al. (2018), whereby the observations differed by  $\pm 30\%$  in SAOD and  $\pm 15\%$  in global aerosol burden. Saturation of the SAGE II instrument (Antuña et al., 2002; Thomason et al., 2018) led to large uncertainties in the tropical optical depth following the Mount Pinatubo eruption. The GloSSAC data is a combination of multiple observations into one dataset and has been found to show peak values close to, but slightly lower than, sun photometer measurements with AVHRR data assumed too high (Thomason et al., 2018). It is reasonable to therefore assume that the correct values lie somewhere between these two datasets, as GloSSAC data does not include data from the upper troposphere/lower stratosphere whereas AVHRR does (Thomason et al., 2018). If this is assumed for this study then tropical SAOD still lies closest to 10 Tg  $\text{SO}_2$ , whereas globally somewhere between 10 and 14 Tg would fit better.

AVHRR data indicate SAOD values match closest with the 10 Tg model simulations here. In this particular comparison, this could suggest a lower estimated mass of  $\text{SO}_2$  was emitted at the time of the Mount Pinatubo eruption, consistent with findings from Dhomse et al. (2014). It may also be that not simulating ash and other particles in the model simulations creates a shift whereby 14 Tg with ash included more closely matches with observations due to early  $\text{SO}_2$  and sulfate aerosol being removed by condensation and coagulation and subsequent sedimentation (e.g. Deshler, 2016). Early GloSSAC values for the peak SAOD after the Mount Pinatubo eruption were 0.22

(Thomason et al., 2018), however, values shown in this chapter are based on newer calculations and account for the theorised underprediction of SAOD for this eruption (Thomason et al., 2018).

With regards to MLO, the layers are only visible when the injection height is 21-23 km and injection heights below this appear to pool the volcanic aerosol into a confined feature that has a steadily rising upper limit to the aerosol cloud. This rising feature is seen in all the model simulations and is due to the radiative heating created from the aerosol, lofting aerosol higher in altitude. This effect can also be seen in other aerosol-climate model studies (e.g. Vernier et al., 2011; Aquila et al., 2012; Dhomse et al., 2014) and is an important radiative effect in the model, though this is seen to be too strong by a factor of 2 across all simulations within UM-UKCA for this eruption causing the volcanic cloud to loft to heights higher than seen in observations. Another possibility is that models not accounting for ash produce higher volcanic clouds as they do not account for the potential scavenging mechanism of ash. The possibility of ash will be addressed in Chapter 6.

21-23 km daily-mean SAOD and sulfate burden is highest for the southern hemisphere in all cases, whereas the 18-20 km injection heights have highest SAOD and sulfate burden values in the northern hemisphere. This potentially shows preferential pathways exist to transport aerosol northwards with lower injection heights whilst mid-level heights transport aerosol more easily to the southern hemisphere. These pathways are also stronger for the 21-23 km injection height in the northern hemisphere as time progresses into the northern hemisphere winter. The opposite is true for the southern hemisphere as the aerosol is preferentially transferred in the 18-20 km injection height simulations during the southern hemisphere winter before plateauing from December 1991 onwards.

SAOD, along with satellite measurements, is usually seen as a key testing point for models against observations in order to decipher whether the model is capturing the global dispersion from a volcanic cloud well. However, it can be seen here that though some model simulations are in good agreement with observations, when examining the details of the volcanic cloud in the vertical stark differences become apparent even for those simulations in which SAOD matches observations well. For example, where the observations for tropical SAOD match with the 10\_deepalt simulation, the same injection height does not match the vertical extinction observations. This is the same

for the SAOD comparison with AVHRR, whereby the 10\_lowalt for SAOD tracks closely with the observations from November 1991 onwards, but the vertical extinction does not match with lidar observations. One possibility is that the integrative nature of calculating SAOD causes details seen in the vertical profiles to be lost.

With regards to a hypothetical tropical lidar station, testing this within the model indicates that the model depicts the tropical reservoir well. Indications by Robock and Antuña (2001) were that a tropical lidar station in Latin America would significantly aid our understanding of the vertical and global dispersion of volcanic aerosol. The vertical profile of aerosols is important for observing the climatic effects of volcanic eruptions and, although satellites can produce global coverage, ground-based lidars are needed for filling gaps where satellites are saturated and for calibrating satellite observations (Robock and Antuña, 2001). As no lidars existed at the tropics during the time of Mount Pinatubo we can only use models to infer the potential dispersion, however, the understanding of future Mount Pinatubo-magnitude eruptions in the tropics would be greatly benefited by more tropical lidar stations, as we would gain a better understanding of the SAOD values and vertical profiles of stratospheric aerosols in the tropics. A major step forward from Robock and Antuña (2001) is the Latin America Lidar Network (LALINET) (Antuña-Marrero et al., 2017) creating a substantial southern hemisphere and cross tropical lidar network which will be imperative to understanding volcanic clouds from future eruptions. There used to be a lidar active on Kiribati (1.4°N) and stations such as that in Paramaribo, Suriname (5.8°N) and Natal, Brazil (5.8°S) and San Jose, Costa Rica (9.6°N) are active, but measure water vapour and ozone (NDACC, 2020). Studying the effects of water vapour and ozone after volcanic eruptions is important, but direct backscatter ratio, depolarisation and particle mass concentration measurements would give a better understanding for the radiative forcing and potential ash measurements from an eruption (e.g. Ansmann et al., 2011; Vernier et al., 2016). A study using Cloud-Aerosol Lidar and Infrared Pathfinder Satellite Observation (CALIPSO) found that adjustments were needed in the tropics to account for increased scattering from particles at ~30-35 km in altitude (Vernier et al., 2009), further indicating that ground-based tropical instruments would be integral to furthering our understanding of aerosol levels and transport that occurs within and out of the tropical stratospheric reservoir following a future major tropical or near-tropical eruption.

## 5.6 Conclusions

Within this chapter an analysis of an ensemble of interactive stratospheric aerosol simulations of the Mount Pinatubo cloud was performed, varying the emitted mass of SO<sub>2</sub> and injection heights of SO<sub>2</sub>. The analysis, following the design of the HErSEA experiment within the international ISA-MIP initiative (Timmreck et al., 2018), effectively assesses how the Mount Pinatubo cloud would have progressed under different eruption source parameter scenarios, such as a deeper SO<sub>2</sub> injection range or an injection closer to the tropopause.

Specifically, the effect varying these eruption source parameters has on the vertical extinction, sulfate burden and SAOD were analysed. These simulations help to understand the variation in SO<sub>2</sub> emission amount interactive stratospheric aerosol models find is needed to represent the same reference Mount Pinatubo observational datasets. The research in this chapter has also applied the model to consider how a hypothetical equatorial lidar station would have observed the Mount Pinatubo aerosol cloud, also considering how this differs from the only tropical aerosol record from the Mauna Loa lidar.

In addition to assessing how the different eruption source parameters influence the optical properties of the cloud, the chapter has analysed the progress of radiative heating and effective radius within the volcanic aerosol cloud. The analysis seeks to understand how the volcanic aerosol cloud from different Mount Pinatubo-like eruptions would influence the radiative and microphysical progression of the cloud. With the radiative heating driving important changes in several other trace species (primarily stratospheric ozone and water vapour), performing this analysis also allows an assessment of the broader effects of future Mount Pinatubo-like aerosol clouds.

Overall, the results from the HerSEA ensemble confirms the results from Dhomse et al. (2020), that a model adjustment is required to reduce the SO<sub>2</sub> emission to the lower limit of the observed 14-23 Tg range (Guo et al., 2004). The analysis also illustrates how the injection height of SO<sub>2</sub> resulted in large differences in vertical extinction, but evaluating the lidar observations shows that whereas a higher SO<sub>2</sub> injection closer to the tropopause (20\_lowalt) can bring SAOD values closer to observations, this would have a very different vertical structure and therefore influence other species quite differently. As in Dhomse et al. (2020), the aerosol extinction from the 10-14 Tg SO<sub>2</sub>, 21-23 km injection height simulation matches best with the lidar observations, reproducing well

the layers seen in observations. However, the aerosol cloud top in this simulation remains too high compared to the observations. Although the heating in the stratosphere following the eruption show a similar pattern to ERA-interim, the radiative heating in the model is too high, on average by a factor of 2, which may be lofting aerosol to altitudes higher than observed. These biases are consistent with the model missing a sedimentation-enhancing pathway, such as via condensation of sulfate aerosol on ash, may also lead to a greater lofting of aerosol to higher than observed altitudes. The potential for sedimentation of sulfate on ash to explain this effect will be explored in an additional HERSEA ensemble of UM-UKCA simulations in Chapter 6.

Previously, SAOD has justifiably been used as the primary diagnostic to assess model performance against observations (e.g. Niemeier et al., 2009; Aquila et al., 2012; Dhomse et al., 2014). Assessing the skill of a model based only on SAOD does not account for the potential for bias in the vertical dispersion of the aerosol, for example this analysis shows that whereas 10 Tg SO<sub>2</sub> may match well with SAOD, 14 Tg SO<sub>2</sub> matches more closely with sulfate burden. Therefore, based on these UM-UKCA simulations SO<sub>2</sub> mass emissions of more than 14 Tg are unlikely for the 1991 Mount Pinatubo eruption. SO<sub>2</sub> mass injections in the range between 10 and 14 Tg may be most likely due to the large uncertainties in observational data with AVHRR potentially overpredicting and GloSSAC underpredicting from a lack of upper tropopause data.

Results from this chapter also highlighted that more ground-based lidar around the tropics and sub-tropics would significantly aid our understanding in the dispersion of volcanic material from the tropical reservoir to the northern and southern hemispheres and allow the retrieval of SAOD and vertical profiles of aerosols following another Pinatubo-scale eruption.

The SAGE II satellite observations from the time of the 1991 Mount Pinatubo eruption were limited to only measure the upper part of the tropical part of the volcanic cloud because of extremely high optical thickness of the volcanic aerosol (Antuña et al., 2002). This gap in the SAGE II record highlights a difficulty to constrain a specific initial SO<sub>2</sub> mass and injection height and further indicates the value for more observational capability, such as ground-based lidars or sun-photometers, around the equator and highlights the value of the ship-borne lidar analysed in Chapter 4. This study indicates that, in this model, an injection height closer to 21-23 km and SO<sub>2</sub> mass between 10-14 Tg agrees best with observations of extinction, SAOD and sulfate

burden. An SO<sub>2</sub> mass of 10-14 Tg is in agreement with studies such as Dhomse et al. (2014), Mills et al. (2016) and Sukhodolov et al. (2018), however Mills et al. (2016) and Sukhodolov et al. (2018) find a better agreement with observations when using an injection height of 18-20 km. Due to recent advances in modelling and observational capabilities (Kremser et al., 2016), our understanding of underlying transport processes and microphysics would likely drastically improve if another major, powerful eruption like 1991 Mount Pinatubo were to occur.

## Chapter 6

# The role of ultra-fine ash in the global dispersion of the 1991 Mount Pinatubo aerosol cloud

### 6.1 Introduction

Volcanic ash is an important eruptive product, due to the potential imminent danger to local communities from its deposition (Newhall et al., 1997; Wilson et al., 2012), and the hazard to aviation (Prata and Rose, 2015) and geochemical cycles (Niemeier et al., 2009; Langmann, 2014). Ash is rarely considered when predicting the climatic impact of a volcanic eruption, as the radiative forcing is known to depend primarily on how much SO<sub>2</sub> reaches the stratosphere, the latitude of the volcano, height of the eruptive plume and the season of an eruption (Dyer, 1974; Toohey et al., 2011; Marshall et al., 2019). The reason ash is rarely considered when simulating the climate impact of volcanic eruptions is due to the assumption that ash particles sediment out of the stratosphere in the first few days after an eruption (Bluth and Rose, 2004; Niemeier et al., 2009; Langmann, 2014).

An interactive stratospheric aerosol modelling study by Niemeier et al. (2009) investigated the effects of the co-emitted volcanic ash and SO<sub>2</sub> from the 1991 Mount Pinatubo eruption, with one ash mode representing ash particle sizes between 1-15 µm in radius. Their study found these super-micron radius particles remained in the stratosphere for no longer than 1 week, but showed that the radiative heating effects from the ash increased global dispersion of the volcanic sulfate cloud slightly with a deeper cloud and greater southward transport in the first 20 days after the eruption. Muser et al. (2020) showed that, even for the much smaller June 2019 Raikoke eruption, both radiative heating and particle-aging have important effects on the dispersion of the volcanic cloud. Although only simulating the volcanic cloud for the first few days after the eruption, Muser et al. (2020) show how the co-emitted ash changes its progression, illustrating the importance of radiative heating and particle-aging for the vertical transport of aerosol and subsequent cloud altitude. The Niemeier et al. (2009) study only explored the radiative heating effects of the ash on the volcanic sulfate aerosol, the simulations not resolving microphysical effects from the uptake of sulfate onto the ash.

This thesis chapter explores the possibility that the longer stratospheric residence time of ash particles  $<1 \mu\text{m}$  geometric mean diameter (hereon referred to as “ultra-fine ash”) may have a substantial impact on the progression of the volcanic aerosol cloud, even though these particles represent less than 1% of the overall mass of ash emitted.

Observational evidence for the presence of volcanic ash within the Mount Pinatubo cloud by initial balloon soundings from Laramie, Wyoming ( $41^\circ\text{N}$ ) (Sheridan et al., 1992; Deshler et al., 1992) showed no obvious signature of ash. The balloon soundings on July 16<sup>th</sup> and 26<sup>th</sup> 1991 contained heated-inlet particle counters, which measured ambient air on balloon ascent, with the inlet heated on descent to measure non-volatile particles (those surviving  $150^\circ\text{C}$ ). The initial flights were also equipped with cascade impactors to sample aerosol particles for later composition analysis. The refractory particle concentrations on these flights showed little enhancement  $\sim 15 \text{ km}$  in the initial volcanic layers, with compositional analysis finding that 99% of measured particles did not contain ash (Sheridan et al., 1992) and heated impactors finding 95-98% of particles were also purely sulfuric aerosol particles. However, a recent re-analysis of the balloon measurements (Deshler, 2016) shows that heated-inlet particle counter on the July 30<sup>th</sup> 1991 in Deshler et al. (1992) and later analysed August 2<sup>nd</sup> 1991 sounding (Deshler, 2016) both showed enhanced refractory particle concentrations in higher altitude layers (at 21-24 km). Analysis of total particles to refractory particles also revealed a signature of very rapid particle size sorting in all 4 of the early flights, consistent with the potential earlier sedimentation of much larger ash particles. The analysis concluded that the involatile particles are the ash cores within internally mixed ash-sulfuric particles.

The two later balloon flights from Laramie that detected the non-volatile (ash) components were 44 and 47 days after the eruption, the earlier flights showing no volcanic ash detected at 30 and 40 days after the eruption, suggesting ash arrived at least 2 weeks later than the initially detected volcanic cloud which was comprised entirely of sulfate (Deshler, 2016). A significant ash component was found at 22-23.5 km with the re-analysis from Deshler (Deshler, 2016) concluding the non-volatile cores were ash particles at  $\sim 0.25 \mu\text{m}$  radius, within overall ash-sulfuric particles at around  $0.48 \mu\text{m}$  radius.

In addition to the balloon measurements, in-situ sampling aircraft-borne impactor measurements (Pueschel et al., 1994) also give mixed evidence for ash particles in the

volcanic aerosol cloud, with analysis of the impactor samples of the ER-2 flights (at 16-20 km) no volcanic ash, whereas the analysis of impactor samples on the DC-8 flights (at 9.5-12.6 km) clearly show ash coated with sulfuric acid. The DC-8 flights with the cascade impactors were primarily between 50-66°N and measured during January-March 1992 (7-9 months after the Mount Pinatubo eruption) and are consistent with lidar depolarisation measurements from Aberystwyth (52°N) (Vaughan et al., 1994) (as outlined in Chapter 3). The Aberystwyth lidar measurements show that whereas the majority of the volcanic cloud was non-depolarising (spherical particles), the backscatter from the base of the Mount Pinatubo aerosol cloud continued to be moderately depolarising throughout August 1991 to March 1992, indicating non-spherical particles were present in the lower portion of the volcanic cloud. The altitude of the >1% depolarising layer was initially in the lower portion of the cloud, descending to only be below 18 km from December 1991 before residing between 10 and 17 km during January and March 1992, broadly consistent with the difference between the DC-8 and ER-2 airborne impactor measurements.

In the previous chapter, interactive stratospheric aerosol simulations investigated the effect of different injection heights and mass of SO<sub>2</sub> on the progression of the initial tropical confinement of the Mount Pinatubo eruption aerosol cloud. In this chapter, additional model experiments that emit both SO<sub>2</sub> and volcanic ash particles are investigated, with one of the 7 modes in the aerosol module having been adapted to also track an internally mixed sulfate component of the ash mode. The same set of injection parameters from the HErSEA-Pinatubo experiment with ISA-MIP (Timmreck et al., 2018) is also used in this chapter to assess the effect ultra-fine ash had on the progression of the Mount Pinatubo aerosol cloud with the equivalent set of model simulations.

Firstly, model simulations using ash particles greater than 1 µm geometric mean diameter (hereon referred to as “fine ash”) are assessed (Section 6.3), investigating the residence time of different emission sizes for these particles. The ultra-fine ash particles are then investigated (Section 6.4.1) to evaluate the simulated vertical distribution of this ultra-fine ash within the Mount Pinatubo aerosol cloud.

The experiments align with the Mount Pinatubo experiment in Niemeier et al. (2009), but here the effect of the ultra-fine ash to potentially scavenge some proportion of the volcanic sulfur is explored. The impact of the co-emitted ash on SAOD (Section 6.5)

and sulfate burden (section 6.6) are first assessed, with the focus first on the changes to the monthly progression of the tropical reservoir. The vertical profiles of ash and sulfate is then explored, also with the daily-timescale variation in extinction compared to the MLO lidar, as in the first two results chapters (Section 6.7).

The tropical and global sulfate burden is compared to that derived from the HIRS/2 satellite observations (Baran and Foot, 1994), with these infrared satellite measurements detecting the volcanic sulfuric acid aerosol from the 8.2  $\mu\text{m}$  water vapour channel. Model simulated SAOD is compared to the GloSSAC volcanic forcing dataset used for CMIP6 and also that measured from the nadir sounding AVHRR measurements. For the Mount Pinatubo period, GloSSAC is based on the SAGE II measurements, and includes the period where the solar occultation instrument could only measure the upper part of the volcanic aerosol cloud due to the extremely high AOD. The dataset is based on the latest version 7.0 of the SAGE II aerosol extinction retrieval algorithm (Damadeo et al., 2018) and used an improved gap-filling method for the saturation period combining with infra-red Cryogenic Limb Array Etalon Spectrometer (CLAES) measurements in mid-latitudes (Thomason et al., 2018), but still uses the original gap-filled dataset in the tropics, combining with lidar measurements from Mauna Loa (Hawaii), Hampton (Virginia) and Camaguey (Cuba) (SPARC, 2006).

The chapter is concluded by suggesting future work related to ash research in both UM-UKCA and other models. A potentially missing important removal pathway for major tropical volcanic aerosol clouds is suggested by Dhomse et al. (2014) and other interactive stratospheric models (see Timmreck et al., 2018), with Mills et al. (2016) reducing their injection estimates of  $\text{SO}_2$  to account for a lack of ash and ice in their model. In Chapter 5 there was a discrepancy with the height of the volcanic aerosol cloud, noted to be due in part to radiative heating being too high in the model, however there may also be a lacking reduction pathway which we hope to resolve in this chapter by including ash in these simulations. The model experiments were designed to test the following two science questions:

a) With ultra-fine ash particles persisting longer in the atmosphere than fine ash particles, how does their presence influence the global dispersion of major volcanic clouds?

b) Does the ultra-fine ash mainly impact the cloud sulfate through scavenging sulfate aerosol via condensation or by acting the self-lofting effect of increased absorption of solar radiation?

## 6.2 Data and methods

The model experiments in Chapters 4 and 5 simulated the Mount Pinatubo aerosol cloud as being composed entirely of aqueous sulfuric acid aerosol particles with subsequent global dispersion and microphysical progression of the cloud. In order to address the impact of ultra-fine ash on the aerosol cloud, a new version of the model was applied to allow co-emission of volcanic ash and volcanic SO<sub>2</sub> at a specified particle size. The approach tracks the ash mass equivalently to simulations with desert dust in the modal scheme (Yoshioka et al., 2019) with the coarse-insoluble mode used exclusively to track volcanic ash.

As explained in Section 3.3.3, in order to explore the scavenging effect of the sulfate uptake onto the ash, the GLOMAP aerosol module was adjusted to track also an extra sulfate aerosol component in that coarse-insoluble mode. These particles are then tracked as internally mixed ash-sulfuric particles. It should also be noted that although a single emission size is given, the sedimentation method within the model accounts for internal variation in particle size, since it sediments both number and mass with the corresponding fall speed (Mann et al., 2010). The ash-sulfuric particles are transported within the coarse-insoluble mode, which has a geometric standard deviation of 2.0, corresponding to particle size range of around a factor of 10 in radius (Mann et al., 2012).

Before carrying out the full HErSEA-Pinatubo ensemble of model experiments with ash (Table 6-1), an initial set of short, 10-day simulations emitting ash at a number of different ash sizes were carried out, using the mid-altitude emission height. These initial simulations were aimed at determining how the ash residence time in the stratosphere varies with particle size. Simulations with emission sizes of 1, 3.16 and 10  $\mu\text{m}$  diameter were used to investigate the smaller to larger fine ash size ranges (Section 6.3), for 50 Tg of ash emitted, as 50 Tg is the upper end of the 34-50 Tg best-estimate range from the HIRS and AVHRR satellite observations (S. Guo et al., 2004). The upper value is thought to be more likely due to signal decrease from clouds upon retrieval (S. Guo et al., 2004). Then, 3-month simulations were carried out to

investigate the effects of the longer lasting ultra-fine ash, using sizes 0.1, 0.316 and 1  $\mu\text{m}$  (Section 6.4).

**Table 6-1** List of performed experiments, with "\_ash" indicating model simulations with ash injected and "non-ash equivalent" outlined in Chapter 5.

Name	Non-ash equivalent	Injected SO <sub>2</sub> (Tg)	Injection height (km)
10_lowalt_ash	10_lowalt	10	18-20
10_midalt_ash	10_midalt	10	21-23
10_deepalt_ash	10_deepalt	10	18-25
14_lowalt_ash	14_lowalt	14	18-20
14_midalt_ash	14_midalt	14	21-23
14_deepalt_ash	14_deepalt	14	18-25
20_lowalt_ash	20_lowalt	20	18-20
20_midalt_ash	20_midalt	20	21-23
20_deepalt_ash	20_deepalt	20	18-25

For these longer ultra-fine ash experiments 1% and 10% of the estimated 50 Tg ash was injected (0.05 Tg and 0.5 Tg), as studies have estimated that smaller ash sizes made up 0.9-9% of the total fine-ash mass (Bluth and Rose, 2004; Niemeier et al., 2009).

To evaluate the progression of ultra-fine ash in altitude, the ash co-emission equivalent of the HErSEA simulations (Chapter 5) are compared to depolarisation measurements from the Aberystwyth lidar (Vaughan et al., 1994), as no other Mount Pinatubo study has compared to this dataset.

The first metric, stratospheric AOD (SAOD) at 550 nm wavelength, is the primary metric used to evaluate interactive Mount Pinatubo aerosol simulations. Two benchmark datasets for SAOD following the eruption are from SAGE II measurements (Thomason and Osborn, 1992) and AVHRR (Long and Stowe, 1994). Here, SAOD from GloSSAC (Thomason et al., 2018) and AVHRR are used to compare to the model simulated SAOD. Sulfate measurements from Baran and Foot (1994) are also compared to model-simulated sulfate burden. These observational measurements are widely used in the modelling community for simulating the Mount Pinatubo eruption, with the GloSSAC data providing a more up to date dataset of the SAGE II data that

was super-saturated at the time of the Mount Pinatubo eruption (e.g. Antuña et al., 2002). Table 6-1 outlines the different model experiments in this chapter.

### 6.3 Stratospheric residence time of fine ash (super-micron)

In this section the 10-day model experiments with fine ash (1,3.16, 10  $\mu\text{m}$  diameter) are analysed. All simulations use the 14\_midalt\_ash HErSEA setup and 50 Tg of ash emitted. For these initial experiments, the rationale is to assess how the ash mass burden progresses and to track how different sized particles are removed.

For the 10  $\mu\text{m}$  mean diameter model simulation, the ash particles are almost completely removed from the stratosphere within 8 days of the eruption, the mass burden in the stratosphere reduced to just 0.65% of the 50 Tg ash initially emitted (0.001 Tg) (Figure 6-1). The model represents the  $\text{SO}_2$  and ash emission as a 24-hour emission on June 15<sup>th</sup> 1991 with a model timestep of 20 minutes. The 50 Tg ash emission is then 0.69 Tg on each of the 72 timesteps. It is important to note that the points of the graph are each 1-day means and maximum burden on the 15<sup>th</sup> June is 25 Tg, so where the 10  $\mu\text{m}$  peak shows 20% it should be taken as double that value.

The subsequent daily means can be considered representative however, and within 2 days of the eruption the 3  $\mu\text{m}$  mean emissions diameter case sees ~30% of emitted ash mass removed from the stratosphere. The 3.16  $\mu\text{m}$  and 1  $\mu\text{m}$  retain 15% and 58% of the original ash mass injected, respectively, one week after the eruption (Figure 6-1). The decline of the 1  $\mu\text{m}$  particles is steadier, losing ~5% of the total mass on average per day. Overall, the e-folding times (calculated after the peak) for each particle size are 2 days, 4 days and 13 days for 10  $\mu\text{m}$ , 3.16  $\mu\text{m}$  and 1  $\mu\text{m}$ , respectively.

According to Junge et al. (1961) (as mentioned in Section 2.2.5) a particle with density 2000  $\text{kg m}^{-3}$  at ~22 km should fall at ~2.6 km/day for a particle with diameter 10  $\mu\text{m}$ , at 0.35 km/day for a particle with diameter 3  $\mu\text{m}$  and 0.07 km/day for a particle with diameter 1  $\mu\text{m}$ . All particles in Figure 6-1 fall at slightly faster speeds than shown by Junge et al. (1961), however, since the model simulated particles are heavier (density of 2650  $\text{kg m}^{-3}$ ), their terminal velocities are higher than particles with a density of 2000  $\text{kg m}^{-3}$ .

An exponential decay in ash burden is seen in the HIRS/2 satellite observations (S. Guo et al., 2004) following the Mount Pinatubo eruption and these data show a removal of ash to ~10% of the original mass within 3 days, in line with the reduction in ash burden

between the 1  $\mu\text{m}$  and 3.16  $\mu\text{m}$  mean diameter two-moment modal sedimentation cases (Figure 6-1).

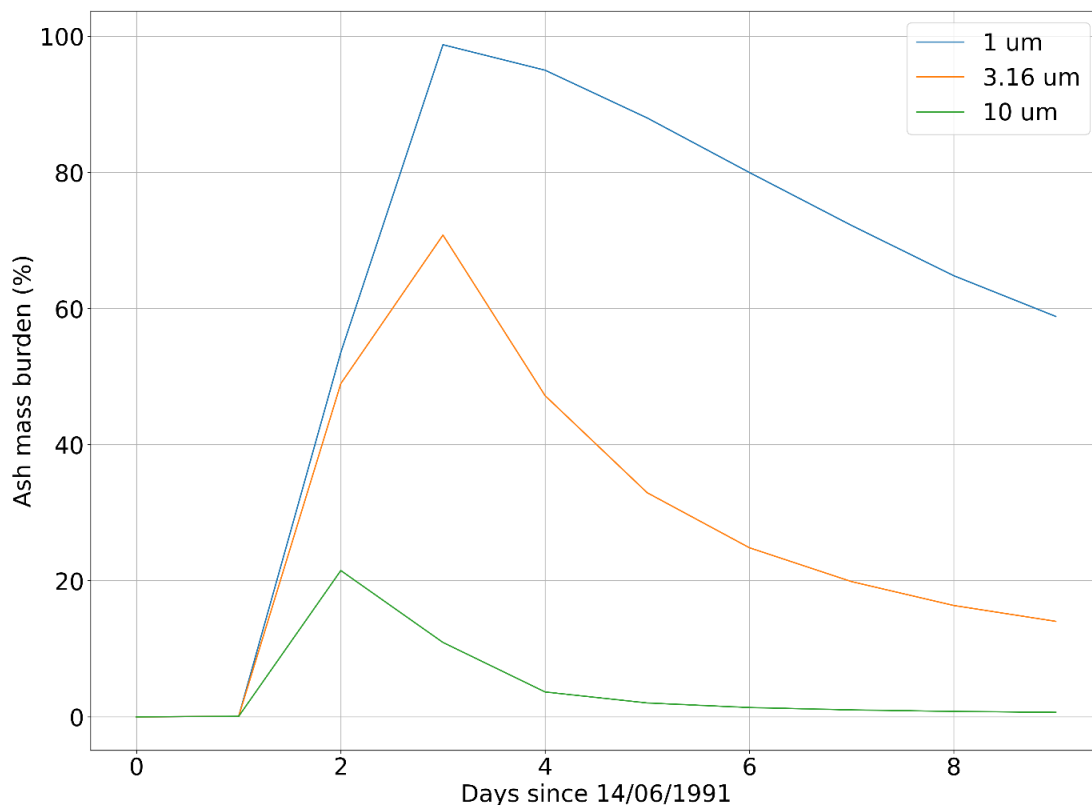


Figure 6-1 Percentage mass of ash over a one-week period following the eruption for 1, 3.16 and 10  $\mu\text{m}$  ash sizes.

#### 6.4 Stratospheric residence time and vertical distribution of ultra-fine ash (sub-micron)

In this section, longer (90-day) ash co-emission experiments were simulated for ultra-fine ash sizes (0.1  $\mu\text{m}$ , 0.316  $\mu\text{m}$  and 1  $\mu\text{m}$  geometric mean emission diameter). In these simulations more realistic ash emission fluxes of 0.05 Tg and 0.5 Tg of ash were investigated (1% and 10% of the estimated 50 Tg ash injected, as mentioned in Section 6.2).

With this reduced emission flux, the 1  $\mu\text{m}$  ash experiment retains 40% of the original ash mass (Figure 6-2), in comparison to the 58% retained with a 50 Tg injection mass (Figure 6-1). This comparison suggests that the 50 Tg simulations have a substantial

radiative heating effect, lofting the ash particles to higher altitudes and extending their stratospheric lifetime.

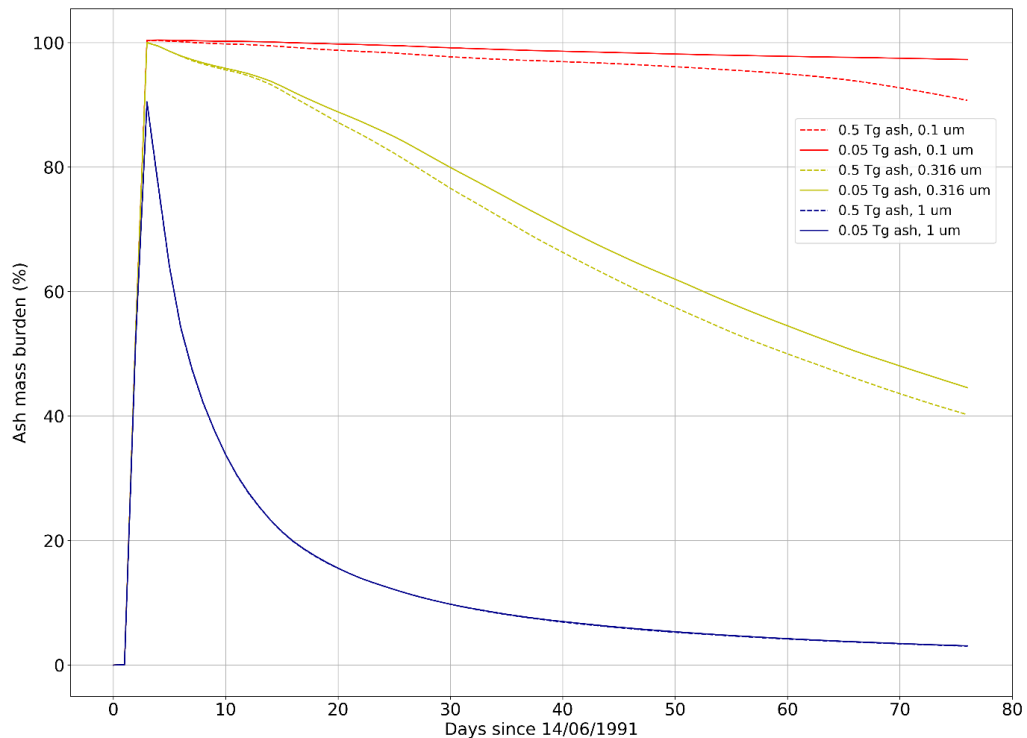


**Figure 6-2 Percentage mass of ash in the first 3 months following the 1991 Mount Pinatubo eruption, for 3 different ash sizes (0.1, 0.316 and 1  $\mu\text{m}$ ) for 0.05 and 0.5 Tg of ash injected. Straight lines denote 0.05 Tg, dashed denote 0.5 Tg ash.**

For the 0.05 Tg and 0.5 Tg ash emissions, 80% of the total ash is removed within 2 weeks of the eruption and the stratosphere is almost entirely depleted of ash after 3 months (Figure 6-2). The 0.316  $\mu\text{m}$  diameter ash decreases by 60% after 3 months in the 0.5 Tg case and 55% in the 0.05 Tg case.

For the 0.1  $\mu\text{m}$  mean emission size experiments, the stratospheric ash burden decreases slightly more after 3 months in the 0.5 Tg case (92%) than in the 0.05 Tg case, where 98% of the ash burden remains (Figure 6-2). Niemeier et al. (2009) found that ash sizes in the range 1-15  $\mu\text{m}$  were short-lived, which agrees with what is found here with the >1  $\mu\text{m}$  mean diameter ash simulations analysed in Section 6.3. These simulations suggest that 0.1 to 1  $\mu\text{m}$  diameter ash particles may play a more important role than suggested by Niemeier et al. (2009). The M7/HAM aerosol scheme used in the ECHAM simulations in that study represent particles from 1-15  $\mu\text{m}$  using a similar two-

moment modal scheme, however their peak diameter was  $\sim 4 \mu\text{m}$ , therefore not exploring the effect of peak emission sizes  $\leq 1 \mu\text{m}$ .

Research to assess the optical properties of ash within the 2014 Kelud (Indonesia) eruption cloud estimated that ash particles  $< 0.3 \mu\text{m}$  in size accounted for 20-25% of the overall volcanic cloud AOD at altitudes between 18 and 23 km (Vernier et al., 2016). This suggests that the ultra-fine diameter sized ash particles in this study may have more of an effect on AOD and climate than previously thought due to their persistence in the atmosphere.

Based on these initial model tests it was decided that 0.05 Tg as the mass of ash and  $0.1 \mu\text{m}$  as the mean emission size were to be studied for the HErSEA ensemble of simulations in Table 6-1. These are the longest lasting particles, as seen in Figure 6-2, and therefore have the potential to impact the stratospheric cloud over the whole time period studied. These particles also have a long enough residence time to be consistent with DC-8 cascade impactor samples (Pueschel et al., 1994) and lidar measurements from Aberystwyth (Vaughan et al., 1994). The hypothesis posed here is that the ultra-fine (specifically  $0.03$  to  $0.3 \mu\text{m}$  diameter: mean of  $0.1 \mu\text{m}$ ) ash particles have the 4-9-month residence time shown in the observations. Therefore, these ash particles are present and have the potential to impact upon the SAOD and sulfate burden, acting also as a faster sedimentation pathway and/or source of increased radiative heating in the stratosphere.

#### **6.4.1 Ultra-fine ash burden for June 1991 - February 1992**

Following on from the previous section, additional simulations with the  $0.1 \mu\text{m}$  mean diameter ash was performed to analyse how the ash burden change in the model depends on injection height and mass of  $\text{SO}_2$  (Figure 6-3). In all simulations (Figure 6-3) at least 40% of the ultra-fine ash is still in the stratosphere by February 1992, with 66% of it still remaining in the case of the 18-25 km injection height simulations. A variation is seen between the different injection heights throughout this period, with 18-20 km simulations retaining the least amount of ash. In the 18-20 km simulations the ash is injected closer to the tropopause and sees the quickest removal of ash of all injection heights from August, showing a fairly steady reduction to 45% in February 1992.

As with Section 5.3.1, where injection height had a greater impact on the vertical profile of extinction than the mass of SO<sub>2</sub> injected, here the same is true for the global ash burden (Figure 6-3), except for the 20\_midalt\_ash simulation where the ash burden reduces more rapidly than 10\_midalt\_ash or 14\_midalt\_ash around the beginning of November 1991. The longest lasting particles initially are those with an injection height of 21-23 km for all 3 SO<sub>2</sub> emissions. A sudden decline in ash burden is seen at the end of October 1991, reaching 58-60% of the original 0.05 Tg mass by the end of February 1992.

By February 1992 the 18-25 km injection height simulations show the largest remaining amount of ash (68%) and the 18-20 km injection height simulations show the least amount of remaining ash (45%). Understanding how the ash burden varies over time is important in order to identify the residence time of the different particle sizes.

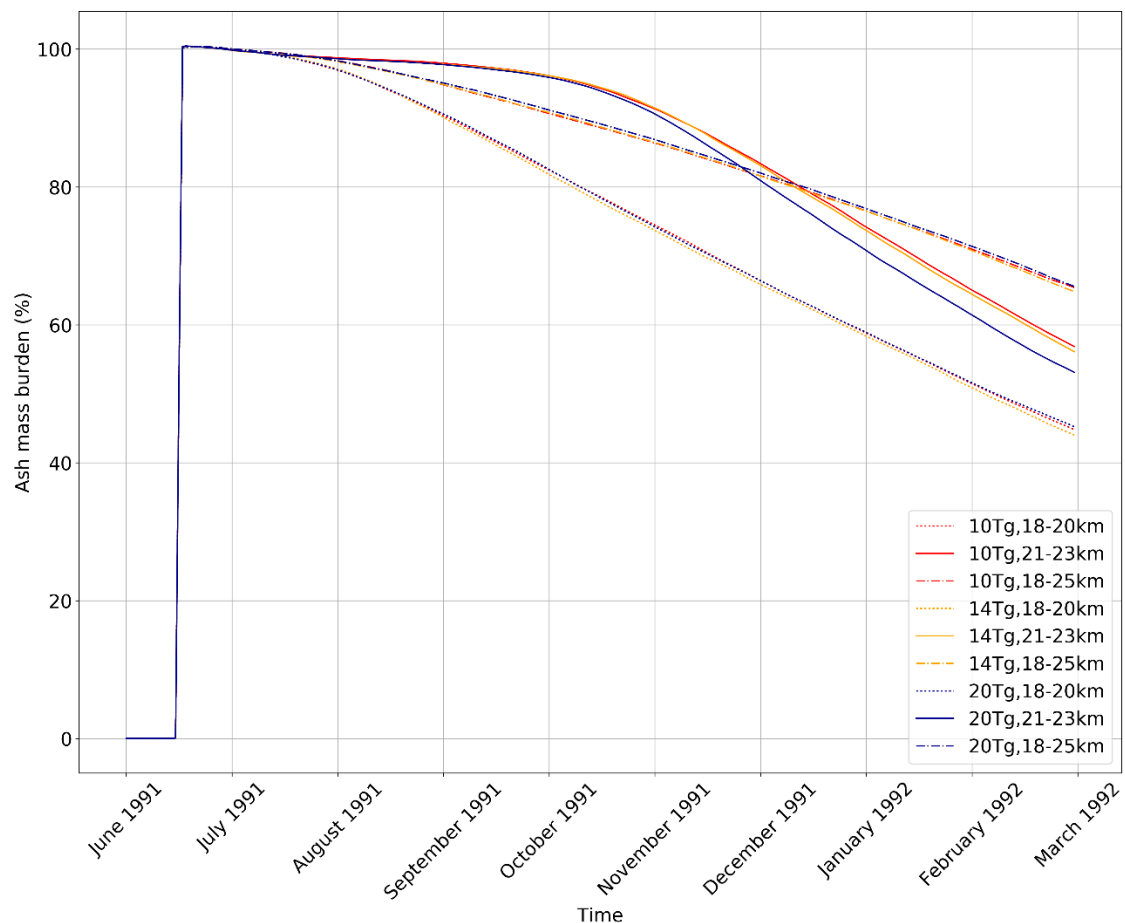


**Figure 6-3** Ash burden percentages for model simulation with 10, 14 and 20 Tg of SO<sub>2</sub> and 18-20, 21-23 and 18-25 km injection heights.

As well as the overall remaining burden of ash, it is important to know where the ash resides in relation to the sulfate aerosol in the vertical. Firstly, to investigate the co-location of the sulfate aerosol and ash and therefore the potential for condensation and coagulation of sulfate onto the ash. Secondly, assessing the vertical profiles of ash and sulfate burden also establishes where the majority of each constituent is located in altitude (i.e. the peak) for these different 0.1  $\mu\text{m}$  mean emission size cases.

Figure 6-4 shows the ash (red) and sulfate (blue) burden for the tropics for all injection heights with a 14 Tg  $\text{SO}_2$  emission and different line styles indicating different injection heights. At all latitudes, the simulations show a clear layer of ultra-fine ash at a slightly lower altitude ( $\sim 1$  km) than the main sulfate layer. The upper part of the ash layer is at the same altitude range as the sulfate layer. This slightly lower, but overlapping ash layer is broadly consistent with later mid-latitude observations from the Aberystwyth lidar (Vaughan et al., 1994) and cascade impactors on the DC-8 and ER-2 flights (Pueschel et al., 1994). Analysis of the 2014 Kelud plume also showed this partial overlap (Vernier et al., 2016).

Figure 6-4 also shows that whereas the sulfate aerosol layer is increasing in altitude slightly over time, continued upwelling from the tropics allows the ash layer to remain at around the same altitude. This suggests the slow sedimentation is offsetting the uplift from the slow tropical upwelling of the BDC.

The 30-day average per panel presented in Figure 6-4 allows an analysis of the changes in vertical distribution of the sulfate and ash. For the most part, the locations of the peak ash and sulfate burdens are seen at the same altitudes for all injection heights, overlapping primarily in the first month following the eruption. An average of 1 km difference in altitude for the peak ash and sulfate values is noticeable for the 18-20 km and 21-23 km injection heights (solid and dashed lines, respectively), with the 18-25 km (dot-dashed line) showing a slightly larger difference of 2-3 km between the peak ash and sulfate burden. A comparison of the northern and southern hemispheres also suggests that more of the sulfate and ash enters the northern hemisphere faster through lower injection heights, whereas the largest burdens appear from the 21-23 km injections in the southern hemisphere (0).

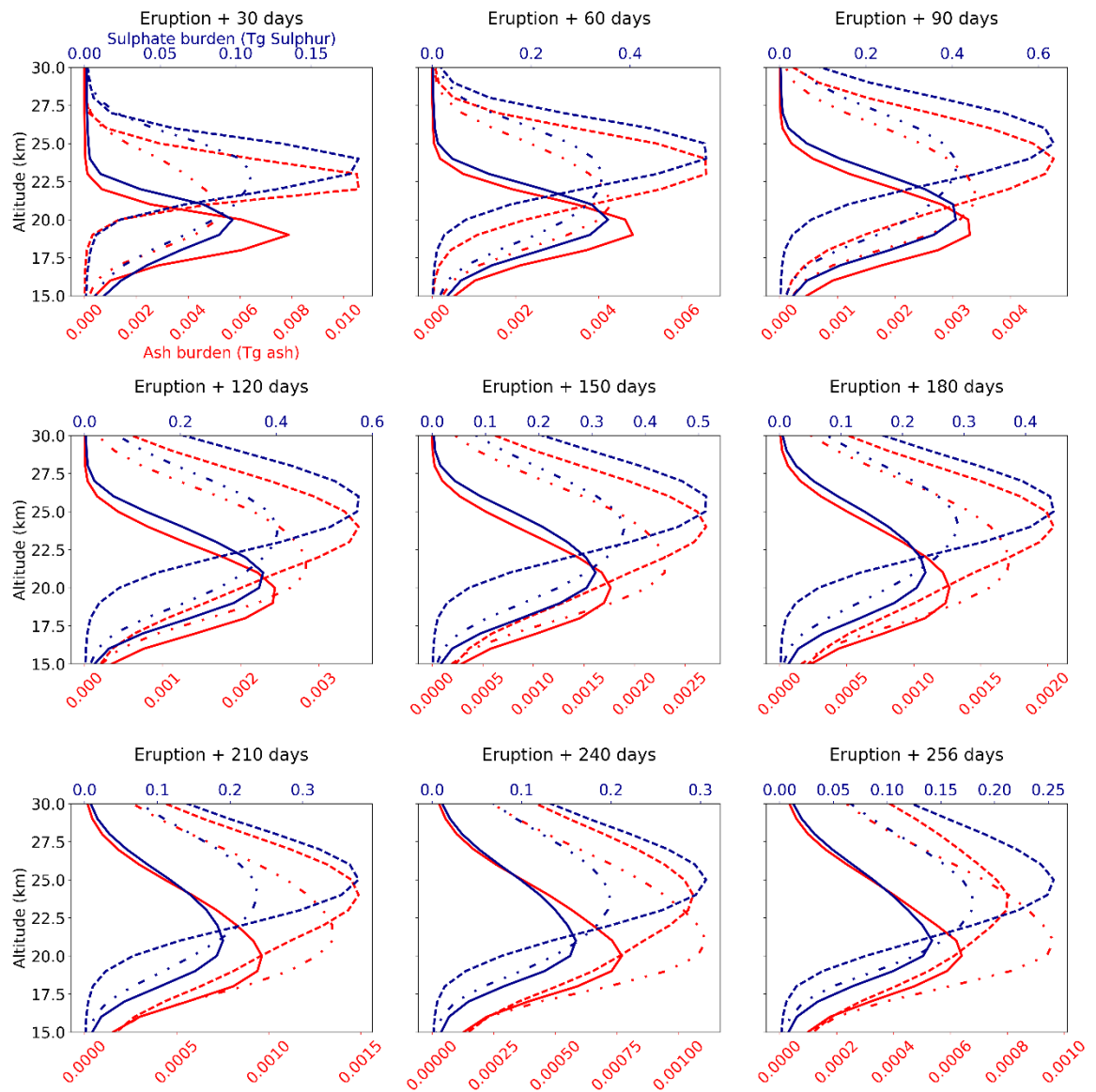


**Figure 6-4** Monthly average ash (red) and sulfate (blue) burden for the tropics (20°S-20°N) for a 14 Tg SO<sub>2</sub> and 0.05 Tg ash injection mass at 18-20 km (solid lines), 21-23 km (dashed lines) and 18-25 km (dot-dashed line).

## 6.5 Impact of ultra-fine ash on optical depth from the Mount Pinatubo cloud

This section explores the impact the co-emitted ultra-fine ash particles have on the Mount Pinatubo cloud, focussing on differences in mid-visible SAOD (550 nm) from the Chapter 5 simulations that did not include ash. The analysis compares model simulated SAOD values with monthly mean datasets of measurements from the AVHRR instrument on the NOAA-11 satellite and the GloSSAC dataset, used to enact Mount Pinatubo forcing in CMIP6. Figures of SAOD are organised based on mass of SO<sub>2</sub> and latitudinal variation, focussing on the tropical (20°S-20°N), midlatitude (60°S-

60°N) and northern (20-60°N) and southern (20-60°S) hemisphere midlatitudes. The solid lines in the figures denote ash-interactive simulations and the dotted lines denote simulations without ash (i.e. the HErSEA ensemble of simulations analysed in Chapter 5). Black lines denote the monthly-mean AVHRR observations and black lines with yellow stars denote monthly-mean GloSSAC data.

For this analysis, the focus is primarily on the difference between the new ash-interacting simulations and the no-ash simulations from Chapter 5, across the Mount Pinatubo HErSEA ensemble. Changes caused by ultra-fine ash in the tropics will impact what is predicted in the mid-latitudes, for example if ultra-fine ash causes a reduction from scavenging in the tropical SAOD, this will reduce SAOD values in the mid-latitudes. If the ultra-fine ash introduced a heating effect, however, greater export from the tropics to mid-latitudes may occur, therefore decreasing tropical SAOD and increasing mid-latitude SAOD. Hence, an assessment of the impact of ultra-fine ash on the tropics (20°S-20°N), mid-latitudes (60°S-60°N) and the mid-latitudes of each hemisphere (20-60°S and 20-60°N) is presented.

### 6.5.1 Tropical SAOD variation

In the tropics, as with Chapter 5, the model data for all simulations show an initial increase in SAOD up to the maximum SAOD, followed by a decay phase. All model simulations have roughly the same timescale decay as in the AVHRR observations, the GloSSAC dataset showing a different variation temporally. The peak SAOD again depends primarily on the magnitude of the injected mass of SO<sub>2</sub> (Figure 6-5), as in Chapter 5. A more in-depth description of the comparison between the no-ash simulations and the measurements is given in Chapter 5, with this section focussing on differences between the no-ash and ash-interactive simulations.

The 10\_lowalt\_ash and 10\_lowalt model data agree with the GloSSAC data in early 1992, but overall agree best with AVHRR data. The GloSSAC data has a far greater e-folding time than AVHRR (20.2 and 6.6 months, respectively). The model simulated SAOD e-folding timescale for the 10-20 Tg eruption clouds vary between 5.50 and 8.63, in all cases agreeing with tropical AVHRR values, much lower than those derived from GloSSAC.

Of the three injection masses of SO<sub>2</sub>, the 10 Tg model simulations either with or without ash agree best with observations, with the 10\_midalt\_ash matching the peak

almost identically with SAOD of  $\sim 0.325$  (Figure 6-5a). All 14 Tg and 20 Tg cases agree with observational values until August 1991; however, they generally produce SAOD values that are too large in comparison to observations from August 1991 onwards (maximum values of 0.45 and 0.63 for 14\_deepalt\_ash and 20\_deepalt\_ash, respectively). The 14\_lowalt\_ash and 14\_lowalt (Figure 6-5b) also agree with AVHRR from December 1991 onwards (0.21, 0.19 and 0.15 for December 1991, January and February 1992, respectively). GloSSAC values are lower than model SAOD from June 1991-February 1992 in all 14 Tg and 20 Tg simulations, particularly in the 20 Tg case where GloSSAC values are lower by up to 0.45.

When comparing between injection heights, irrespective of ash or no ash, the 10 Tg and 20 Tg simulations show 18-20 km with lowest SAOD values, followed by 21-23 km and 18-25 km (Figure 6-5a and c), however, in the 14 Tg case the 21-23 km injection height simulations overtake the 18-25 km from November 1991 onwards (Figure 6-5b). The 21-23 km and 18-25 km simulations also show similar peak values for the 10 Tg and 14 Tg cases, but 21-23 km simulations have 0.05 lower SAOD values in the 20 Tg case.

Considering the 10 Tg Mount Pinatubo cloud simulations (Figure 6-5a) the model predicts the ultra-fine ash has a significant effect on peak SAOD values only in the low-altitude injection cases. The 10\_lowalt\_ash simulation shows peak SAOD values  $\sim 10\%$  lower than in the 10\_lowalt simulation (0.18 compared to 0.2 in November 1991). In contrast, the ultra-fine ash has no effect on the peak SAOD for the 10\_deepalt case. It is interesting to note, however, that the ultra-fine ash does have a substantial effect on 10\_deepalt later in the simulation, with the influence being to increase the tropical SAOD rather than decrease it, with 25% higher SAOD values - 0.17 compared to 0.14 in February 1992. A lower peak SAOD occurs most significantly when  $\text{SO}_2$  is injected near the tropopause, likely due to the sub-tropical pipe being weaker in the lowermost stratosphere (Holton et al., 1995) with significant potential to export aerosol to mid-latitudes (see discussion in Chapter 5 and Chapter 2).

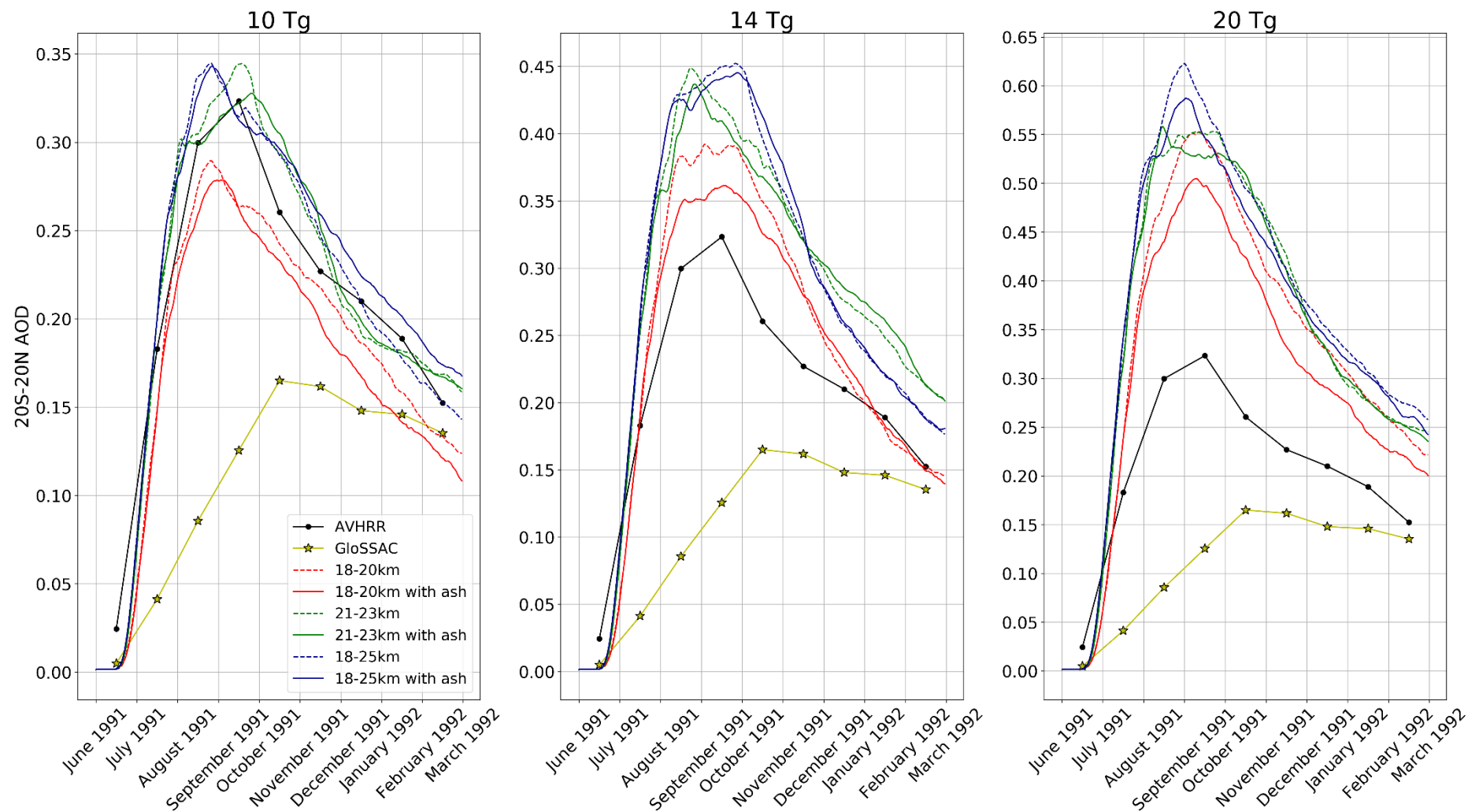


Figure 6-5 SAOD for the tropics in all injection height scenarios for (left) 10 Tg, (middle) 14 Tg and (right) 20 Tg. Solid lines are ash simulations and dashed are non-ash simulations, note the difference in scale on the y-axis.

Whereas the lower peak SAOD values for the ash-interactive simulations was only occurring for the case injecting closer to the tropopause in the 10 Tg simulations (10\_lowalt), a more consistent picture emerges for the 14 Tg and 20 Tg cases. The ultra-fine ash causes substantially lower peak SAOD values in all cases, the magnitude increasing proportionally with the increased injection of SO<sub>2</sub> mass (Table 6-2). Smaller relative increases are seen for the 21-23 km injection height simulations (green lines), consistent with altitude sensitivity seen in the 10 Tg simulations. For example, from October to mid November 1991 14\_lowalt\_ash, 14\_midalt\_ash and 14\_deepalt\_ash show higher (by 0.01-0.02) or equal values of SAOD compared to the non-ash simulations. Prior to November 1991 14\_lowalt\_ash, 14\_midalt\_ash and 14\_deepalt\_ash have consistently lower SAOD values than their non-ash equivalents (Figure 6-5b).

The effect the ultra-fine ash has on extending the lifetime of 10\_deepalt\_ash does not occur in any of the higher SO<sub>2</sub> emission cases (Figure 6-5b and Figure 6-5c). This single model simulation indicates that SO<sub>2</sub> oxidation proceeds quickly enough to interact with the ash before it separates from the sulfate cloud. In the other injection height cases the injection is more concentrated (2 km) and limited oxidation occurs.

Overall, these modest effects from the ultra-fine ash mean that each of the 10 Tg model simulations continue to agree well with the temporal variation of the AVHRR measurements, but are too high compared to GloSSAC, whereas 14 and 20 Tg model simulations produce higher SAOD values than observations suggest.

18-20 km injection heights show ash simulations having a lower SAOD in the tropics than their non-ash counterparts, whereas 21-23 km and 18-25 km injection heights produce different results depending on the mass of SO<sub>2</sub> emitted. The peak in the 21-23 km injection heights seems least consistent, particularly in the 10 and 20 Tg cases which both indicate a difference in the peak time of the ash and non-ash cases.

**Table 6-2 Reduction in peak SAOD between ash and non-ash simulations.**

	<b>10 Tg</b>	<b>14 Tg</b>	<b>20 Tg</b>
<b>18-20 km</b>	0.02	0.05	0.06
<b>21-23 km</b>	0.02	0.01	0.02
<b>18-25 km</b>	0	0.01	0.04

Peak differences of 0.01 are equivalent to variations in SAOD seen following the 2008 Kasatochi eruption (Andersson et al., 2015), for example, with differences from 0.02 - 0.04 equivalent to values seen in 1994 following the Rabaul eruption and differences of 0.05-0.06 equating to differences seen across the midlatitudes following the Mount Pinatubo eruption (Mills et al., 2016, Figure.4). The most significant differences in SAOD when including ash are for 14 Tg and 20 Tg with injection height 18-20 km, however all the differences seen indicate significant differences.

For this analysis of the influence of the ultra-fine ash particles on the Mount Pinatubo cloud, the focus is primarily on the difference between the new ash-interacting runs and the no-ash simulations from Chapter 5, across the different Pinatubo realisations in the HErSEA ensemble. Comparisons to the GloSSAC and AVHRR observations are discussed in chapter 5. One thing to take into consideration in the subsequent discussion, is that any change the ultra-fine ash causes in the tropics, will affect what is predicted in the mid-latitudes. For example, if the ash causes more removal of aerosol in the tropics, then less will be available to transport to mid-latitudes, the reduction in the tropics reducing mid-latitude SAOD. SAOD at 550 nm values reflect both aerosol mass and size distribution, therefore a modest SAOD change could also be caused by a change in size distribution (e.g. modified particle growth). If the ash enacts a substantial heating effect, then there could also be an increase of fresh (non-volcanic) air from the tropical troposphere, which would cause a change of opposite sign, with a decrease in tropical SAOD effecting an increase in mid-latitude SAOD due to greater export from the tropical reservoir.

### 6.5.2 Mid-latitude SAOD variation

In the mid-latitudes the maximum model simulated SAOD is around half the values seen in the tropics (0.16 and 0.35 for 10 Tg; 0.23 and 0.45 for 14 Tg; 0.30 to 0.62 for 20 Tg) (Figure 6-6). There is a similar pattern as in the tropics (Figure 6-5), whereby in both the ash and non-ash simulations, the 10 Tg (Figure 6-6a) simulations match closely with observations and the 14 and 20 Tg simulations give SAOD values that are mostly too high (Figure 6-6b and c). For example, peak SAOD for AVHRR is 0.18 in September 1991, whereas peak model SAOD is 0.23 and 0.30 for 14 and 20 Tg, respectively.

20 Tg has SAOD values far higher (0.3) than AVHRR values, though has a similar shape to AVHRR (Figure 6-6c). The 10 Tg simulations match AVHRR data closely

until September 1991. The GloSSAC data then shows lower values than all model simulations, with the exception of January 1992 where 10\_lowalt has similar values ~0.12. GloSSAC peaks at 0.12 in the midlatitudes, whereas AVHRR has an AOD of 0.18 in September 1991, which is higher than all 10 Tg model simulations.

As with the tropics, the 18-25 km simulation shows the highest SAOD values in the 10 Tg injection case, followed by the 21-23 km and 18-20 km simulations, respectively (Figure 6-6a). However, for the 14 and 20 Tg cases the peak 18-20 km SAOD values are higher (0.21 and 0.28, respectively) than those for the 21-23 km SAOD values (0.20 and 0.27, respectively), with the 18-20 km SAOD values matching the shape of the AVHRR data best in both cases (Figure 6-6b and c).

Differences between the ash and non-ash cases are again non-linear following the peak of the SAOD. In the 10 and 20 Tg injections of SO<sub>2</sub> the 18-20 km and 18-25 km simulations peak and then decline, whereas the 21-23 km cases decline steeply after the peak and then plateau (Figure 6-6a and c). In the 14 Tg cases it appears that the 18-20 and 18-25 km injections heights decline more steeply than their 10 and 20 Tg counterparts and the 21-23 km simulation has a much more gradual decline (Figure 6-6b).

The injection heights themselves show interesting differences for ash and non-ash cases. 10\_lowalt\_ash and 20\_lowalt\_ash have higher SAOD values initially, but by November 1991 have lower SAOD values than their non-ash counterparts. In 10\_deepalt\_ash SAOD is lower at the peak and then by November has higher SAOD values than 10\_deepalt, whereas 20\_deepalt\_ash is largely equal to 20\_deepalt. 21-23 km simulations are variable between injection amounts.

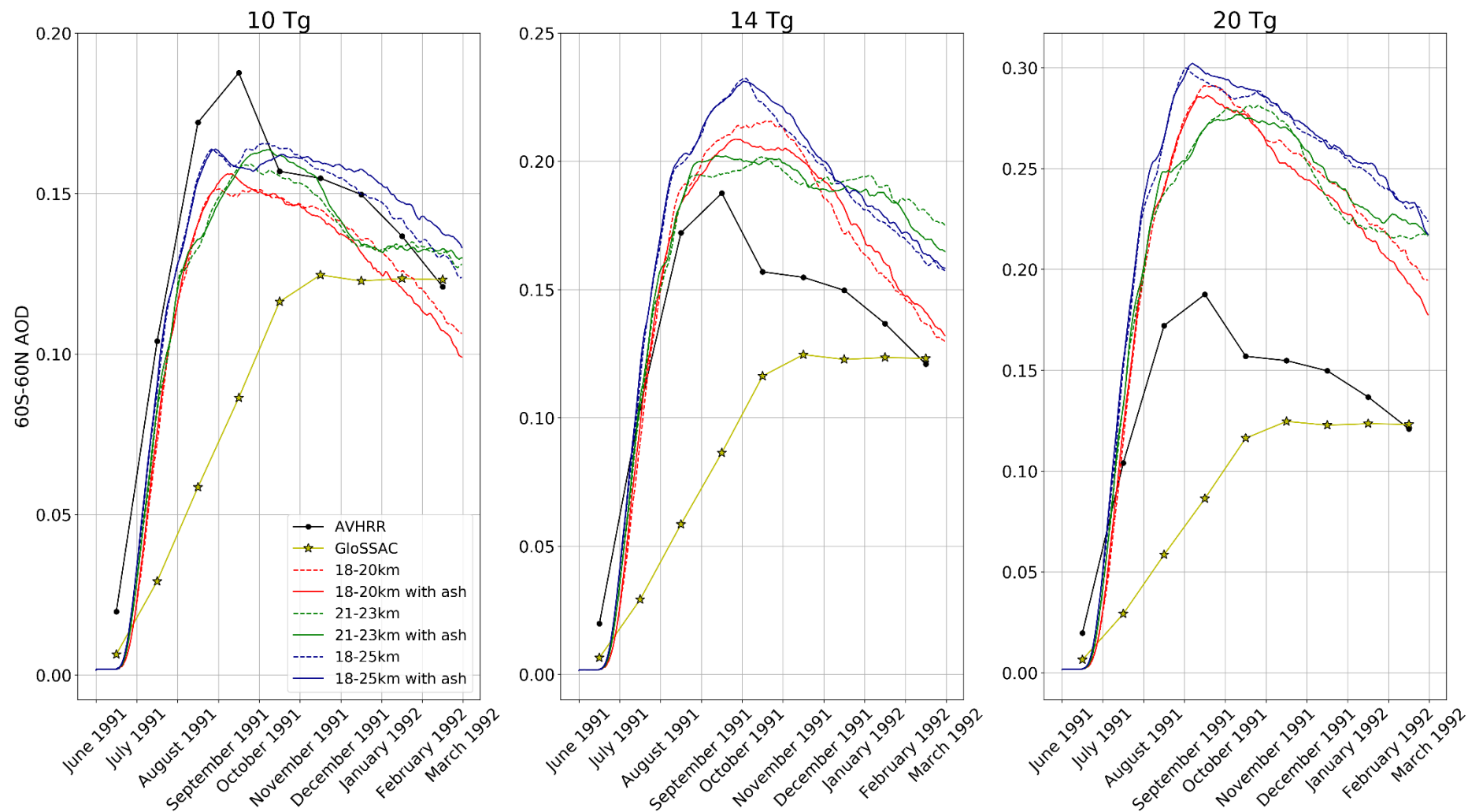


**Figure 6-6** SAOD for the midlatitudes (inclusive of the tropics) (60°S-60°N) in all injection height scenarios for a) 10 Tg, b) 14 Tg and c) 20 Tg. Solid lines are ash simulations and dashed are non-ash simulations, note the difference in scale on the y-axis.

For 10 and 14 Tg SO<sub>2</sub>, 10\_midalt\_ash and 14\_midalt\_ash have generally higher SAOD values between September and December 1991 before converging or showing values lower than 10\_midalt and 14\_midalt. In the 20 Tg case the 20\_midalt\_ash values are lower between September and December 1991 before showing higher values than 20\_midalt into the beginning of 1992.

Overall, the 10 Tg cases again match closely with AVHRR observations, however 14 Tg matches the AVHRR shape and agrees with AVHRR values until August 1991. The 20 Tg cases are all higher than observed values. There are differences between the ash and non-ash cases, however these all vary depending on the injection of SO<sub>2</sub>. 18-20 km injection heights show higher peak SAOD values than 21-23 km injection heights for 14 and 20 Tg SO<sub>2</sub>.

#### **6.5.2.1 Northern and southern hemisphere midlatitudes SAOD variation**

For the northern hemisphere, the trend of the SAOD data most closely matches with the GloSSAC data, with the AVHRR SAOD values lower than all model data from October 1991 onwards. The GloSSAC data matches closest with the 10\_midalt and 10\_midalt\_ash.

For 10 and 20 Tg SO<sub>2</sub> (Figure 6-7a and c) the ash inclusive simulations all have SAOD values higher than their non-ash counterparts by 0.03 on average, whereas for 14 Tg this is true for 18-20 km and most of 18-25 km, but the non-ash case shows higher SAOD from November onwards in the 21-23 km case by up to 0.04 in January 1992.

In the northern hemisphere, there is a noticeable contrast to the tropics and total midlatitudes, whereby the 18-20 km simulations have the highest SAOD values for the majority of the time period, followed by the 18-25 km and then the 21-23 km (Figure 6-7). The GloSSAC data for the northern hemisphere matches well with model data for 10 Tg simulations and AVHRR is broadly lower than model data in contrast to the tropics and mid-latitudes. Large differences between AVHRR and GloSSAC here are from no overpasses of AVHRR from 40-60°N from September 1991 to early 1992 (Long and Stowe, 1994).

In the southern hemisphere, the observed SAOD is much higher than the 10 and 14 Tg model SAOD, with observed peak values of 0.12 and 0.10 for AVHRR and GloSSAC, respectively and the highest model values peaking at 0.075 and 0.08 for 10\_midalt and

14\_midalt simulations, respectively. 20\_midalt broadly follows GloSSAC data and AVHRR values compare closely with 20\_midalt\_ash and 20\_deepalt\_ash (Figure 6-8c).

In contrast with the northern hemisphere, the southern hemisphere shows 21-23 km injection height SAOD values are highest, followed by 18-25 km and then 18-20 km. For 10 Tg and 14 Tg all non-ash simulations are higher than ash simulations, though 14 Tg at 21-23 km shows ash SAOD values higher by 0.01 in August and October 1991. 20 Tg cases are closest to observations in the southern hemisphere. In the 20 Tg simulations (Figure 6-8c) 20\_midalt is much higher with peak values of 0.14 and 0.17 for 20\_midalt\_ash and 20\_midalt, respectively. In contrast, 20\_deepalt\_ash is much higher than 20\_deepalt from September onwards by an average of 0.03. 20\_low alt and 20\_lowalt\_ash broadly match throughout the 20 Tg case, peaking at 0.07 in comparison to 0.12 and 0.10 for AVHRR and GloSSAC, respectively.

Overall, there are large differences in SAOD seen based on differences in amount of SO<sub>2</sub>, injection height, whether ash is included or not and latitude. 14\_midalt and 14\_midalt\_ash cases in the tropics and midlatitudes all show the largest SAOD from December 1991 until March 1992, but not in the 10 Tg or 20 Tg cases. Generally, the 10 Tg cases appear to match observations best, unless looking in either hemisphere separately, when some 10 Tg and 14 Tg cases match the GloSSAC data best. 20 Tg consistently appears too high in comparison to observations, except when looking in either hemisphere where specific times match either AVHRR or GloSSAC data. There does not appear to be a linear trend when adding ash to these particular model simulations, but ash does appear to impact SAOD values in all cases, primarily at the peaks in the tropics and in the mid-latitudes. The extent to which ash impacts on SAOD is small overall, however the largest differences can be seen when comparing between the northern and southern hemisphere midlatitudes, where SAOD appears to decrease in the southern hemisphere and increase in the northern hemisphere.

Errors associated with the observations should be noted, for example the lacking overpass for AVHRR from 40-60°N during September-December 1991 (Long and Stowe, 1994) and a random error of ~0.04 (Stowe et al., 1992). The GloSSAC data was produced in part as a gap-filling exercise for when SAGE II measurements were saturated during the Mount Pinatubo eruption, therefore underestimating SAOD values. GloSSAC is, therefore, a product of multiple instruments which all have their own associated errors and, particularly early months following the eruption should be viewed

with the potential for substantial error (Thomason et al., 2018). Sun photometers from the time, such as from America Samoa, do suggest a peak SAOD of 0.2 to as high as 0.3, though these will include tropospheric data (Dutton and Christy, 1992; Dutton et al., 1994; Russell et al., 1996).

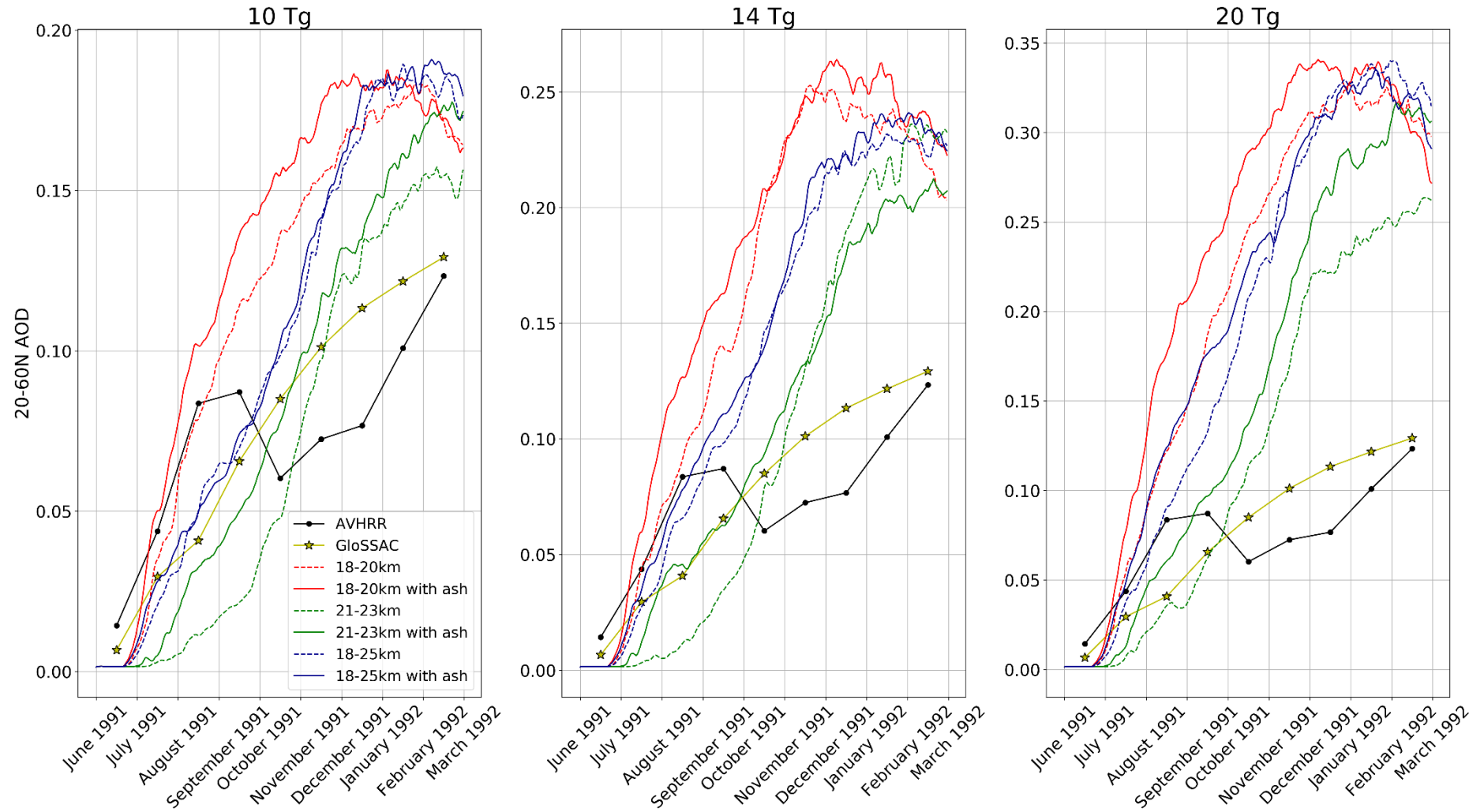


**Figure 6-7 SAOD for the northern hemisphere midlatitudes (20-60°N) in all injection height scenarios for a) 10 Tg, b) 14 Tg and c) 20 Tg. Solid lines are ash simulations and dashed are non-ash simulations, note the difference in scale on the y-axis.**

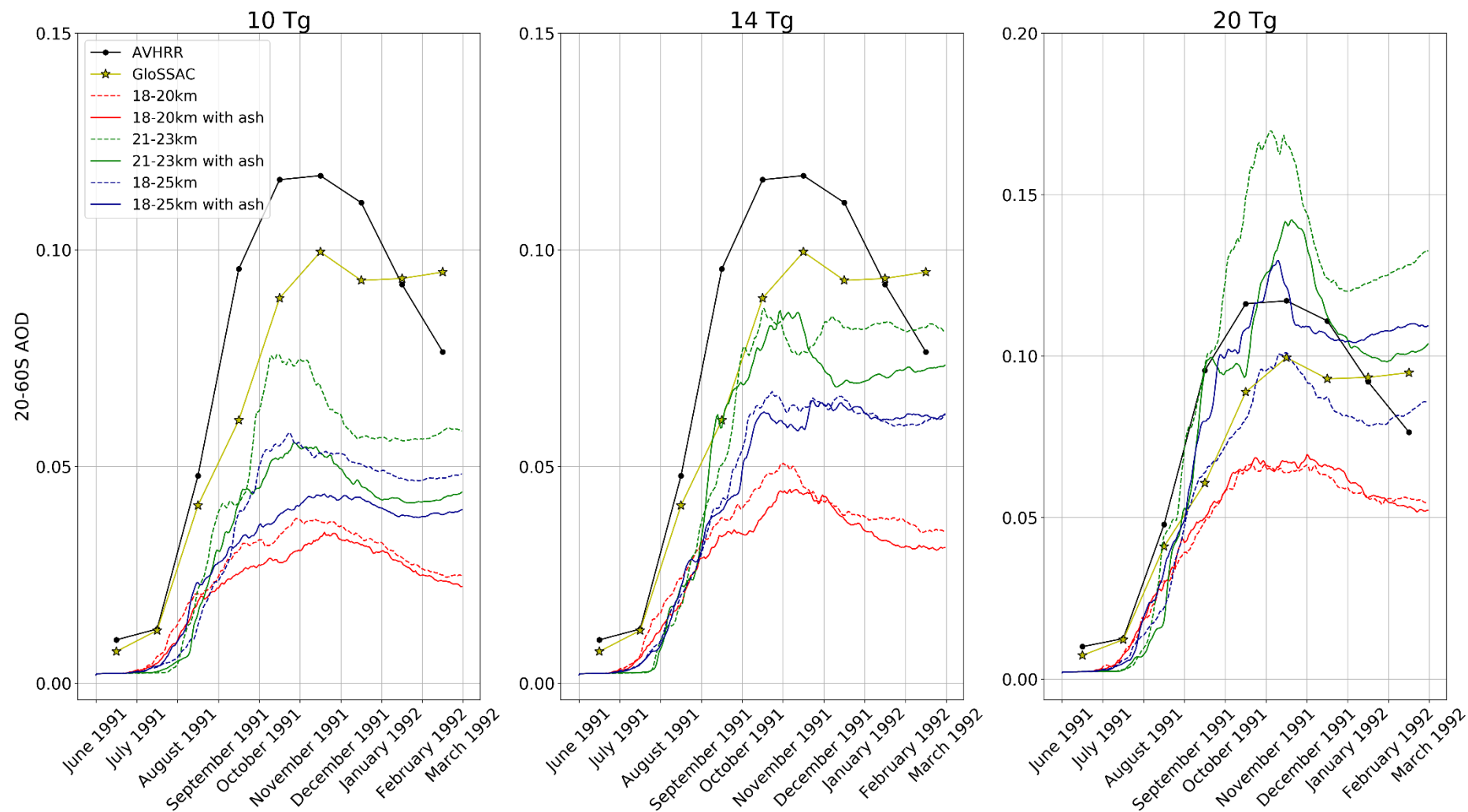


**Figure 6-8 SAOD for the southern hemisphere midlatitudes (20-60°S) in all injection height scenarios for a) 10 Tg, b) 14 Tg and c) 20 Tg. Solid lines are ash simulations and dashed are non-ash simulations, note the difference in scale on the y-axis.**

## 6.6 Sulfur burden

In order to present the differences in sulfur burden between Chapter 5 where there was no ash included in the simulations and this chapter where ash has been included, the sulfur burden has been presented in three separate plots to represent each different amount of SO<sub>2</sub> injected, with a dashed line representing Chapter 5 results and a solid line for the current results including ash (Figure 6-9 to Figure 6-11). The left-hand plot in each case indicates the burdens (in Tg of sulfur) for SO<sub>2</sub> (sulfur in the gas phase) and the right-hand plot for sulfate aerosol burden (particle phase) in each case, henceforth referred to as SO<sub>2</sub> burden and sulfate burden, respectively.

### 6.6.1 Tropical sulfur burden

Overall, the model captures the shape of the tropical sulfate burden during this time period (June 1991-February 1992) well in all cases. Baran and Foot (1994) measurements also clearly coincide with multiple model simulations at particular times, primarily 14\_deepalt and 14\_deepalt\_ash, with sulfate measurements too low in all the 10 Tg cases. The largest difference can be seen between the 20\_lowalt and 20\_lowalt\_ash simulations with a maximum difference of 0.6 Tg sulfur (Figure 6-11). The highest sulfate burden values of 3.5 Tg, 5 Tg and 6.5 Tg are seen in the 21-23 km 10 Tg, 14 Tg and 20 Tg cases, respectively, followed by the 18-25 km and 18-20 km injection heights for all SO<sub>2</sub> injections, respectively. In the tropics, all simulations that include ash show a clear decrease in peak sulfate burden from a minimum difference of 0.1 Tg to a maximum difference of 0.6 Tg at the peak burden (Figure 6-11), especially in the 14 and 20 Tg cases (Figure 6-10 to Figure 6-11). The SO<sub>2</sub> burden differences are less apparent; however, all ash-interactive cases show lower SO<sub>2</sub> burdens than their non-ash counterparts.

All model simulations follow a similar increase up towards the peak until August 1991 when the differences become apparent. In the 10 Tg case, the differences are less than for the other injections of SO<sub>2</sub>. The sulfate burden for 10\_midalt and 10\_midalt\_ash is almost identical. For the 18-25 km case 10\_deepalt\_ash shows a noticeable increase in the sulfate burden after the peak, which can also be seen in the 14\_midalt\_ash case. 10 Tg at 21-23 km, 14 Tg at 18-25 km and 20 Tg at 21-23 km all show the least differences between the inclusion and exclusion of ash. Table 6-3 outlines the maximum differences between all the model simulations in order of highest to lowest, showing

that the largest differences were mostly in the 20 Tg simulations and the smallest were in the 10 Tg simulations, with no real pattern seen with regards to injection height.

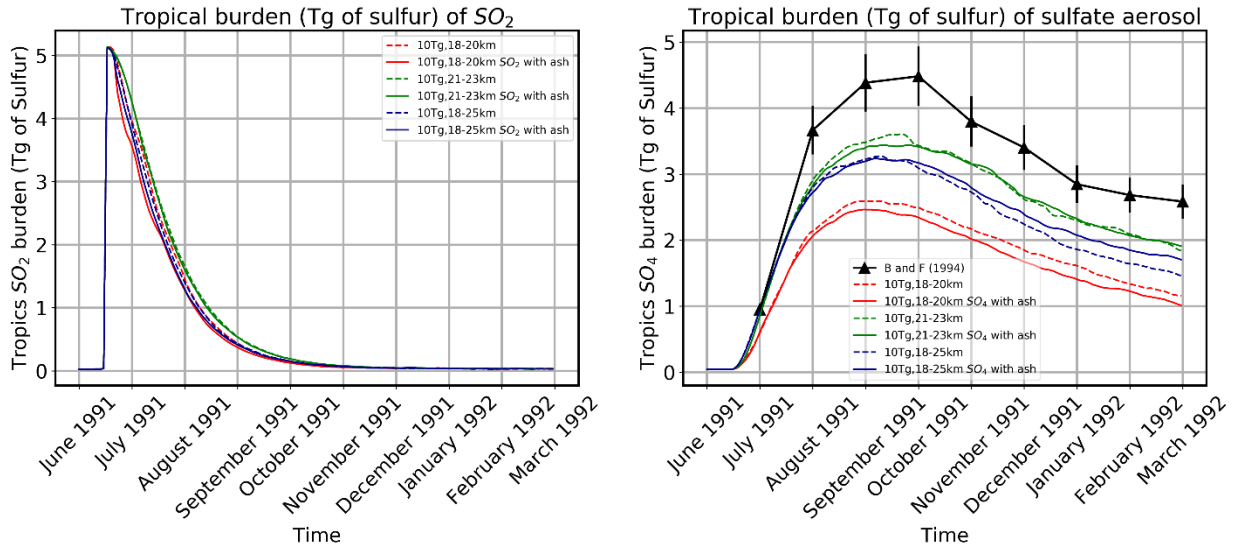


**Figure 6-9 Tropical (Left) SO<sub>2</sub> burden and (Right) SO<sub>4</sub> burden for 10 Tg ash (solid line) and non-ash (dashed) simulations.**

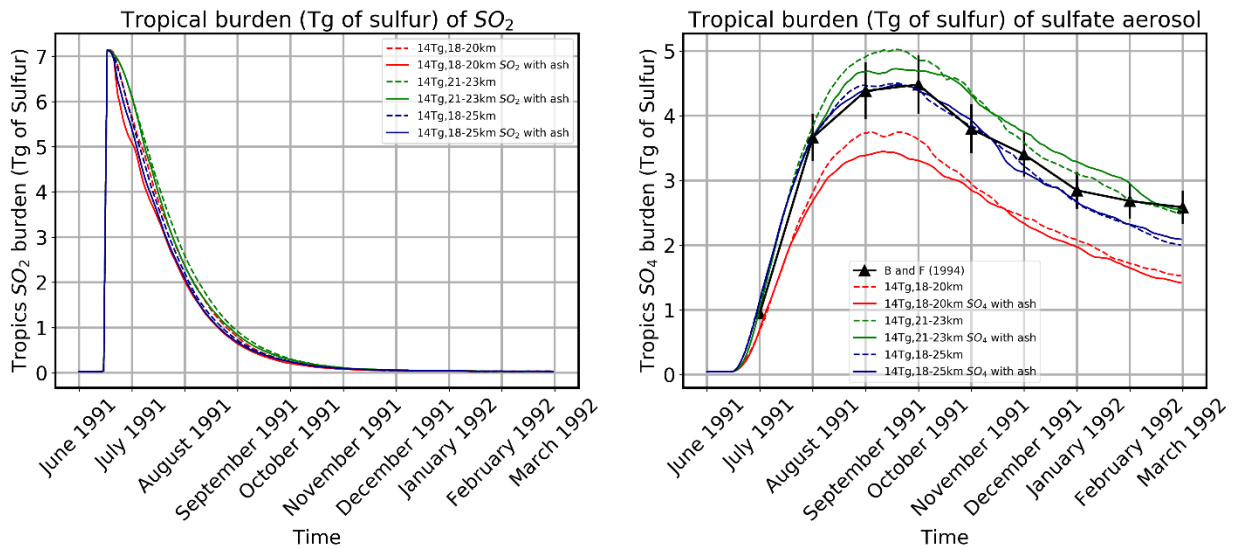


**Figure 6-10 Tropical (Left) SO<sub>2</sub> burden and (Right) SO<sub>4</sub> burden for 14 Tg ash (solid line) and non-ash (dashed) simulations.**

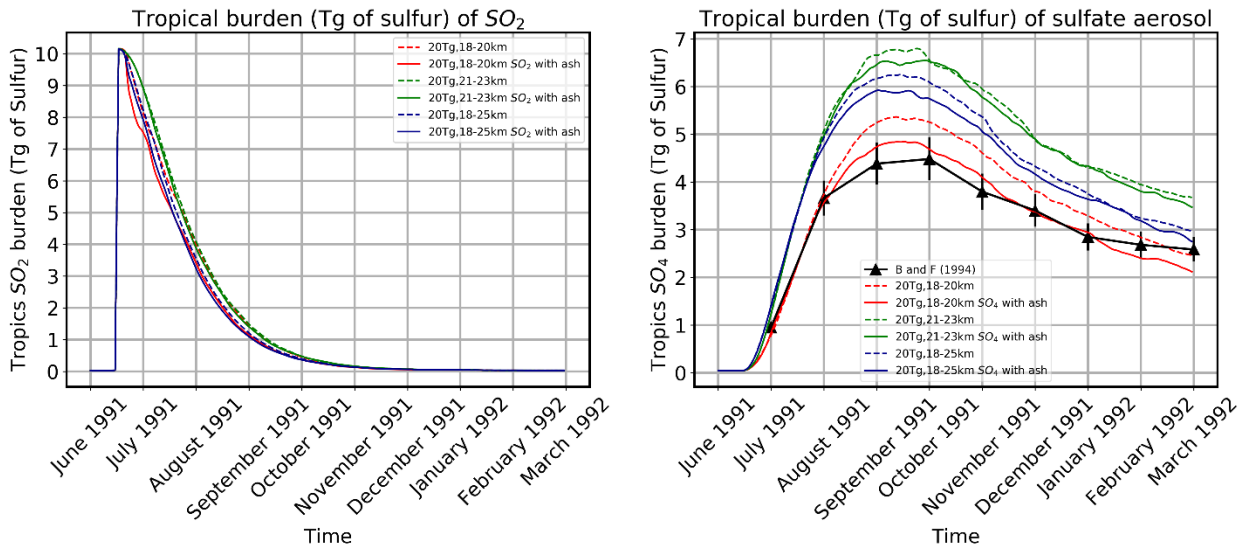


**Figure 6-11 Tropical (Left) SO<sub>2</sub> burden and (Right) SO<sub>4</sub> burden for 20 Tg ash (solid line) and non-ash (dashed) simulations.**

### 6.6.2 Global sulfur burden

On the global scale the differences in sulfate burden between model simulations with and without ash appear much smaller and the biggest differences can be seen in the 18-20 km cases then the 21-23 km and finally the 18-25 km cases (Figure 6-12 - Figure 6-14). The 18-20 km model simulations show the lowest sulfate values, followed by 21-23 km and then 18-25 km for all amounts of SO<sub>2</sub> injected.

When comparing to the measurements, the 10 Tg model simulations have far lower sulfate values than Baran and Foot (1994), with a maximum difference of 3.4 Tg. The 14 Tg values match well early on and into 1992, but have a maximum difference of 2.0 Tg at the peak seen in the measurements. In the 20 Tg case, again the early July-August 1991 values match well but then appear much higher than the observed values by 3.1 Tg in comparison with the 21-23 km case.

10\_lowalt\_ash, 14\_lowalt\_ash and 20\_lowalt\_ash all show a decrease in sulfate burden compared to their non-ash counterparts, with the smallest difference seen in the 10 Tg injection. In contrast, 18-25 km cases show the inclusion of ash yields slightly higher sulfate values (Figure 6-12 - Figure 6-14). In the 21-23 km cases, both including and excluding ash simulations equate to almost equal sulfate values in both cases, besides the 10 Tg case where the ash-inclusive sulfur burden is slightly higher (Figure 6-12).

**Table 6-3 Maximum differences in Tg of sulfur in the tropical and global sulfate burden between non-ash and ash simulations in order of highest to lowest difference**

<b>Model simulation</b>	<b>Tropics</b> <b>Maximum difference in SO<sub>4</sub></b> <b>between simulations with and</b> <b>without ash (Tg sulfur)</b>
20 Tg, 18-20 km	0.60
20 Tg, 18-25 km	0.42
14 Tg, 18-20 km	0.38
14 Tg, 21-23 km	0.35
20 Tg, 21-23 km	0.32
10 Tg, 18-20 km	0.21
14 Tg, 18-25 km	0.20
10 Tg, 21-23 km	0.18
10 Tg, 18-25 km	0.10
<b>Model simulation</b>	<b>Globally</b> <b>Maximum difference in SO<sub>4</sub></b> <b>between simulations with and</b> <b>without ash (Tg sulfur)</b>
20 Tg, 18-20km	0.36
14 Tg, 18-20 km	0.26
14 Tg, 21-23 km	0.13
20 Tg, 21-23 km	0.09
10 Tg, 18-20 km	0.05
14 Tg, 18-25 km	0.01
10 Tg, 18-25 km	0.01
20 Tg, 18-25 km	-0.0002
10 Tg, 21-23 km	-0.0002

Investigating the northern and southern hemisphere burdens consistently shows higher sulfate burdens when ash is included for the northern hemisphere, and the opposite for the southern hemisphere.

The differences outlined in Table 6-3 show that changes in sulfate aerosol burden indicate that the largest differences in the tropics are broadly seen in the same simulations globally (i.e. for the same mass of SO<sub>2</sub> injected and injection height.), with the exception of the 20 Tg 18-25 km simulations, as this shows the second highest difference in the tropics and the second lowest globally. The values seen in Table 6-3 are most significant in the tropics, as shown by the larger differences between the simulations with and without ash, with values between 0.3 and 0.5 Tg equating to

similar increases in simulated sulfate aerosol mass following the Kasatochi eruption in 2008 (0.5 Tg), Redoubt eruption in 2009 (0.4 Tg) and Nabro in 2011 (0.3 Tg) (Mills et al., 2016).

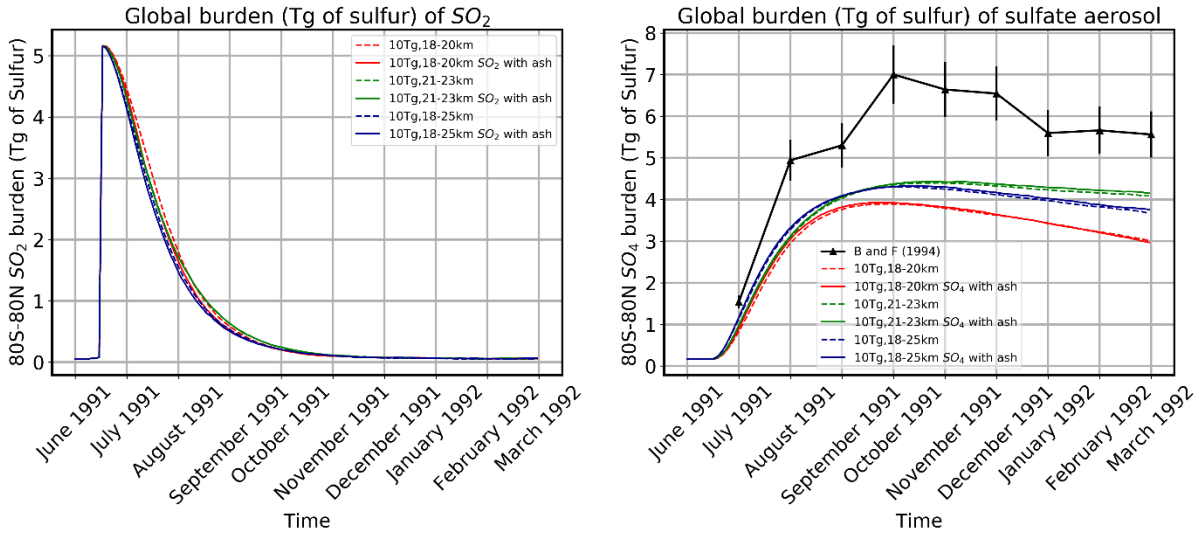


**Figure 6-12 Global sulfur burden for (left) SO<sub>2</sub> gas-phase sulfur and (right) sulfate aerosol for 10 Tg injected SO<sub>2</sub> at all injection heights comparing with and without ash.**

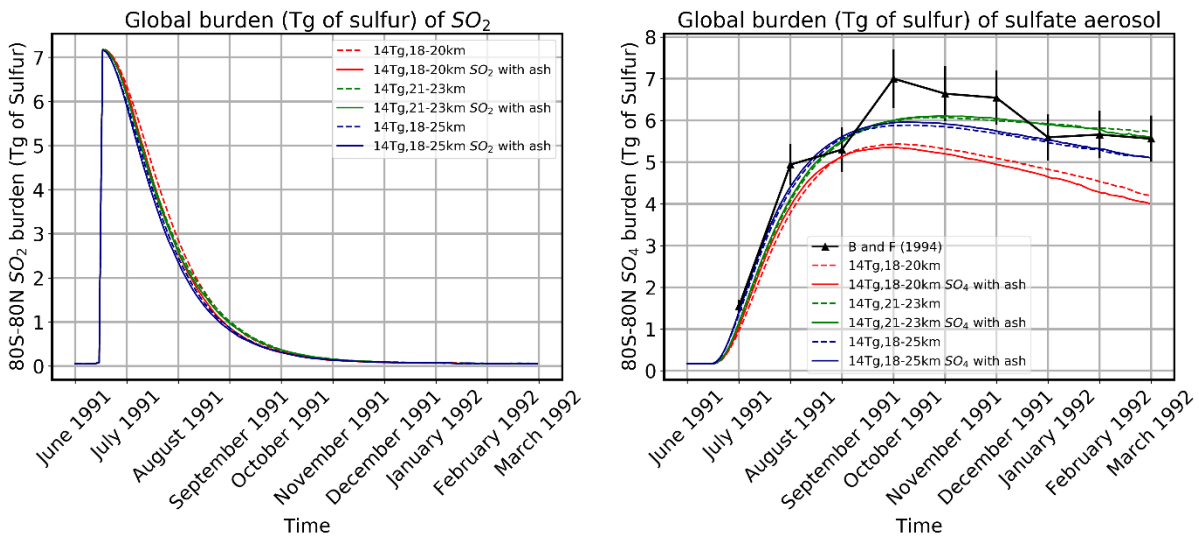


**Figure 6-13 Global sulfur burden for (left) SO<sub>2</sub> gas-phase sulfur and (right) sulfate aerosol for 14 Tg injected SO<sub>2</sub> at all injection heights comparing with and without ash.**

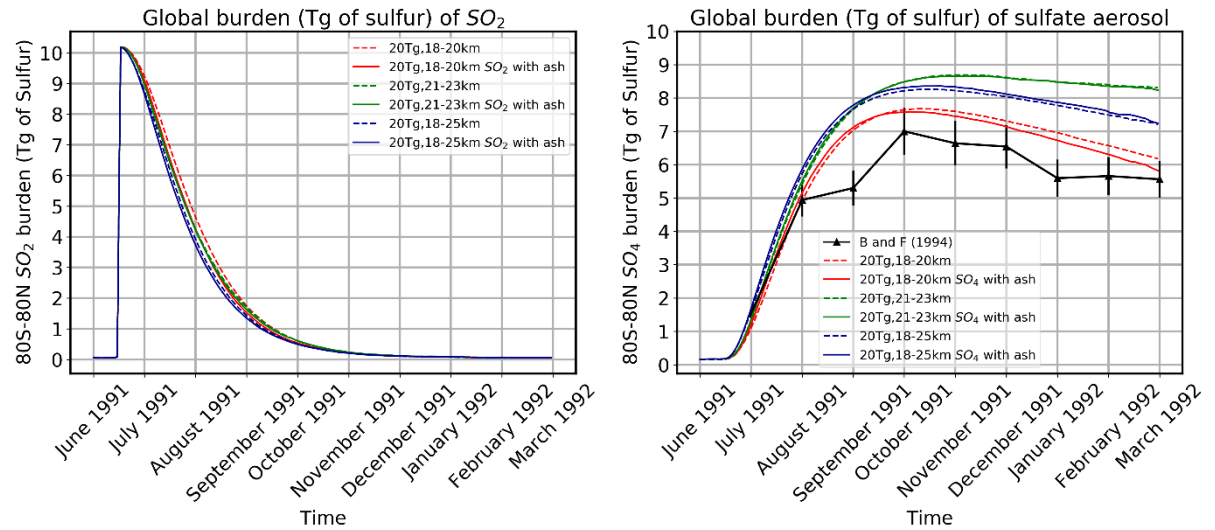


**Figure 6-14** Global sulfur burden for (left)  $\text{SO}_2$  gas-phase sulfur and (right) sulfate aerosol for 20 Tg injected  $\text{SO}_2$  at all injection heights comparing with and without ash.

## 6.7 Vertical profile of aerosol extinction

This section outlines the changes in vertical dispersion of extinction over time caused by the inclusion of ash in all cases outlined in Chapter 5. 14 Tg injection height comparisons with observations are shown in this chapter. All other comparisons with 10 Tg of  $\text{SO}_2$  are outlined in 0, as 20 Tg simulations all produce clouds 11-13 km higher than observations and the 14 Tg simulations all follow the same spatio-temporal patterns of the 10 Tg simulations (0) with slightly higher extinction values (1.5-2 times higher on average).

In the case for 14\_midalt there are distinct layers seen at MLO (Figure 6-15b), with a tail in the first layer, as well as the second and third layers similar to those seen in the lidar observations. The peak of the first layer is at 25 km which is also the same as seen in the lidar, however, the second and third layers reach 27 and 29 km which is 2-3 km higher than those in the observations. The bulk of the cloud in the later months is between 19 and 28 km, similar to the observations, though the upper part of the aerosol cloud is still too high, with a shallowing cloud is noticeable in the model from December 1991 onwards, also noted in the observations. The addition of ash brings the model extinction values closer to the observational extinction values, which are  $>0.05$ , especially at the beginning of the first layer. More obvious trailing tails on each of the layers are also seen in the ash-interactive simulations in all cases, reaching altitudes  $\sim 18$  km which is closer to observations than the simulations without ash. Slightly thicker

layers by  $\sim 0.5$  km can be seen with the addition of ash, but no significant additional height to the overall cloud aside from a slight increase in the height of the third layer from 29.5 km to 30 km.

As seen in Chapter 5, 14\_lowalt\_ash shows a very different pattern to those seen in the observations and the cloud remains confined to lower altitudes between tropopause values and a maximum of  $\sim 25$  km for all  $\text{SO}_2$  injection masses (Figure 6-16). In the ash-interactive cases, a noticeable minor layer structure is seen at the beginning of July, the end of July and the latter part of August at altitudes of 22, 24 and 25 km, respectively, similar to the timings of the layers for the lidar observations (Figure 6-16).

The 14\_deepalt\_ash simulation also shows a difference to the patterns seen in Chapter 5 (Figure 6-17). In Chapter 5 there was a structure  $\sim 18$ -20 km noted with layers noticeable above these, however, with ash there seem to be more noticeable layers that are longer and thicker than those seen before with the first layer from July 1<sup>st</sup> to 28<sup>th</sup> August 1991 at 24.5 km to 17 km matching almost identically with that seen at MLO (Figure 6-16). Largely, values of extinction in the 14 and 20 Tg simulations are around the same as those seen in the observations, but the 10 Tg simulation are slightly lower.

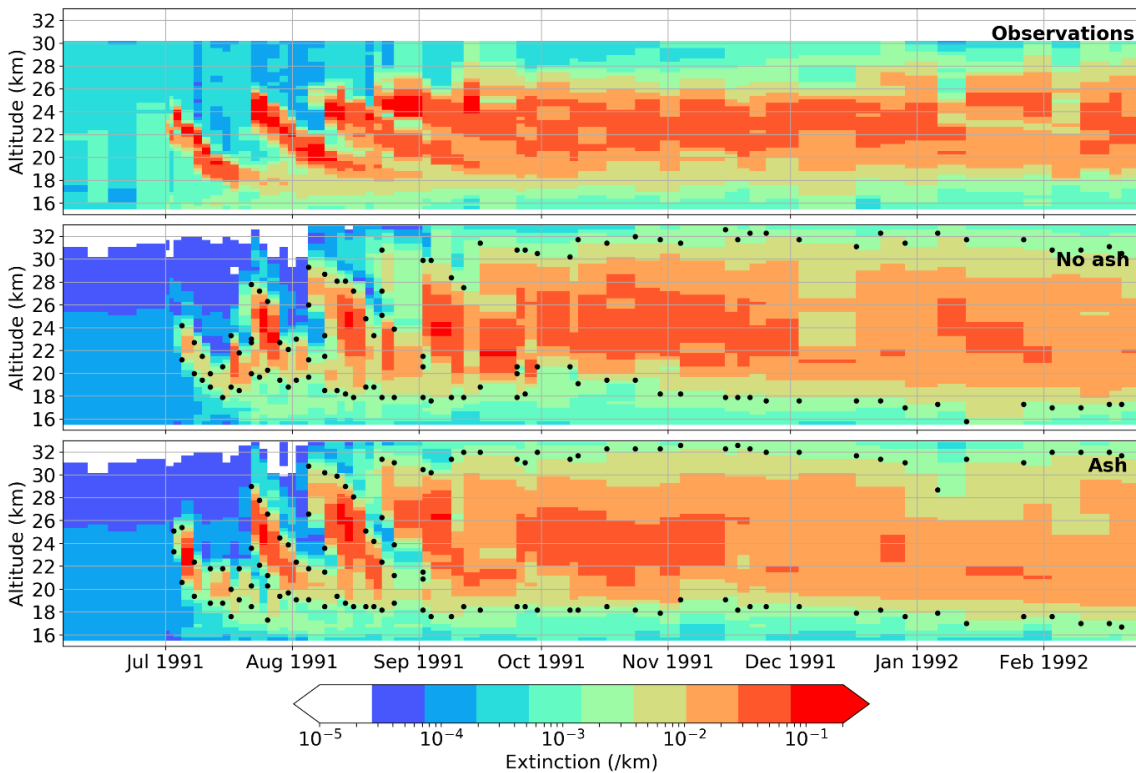


**Figure 6-15** Extinction plots for MLO with 14 Tg  $\text{SO}_2$  and 21-23 km injection height. Plots show observations (top), no ash (middle) and with ash (bottom). Black dots denote where layers are picked out from the layer finding algorithm.

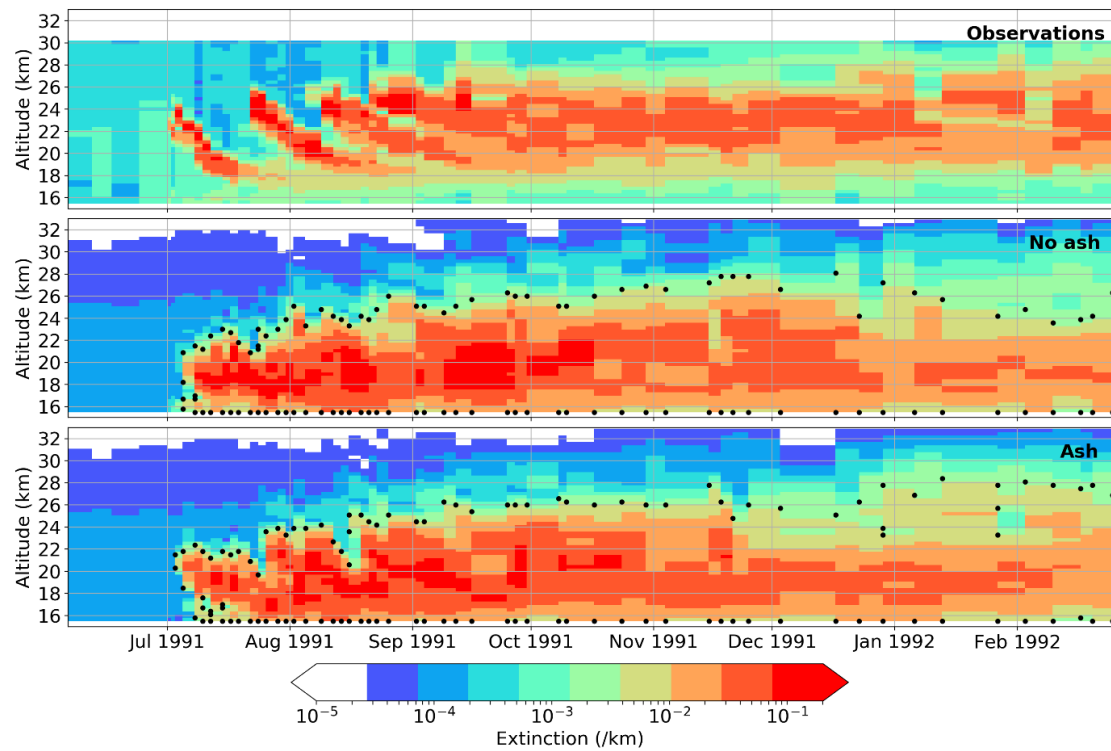


**Figure 6-16** Extinction plots for MLO with 14 Tg SO<sub>2</sub> and 18-20 km injection height. Plots show observations (top), no ash (middle) and with ash (bottom). Black dots denote where layers are picked out from the layer finding algorithm.

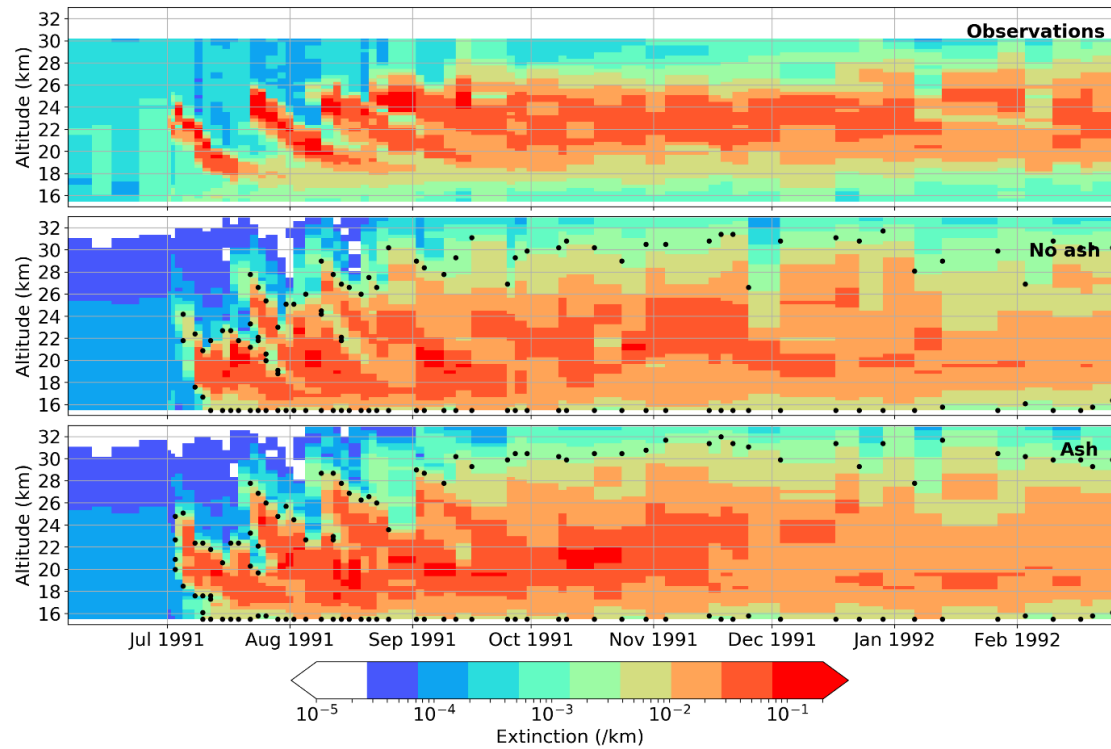


**Figure 6-17** Extinction plots for MLO with 14 Tg SO<sub>2</sub> and 18-25 km injection height. Plots show observations (top), no ash (middle) and with ash (bottom). Black dots denote where layers are picked out from the layer finding algorithm.

The upper parts of the cloud are still too high in the model (by ~2km compared to the lidar) in the 21-23 km and 18-25 km cases both with and without ash, but broadly the correct height in the 18-20 km cases.

At the mid-latitude sites, the 14\_midalt\_ash simulation matches well with the timings of the cloud being seen at these lidar sites and shows only minor differences in extinction values (Figure 6-18). A direct comparison between the ash and non-ash simulation, however, show minor differences, for example at TAB the inclusion of ash shows an earlier detection of the volcanic aerosol in late August 1991, at the same time as the observations (Figure 6-18). The same is true for OHP (Figure 6-19), however the overall cloud in the later months is thicker than in the observations, with the area of the cloud with the highest extinction values showing a deeper cloud by 4 km in the model simulation (9 km in the model simulation, 5 km in the observations). TOR shows little difference between non-ash and ash, besides a slight increase in extinction values in October-November 1991 (not shown here).

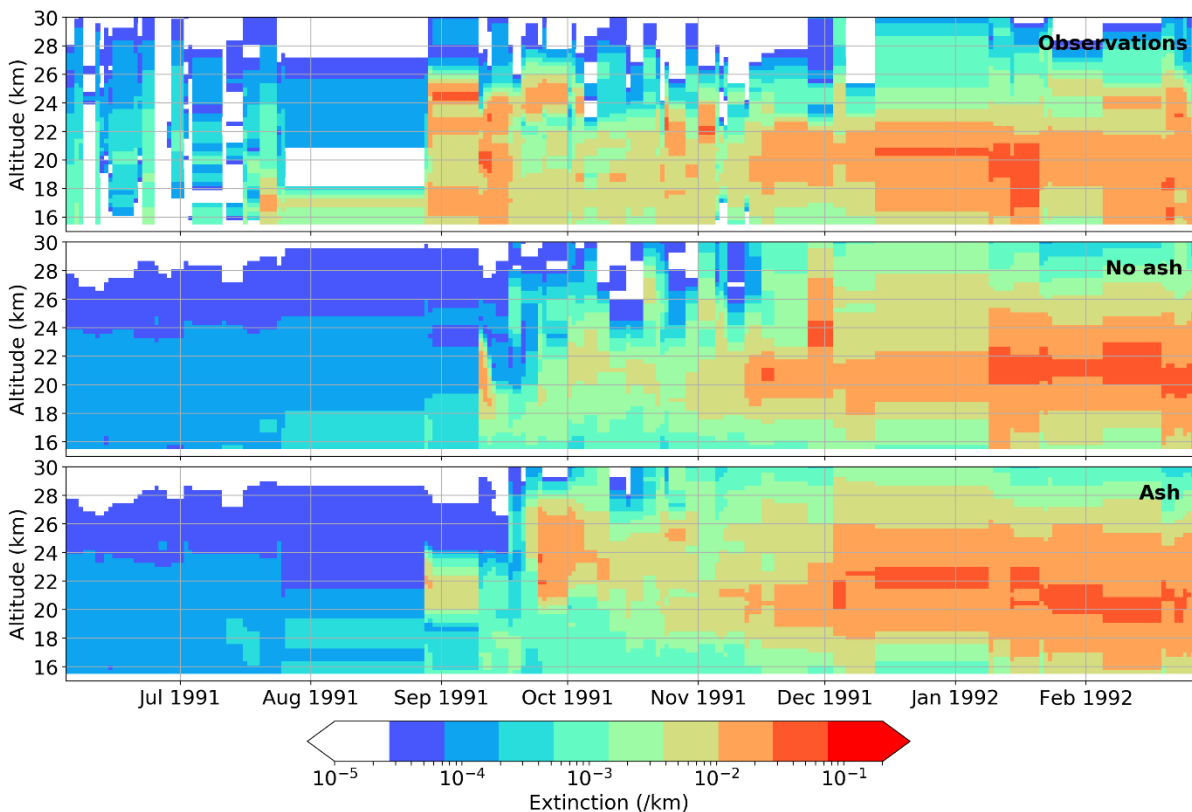


**Figure 6-18** Extinction plots for TAB with 14 Tg SO<sub>2</sub> and 21-23 km injection height. Plots show observations (top), no ash (middle) and with ash (bottom).

In the 21-23 km instance for the northern hemisphere, the 10 Tg simulation has slightly delayed timings, for example the bulk of the cloud does not reach OHP until December 1991, a month later than seen in observations, though modelled extinction values are closer to observed values. The 20 Tg comparison shows fairly well-matched initial values of extinction for MLO ( $>0.1$  ~25 km in the layers), but a cloud ~5 km too high from late September onwards and values too high for all the other sites, ~0.09 at all northern hemisphere sites from December 1991 onwards. In all 18-20 and 18-25 km cases the timing for the northern hemisphere is too early, with the earliest detection at OHP seen before that at MLO (0).

As noted in Chapter 3 there is ~10% error associated with converting between backscatter ratio and extinction plus any error associated with averaging over 5 km intervals and general instrument error (Jäger and Deshler, 2002; 2003), therefore these errors should be considered when noting changes in extinction values due to ash and subsequent comparisons to observations.

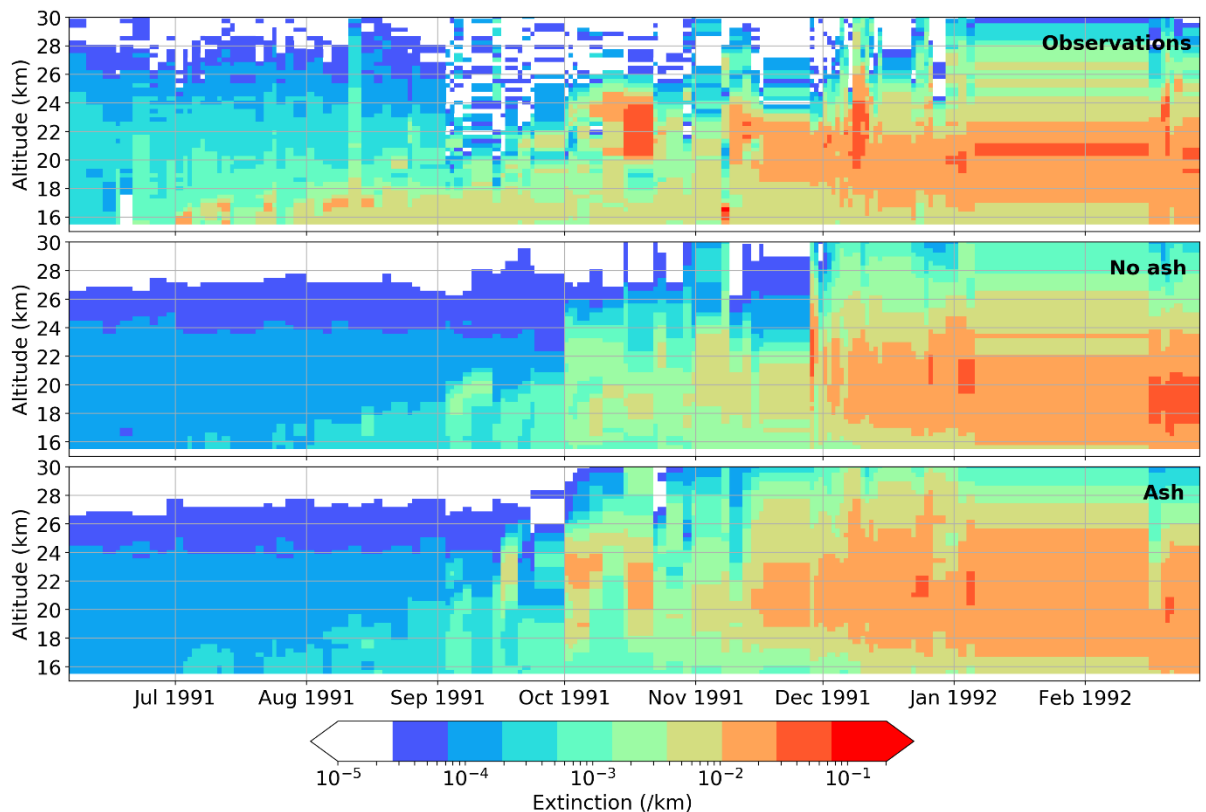


**Figure 6-19** Extinction plots for OHP with 14 Tg SO<sub>2</sub> and 21-23 km injection height. Plots show observations (top), no ash (middle) and with ash (bottom).

In summary, the 21-23 km injection height best matches the timing of the aerosol detection at each of the sites from near-tropics to the mid-latitudes, as the 18-20 km and 18-25 km injection heights both create a low-altitude area of aerosol at much higher extinction values at each of the mid-latitude sites than seen in the observations. The inclusion of ash for the 21-23 km injection height brings extinction values from the model and the overall shapes of the vertical cloud closer to those seen in the observations. The ash appears to cause a slightly earlier dispersion to the northern hemisphere in the 21-23 km cases creating a better match with observations. Earlier northern hemisphere detection occurs too in the 18-20 km cases, mostly at TOR and OHP and in all cases the northern hemisphere sees higher extinction values and the top of the aerosol cloud is lifted in the ash-containing cases.

### 6.7.1 Aberystwyth depolarisation and model data comparison

Depolarisation data from Aberystwyth (52.4°N) from September 1991 until March 1992 (Vaughan et al., 1994) is a useful test case for this study as it lies directly in the time period looked at and allows the investigation of ash in the midlatitudes. As the model does not output depolarisation data a proxy, termed “ash ratio”, was created by dividing the total amount of ash burden by the sum of the ash and the sulfate burden. The layer finding algorithm was also applied here in order to assess the cloud depth of the ash ratios found in each of the model simulations. Error associated with these depolarisation ratios is ~7% before October 1991 and ~5% after October 1991, primarily associated with vertical density profiles, assessed using ozonesonde and radiosonde measurements (Vaughan et al., 1994).

Figure 6-20 shows the backscatter ratio and depolarisation data, as presented in Vaughan et al. (1994), by denoting depolarisation values >1.4% as non-spherical with each colour denoting a 0.5% interval increase, whereby lighter colours show higher depolarisation values and, therefore, an increase in non-spherical particles relative to background levels and spherical particles. The top row of Figure 6-20 shows that the 10\_lowalt\_ash simulation has a similar pattern to that seen in the Aberystwyth observations. The highest ash ratios are centred around 15 km, whereas they lie between 17.5 and 21 km in the observations, however the overall decreasing trend of the model data shows a good match. The right-hand plot shows a contrasting model simulation for 14\_midalt\_ash which indicates the highest levels of ash are between 10 and 17 km and there is no evidence for the higher ash layers ~20 km as seen in

observations around the middle of September 1991. The cloud layer plots below these contour plots outline these features, as the 10\_lowalt\_ash plot shows evidence for the correct timing and overall depth of the observations, but lower overall heights. The 14\_midalt\_ash plot indicates later values of high ash ratio and much deeper layers of these higher ratios. The pattern seen in all model simulations indicates that the model shows the ash at lower heights over Aberystwyth than seen in observations. It should be acknowledged that 4% depolarisation is still very small and may not be conclusive of an ash layer, as this may be related to instrument error and leakage between channels in the lidar (Russell et al., 1979; Vaughan et al., 1994).

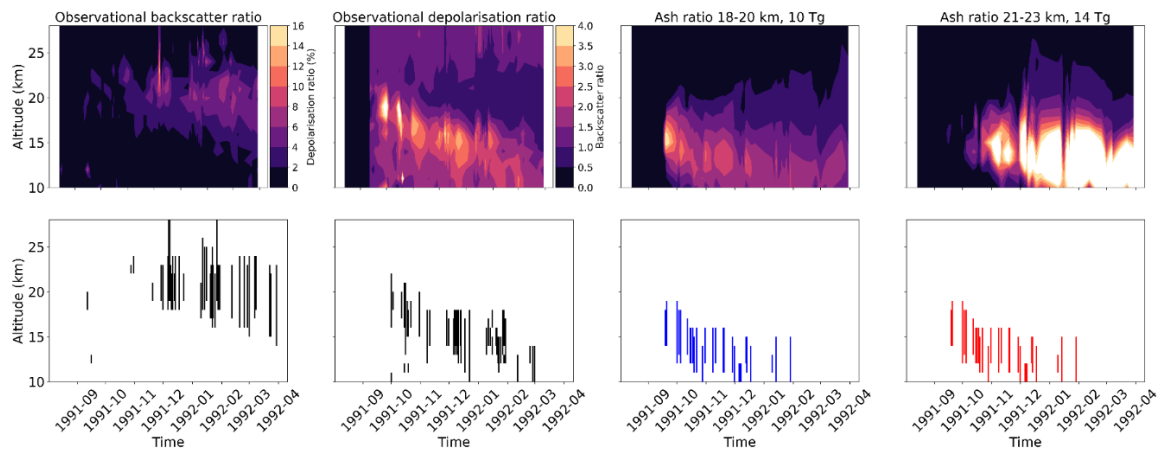


**Figure 6-20 (Top) Contour plots of backscatter ratio and depolarisation data from Aberystwyth compared to ash ratio model data in 2 scenarios, (bottom) depth of cloud from the layer finding algorithm for observations and the same 2 model scenarios from the top row.**

## 6.8 Ash-core sulfate particles

The following section outlines the amount of condensation that occurred of sulfate aerosol onto ash particles and an assessment of the effective radius for each model simulation.

Figure 6-21 shows the values of condensed sulfate aerosol condensed onto ash for every model simulation containing ash. There is a clear pattern with injection height, whereby the 21-23 km injection height has highest levels of condensation, followed by an injection height of 18-25 km, with the lowest values evident for an injection height of 18-20 km. This pattern can equally be seen with the amount of SO<sub>2</sub> emitted, as 20 Tg produces the highest values for all injection heights, followed by 14 Tg and then 10 Tg.

In total the values for condensed ash are low, peaking at 0.001 Tg for 20\_midalt\_ash with the lowest peak at 0.004 Tg for 10\_lowalt\_ash. The peak values are all ~1 week following the eruption and by October 1991 all values have tended towards zero, with an e-folding time between 43 (20\_lowalt\_ash) and 111 days (20\_midalt\_ash).

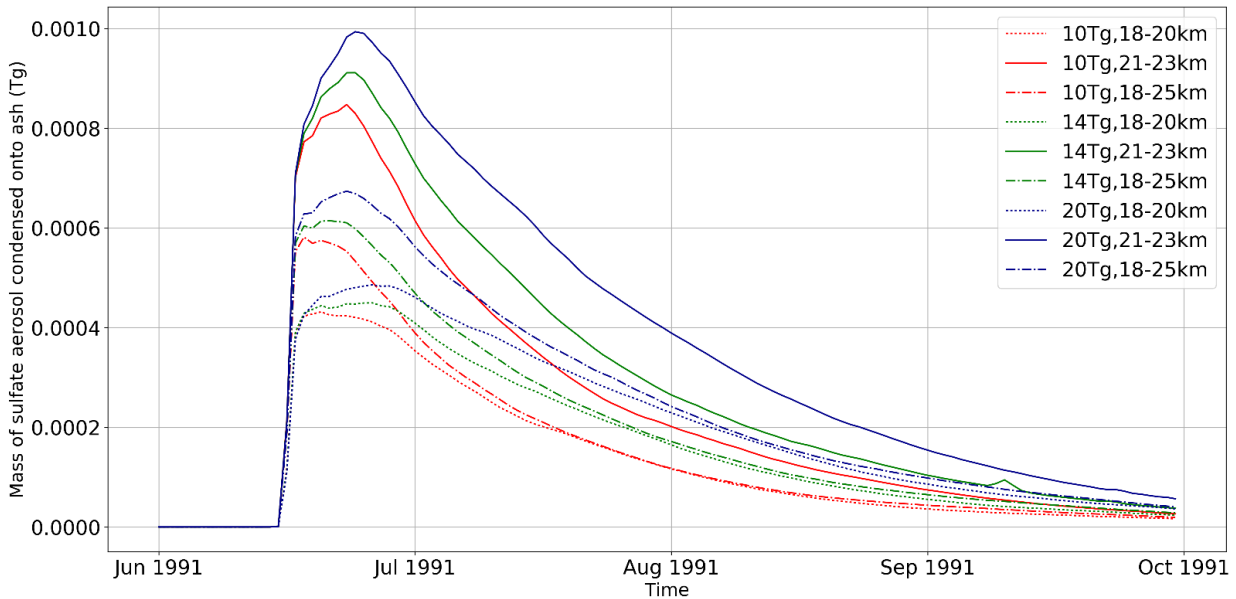


**Figure 6-21** Mass of sulfate aerosol condensed onto ash from June 1992 to October 1991 for all amounts of injected SO<sub>2</sub> and injection height.

## 6.9 Discussion

The analysis in this chapter has explored how major volcanic clouds are influenced by ultra-fine ash. Specifically, this chapter has focused on the volcanic aerosol cloud from the 1991 Mount Pinatubo eruption, known to have had ash particles present up to 9 months following the eruption (Pueschel et al., 1994). When major volcanic aerosol clouds are simulated within interactive stratospheric aerosol models, the influence from volcanic ash is often neglected because super-micron ash particles have a residence time of only ~10 days in the stratosphere and are therefore, usually thought to have an insignificant effect on climate (Niemeier et al., 2009; Langmann, 2014). Super-micron ash from the 1991 Mount Pinatubo eruption has been simulated using the interactive stratospheric aerosol model MAECHAM5 and showed that the radiative effects of these short-lived ash particles still affected winds locally (Niemeier et al., 2009). A recent study of the Raikoke ash plume (Muser et al., 2020) showed that even for smaller eruptions the uptake of sulfur on ash can have significant effects.

Lidar observations from the initial NASA aircraft mission to measure the Mount Pinatubo aerosol cloud (Winker and Osborn, 1992a), show that 3 weeks after the eruption there were highly depolarising layers at ~23 km with modest depolarisation throughout the cloud. Whereas the first two mid-latitude balloon flights sampling initial layers of the Mount Pinatubo aerosol cloud at 16-17 km showed no presence of ash (Sheridan et al., 1992; Deshler et al., 1992), ash was found to be present in the higher volcanic aerosol layers (22-23km) in the third and fourth Laramie flights, 40 and 44 days after the eruption (Deshler, 2016), although still not in the lower layer at 15-18 km. The re-analysis of the data from Deshler et al. (1992) now interprets the refractory particles within the 22-23 km layers as being ash particles at ~0.25  $\mu\text{m}$  radius, within internally mixed ash-sulfuric particles ~0.48  $\mu\text{m}$  radius (Deshler, 2016).

Mid-latitude ground-based lidar measurements from Aberystwyth (Vaughan et al., 1994) show the base of the Mount Pinatubo cloud was moderately depolarising throughout August 1991 to February 1992, initially at 17-21 km and descending to 12-17 km after November 1991. Similarly, SEM analysis of DC-8 impactor samples of the aerosol cloud 8 months after the eruption proved ash-sulfuric particles with radii up to 0.8  $\mu\text{m}$  (Pueschel et al., 1994) in the base of the cloud. These measurements firmly attributed the Aberystwyth depolarisation measurements and those from aircraft (Browell et al., 1993) and in the southern hemisphere (Young et al., 1994) must have been caused by ash. Ground based lidars in Japan have also found depolarising layers and evidence for long lasting ash in both the 1982 El Chichón and 1991 Mount Pinatubo clouds (Hayashida et al., 1984; Nagai et al., 1993). All these observations suggest a longer lifetime for ash in the Mount Pinatubo cloud than is often presumed. Vernier et al. (2016) show that ash following the 2014 Kelud eruption persisted for at least 3 months and ash < 0.3  $\mu\text{m}$  in size represented up to 28% of the total AOD and, therefore, ash may affect surface cooling following eruptions and should be accounted for in climate simulations.

Interactive stratospheric aerosol model experiments simulating the mixed sulfate aerosol and ultra-fine ash in the Mount Pinatubo aerosol cloud show that these smaller ash particles (~100-300 nm) can remain in the stratosphere for 9 months, much longer than ash is often assumed to persist. These simulations show that even ash particles at ~1  $\mu\text{m}$  diameter will have remained in the Mount Pinatubo cloud for ~2 weeks, but were completely removed from the stratosphere after ~90 days. For 0.3  $\mu\text{m}$  sized particles, their burden in the stratosphere reduced by half in 90 days, but likely still had a

substantial effect on the SAOD and how the cloud subsequently dispersed to the mid-latitudes. The very finest 0.1  $\mu\text{m}$  ash particles retain 98% of their mass in the first 90 days following the eruption and are prevalent for the first 9-month period after the eruption. Bluth and Rose (2004) found that ash particles of  $<1 \mu\text{m}$  diameter were found to remain for a number of years and 10  $\mu\text{m}$  particles fell out within  $\sim 12$  days. Our findings here account for increased fall velocity from the longer mean free path in the stratosphere. The results from the UM-UKCA simulations for  $>1 \mu\text{m}$  particles are similar to those in Bluth and Rose (2004), although 10  $\mu\text{m}$  particles fall out faster in UM-UKCA within  $\sim 3$  days. Bluth and Rose (2004) results are based on a simple laminar flow to calculate the fallout values and physical characteristics such as shape and density will likely affect the fall speed of these particles. Saxby et al. (2018), for example, suggest that particle shape is more important for sizes  $>1 \mu\text{m}$  whilst Beckett et al. (2015) maintain particle size distribution is more important for determining particle fall speeds than shape and density. The simulations here only account for condensation of sulfuric acid vapour on the ash particles, with initial results from additional 10-day simulations suggesting coagulation increases scavenging by  $\sim 30\%$ . Simulating the reactive uptake of  $\text{SO}_2$  onto ash potentially has more of a scavenging effect (Ayris et al., 2013), as heterogenous oxidation can occur for the full time the air is in contact with ash, whereas condensation and coagulation of  $\text{H}_2\text{SO}_4$  can only occur after  $\text{SO}_2$  has oxidised. The initial condensation-only results do confirm however that the ash is acting as a successful removal mechanism for the sulfur within Mount Pinatubo magnitude major eruption clouds.

Injection height was found in Chapter 5 to be a very strong determinant of the early-phase dispersion to mid-latitudes, and here is shown to also impact residence time of the ultra-fine ash, again with the fastest removal with the nearest-tropopause 18-20 km injection height cases. The 21-23 km injection height simulations had the highest ash burden until November 1991 when the mass rapidly decreases whereas the 18-25 km injections steadily decline, retaining 65% of their original ash mass by February 1992. These differences seen between injection heights along with the initial very slow decrease in an ash particle with 0.1  $\mu\text{m}$  diameter suggests that these very fine ash particles may survive for longer in the atmosphere than previously thought and/or modelled, in agreement with findings from Vernier et al. (2016).

SAOD varies the most in the tropics and when looking at the dispersion to the midlatitudes. For all of the injection height settings within the HErSEA ensemble, the

majority of the volcanic material is transported to the northern hemisphere, particularly in the simulations including ash suggesting that the inclusion of ash also causes more effective transport of volcanic material to disperse to the northern hemisphere mid-latitudes. These simulations show that the increased dispersion is very likely caused by the increased radiative heating from the ash, consistent with the findings in Niemeier et al. (2009). A number of modelling studies have found it necessary to disperse volcanic material over a number of grid boxes in order to simulate the dispersion to both hemispheres correctly (Timmreck, Graf and Feichter, 1999; Timmreck, Graf and Kirchner, 1999; Dhomse et al., 2014; Sheng et al., 2015; Mills et al., 2016; Mills et al., 2017). This study suggests that fewer grid boxes may be necessary if ash is included in model simulations and that ash may influence volcanic cloud dispersion more than previously considered. The effect is that ash heats the air surrounding it, sending more aerosol into higher branches of the BDC, leading to less aerosol loss through lower branches of the BDC and increased transport to the winter hemisphere (northern hemisphere for Mount Pinatubo). This is potentially consistent with model simulations that are missing an early-phase heating effect or incorrectly dispersing the Mount Pinatubo eruption, and could be important for aerosol microphysics model predictions of the aerosol clouds from a future major eruption.

These simulations also indicate that the 18-20 km simulations, followed by the 18-25 km simulations have the highest SAOD values in the northern hemisphere, suggesting a lower injection height leads to a more likely injection to the northern hemisphere and an injection height over 20 km is more likely to reach the southern hemisphere in UM-UKCA. This has been seen previously in Jones et al. (2017) whereby their 16-23 km injection height almost exclusively transported to the northern hemisphere, whereas injecting between 23-28 km led to a higher dispersion to the southern hemisphere.

The impact of injection height is understandably mirrored in the sulfate and SO<sub>2</sub> burden, where the lower injection height leads to more sulfate and SO<sub>2</sub> in the northern hemisphere. In the peak of both midlatitude areas the northern hemisphere has 1.3, 1.6 and 2.4 Tg more sulfate aerosol in the 10, 14 and 20 Tg injections, than the southern hemisphere, respectively. The inclusion of ash does have an effect on sulfate burden, again particularly in the tropics, whereby the ash simulations have a lower sulfate burden at the peak of the sulfate production in September 1991. This was hypothesized to be due to the removal of sulfate on ash particles, when the ash acts as a sulfate core that the sulfate coagulates with, growing the particle to a larger size and therefore

making it sediment out of the atmosphere faster (Sheridan et al., 1992; Deshler et al., 1993; Pueschel et al., 1994; Deshler, 2016). An investigation of the amount of sulfate condensed onto ash particles, however, revealed this only accounted for 0.001 Tg at most in the 20\_midalt\_ash simulation, indicating that removal processes through lower branches of the BDC in the model are more prevalent. The differences seen in sulfate burden and SAOD can be roughly compared to the sulfate burden and SAOD produced by low to medium sized eruptions, such as Kasatochi in 2008 (0.5 difference in sulfate) (Mills et al., 2016) indicating a significant impact of including ash.

When comparing the vertical profiles of extinction at the near-tropical and mid-latitude lidar sites in the model, it is clear that ash is having an impact in the vertical and in the dispersion of the aerosol globally. Ash appears to increase the appearance of layers in the 18-20 km simulations, likely due to the increased upward lofting induced by the absorbent properties of the ash in comparison to purely higher scattering sulfate. As discussed in Niemeier et al. (2009), ash strongly absorbs SW and LW radiation and increases heating rates locally, lofting material to higher altitudes and advecting material preferentially northwards. The effect of ash on lofting aerosol and creating layers in the vertical profile can also be said of the 18-25 km simulations, as they begin to match more closely with the observations in the ash cases than in the non-ash cases. The inclusion of ash does also appear to induce a slightly earlier dispersion to the northern hemisphere mid-latitudes. As the BDC is changing to an autumnal/winter phase following the eruption, it is possible that injection at a lower altitude leads to more dispersion to the north in a lower branch (Holton et al., 1995), whereas with 21-23 km it may be more confined in the tropical pipe and with 18-25 km there may be a combination of northern hemisphere dispersion at the base, some restriction tropically and then dispersion to southern hemisphere in a higher branch of the BDC.

Balloon-borne particle counters have had a gap in their particle measurements between the smallest measured particles (10 nm) to the next particle size channel (>150 nm) with recent measurements allowing particles with radius 75 nm to be detected (Ward et al., 2014). However, Pueschel et al. (1994) show that aircraft impactor measured down to size fractions in the range  $0.1 \pm 0.04 \mu\text{m}$  following the Mount Pinatubo eruption.

This analysis highlights the importance of measurements with these smaller cut-off sizes and an understanding of the proportion of ultra-fine ash after any future major eruptions will be an important element to assess in initial measurement capabilities

deployed to sample the subsequent cloud. The model simulations show that ultra-fine ash particles do impact on the sulfate burden and optical depth and therefore potentially impact radiative forcing from volcanic eruptions. In order to directly compare measurements and model data, comparing to observations that can detect these size fractions is imperative, therefore this advancement in balloon-borne particle counters, for example will be an extremely useful capability.

## **6.10 Conclusions**

The overall aim of this chapter is to investigate the role of ash in an major tropical eruption of a similar magnitude to the 1991 Mount Pinatubo eruption and its effects on sulfate, optical depth and vertical profile of extinction of the resulting volcanic aerosol cloud. By investigating different size fractions of ash using UM-UKCA, the simulations predict that 10  $\mu\text{m}$  diameter ash particles are removed from the atmosphere within 8 days of the eruption, in line with theory and other modelling studies, 1  $\mu\text{m}$  ash particles are reduced by 95% after 75 days and 0.1  $\mu\text{m}$  ash particles lose just 5% after 75 days. These 0.1  $\mu\text{m}$  particles also only reduce by a maximum of 50% depending on injection height after 9 months, therefore remaining prevalent in the atmosphere for far longer than the few days assumed by most modelling studies and in agreement with Vernier et al. (2016) who confirmed the presence and impact of ash  $<0.3 \mu\text{m}$  on AOD 3 months after the 2014 Kelud eruption.

Though non-linear in response, ultra-fine ash does have an impact on sulfate burden, SAOD and vertical dispersion. The most obvious differences are seen in sulfate burdens, particularly for the 18-20 km and 21-23 km cases and for 14 Tg and 20 Tg injected  $\text{SO}_2$ . These differences are seen in the peaks of the SAOD and sulfate burden and show up to 2.4 Tg decrease in sulfate in the ash-containing case, indicating that the model successfully represents the scavenging effect of sulfate condensing onto ash particles although this process does not have as significant of an effect as removal due to the BDC.

The SAOD broadly decreases when ash is included in model simulations, corresponding to less mass. This effect is also primarily seen at the peak, indicating that the reduction in sulfate is reflected in the optical depth. Overall, the 18-20 km injection height and ash containing simulations show the highest SAOD values of 0.18, 0.26 and 0.34 for 10,

14 and 20 Tg of SO<sub>2</sub>, respectively, for the northern hemisphere, indicating that a lower injection height preferentially disperses aerosol to the northern hemisphere through the lower branch of the BDC and that including ash aids the dispersion of aerosol to the northern hemisphere. The increase in SAOD in the northern hemisphere when including ash indicates there is more of a heating effect from the ash, lofting aerosol preferentially towards the mid-latitudes, as opposed to the scavenging effect which would have created a decrease in SAOD in both the tropics and the mid-latitudes.

The inclusion of ash in simulations bring extinction values closer to those observed at ground-based lidar sites and indicates ash may partially be the cause for the shape and height of the layers seen in the observations. This is not without the uncertainty created by lidar retrieval, extinction to backscatter and wavelength conversion factors, however, qualitatively better matches to observations are evident. Qualitatively, the inclusion of ash creates layers in the MLO model simulated extinction for 18-20 km and 18-25 km simulations in comparison to the vertical profiles noted in Chapter 5.

Measurements are crucial for determining the presence of ash in the atmosphere and have been gradually increasing in accuracy in recent years, but climate models are imperative for furthering our understanding on how volcanoes impact our atmosphere and understanding potential microphysical processes not detectable by instruments. Climate models can dramatically impact our understanding on how ash may impact the dispersion of volcanic material and the climate response from volcanic eruptions and more modelling work is needed to further understand the impact of ash during the Mount Pinatubo eruption and future major tropical eruptions.

## Chapter 7 Conclusions and Future Work

The overarching aim of this thesis is to investigate the early global dispersion of the 1991 Mount Pinatubo volcanic aerosol cloud, analysing ground-based lidar measurements and interactive stratospheric aerosol simulations from UM-UKCA. This research was carried out to understand how the cloud evolved in the tropical reservoir and assess potential influence from ultra-fine ash.

The first part of this thesis analysed the progression of the vertical profile of the Mount Pinatubo cloud, as measured from a ground-based lidar at the tropical Mauna Loa site and three northern hemisphere ground-based lidar sites. Distinct phases in this initial global dispersion of the plume were identified, with comparisons to interactive stratospheric aerosol simulations providing a new perspective to evaluate recent UM-UKCA model simulations of the Mount Pinatubo cloud for the international ISA-MIP initiative (Timmreck et al., 2018). A related aim is to explore how the global dispersion proceeds differently across similar initial meteorological conditions, comparing simulations to assess how precise the 1991 QBO phase-transition needs to be modelled for accurate simulation of the aerosol cloud dispersion.

The second part of this thesis aimed to understand the effects of varying eruption source parameters for the Mount Pinatubo eruption, namely injection height and SO<sub>2</sub> emission, on vertical extinction profiles, sulfate burden and SAOD. The simulations were also aimed at improving constraint estimates of SO<sub>2</sub> and injection height in UM-UKCA for Mount Pinatubo and to assess the subsequent changes in effective radius under different eruption source parameter conditions.

The third and final aim of this thesis is to understand how the presence of ultra-fine ash within the Mount Pinatubo cloud affected its initial progression in the tropics and its later dispersion to the mid-latitudes. Stratospheric aerosol simulations emitting ash particles as well as SO<sub>2</sub> were specifically designed to assess this issue, comparing directly to the equivalent model ensemble from the Chapter 5. Ground-based lidar measurements from Aberystwyth were gathered during the PhD thesis, allowing an evaluation of the vertical profile of ash particles in the volcanic aerosol cloud.

Combining this observational constraint for the ultra-fine ash with effects on vertical extinction profiles, sulfate burden and SAOD presents a substantial test for the model.

This chapter summarises the main findings from each chapter with suggestions for future work for each.

## **7.1 Initial dispersion of the 1991 Mount Pinatubo aerosol cloud – a ground-based lidar and interactive composition climate model comparison**

The aim of the first results chapter was to investigate the initial dispersion of the 1991 Mount Pinatubo aerosol cloud using ground-based lidars and to evaluate the evolving vertical structure of the UM-UKCA interactive stratospheric aerosol simulations. An assessment of the initial conditions was also conducted using UM-UKCA by comparing an approximate-QBO initial condition with a pre-nudged initial condition configuration. The time period for this study was June 1991 – February 1992 and approximate-QBO conditions used model initial conditions from 01/02/1996 where the QBO was in a similar condition to the time of the Mount Pinatubo eruption, the pre-nudged initial conditions were nudged to the point of 2 months prior to the eruption. For this initial model comparison an injection mass of 14 Tg SO<sub>2</sub> and injection height of 21-23 km was used.

### **7.1.1 Main conclusions**

- a. Ground-based lidar are extremely useful for investigating the full vertical structure of a volcanic aerosol cloud and its progression globally and through time. In particular, the tropical Mauna Loa (MLO) site, due to the saturation of the tropical measurements of the Mount Pinatubo cloud from SAGE II. The analysis has demonstrated that the lidars are a highly valuable tool to assess the evolving vertical structure of the Mount Pinatubo aerosol cloud whilst it was sheared by the strengthening easterly winds with altitude and affected by SO<sub>2</sub> oxidation and subsequent microphysics. At the MLO site, distinct phases of the evolution of the aerosol cloud were identified, divided into a first inhomogeneous phase, when the initial volcanic plume was still a concentrated

plume spreading out globally, the sheared nature of the aerosol cloud observed at MLO as seemingly descending layers of aerosol. The descending layers in the first phase of the MLO record are caused by easterly winds increasing with height over time, the cloud detected at 25 km a day before it is seen at 23 km. The period of increasing shear eventually progresses to a well-mixed mature phase where the aerosol is fully mixed within the tropical reservoir. The distinction of phases in these measurements allows a more precise timing of when the volcanic cloud spread out inhomogeneously (Phase 1) into the tropical reservoir (Phase 2) and dispersed globally (Phase 3).

- b. UM-UKCA is able to replicate the timing of these layers and phases seen in the observations at MLO and reproduces the altitude of the top of the first layer well, though the altitude of the top of the other layers is higher by 2-4 km. The model also reproduces timings at the northern hemisphere mid-latitudes quite well initially with the aerosol cloud below 20 km until September, rising to ~17-23 km in later months (November 1991-February 1992). A possible reason for the higher model simulated aerosol cloud top is too much radiative heating in the model, an injection height that is too high or a lack of scavenging mechanism, such as ash, in the model. UM-UKCA produces anomalous temperatures following the eruption two times higher than those from ERA-interim, potentially lofting aerosol to these higher altitudes, though exact temperature anomalies are difficult to quantify due to the calculation of anomalies by ERA-interim. Extinction values in the model are also lower than those calculated for the observations, however absolute differences are difficult to calculate due to errors associated with the backscatter-to-extinction conversion.
- c. As with other studies, using pre-nudged initial conditions produces values and a better qualitative agreement to observations in the vertical profiles. Dhomse et al. (2014) found easterlies in their study were slightly weaker than in observations, with this study showing the timing of the initial conditions used to investigate the Mount Pinatubo eruption can produce model simulations that agree better with observations. A comparison of wind patterns for the first 2 weeks after the eruption show the pre-nudged conditions compare better with observations from Trepte et al. (1993). Using pre-nudged conditions is therefore a good solution for allowing free-running simulations whilst starting simulations from an accurate starting point. The pre-nudged conditions allow a closer match

to the initial progression of the Mount Pinatubo cloud as seen by ground-based lidar observations and should be considered as initial conditions for future studies of the Mount Pinatubo and future major tropical eruptions.

### **7.1.2 Future work**

This research found distinct descending layers and phases of the progression of the Mount Pinatubo aerosol cloud at MLO, which in turn led to an assessment of the initial conditions used for assessing the 1991 Mount Pinatubo eruption, with pre-nudged conditions leading to a better comparison to vertical profiles of extinction at ground-based lidar sites. A further assessment of this use of pre-nudged conditions for other large-magnitude and smaller eruptions would aid future research into the dispersion of volcanic eruptions.

An assessment of differing injection heights with and without radiative heating would allow a better understanding of how the radiative heating in UM-UKCA affects the vertical lofting of volcanic aerosol. An investigation of different scavenging mechanisms, such as ash and ice would further aid our understanding of the balance between scavenging mechanisms and radiative heating.

## **7.2 Exploring varying eruption source parameters: a Pinatubo case study**

The aim of this chapter was to explore the Historical Eruptions SO<sub>2</sub> Emission Assessment (HerSEA) Mount Pinatubo eruption source parameters within UM-UKCA. An assessment of the effect of varying injection mass of SO<sub>2</sub> and injection height on vertical profiles of extinction was made. A comparison of the effects of these parameters on the lidar profiles introduced in the first results chapter was made, primarily focussing on the MLO lidar site to assess the impact of these parameters on the top of the aerosol cloud altitude which was noted to be too high in the model when compared in the first results chapter. The effects of varying these parameters on sulfate burden and SAOD was also investigated with a comparison to satellite measurements. A hypothetical tropical lidar site was introduced, as satellite measurements at the time of the Mount Pinatubo eruption were saturated and could not, therefore, retrieve accurate values of extinction or SAOD. Analysing the vertical profile of extinction

from hypothetical lidar sites at 10°N, at the equator and 10°S allowed a further assessment of the possible progression of the Mount Pinatubo aerosol cloud from the tropical reservoir to the midlatitudes.

### 7.2.1 Main conclusions

- a. The main conclusion in relation to vertical profiles of extinction was that the 21-23 km injection height led to the closest qualitative comparison with the MLO lidar site. This injection height produced the correct descending layers seen in observations and resultant phase 1, 2 and 3 that were outlined in the first results chapter. An injection height of 18-20 km led to a confined layer of aerosol and no layer pattern; however, extinction values were closest to observed values. An 18-25 km injection height led to a similar layer in the 18-20 km region and an attached layer pattern up to 25 km in altitude initially, leading to layer heights of 24, 28 and 29 km respectively. These results suggest that for UM-UKCA an injection height closer to 21-23 km will produce extinction profiles that are well-matched to lidar observations and that injecting below 20 km will confine aerosol and not allow the wind shear to take effect.
- b. An assessment of SAOD and sulfate burden led to the conclusion that, for UM-UKCA, SO<sub>2</sub> values between 10-14 Tg lead to values of SAOD and sulfate burden that are closest to observed values. This is in agreement with other Mount Pinatubo modelling studies, though many of these find better agreement with an injection height between 18-20 km. Injection heights of 21-23 km and 18-25 km agree best with observations, an injection height of 21-23 km matching closest across extinction, SAOD and sulfur burden.
- c. The use of a hypothetical tropical lidar shows the volcanic aerosol is detected at the equator within 4 days following the eruption. The southern and northern hemisphere tropical sites both detect the volcanic aerosol cloud at the very end of June, with the northern tropical site producing a thicker cloud (16-32 km in depth) showing evidence for layers. The southern tropical site has a thinner cloud (22-31km predominantly) and shows less obvious layers. Higher extinction values are noted in the northern hemisphere tropics than the southern hemisphere tropics. Clear benefits can be seen of having more observational capability at tropical sites, in order to account for potential satellite saturation during major eruptions.

### 7.2.2 Future work

A further assessment of different injection heights and depths would build a clearer picture of the effects of these eruption source parameters. For example, testing different injection depths and altitudes and perhaps injecting greater values of SO<sub>2</sub> at specific heights. Marshall et al. (2019) began this work for major eruptions in general, with 3km depth injection heights over the range 15-25 km and SO<sub>2</sub> emissions of 10-100 Tg and a further assessment of different injection heights or specifying a greater amount of SO<sub>2</sub> at specific altitudes would be beneficial to better understand the effect of these eruption source parameters. An assessment of the effects for smaller magnitude eruptions would also be valuable, in order to assess the impact of injection height on more frequent smaller eruptions. Assessing smaller volcanic eruptions would help determine whether injection height and SO<sub>2</sub> mass are as important for smaller eruptions as they are for major eruptions.

## 7.3 The role of ash in the initial dispersion of the 1991 Mount Pinatubo aerosol cloud

The aim of this results chapter was to assess the role of ash as a potential scavenging and self-lofting mechanism within the Mount Pinatubo aerosol cloud. The first aim was to investigate the fine ash particles and assess their lifetime using UM-UKCA. The next aim was to investigate how long ultra-fine ash particles persisted in the atmosphere using UM-UKCA. Following on from this, an investigation of these sub-micron ash particles on the vertical dispersion, sulfate burden and SAOD was carried out, with a direct comparison to the second results chapter as well as with depolarisation data taken from a northern hemisphere site (Aberystwyth) following the Mount Pinatubo eruption.

### 7.3.1 Main conclusions

- a. The key conclusion from investigating the fine ash particles was that particles of 10 µm diameter are removed from the atmosphere within 8 days of the eruption and 1 µm particles are reduced by 95% after 75 days. Only particles <1 µm in size remained in the atmosphere for longer than 75 days, with 0.1 µm particles retaining >90% of the original mass of ash injected after 75 days. These results show that super-micron particles do fall out of the stratosphere within days of

- the eruption, but that sub-micron, ultra-fine ash particles can persist in the stratosphere for over 9 months following a major tropical eruption.
- b. When assessing the impact of injection height and mass of SO<sub>2</sub> on the remaining burden of ash, the injection height has the largest effect, with an 18-25 km injection height retaining the largest percentage of originally erupted mass of ash (70%) by March 1992. 21-23 km retains 60% and 18-20 km retains 44% by March 1992, respectively. This study shows that a deeper injection height up to higher altitudes allows ultra-fine ash particles to persist in the stratosphere for longer, whilst an injection height closer to the tropopause results in large sedimentation of ash.
  - c. Including ultra-fine ash particles (0.1 μm) in UM-UKCA simulations of the Mount Pinatubo eruption affects vertical dispersion, sulfate burden and SAOD. Increased lofting of the layers noted at MLO can be seen in the 18-20 km and 18-25 km injection height simulations when ash is included and values for the 21-23 km injection height are brought closer to observed values. SAOD and sulfate burden values broadly decrease when ash is included in the model, primarily seen at the peak for each simulation. A decrease in SAOD and sulfate burden suggest ash is scavenging sulfate from the volcanic aerosol cloud which has the potential to impact on resultant climatic effects of the sulfate cloud.
  - d. 18-20 km injection height simulations show the highest SAOD values for the northern hemisphere, suggesting that there is a preferential dispersion to the northern hemisphere through a lower branch of the BDC with a lower injection height. Including ash also appears to increase dispersion to the northern hemisphere, suggesting that an inclusion of ash may allow a reduction in the number of grid boxes that the aerosol is initially injected over. Ultra-fine ash increases dispersion to the northern hemisphere, suggesting the radiative heating impact of the ash significantly lofts the aerosol cloud when ultra-fine ash is included in simulations before being affected by the BDC to be transported to the winter hemisphere (the northern hemisphere for the Mount Pinatubo eruption).

### 7.3.2 Future work

Further work based on the ash size and density are needed to further understand the impacts of ash on dispersion and sulfate deposition. Density and shape of ash can vary

for eruption types and for particle size (Saxby et al., 2018) and an assessment for these would allow a better understanding of different eruptions, both of large and smaller magnitudes.

An assessment of the effects of ash when dispersing over different numbers of grid boxes would allow an assessment of the affect that ash may have on dispersion to different hemispheres, depending on volcano latitude. The inclusion of ash may allow for fewer grid boxes to be injected over for the Mount Pinatubo case study due to the fact that ash has been found in this thesis to transport aerosol preferentially towards the northern hemisphere. The requirement to inject over multiple grid boxes is noted in a number of modelling studies for the Mount Pinatubo eruption, therefore it would be useful to assess this effect in multiple models.

The effects of heterogenous reactions of  $\text{SO}_2$  on ash particles is not currently included in UM-UKCA, but may act as a further removal pathway (Maters et al., 2017; Urupina et al., 2019). An assessment of this may lead to lower values of injected  $\text{SO}_2$  being required to compare well with observations for the Mount Pinatubo eruption.

Further research into the effects of ash in smaller-scale and other major eruptions is required. Research on the optical properties of ash in the 2014 Kelud eruption cloud (Vernier et al., 2016) indicated that ash may have been more significant than previously thought, therefore, it is important for modelling studies including ash to be conducted across a wide spectrum of volcanic eruptions in order to understand the strength of the effects of ash.

## References

- Abraham, N.L. 2017. Release Job RJ4.0. *Online*. [Online]. Available from:  
[http://www.ukca.ac.uk/wiki/index.php/Release\\_Job\\_RJ4.0](http://www.ukca.ac.uk/wiki/index.php/Release_Job_RJ4.0).
- Abraham, N.L., Archibald, A.T., Bellouin, N., Boucher, O., Braesicke, P., Bushell, A., Carslaw, K., Collins, B., Dalvi, M., Emmerson, K., Folberth, G., Haywood, J., Johnson, C., Kipling, Z., Macintyre, H., Mann, G., Telford, P., Merikanto, J., Morgenstern, O., O'Connor, F., Ordonez, C., Osprey, S., Pringle, K., Pyle, J., Rae, J., Reddington, C., Savage, N., Spracklen, D., Stier, P. and West, R. 2012. *Unified Model Documentation Paper No. 84: United Kingdom Chemistry and Aerosol (UKCA) Technical Description MetUM Version 8.4* [Online]. Exeter. Available from: [https://www.ukca.ac.uk/images/b/b1/Umdp\\_084-umdp84.pdf](https://www.ukca.ac.uk/images/b/b1/Umdp_084-umdp84.pdf).
- Akiyoshi, H., Nakane, H., Uchino, O., Nagai, T., Fujimoto, T., Fujiwara, M., Yasumatsu, S., Hayashida, S., Sasano, Y., Nakane, H., Iwasaka, Y., Hase, M., Shibata, T., Itabe, T., Asai, K., Nomura, A., Saito, Y., Kano, T., Sai, Y., Tamaki, K., Nomura, R., Sunagawa, T., Nagasawa, C., Abo, M., Idesako, Y. and Kai, K. 1993. Observation of the Pinatubo Volcanic Cloud by Lidar Network in Japan Atmospheric research in the Arctic View project Environmental Measurement Analyses View project Observation of the Pinatubo Volcanic Cloud by Lidar Network in Japan. *Article in Journal of the Meteorological Society of Japan Journal of the Meteorological Society of Japan*. **71**(2).
- Allen, A.G., Oppenheimer, C., Ferm, M., Baxter, P.J., Horrocks, L.A., Galle, B., McGonigle, A.J.S. and Duffell, H.J. 2002. Primary sulfate aerosol and associated emissions from Masaya Volcano, Nicaragua. *Journal of Geophysical Research: Atmospheres*. **107**(D23), pp.1–8.
- Andersson, S.M., Martinsson, B.G., Vernier, J.P., Friberg, J., Brenninkmeijer, C.A.M., Hermann, M., Van Velthoven, P.F.J. and Zahn, A. 2015. Significant radiative impact of volcanic aerosol in the lowermost stratosphere. *Nature Communications*. **6**.
- Ansmann, A., Mattis, I., Wandinger, U., Wagner, F., Reichardt, J. and Deshler, T. 1997. Evolution of the Pinatubo Aerosol: Raman Lidar Observations of Particle Optical

- Depth, Effective Radius, Mass, and Surface Area over Central Europe at 53.4N. *Journal of Atmospheric Sciences*. **54**, pp.2630–2641.
- Ansmann, A. and Müller, D. 2005. Lidar and Atmospheric Aerosol Particles *In: Lidar: Range-Resolved Optical Remote Sensing of the Atmosphere.*, pp.105–141.
- Ansmann, A., Tesche, M., Seifert, P., Groß, S., Freudenthaler, V., Apituley, A., Wilson, K.M., Serikov, I., Linné, H., Heinold, B., Hiebsch, A., Schnell, F., Schmidt, J., Mattis, I., Wandinger, U. and Wiegner, M. 2011. Ash and fine-mode particle mass profiles from EARLINET-AERONET observations over central Europe after the eruptions of the Eyjafjallajökull volcano in 2010. *Journal of Geophysical Research Atmospheres*. **116**(12).
- Antuña-Marrero, J.C., Landulfo, E., Estevan, R., Barja, B., Robock, A., Wolfram, E., Ristori, P., Clemesha, B., Zaratti, F., Forno, R., Armandillo, E., Bastidas, Á.E., De Frutos Baraja, Á.M., Whiteman, D.N., Quel, E., Barbosa, H.M.J., Lopes, F., Montilla-Rosero, E. and Guerrero-Rascado, J.L. 2017. LALINET: The first Latin American-born regional atmospheric observational network. *Bulletin of the American Meteorological Society*. **98**(6), pp.1255–1275.
- Antuña, J.-C., Robock, A., Stenchikov, G.L., Thomason, L.W. and Barnes, J.E. 2002. Lidar validation of SAGE II aerosol measurements after the 1991 Mount Pinatubo eruption. *Journal of Geophysical Research Atmospheres*. **107**(D14), pp.1–9.
- Antuña, J.C. 1996. Lidar measurements of stratospheric aerosols from Mount Pinatubo at Camaguey, Cuba. *Atmospheric Environment*. **30**(10/11), pp.1857–1860.
- Aquila, V., Oman, L.D., Stolarski, R., Douglass, A.R. and Newman, P.A. 2013. The response of ozone and nitrogen dioxide to the eruption of mt. pinatubo at southern and northern midlatitudes. *Journal of the Atmospheric Sciences*. **70**(3), pp.894–900.
- Aquila, V., Oman, L.D., Stolarski, R.S., Colarco, P.R. and Newman, P.A. 2012. Dispersion of the volcanic sulfate cloud from a Mount Pinatubo-like eruption. *Journal of Geophysical Research Atmospheres*. **117**, pp.1–14.
- Arfeuille, F., Luo, B.P., Heckendorn, P., Weisenstein, D., Sheng, J.X., Rozanov, E., Schraner, M., Brönnimann, S., Thomason, L.W. and Peter, T. 2013a. Modeling the stratospheric warming following the Mt. Pinatubo eruption: Uncertainties in aerosol extinctions. *Atmospheric Chemistry and Physics*. **13**, 11,221–11,234.

- Arfeuille, F., Luo, B.P., Heckendorn, P., Weisenstein, D., Sheng, J.X., Rozanov, E., Schraner, M., Brönnimann, S., Thomason, L.W. and Peter, T. 2013b. Modeling the stratospheric warming following the Mt. Pinatubo eruption: Uncertainties in aerosol extinctions. *Atmospheric Chemistry and Physics*. **13**(22), pp.11221–11234.
- Arfeuille, F., Weisenstein, D., MacK, H., Rozanov, E., Peter, T. and Brönnimann, S. 2014. Volcanic forcing for climate modeling: A new microphysics-based data set covering years 1600-present. *Climate of the Past*. **10**(1), pp.359–375.
- Avdyushin, S., Tulinov, G., Ivanov, M., Kuzmenko, B. and Mezhuev, I. 1993. *Temporal evolution of the optical thickness of the Pinatubo aerosol cloud in the Northern hemisphere from a network of ship-borne and stationary lidars*.
- Ayris, P.M., Lee, A.F., Wilson, K., Kueppers, U., Dingwell, D.B. and Delmelle, P. 2013. SO<sub>2</sub> sequestration in large volcanic eruptions: High-temperature scavenging by tephra. *Geochimica et Cosmochimica Acta*. **110**, pp.58–69.
- Baldwin, M.P., Gray, L.J., Dunkerton, T.J., Hamilton, K., Haynes, P.H., Randel, W.J., Holton, J.R., Alexander, M.J., Hirota, I., Horinouchi, T., Jones, D.B.A., Kinnersley, J.S., Marquardt, C., Sato, K. and Takahashi, M. 2001. The quasi-biennial oscillation. *Reviews of Geophysics*. **39**(2), pp.179–229.
- Balkanski, Y., Schulz, M., Claquin, T. and Guibert, S. 2007. *Atmospheric Chemistry and Physics Reevaluation of Mineral aerosol radiative forcings suggests a better agreement with satellite and AERONET data* [Online]. Available from: [www.atmos-chem-phys.net/7/81/2007/](http://www.atmos-chem-phys.net/7/81/2007/).
- Baran, A.J. and Foot, J.S. 1994. New application of the operational sounder HIRS in determining a climatology of sulphuric acid aerosol from the Pinatubo eruption. *Journal of Geophysical Research*. **99**(D12).
- Barnes, J.E. and Hofmann, D.J. 1997. Lidar measurements of stratospheric aerosol over Mauna Loa Observatory. *Geophysical Research Letters*. **24**(15), pp.1923–1926.
- Beckett, F.M., Witham, C.S., Hort, M.C., Stevenson, J.A., Bonadonna, C. and Millington, S.C. 2015. Sensitivity of dispersion model forecasts of volcanic ash clouds to the physical characteristics of the particles. *Journal of Geophysical Research*. **120**(22), 11,636–11,652.
- Bekki, S. 1995. Oxidation of volcanic SO<sub>2</sub>: a sink for stratospheric OH and H<sub>2</sub>O.

- Geophysical Research Letters*. **22**(8), pp.913–916.
- Bekki, S., Pyle, J.A., Zhong, W., Toumi, R., Haigh, J.D. and Pyle, D.M. 1996. The role of microphysical and chemical processes in prolonging the climate forcing of the Toba eruption. *Geophysical Research Letters*. **23**(19), pp.2669–2672.
- Bellouin, N., Mann, G.W., Woodhouse, M.T., Johnson, C., Carslaw, K.S. and Dalvi, M. 2013. Impact of the modal aerosol scheme GLOMAP-mode on aerosol forcing in the hadley centre global environmental model. *Atmospheric Chemistry and Physics*. **13**(6), pp.3027–3044.
- Bluth, G., Doiron, S., Schnetzler, C., Krueger, A. and Walter, L. 1992. Global Tracking of the SO<sub>2</sub> clouds from the June, 1991 Mount-Pinatubo Eruptions. *Geophys. Res. Lett.* **19**(2), pp.151–154.
- Bluth, G.J.S. and Rose, W.I. 2004. Removal processes of volcanic ash particles from the atmosphere In: *Proceedings, 2nd International Conference on Volcanic Ash and Aviation Safety*. Office of the Federal Coordinator for Meteorology (OFCM), Washington, DC.
- Bönisch, H., Engel, A., Birner, T., Hoor, P., Tarasick, D.W. and Ray, E.A. 2011. On the structural changes in the Brewer-Dobson circulation after 2000. *Atmospheric Chemistry and Physics*. **11**(8), pp.3937–3948.
- Brewer, A. 1949. Evidence for a world circulation provided by measurements of helium and water vapour distribution in the stratosphere. *Quarterly Journal of the Royal Meteorological Society*. **75**, pp.351–363.
- Brock, C.A., Hamill, P., Wilson, J.C., Jonsson, H.H. and Chan, K.R. 1995. Particle Formation in the Upper Tropical Troposphere: A Source of Nuclei for the Stratospheric Aerosol. *Science*. **270**(5242), pp.1650–1653.
- Brooke, J.S.A., Feng, W., Carrillo-Sánchez, J.D., Mann, G.W., James, A.D., Bardeen, C.G. and Plane, J.M.C. 2017. Meteoric Smoke Deposition in the Polar Regions: A Comparison of Measurements With Global Atmospheric Models. *Journal of Geophysical Research: Atmospheres*. **122**(20), 11,112-11,130.
- Browell, E. V, Butler, C.F., Fenn, M.A., Grant, W.B., Ismail, S., Schoeberl, M.R., Toon, O.B., Loewenstein, M. and Podolske, J.R. 1993. Ozone and Aerosol Changes During the 1991-1992 Airborne Arctic Stratospheric Expedition. *Science*.

- 261, pp.1155–1158.
- Brühl, C., Lelieveld, J., Crutzen, P.J. and Tost, H. 2012. The role of carbonyl sulphide as a source of stratospheric sulphate aerosol and its impact on climate. *Atmospheric Chemistry and Physics*. **12**(3), pp.1239–1253.
- Butchart, N. 2014. The Brewer-Dobson circulation. *Reviews of Geophysics*. **52**(2), pp.157–184.
- Butt, E.W., Turnock, S.T., Rigby, R., Reddington, C.L., Yoshioka, M., Johnson, J.S., Regayre, L.A., Pringle, K.J., Mann, G.W. and Spracklen, D. V. 2017. Global and regional trends in particulate air pollution and attributable health burden over the past 50 years. *Environmental Research Letters*. **12**(10).
- Campbell, P. and Deshler, T. 2014. Condensation nuclei measurements in the midlatitude (1982–2012) and Antarctic (1986–2010) stratosphere between 20 and 35 km. *Journal of Geophysical Research: Atmospheres*. **119**(1), pp.137–152.
- Campbell, P., Mills, M. and Deshler, T. 2014. The global extent of the mid stratospheric CN layer: A three-dimensional modeling study. *Journal of Geophysical Research*. **119**(2), pp.1015–1030.
- Carn, S.A., Clarisse, L. and Prata, A.J. 2016. Multi-decadal satellite measurements of global volcanic degassing. *Journal of Volcanology and Geothermal Research*. **311**, pp.99–134.
- Carslaw, K.S., Luo, B. and Peter, T. 1995. An analytic expression for the composition of aqueous HNO<sub>3</sub>-H<sub>2</sub>SO<sub>4</sub> stratospheric aerosols including gas phase removal of HNO<sub>3</sub>. *Geophysical Research Letters*. **22**(14), pp.1877–1880.
- Cashman, K. V. and Scheu, B. 2015. Magmatic Fragmentation *In: The Encyclopedia of Volcanoes*. Elsevier, pp.459–471.
- Crutzen, P.J. 2006. Albedo enhancement by stratospheric sulfur injections: A contribution to resolve a policy dilemma? *Climatic Change*. **77**(3–4), pp.211–220.
- Crutzen, P.J. 1976. The possible importance of CSO for the sulfate layer of the stratosphere. *Geophysical Research Letters*. **3**(2), pp.73–76.
- Damadeo, R.P., Zawodny, J.M., Remsberg, E.E. and Walker, K.A. 2018. The impact of nonuniform sampling on stratospheric ozone trends derived from occultation instruments. *Atmospheric Chemistry and Physics*. **18**(2), pp.535–554.

- Davies, T., Cullen, M.J.P., Malcolm, A.J., Mawson, M.H., Staniforth, A., White, A.A. and Wood, N. 2005. A new dynamical core of the Met Office's global and regional modelling of the atmosphere. *Quarterly Journal of the Royal Meteorological Society*. **131**(608), pp.1759–1782.
- Dee, D.P., Uppala, S.M., Simmons, A.J., Berrisford, P., Poli, P., Kobayashi, S., Andrae, U., Balmaseda, M.A., Balsamo, G., Bauer, P., Bechtold, P., Beljaars, A.C.M., van de Berg, L., Bidlot, J., Bormann, N., Delsol, C., Dragani, R., Fuentes, M., Geer, A.J., Haimberger, L., Healy, S.B., Hersbach, H., Hólm, E. V., Isaksen, L., Kållberg, P., Köhler, M., Matricardi, M., McNally, A.P., Monge-Sanz, B.M., Morcrette, J.J., Park, B.K., Peubey, C., de Rosnay, P., Tavolato, C., Thépaut, J.N. and Vitart, F. 2011. The ERA-Interim reanalysis: Configuration and performance of the data assimilation system. *Quarterly Journal of the Royal Meteorological Society*.
- DeFoor, T.E., Robinson, E. and Ryan, S. 1992. Early lidar observations of the June 1991 Pinatubo eruption plume at Mauna Loa Observatory, Hawaii. *Geophysical Research Letters*. **19**(2), pp.187–190.
- Deshler, T. 2008. A review of global stratospheric aerosol: Measurements, importance, life cycle, and local stratospheric aerosol. *Atmospheric Research*. **90**(2–4), pp.223–232.
- Deshler, T. 2016. In Situ Observations of Volatile and Nonvolatile Particle Size Distributions From Balloon-Borne Platforms *In: Volcanic Ash: Hazard Observation*. Elsevier Inc., pp.115–128.
- Deshler, T., Hofmann, D.J., Johnson, B.J. and Rozier, W.R. 1992. Balloonborne measurements of the Pinatubo aerosol size distribution and volatility at Laramie, Wyoming during the summer of 1991. *Geophysical Research Letters*. **19**(2), pp.199–202.
- Deshler, T., Johnson, B.J., Rozier, W.R. and Rozier, W.R. 1993. Balloonborne measurements of Pinatubo aerosol during 1991 and 1992 at 41 N: Vertical profiles, size distribution, and volatility. *Geophysical Research Letters*. **20**(14), pp.1435–1438.
- Dhomse, S.S., Chipperfield, M.P., Feng, W., Hossaini, R., Mann, G.W. and Santee, M.L. 2015. Revisiting the hemispheric asymmetry in midlatitude ozone changes

- following the Mount Pinatubo eruption: A 3-D model study. *Geophysical Research Letters*. **42**, pp.3038–3047.
- Dhomse, S.S., Emmerson, K.M., Mann, G.W., Bellouin, N., Carslaw, K.S., Chipperfield, M.P. and Hommel, R. 2014. Aerosol microphysics simulations of the Mt . Pinatubo eruption with the UM-UKCA composition-climate model. , pp.11221–11246.
- Dhomse, S.S., Mann, G.W., Carlos, J., Marrero, A., Shallcross, S.E., Chipperfield, M.P., Carslaw, K.S., Marshall, L., Abraham, N.L., Johnson, C.E., Dhomse, S. and Mann, G. 2020. Evaluating the simulated radiative forcings, aerosol properties and stratospheric warmings from the 1963 Agung, 1982 El Chichón and 1991 Mt Pinatubo volcanic aerosol clouds. *Atmospheric Chemistry and Physics*. **20**, pp.13627–13654.
- Driscoll, S., Bozzo, A., Gray, L.J., Robock, A. and Stenchikov, G. 2012. Coupled Model Intercomparison Project 5 (CMIP5) simulations of climate following volcanic eruptions. *Journal of Geophysical Research Atmospheres*. **117**(17).
- Durant, A.J., Bonadonna, C. and Horwell, C.J. 2010. Atmospheric and environmental impacts of volcanic particulates. *Elements*. **6**, pp.235–240.
- Dutton, E.G. and Christy, J.R. 1992. Solar Radiative Forcing at Selected Locations and Evidence for Global Lower Tropospheric Cooling Following the Eruptions of El-Chichon and Pinatubo. *Geophysical Research Letters*. **19**, pp.2313–2316.
- Dutton, E.G., Reddy, P., Ryan, S. and Deluisi, J.J. 1994. Features and effects of aerosol optical depth observed at Mauna Loa, Hawaii: 1982-1992. *Journal of Geophysical Research*. **99**(D4), pp.8295–8306.
- Dyer, J.A. 1974. The effect of volcanic eruptions on global turbidity, and an attempt to detect long-term trends due to man. *Quarterly Journal of the Royal Meteorological Society*. **100**, pp.563–571.
- Edwards, J.M. and Slingo, A. 1996. Studies with a flexible new radiation code. I: Choosing a configuration for a large-scale model. *Quarterly Journal of the Royal Meteorological Society*. **122**, pp.689–719.
- English, J.M., Toon, O.B. and Mills, M.J. 2013. Microphysical simulations of large volcanic eruptions: Pinatubo and Toba. *Journal of Geophysical Research*

*Atmospheres*. **118**(4), pp.1880–1895.

- Fahey, D.W., Kawa, S.R., Woodbridge, E.L., Tin, P., Wilson, J.C., Jonsson, I., H.H., Dye, J.E., Baumgardner, D., Borrmann, S., Toohey, D.W., Avallone, L.M., Proffitt, M.H., Margitan, J., Loewenstein, M., Podolske, J.R., Salawitch, R.J., Wofsy, S.C., Ko, M.K.W., Anderson, D.E., Schoeberl, M.R. and Chan, K.R. 1993. *In situ measurements constraining the role of sulphate aerosols in mid-latitude ozone depletion Data collection and model calculations*.
- Fernald, F.G., Herman, B.M. and Reagan, J.A. 1972. Determination of Aerosol Height Distributions by Lidar. *Journal of Applied Meteorology*. **11**, pp.482–489.
- Fiocco, G. and Grams, G. 1964. Observations of the Aerosol Layer at 20 km by Optical Radar. *Journal of The Atmospheric Sciences*. **21**, pp.323–324.
- Gooding, J.L., Clanton, U.S., Gabel, E.M. and Warren, J.L. 1983. *El Chichon volcanic ash in the stratosphere: particle abundances and size distributions after the 1982 eruption*.
- Grant, W.B., Browell, E. V., Long, C.S., Stowe, L.L., Grainger, R.G. and Lambert, A. 1996. Use of volcanic aerosols to study the tropical stratospheric reservoir. *Journal of Geophysical Research Atmospheres*. **101**(D2), pp.3973–3988.
- Gregg, J.S.B., Doiron, S.D., Schnetzler, C.C., Krueger, A.J. and Walter, L.S. 1992. Global tracking of the SO<sub>2</sub> clouds from the June 1991 Mount Pinatubo eruptions. *Geophysical Research Letters*. **19**(2), pp.151–154.
- Guo, S., Bluth, G.J.S., Rose, W.I., Watson, I.M. and Prata, A.J. 2004. Re-evaluation of SO<sub>2</sub> release of the 15 June 1991 Pinatubo eruption using ultraviolet and infrared satellite sensors. *Geochemistry, Geophysics, Geosystems*. **5**(4), pp.1–31.
- Guo, S., Rose, W.I., Bluth, G.J.S. and Watson, I.M. 2004. Particles in the great Pinatubo volcanic cloud of June 1991: The role of ice. *Geochemistry, Geophysics, Geosystems*. **5**(5), pp.1–35.
- Hamill, P., Jensen, E.J., Russell, P.B. and Bauman, J.J. 1997. The Life Cycle of Stratospheric Aerosol Particles. *Bulletin of the American Meteorological Society*. **78**(7), pp.1395–1410.
- Hansen, J., Laci, A., Ruedy, R. and Makiko, S. 1992. Potential climate impact of mount Pinatubo eruption. *Geophysical Research Letters*. **19**(2), pp.215–218.

- Hansen, J., Sato, M., Ruedy, R., Lacis, A., Asamoah, K., Borenstein, S., Brown, E., Cairns, B., Caliri, G., Campbell, M., Curran, B., de Castro, S., Druyan, L., Fox, M., Johnson, C., Lerner, J., McCormick, M.P., Miller, R., Minnis, P., Morrison, A., Pandolfo, L., Ramberrann, I., Zaucker, F., Robinson, M., Russell, P., Shah, K., Stone, P., Tegen, I., Thomason, L., Wilder, J. and Wilson, H. 1996. A Pinatubo Climate Modeling Investigation *In: The Mount Pinatubo Eruption*. Springer Berlin Heidelberg, pp.233–272.
- Hansen, J., Sato, M., Ruedy, R., Nazarenko, L., Lacis, A., Schmidt, G.A., Russell, G., Aleinov, I., Bauer, M., Bauer, S., Bell, N., Cairns, B., Canuto, V., Chandler, M., Cheng, Y., Del Genio, A., Faluvegi, G., Fleming, E., Friend, A., Hall, T., Jackman, C., Kelley, M., Kiang, N., Koch, D., Lean, J., Lerner, J., Lo, K., Menon, S., Miller, R., Minnis, P., Novakov, T., Oinas, V., Perlwitz, J., Perlwitz, J., Rind, D., Romanou, A., Shindell, D., Stone, P., Sun, S., Tausnev, N., Thresher, D., Wielicki, B., Wong, T., Yao, M. and Zhang, S. 2005. Efficacy of climate forcings. *Journal of Geophysical Research D: Atmospheres*. **110**(18), pp.1–45.
- Hayashida, S., Kobayashi, A. and Iwasaka, Y. 1984. Lidar measurements of stratospheric aerosol content and depolarisation ratios after the eruption of El Chichon volcano: measurements at Nagoya, Japan. *Geofisica International*. **23**(2), pp.277–288.
- Haywood, J.M., Jones, A., Bellouin, N. and Stephenson, D. 2013. Asymmetric forcing from stratospheric aerosols impacts Sahelian rainfall. *Nature Climate Change*. **3**(7), pp.660–665.
- Hitchman, M.H., McKay, M. and Trepte, C.R. 1994. A climatology of stratospheric aerosol. *Journal of Geophysical Research*. **99**(D10).
- Hofmann, D.J., Oltmans, S.J., Komhyr, W.D., Harris, J.M., Lathrop, J.A., Langford, A.O., Deshler, T., Johnson, B.J., Torres, A. and Matthews, W.A. 1994. Ozone loss in the lower stratosphere over the United States in 1992-1993: Evidence for heterogeneous chemistry on the Pinatubo aerosol. *Geophysical Research Letters*. **21**(1), pp.65–68.
- Hofmann, D.J., Rosen, J.M. and Gringel, W. 1985. Delayed production of sulfuric acid condensation nuclei in the polar stratosphere, from El Chichon volcanic vapors. *Journal of Geophysical Research*. **90**(D1), pp.2341–2354.

- Hofmann, D.J. and Solomon, S. 1989. Ozone Destruction Through Heterogeneous Chemistry Following the Eruption of El Chichón. *Journal of Geophysical Research*. **94**(D4), pp.5029–5041.
- Holton, J.R., Haynes, P.H., McIntyre, M.E., Douglass, A.R., Rood, R.B. and Pfister, L. 1995. Stratosphere-Troposphere exchange. *Reviews of Geophysics*. **33**(4), pp.403–439.
- Iles, C.E. and Hegerl, G.C. 2014. The global precipitation response to volcanic eruptions in the CMIP5 models. *Environmental Research Letters*. **9**, pp.1–10.
- Irvine, P.J., Kravitz, B., Lawrence, M.G. and Muri, H. 2016. An overview of the Earth system science of solar geoengineering. *Wiley Interdisciplinary Reviews: Climate Change*. **7**(6), pp.815–833.
- Jacob, J.D. 1999. *Introduction to Atmospheric Chemistry*. Princeton, New Jersey: Princeton University Press.
- Jäger, H. 2005. Long-term record of lidar observations of the stratospheric aerosol layer at Garmisch-Partenkirchen. *Journal of Geophysical Research*. **110**, pp.1–9.
- Jäger, H. 1992. The Pinatubo eruption cloud observed by lidar at Garmisch-Partenkirchen. *Geophysical Research Letters*. **19**(2), pp.191–194.
- Jäger, H. and Deshler, T. 2003. Correction to ‘Lidar backscatter to extinction, mass and area conversions for stratospheric aerosols based on midlatitude balloonborne size distribution measurements’. *Geophysical Research Letters*. **30**(7), p.1.
- Jäger, H. and Deshler, T. 2002. Lidar backscatter to extinction, mass and area conversions for stratospheric aerosols based on midlatitude balloonborne size distribution measurements. *Geophysical Research Letters*. **29**(19), pp.1–4.
- Jäger, H., Uchino, O., Nagai, T., Fujimoto, T., Freudenthaler, V. and Homburg, F. 1995. Ground-based remote sensing of the decay of the Pinatubo eruption cloud at three northern hemisphere sites. *Geophysical Research Letters*. **22**(5), pp.607–610.
- Johnson, B.T. and Osborne, S.R. 2011. Physical and optical properties of mineral dust aerosol measured by aircraft during the gerbils campaign. *Quarterly Journal of the Royal Meteorological Society*. **137**(658), pp.1117–1130.
- Jones, A.C., Haywood, J.M., Dunstone, N., Emanuel, K., Hawcroft, M.K., Hodges, K.I. and Jones, A. 2017. Impacts of hemispheric solar geoengineering on tropical

- cyclone frequency. *Nature Communications.*, pp.1–10.
- Jones, A.C., Haywood, J.M., Jones, A. and Aquila, V. 2016. Sensitivity of volcanic aerosol dispersion to meteorological conditions: A Pinatubo case study. *Journal of Geophysical Research: Atmospheres.* **121**(12), pp.6892–6908.
- Jones, G.S., Gregory, J.M., Stott, P.A., Tett, S.F.B. and Thorpe, R.B. 2005. An AOGCM simulation of the climate response to a volcanic super-eruption. *Climate Dynamics.* **25**(7–8), pp.725–738.
- Junge, C.E., Chagnon, C.W. and Manson, J.E. 1961. Stratospheric Aerosols. *Journal of Meteorology.* **18**, pp.81–108.
- Junge, C.E. and Manson, J.E. 1961. Stratospheric Aerosol Studies. *Journal of Geophysical Research.* **66**(7), pp.2163–2182.
- Kasten, F. 1968. Falling Speed of Aerosol Particles. *Journal of Applied Meteorology.* **7**(5), pp.944–947.
- Kinne, S., Toon, O.B. and Prather, M.J. 1992. Buffering of stratospheric circulation by changing amounts of tropical ozone: A Pinatubo case study. *Geophysical Research Letters.* **19**(19), pp.1927–1930.
- Kipling, Z., Stier, P., Schwarz, J.P., Perring, A.E., Spackman, J.R., Mann, G.W., Johnson, C.E. and Telford, P.J. 2013. Constraints on aerosol processes in climate models from vertically-resolved aircraft observations of black carbon. *Atmospheric Chemistry and Physics.* **13**(12), pp.5969–5986.
- Kleinschmitt, C., Boucher, O. and Platt, U. 2018. Sensitivity of the radiative forcing by stratospheric sulfur geoengineering to the amount and strategy of the SO<sub>2</sub> injection studied with the LMDZ-S3A model. *Atmospheric Chemistry and Physics.* **18**(4), pp.2769–2786.
- Kokkola, H., Hommel, R., Kazil, J., Niemeier, U., Partanen, A.-I., Feichter, J. and Timmreck, C. 2009. *Geoscientific Model Development Aerosol microphysics modules in the framework of the ECHAM5 climate model-intercomparison under stratospheric conditions* [Online]. Available from: [www.geosci-model-dev.net/2/97/2009/](http://www.geosci-model-dev.net/2/97/2009/).
- Korhonen, H., Napari, I., Timmreck, C., Vehkamäki, H., Pirjola, L., Lehtinen, K.E.J., Lauri, A. and Kulmala, M. 2003. Heterogeneous nucleation as a potential sulphate-

- coating mechanism of atmospheric mineral dust particles and implications of coated dust on new particle formation. *Journal of Geophysical Research*. **108**(D17, 4546), pp.1–9.
- Kremser, S., Thomason, L.W., von Hobe, M., Hermann, M., Deshler, T., Timmreck, C., Toohey, M., Stenke, A., Schwarz, J.P., Weigel, R., Fueglistaler, S., Prata, F.J., Vernier, J.-P., Schlager, H., Barnes, J.E., Antuña-Marrero, J.-C., Fairlie, D., Palm, M., Mahieu, E., Notholt, J., Rex, M., Bingen, C., Vanhellemont, F., Bourassa, A., Plane, J.M.C., Klocke, D., Carn, S.A., Clarisse, L., Trickl, T., Neely, R., James, A.D., Rieger, L., Wilson, J.C. and Meland, B. 2016. Stratospheric aerosol - Observations, processes and impact on climate. *Reviews of Geophysics*. **54**, pp.278–335.
- Kulmala, M., Laaksonen, A. and Pirjola, L. 1998. Parameterizations for sulfuric acid/water nucleation rates. *Journal of Geophysical Research*. **103**(D7), pp.8301–8307.
- Kulmala, M., Vehkamäki, H., Petäjä, T., Dal Maso, M., Lauri, A., Kerminen, V.M., Birmili, W. and McMurry, P.H. 2004. Formation and growth rates of ultrafine atmospheric particles: A review of observations. *Journal of Aerosol Science*. **35**(2), pp.143–176.
- Labitzke, K. and McCormick, M.P. 1992. Stratospheric temperature increases due to Pinatubo aerosols. *Geophysical Research Letters*. **19**(2), pp.207–210.
- Lacis, A., Hansen, J. and Sato, M. 1992. Climate forcing by stratospheric aerosols. *Geophysical Research Letters*. **19**(15), p.1607.
- Langmann, B. 2014. On the role of climate forcing by volcanic sulphate and volcanic ash. *Advances in Meteorology*., pp.1–17.
- Long, C.S. and Stowe, L.L. 1994. Using the NOAA/AVHRR to study stratospheric aerosol optical thicknesses following the Mt Pinatubo eruption. *Geophysical Research Letters*. **21**(20), pp.2215–2218.
- Loosmore, G.A. and Cederwall, R.T. 2004. Precipitation Scavenging of atmospheric aerosols for emergency response applications: testing an updated model with new real-time data. *Atmospheric Environment*. **38**, pp.993–1003.
- Lynch, J.S. and Stephens, G. 1996. Mount Pinatubo: A Satellite Perspective of the June

- 1991 Eruptions In: R. S. P. C.G. Newhall, ed. *Fire and Mud: The Eruptions and Lahars of Mount Pinatubo, Philippines*. Quezon City, Philippine Institute of Volcanology and Seismology: University of Washington Press, Seattle, pp.637–646.
- Mann, G.W., Carslaw, K.S., Reddington, C.L., Pringle, K.J., Schulz, M., Asmi, A., Spracklen, D. V., Ridley, D.A., Woodhouse, M.T., Lee, L.A., Zhang, K., Ghan, S.J., Easter, R.C., Liu, X., Stier, P., Lee, Y.H., Adams, P.J., Tost, H., Lelieveld, J., Bauer, S.E., Tsigaridis, K., Van Noije, T.P.C., Strunk, A., Vignati, E., Bellouin, N., Dalvi, M., Johnson, C.E., Bergman, T., Kokkola, H., Von Salzen, K., Yu, F., Luo, G., Petzold, A., Heintzenberg, J., Clarke, A., Ogren, J.A., Gras, J., Baltensperger, U., Kaminski, U., Jennings, S.G., O’Dowd, C.D., Harrison, R.M., Beddows, D.C.S., Kulmala, M., Viisanen, Y., Ulevicius, V., Mihalopoulos, N., Zdimal, V., Fiebig, M., Hansson, H.C., Swietlicki, E. and Henzing, J.S. 2014. Intercomparison and evaluation of global aerosol microphysical properties among AeroCom models of a range of complexity. *Atmospheric Chemistry and Physics*. **14**(9), pp.4679–4713.
- Mann, G.W., Carslaw, K.S., Ridley, D.A., Spracklen, D. V., Pringle, K.J., Merikanto, J., Korhonen, H., Schwarz, J.P., Lee, L.A., Manktelow, P.T., Woodhouse, M.T., Schmidt, A., Breider, T.J., Emmerson, K.M., Reddington, C.L., Chipperfield, M.P. and Pickering, S.J. 2012. Intercomparison of modal and sectional aerosol microphysics representations within the same 3-D global chemical transport model. *Atmospheric Chemistry and Physics*. **12**(10), pp.4449–4476.
- Mann, G.W., Carslaw, K.S., Spracklen, D. V., Ridley, D.A., Manktelow, P.T., Chipperfield, M.P., Pickering, S.J. and Johnson, C.E. 2010. Description and evaluation of GLOMAP-mode: A modal global aerosol microphysics model for the UKCA composition-climate model. *Geoscientific Model Development*. **3**(2), pp.519–551.
- Marshall, L., Johnson, J.S., Mann, G.W., Lee, L., Dhomse, S.S., Regayre, L., Yoshioka, M., Carslaw, K.S. and Schmidt, A. 2019. Exploring How Eruption Source Parameters Affect Volcanic Radiative Forcing Using Statistical Emulation. *Journal of Geophysical Research: Atmospheres*. **124**(2), pp.964–985.
- Marshall, L., Schmidt, A., Toohey, M., Carslaw, K.S., Mann, G.W., Sigl, M., Khodri,

- M., Timmreck, C., Zanchettin, D., Ball, W.T., Bekki, S., Brooke, J., Dhomse, S., Johnson, C., Lamarque, J.F., Legrande, A.N., Mills, M.J., Niemeier, U., Pope, J.O., Poulain, V., Robock, A., Rozanov, E., Stenke, A., Sukhodolov, T., Tilmes, S., Tsigaridis, K. and Tummon, F. 2018. Multi-model comparison of the volcanic sulfate deposition from the 1815 eruption of Mt. Tambora. *Atmospheric Chemistry and Physics*. **18**(3), pp.2307–2328.
- Maters, E.C., Delmelle, P., Rossi, M.J. and Ayris, P.M. 2017. Reactive Uptake of Sulfur Dioxide and Ozone on Volcanic Glass and Ash at Ambient Temperature. *Journal of Geophysical Research: Atmospheres*. **122**(18), 10,077-10,088.
- McCormick, M.P. 1992. *Sixteenth International Laser Radar Conference*.
- McCormick, M.P. and Fuller, W.H. 1973. Lidar techniques for pollution studies. *American Institute of Aeronautics and Astronautics*. **11**(2), pp.244–246.
- McCormick, M.P., Thomason, L.W. and Trepte, C.R. 1995. Atmospheric effects of the Mt Pinatubo eruption. *Nature*. **373**(2), p.399.
- McCormick, M.P. and Veiga, R.E. 1992. SAGE II Measurements of early Pinatubo aerosols. *Geophysical Research Letters*. **19**(2), pp.155–158.
- McGill, M. 2002. *Lidar Remote Sensing*.
- Metzner, D., Kutterolf, S., Toohey, M., Timmreck, C., Niemeier, U., Freundt, A. and Krüger, K. 2014. Radiative forcing and climate impact resulting from SO<sub>2</sub> injections based on a 200,000-year record of Plinian eruptions along the Central American Volcanic Arc. *International Journal of Earth Sciences*. **103**(7), pp.2063–2079.
- Mills, M.J., Richter, J.H., Tilmes, S., Kravitz, B., Macmartin, D.G., Glanville, A.A., Tribbia, J.J., Lamarque, J.F., Vitt, F., Schmidt, A., Gettelman, A., Hannay, C., Bacmeister, J.T. and Kinnison, D.E. 2017. Radiative and chemical response to interactive stratospheric sulfate aerosols in fully coupled CESM1(WACCM). *Journal of Geophysical Research: Atmospheres*. **122**(23), 13,061-13,078.
- Mills, M.J., Schmidt, A., Easter, R., Solomon, S., Kinnison, D.E., Ghan, S.J., Neely III, R.R., Marsh, D.R., Conley, A., Bardeen, C.G. and Gettelman, A. 2016. Global volcanic aerosol properties derived from emissions, 1990–2014, using CESM1(WACCM). *Journal of Geophysical Research: Atmospheres*. **121**, pp.1–17.

- Mills, M.J., Toon, O.B., Vaida, V., Hintze, P.E., Kjaergaard, H.G., Schofield, D.P. and Robinson, T.W. 2005. Photolysis of sulfuric acid vapor by visible as a source of the polar stratospheric CN layer. *Journal of Geophysical Research*. **110**(D08201), pp.1–7.
- Minnis, P., Stowe, H.L.L., Gibson, G.G., Denn, F.M., Doelling, D.R. and Smith, W.L. 1993. Radiative climate forcing by the Mount Pinatubo eruption. *Science*. **259**(5100), pp.1411–1415.
- Mossop, S.C. 1965. *Stratospheric particles at 20 km altitude*. Pergamon Press Ltd.
- Mossop, S.C. 1964. Volcanic dust collected at an altitude of 20km. *Nature*. **203**(4947), pp.824–827.
- Muser, L.O., Hoshyaripour, G.A., Bruckert, J., Horvath, A., Malinina, E., Peglow, S., Prata, F.J., Rozanov, A., Von Savigny, C., Vogel, H. and Vogel, B. 2020. Particle Aging and Aerosol-Radiation Interaction Affect Volcanic Plume Dispersion: Evidence from Raikoke Eruption 2019. *Atmospheric Chemistry and Physics Discussion*.
- Nagai, T., Uchino, O., Fujimoto, T., Sai, Y., Tamashiro, K., Nomura, R. and Sunagawa, T. 1993. Lidar Observation of the Stratospheric Aerosol Layer over Okinawa, Japan, after the Mt. Pinatubo Volcanic Eruption. *Journal of the Meteorological Society of Japan*. **71**(6), pp.749–755.
- NDACC 2020. Network for the Detection of Atmospheric Composition Change. Available from: <http://www.ndaccdemo.org/>.
- Newhall, C.G. and Self, S. 1982. The Volcanic Explosivity Index (VEI): An Estimate of Explosive Magnitude for Historical Volcanism. *JOURNAL OF GEOPHYSICAL RESEARCH*. **87**(C2), pp.1231–1238.
- Newhall, C.G., Stauffer, P.H. and Hendley II, J.W. 1997. *Lahars of Mount Pinatubo, Philippines*.
- Niemeier, U. and Schmidt, H. 2017. Changing transport processes in the stratosphere by radiative heating of sulfate aerosols. *Atmospheric Chemistry and Physics*.
- Niemeier, U., Schmidt, H. and Timmreck, C. 2011. The dependency of geoengineered sulfate aerosol on the emission strategy. *Atmospheric Science Letters*. **12**(2), pp.189–194.

- Niemeier, U. and Timmreck, C. 2015. What is the limit of climate engineering by stratospheric injection of SO<sub>2</sub>? *Atmospheric Chemistry and Physics*. **15**(16), pp.9129–9141.
- Niemeier, U., Timmreck, C., Graf, H.-F., Kinne, S., Rast, S. and Self, S. 2009. Initial fate of fine ash and sulfur from large volcanic eruptions. *Atmospheric Chemistry and Physics Discussions*. **9**(4), pp.17531–17577.
- Northam, G.B., Rosen, J.M., Melfi, S.H., Pepin, T.J., McCormick, M.P., Hofmann, D.J. and Fuller, W.H. 1974. Dustsonde and Lidar Measurements of Stratospheric Aerosols: a Comparison. *Applied Optics*. **13**(10), pp.2416–2421.
- Pinto, J.P., Turco, R.P. and Toon, O.B. 1989. Self-Limiting Physical and Chemical Effects in Volcanic Eruption Clouds. *Journal of Geophysical Research*. **94**(D8), 11,165-11,174.
- Plumb, R.A. 1996. A ‘tropical pipe’ model of stratospheric transport. *Journal of Geophysical Research Atmospheres*. **101**(D2), pp.3957–3972.
- Post, M.J., Grund, C.J., Langford, A.O. and Proffitt, M.H. 1992. Observations of Pinatubo ejecta over Boulder, Colorado by lidars of three different wavelengths. *Geophysical Research Letters*. **19**(2), pp.195–198.
- Prata, A.T., Young, S.A., Siems, S.T. and Manton, M.J. 2017. Lidar ratios of stratospheric volcanic ash and sulfate aerosols retrieved from CALIOP measurements. *Atmospheric Chemistry and Physics*. **17**(13), pp.8599–8618.
- Prata, F. and Rose, B. 2015. Volcanic Ash Hazards to Aviation In: *The Encyclopedia of Volcanoes*. Elsevier, pp.911–934.
- Pringle, K. 2006. *Aerosol-cloud interactions in a global model of aerosol microphysics*. University of Leeds.
- Pueschel, R.F., Russell, P.B., Allen, D.A., Ferry, G.V., Snetsinger, K.G., Livingston, J. and Verma, S. 1994. Physical and optical properties of the Pinatubo volcanic aerosol: Aircraft observations with impactors and a Sun-tracking photometer. *Geophysical Research Letters*. **99**(D6), 12,915-12,922.
- Puma, M.J., Bose, S., Chon, S.Y. and Cook, B.I. 2015. Assessing the evolving fragility of the global food system. *Environmental Research Letters*. **10**(2).
- Punge, H.J., Konopka, P., Giorgetta, M.A. and Müller, R. 2009. Effects of the quasi-

- biennial oscillation on low-latitude transport in the stratosphere derived from trajectory calculations. *Journal of Geophysical Research Atmospheres*. **114**(3).
- Ramachandran, S., Ramaswamy, V., Stenchikov, G.L. and Robock, A. 2000. Radiative impact of the Mount Pinatubo volcanic eruption: Lower stratospheric response. *Journal of Geophysical Research*. **105**, p.24409.
- Randel, W.J., Wu, F., Waters, J.W. and Froidevaux, L. 1995. Ozone and temperature changes in the stratosphere following the eruption of Mount Pinatubo. *Journal of Geophysical Research*. **100**(D8), pp.16753–16764.
- Read, W.G., Froidevaux, L. and Waters, J.W. 1993. Microwave Limb Sounder measurement of stratospheric SO<sub>2</sub> from the Mt. Pinatubo volcano. *Geophysical Research Letters*. **20**, pp.1299–1301.
- Remy, S., Boucher, O. and Mann, G.W. 2018. *Assistance to ECMWF in setting up and validating simulations of volcanic eruptions*. CAMS43 phase 1 Deliverable report D43.1.5.1, July 2018.
- Remy, S., Huijnen, V., Mann, G.W., Sengupta, K. and Chabrillat, S. 2019. *Coupling of IFS-GLOMAP and IFS-CB05-BASCOE*.
- Revell, L.E., Stenke, A., Luo, B., Kremser, S., Rozanov, E., Sukhodolov, T. and Peter, T. 2017. Impacts of Mt Pinatubo volcanic aerosol on the tropical stratosphere in chemistry-climate model simulations using CCM1 and CMIP6 stratospheric aerosol data. *Atmospheric Chemistry and Physics*. **17**, 13,139-13,150.
- Ridley, D. and Solomon, S. 2014. Total volcanic stratospheric aerosol optical depths and implications for global climate change. *Geophysical ...*, pp.1–7.
- Robock, A. 2000. *Volcanic Eruptions and Climate*. . (1998), pp.191–219.
- Robock, A. and Antuña, J.C. 2001. Support for a tropical lidar in latin America. *Eos*. **82**(26), pp.285–289.
- Rose, W.I. and Durant, A.J. 2009. Fine ash content of explosive eruptions. *Journal of Volcanology and Geothermal Research*. **186**(1–2), pp.32–39.
- Russell, P.B., Livingston, J.M., Pueschel, R.F., Bauman, J.J., Pollack, J.B., Brooks, S.L., Hamill, P., Thomason, L.W., Stowe, L.L., Deshler, T., Dutton, E.G. and Bergstrom, R.W. 1996. Global to microscale evolution of the Pinatubo volcanic aerosol derived from diverse measurements and analyses. *Journal of Geophysical*

- Research: Atmospheres*. **101**(D13), pp.18745–18763.
- Russell, P.B., Swissler, T.J. and McCormick, M.P. 1979. Methodology for error analysis and simulation of lidar aerosol measurements. *Applied Optics*. **18**(22), pp.3783–3797.
- di Sarra, A., Bernardini, L., Cacciani, M., Fiocco, G. and Fuà, D. 1998. Stratospheric aerosols observed by lidar over northern Greenland in the aftermath of the Pinatubo eruption. *Journal of Geophysical Research*. **103**(D13), 13,873-13,891.
- Sato, M., Hansen, J.E., McCormick, M.P. and Pollack, J.B. 1993. Stratospheric aerosol optical depths, 1850-1990. . **98**(D12), 22,987-22,994.
- Saxby, J., Beckett, F., Cashman, K., Rust, A. and Tennant, E. 2018. The impact of particle shape on fall velocity: Implications for volcanic ash dispersion modelling. *Journal of Volcanology and Geothermal Research*. **362**, pp.32–48.
- Schmidt, A., Mills, M.J., Ghan, S., Gregory, J.M., Allan, R.P., Andrews, T., Bardeen, C.G., Conley, A., Forster, P.M., Gettelman, A., Portmann, R.W., Solomon, S. and Toon, O.B. 2018. Volcanic Radiative Forcing From 1979 to 2015. *Journal of Geophysical Research: Atmospheres*.
- Schneider, D.P., Ammann, C.M., Otto-Bliesner, B.L. and Kaufman, D.S. 2009. Climate response to large, high-latitude and low-latitude volcanic eruptions in the community climate system model. *Journal of Geophysical Research Atmospheres*. **114**(15).
- Seinfeld, J.H. and Pandis, S.N. 2006. *Atmospheric Chemistry and Physics*. Hoboken, New Jersey: John Wiley.
- Self, S., Zhao, J.-X., Holasek, R.E., Torres, R.C. and King, A.J. 1996. The atmospheric impact of the Mount Pinatubo eruption *In*: R. S. Newhall, C.G., and Punongbayan, ed. *Fire and Mud: Eruptions and lahars of Mount Pinatubo, Philippines*. Quezon City, Philippine Institute of Volcanology and Seismology: University of Washington Press, Seattle, pp.1089–1115.
- Shapiro, M.A. 1980. Turbulent Mixing within Tropopause Folds as a Mechanism for the Exchange of Chemical Constituents between the Stratosphere and Troposphere. *Journal of Atmospheric Sciences*. **37**(5), pp.994–1004.
- Sheng, J.X., Weisenstein, D.K., Luo, B.P., Rozanov, E., Arfeuille, F. and Peter, T.

2015. A perturbed parameter model ensemble to investigate Mt. Pinatubo's 1991 initial sulfur mass emission. *Atmospheric Chemistry and Physics*. **15**(20), pp.11501–11512.
- Sheridan, P.J., Schnell, R.C., Hofmann, D. 1 and Deshler, T. 1992. Electron microscope studies of Mt Pinatubo aerosol layers over Laramie, Wyoming during summer 1991. *Geophysical Research Letters*. **19**(2), pp.203–206.
- Sigl, M., Winstrup, M., McConnell, J.R., Welten, K.C., Plunkett, G., Ludlow, F., Büntgen, U., Caffee, M., Chellman, N., Dahl-Jensen, D., Fischer, H., Kipfstuhl, S., Kostick, C., Maselli, O.J., Mekhaldi, F., Mulvaney, R., Muscheler, R., Pasteris, D.R., Pilcher, J.R., Salzer, M., Schüpbach, S., Steffensen, J.P., Vinther, B.M. and Woodruff, T.E. 2015. Timing and climate forcing of volcanic eruptions for the past 2,500 years. *Nature*. **523**(7562), pp.543–549.
- Slinn, W.G.N. 1982. Predictions for particle deposition to vegetative canopies. *Atmospheric Environment*. **16**(7), pp.1785–1794.
- Solomon, S. 1999. Stratospheric ozone depletion: A review of concepts and history. *Reviews of Geophysics*. **37**(3), pp.275–316.
- Solomon, S., Ivy, D.J., Kinnison, D., Mills, M.J., Neely III, R.R. and Schmidt, A. 2016. Emergence of healing in the Antarctic ozone layer. *Science*. **353**(6296), pp.269–274.
- SPARC 2010. Chapter 8: Natural Variability of Stratospheric Ozone *In*: V. Eyring, T. Shepherd and D. Waugh, eds. *CCMVal Report on the Evaluation of Chemistry-Climate Models*. [Online]. , WCRP-30/2010, WMO/TD – No. 40, pp.306–426. Available from: [www.sparc-climate.org/publications/sparc-reports/](http://www.sparc-climate.org/publications/sparc-reports/).
- SPARC 2006. SPARC Assessment of stratospheric aerosol properties (ASAP) *In*: L. Thomason and T. Peter, eds. *Stratospheric Processes and their role in Climate* [Online]. Available from: [www.sparc-climate.org/publications/sparc-reports/](http://www.sparc-climate.org/publications/sparc-reports/).
- Spracklen, D. V, Pringle, K.J., Carslaw, K.S., Chipperfield, M.P. and Mann, G.W. 2005. A global off-line model of size-resolved aerosol microphysics: I. Model development and prediction of aerosol properties. *Atmospheric Chemistry and Physics*. **5**, pp.2227–2252.
- Spracklen, D. V, Pringle, K.J., Carslaw, K.S., Mann, G.W., Manktelow, P. and

- Heintzenberg, J. 2007. Evaluation of a global aerosol microphysics model against size-resolved particle statistics in the marine atmosphere. *Atmospheric Chemistry and Physics*. **7**, pp.2073–2090.
- Stenchikov, G.L., Kirchner, I., Robock, A., Graf, H.-F., Antuña, J.C., Grainger, R.G., Lambert, A. and Thomason, L. 1998. Radiative forcing from the 1991 Mount Pinatubo volcanic eruption. *Journal of Geophysical Research*. **103**, pp.13837–13857.
- Stevens, T.D., Haris, P.A.T., Rau, Y.C. and Philbrick, C.R. 1994. Latitudinal lidar mapping of stratospheric particle layers. *Advances in Space Research*. **14**(9), pp.193–198.
- Stoffel, M., Khodri, M., Corona, C., Guillet, S., Poulain, V., Bekki, S., Guiot, J., Luckman, B.H., Oppenheimer, C., Lebas, N., Beniston, M. and Masson-Delmotte, V. 2015. Estimates of volcanic-induced cooling in the Northern Hemisphere over the past 1,500 years. *Nature Geoscience*. **8**(10), pp.784–788.
- Stowe, L.L., Carey, R.M. and Pellegrino, P.P. 1992. Monitoring the Mt Pinatubo aerosol layer with NOAA/11 AVHRR data. *Geophysical Research Letters*. **19**(2), pp.159–162.
- Sukhodolov, T., Sheng, J.-X., Feinberg, A., Luo, B.-P., Peter, T., Revell, L., Stenke, A., Weisenstein, D.K. and Rozanov, E. 2018. Size-Resolved Stratospheric Aerosol Distributions after Pinatubo Derived from a Coupled Aerosol-Chemistry-Climate Model. *Geoscientific Model Development Discussions*. **11**, pp.2633–2647.
- Tabazadeh, A., Drdla, K., Schoeberl, M.R., Hamill, P. and Toon, O.B. 2002. Arctic “ozone hole” in a cold volcanic stratosphere. *PNAS*. **99**(5), pp.2609–2612.
- Telford, P.J., Braesicke, P., Morgenstern, O. and Pyle, J.A. 2008. Technical Note: Description and assessment of a nudged version of the new dynamics Unified Model. *Atmospheric Chemistry and Physics*. **8**, pp.1701–1712.
- Textor, C., Graf, H.-F., Timmreck, C. and Robock, A. 2003. Chapter 7 - Emissions from volcanoes *In: Emissions of Chemical Compounds and Aerosols in the Atmosphere.*, pp.1–32.
- Thomas, M.A., Giorgetta, M.A., Timmreck, C., Graf, H.F. and Stenchikov, G. 2009. Simulation of the climate impact of Mt. Pinatubo eruption using ECHAM5-Part 2:

- Sensitivity to the phase of the QBO and ENSO. *Atmospheric Chemistry and Physics*. **9**(9), pp.3001–3009.
- Thomason, L.W. 1992. Observations of a new SAGE-II aerosol extinction mode following the eruption of Mount Pinatubo. *Geophysical Research Letters*. **19**(21), pp.2179–2182.
- Thomason, L.W., Ernest, N., Millán, L., Rieger, L., Bourassa, A., Vernier, J.P., Manney, G., Luo, B., Arfeuille, F. and Peter, T. 2018. A global space-based stratospheric aerosol climatology: 1979-2016. *Earth System Science Data*. **10**(1), pp.469–492.
- Thomason, L.W. and Osborn, M.T. 1992. Lidar conversion parameters derived from SAGE II extinction measurements. *Geophysical Research Letters*. **19**(16), pp.1655–1658.
- Tie, X. and Brasseur, G. 1995. The response of stratospheric ozone to volcanic eruptions: Sensitivity to atmospheric chlorine loading. *Geophysical Research Letters*. **22**(22), pp.3035–3038.
- Tilmes, S., Richter, J.H., Mills, M.J., Kravitz, B., MacMartin, D.G., Garcia, R.R., Kinnison, D.E., Lamarque, J.F., Tribbia, J. and Vitt, F. 2018. Effects of Different Stratospheric SO<sub>2</sub> Injection Altitudes on Stratospheric Chemistry and Dynamics. *Journal of Geophysical Research: Atmospheres*. **123**(9), pp.4654–4673.
- Timmreck, C. 2012. Modeling the climatic effects of large explosive volcanic eruptions. *Wiley Interdisciplinary Reviews: Climate Change*. **3**(6), pp.545–564.
- Timmreck, C., Graf, H.F. and Feichter, J. 1999. Simulation of Mt. Pinatubo Volcanic Aerosol with the Hamburg Climate Model ECHAM4. *Theoretical and Applied Climatology*. **62**, pp.85–108.
- Timmreck, C., Graf, H.F. and Kirchner, I. 1999. A one and half year interactive MA/ECHAM4 simulation of Mount Pinatubo Aerosol. *Journal of Geophysical Research*. **104**(D8), pp.9337–9359.
- Timmreck, C., Graf, H.F., Lorenz, S.J., Niemeier, U., Zanchettin, D., Matei, D., Jungclaus, J.H. and Crowley, T.J. 2010. Aerosol size confines climate response to volcanic super-eruptions. *Geophysical Research Letters*. **37**(24).
- Timmreck, C., Lorenz, S.J., Crowley, T.J., Kinne, S., Raddatz, T.J., Thomas, M.A. and

- Jungclaus, J.H. 2009. Limited temperature response to the very large AD 1258 volcanic eruption. *Geophysical Research Letters*. **36**(L21708), pp.1–5.
- Timmreck, C., Mann, G.W., Aquila, V., Hommel, R., Lee, L.A., Schmidt, A., Brühl, C., Carn, S., Chin, M., Dhomse, S.S., Diehl, T., English, J.M., Mills, M.J., Neely, R., Sheng, J., Toohey, M. and Weisenstein, D. 2018. The Interactive Stratospheric Aerosol Model Intercomparison Project (ISA-MIP): Motivation and experimental design. *Geoscientific Model Development*.
- Toohey, M., Krüger, K., Niemeier, U. and Timmreck, C. 2011. The influence of eruption season on the global aerosol evolution and radiative impact of tropical volcanic eruptions. *Atmospheric Chemistry and Physics*. **11**, 12,351–23,367.
- Toohey, M., Krüger, K., Sigl, M., Stordal, F. and Svensen, H. 2016. Climatic and societal impacts of a volcanic double event at the dawn of the Middle Ages. *Climatic Change*. **136**(3–4), pp.401–412.
- Trepte, C.R. and Hitchman, M.H. 1992. Tropical stratospheric circulation deduced from satellite aerosol data. *Nature*. **355**(6361), pp.626–628.
- Trepte, C.R., Veiga, R.E. and McCormick, M.P. 1993. The poleward dispersal of Mount Pinatubo volcanic aerosol. *Journal of Geophysical Research*. **98**, 18,563–18,573.
- Turco, R.P., Hamill, P., Toon, O.B., Whitten, R.C. and Kiang, C.S. 1979. A one-dimensional model describing aerosol formation and evolution in the stratosphere: I. physical processes and mathematical analogs. *Journal of Atmospheric Sciences*. **36**, pp.699–717.
- Turco, R.P., Toon, O.B., Whitten, R.C., Hamill, P. and Keesee, R.G. 1983. The 1980 eruptions of Mount St Helens: physical and chemical processes in the stratospheric clouds. *Journal of Geophysical Research*. **88**(C9), pp.5299–5319.
- Turnock, S.T., Spracklen, D. V., Carslaw, K.S., Mann, G.W., Woodhouse, M.T., Forster, P.M., Haywood, J., Johnson, C.E., Dalvi, M., Bellouin, N. and Sanchez-Lorenzo, A. 2015. Modelled and observed changes in aerosols and surface solar radiation over Europe between 1960 and 2009. *Atmospheric Chemistry and Physics*. **15**(16), pp.9477–9500.
- Urupina, D., Lasne, J., Romanias, M.N., Thiery, V., Dagsson-Waldhauserova, P. and Thevenet, F. 2019. Uptake and surface chemistry of SO<sub>2</sub> on natural volcanic dusts.

*Atmospheric Environment*. **217**.

- Vaughan, G., Wareing, D.P., Jones, S.B., Thomas, L. and Larsen, N. 1994. Lidar measurements of Mt. Pinatubo aerosols at Aberystwyth from August 1991 through March 1992. *Geophysical Research Letters*. **21**(13), pp.1315–1318.
- Vega, A.R. and Antuña Marrero, J.C. 2017. Standardizing the determination of the molecular backscatter coefficient profiles for LALINET lidar stations using ERA-Interim Reanalysis Estandarización en la determinación de los perfiles del coeficiente de retrodispersión molecular 45 para las estaciones. *Optica Pura y Aplicada*. **50**, pp.103–114.
- Vehkamäki, H., Kulmala, M., Napari, I., Lehtinen, K.E.J., Timmreck, C., Noppel, M. and Laaksonen, A. 2002. An improved parameterization for sulfuric acid-water nucleation rates for tropospheric and stratospheric conditions. *Journal of Geophysical Research*. **107**(D22), pp.1–10.
- Vernier, J.-P., Thomason, L.W., Pommereau, J.-P., Bourassa, A., Pelon, J., Garnier, A., Hauchecorne, A., Blanot, L., Trepte, C., Degenstein, D. and Vargas, F. 2011. Major influence of tropical volcanic eruptions on the stratospheric aerosol layer during the last decade. *Geophysical Research Letters*. **38**, pp.1–8.
- Vernier, J.P., Fairlie, T.D., Deshler, T., Natarajan, M., Knepp, T., Foster, K., Wienhold, F.G., Bedka, K.M., Thomason, L. and Trepte, C. 2016. In situ and space-based observations of the Kelud volcanic plume: The persistence of ash in the lower stratosphere. *Journal of Geophysical Research: Atmospheres*. **121**, 11,104–11,118.
- Vernier, J.P., Pommereau, J.P., Garnier, A., Pelon, J., Larsen, N., Nielsen, J., Christensen, T., Cairo, F., Thomason, L.W., Leblanc, T. and McDermid, I.S. 2009. Tropical Stratospheric aerosol layer from CALIPSO Lidar observations. *Journal of Geophysical Research Atmospheres*. **114**(24), pp.1–12.
- Wandinger, U. 2005. Introduction to Lidar In: C. Weitkamp, ed. *Lidar: Range-Resolved Optical Remote Sensing of the Atmosphere*. New York: Springer, pp.6–11.
- Ward, S.M., Deshler, T. and Hertzog, A. 2014. Quasi-lagrangian measurements of nitric acid trihydrate formation over Antarctica. *Journal of Geophysical Research*. **119**(1), pp.245–258.
- Weisenstein, D.K., Yue, G.K., Ko, M.K.W., Sze, N.-D., Rodriguez, J.M. and Scott, C.J.

1997. A two-dimensional model of sulfur species and aerosols. *Journal of Geophysical Research*. **102**(D11), pp.13019–13035.
- Whitby, K.T. 1978. The physical characteristics of sulfur aerosols. *Atmospheric Environment*. **12**, pp.135–159.
- Willeke, K. and Whitby, K.T. 1975. Atmospheric aerosols: size distribution interpretation. *Journal of the Air Pollution Control Association*. **25**(5), pp.529–534.
- Wilson, T., Cole, J., Johnston, D., Cronin, S., Stewart, C. and Dantas, A. 2012. Short- and long-term evacuation of people and livestock during a volcanic crisis: Lessons from the 1991 eruption of Volcán Hudson, Chile. *Journal of Applied Volcanology*. **1**(1).
- Winker, D.M. and Osborn, M.T. 1992a. Airborne lidar observations of the Pinatubo volcanic plume. *Geophysical Research Letters*. **19**(2), pp.167–170.
- Winker, D.M. and Osborn, M.T. 1992b. Preliminary analysis of observations of the Pinatubo volcanic plume with a polarization sensitive lidar. *Geophysical Research Letters*. **19**(2), pp.171–174.
- Wolfe, E.W. and Hoblitt, R.P. 1996. Overview of the eruptions *In: C. G. Newhall and R. S. Punongbayan, eds. Fire and mud: Eruptions and Lahars of Mount Pinatubo, Philippines*. Seattle: University of Washington Press, Seattle, pp.415–133.
- Wong, T., Wielicki, B.A., Lee III, R.B., Smith, G.L., Bush, K.A. and Willis, J.K. 2006. Reexamination of the observed decadal variability of the earth radiation budget using altitude-corrected ERBE/ERBS nonscanner WFOV data. *Journal of Climate*. **19**, pp.4028–4040.
- Yoshioka, M., Regayre, L.A., Pringle, K.J., Johnson, J.S., Mann, G.W., Partridge, D.G., Sexton, D.M.H., Lister, G.M.S., Schutgens, N., Stier, P., Kipling, Z., Bellouin, N., Browse, J., Booth, B.B.B., Johnson, C.E., Johnson, B., Mollard, J.D.P., Lee, L. and Carslaw, K.S. 2019. Ensembles of Global Climate Model Variants Designed for the Quantification and Constraint of Uncertainty in Aerosols and Their Radiative Forcing. *Journal of Advances in Modeling Earth Systems*. **11**(11), pp.3728–3754.
- Young, R.E., Houben, H. and Toon, O.B. 1994. Radiatively forced dispersion of the Mt. Pinatubo volcanic cloud and induced temperature perturbations in the stratosphere

- during the first few months following the eruption. *Geophysical Research Letters*. **21**(5), pp.369–372.
- Young, S.A., Manson, P.J. and Patterson, G.R. 1994. Southern Hemisphere Lidar measurements of the Aerosol Clouds from Mt Pinatubo and Mt Hudson *In: Extended Abstracts of the 16th International Laser Radar Conference, July 1992*. Cambridge, Massachusetts.
- Zambri, B., LeGrande, A.N., Robock, A. and Slawinska, J. 2017. Northern Hemisphere winter warming and summer monsoon reduction after volcanic eruptions over the last millennium. *Journal of Geophysical Research*. **122**(15), pp.7971–7989.
- Zanchettin, D., Khodri, M., Timmreck, C., Toohey, M., Schmidt, A., Gerber, E.P., Hegerl, G., Robock, A., Pausata, F.S.R., Ball, W.T., Bauer, S.E., Bekki, S., Dhomse, S.S., Le Grande, A.N., Mann, G.W., Marshall, L., Mills, M., Marchand, M., Niemeier, U., Poulain, V., Rozanov, E., Rubino, A., Stenke, A., Tsigaridis, K. and Tummon, F. 2016. The Model Intercomparison Project on the climatic response to Volcanic forcing (VolMIP): Experimental design and forcing input data for CMIP6. *Geoscientific Model Development*.
- Zerefos, C.S., Tourpali, K. and Bais, A.F. 1994. Further studies on possible volcanic signal to the ozone layer. *Journal of Geophysical Research*. **99**(D12), pp.25741–25746.
- Zhang, L., Gong, S., Padro, J. and Barrie, L. 2001. A size-segregated particle dry deposition scheme for an atmospheric aerosol module. *Atmospheric Environment*. **35**, pp.549–560.
- Zielinski, G.A., Mayewski, P.A., Meeker, L.D., Whitlow, S., Twickler, M.S. and Taylor, K. 1996. Atmospheric Impact of the Toba Mega-Eruption ~71,000 Years Ago. *Geophysical Research Letters*. **23**(8), pp.837–840.

## **Appendix A Method for layer finding algorithm and conversion factors for BSR-EXT**

### **A.1 Layer finding algorithm explanation**

The steps below outline how the algorithm for finding volcanic layers within the data is implemented:

- 1) Load 2D array of data (BSR or extinction values on time vs altitude grid).
- 2) Set a background and delta value for backscatter ratio or extinction. The background value accounts for usual background conditions (0.003 for extinction) and the delta value (0.001) removes possible noise peaks in order to pick out the large layers, i.e. the bulk of the volcanic cloud. Figure 3-3 shows how this works visually.
- 3) Find all values where the data goes above background level and then all values that are below background level. The first value of a layer is then set to be the first value which reaches above the set background level (“lower” value) and then the top of that layer is set to be where the BSR goes back below the background value (“upper” value). It then searches to see if there is more than one value above the background level and restarts this search from the first point that goes back above the background level above the other layer. This function requires altitude points, BSR values, a start index and your background value.
- 4) In order to account for noise within the data, i.e. small peaks within or around the larger peaks, the maximum point of a found layer must exceed the background value + delta.

## A.2 Conversion factors for converting between 694 nm and 532 nm.

These values are spilt for 3 monthly intervals and 5 km altitude resolution.

Year	TP-15 km	15-20 km	20-25 km	25-30 km
91.375	-1.40E+00	-1.47E+00	-1.35E+00	-1.51E+00
91.625	-1.28E+00	-1.37E+00	-1.29E+00	-1.40E+00
91.875	-1.22E+00	-1.35E+00	-1.41E+00	-1.42E+00
92.125	-1.11E+00	-1.29E+00	-1.44E+00	-1.48E+00
92.375	-1.01E+00	-1.18E+00	-1.41E+00	-1.51E+00
92.625	-9.30E-01	-1.07E+00	-1.45E+00	-1.44E+00
92.875	-1.06E+00	-1.26E+00	-1.48E+00	-1.48E+00
93.125	-1.13E+00	-1.33E+00	-1.47E+00	-1.50E+00
93.375	-1.08E+00	-1.26E+00	-1.43E+00	-1.48E+00
93.625	-1.17E+00	-1.23E+00	-1.46E+00	-1.47E+00
93.875	-1.25E+00	-1.34E+00	-1.53E+00	-1.55E+00
94.125	-1.30E+00	-1.41E+00	-1.55E+00	-1.58E+00
94.375	-1.33E+00	-1.42E+00	-1.52E+00	-1.56E+00
94.625	-1.35E+00	-1.42E+00	-1.47E+00	-1.48E+00
94.875	-1.28E+00	-1.43E+00	-1.39E+00	-1.41E+00
95.125	-1.29E+00	-1.43E+00	-1.38E+00	-1.37E+00
95.375	-1.35E+00	-1.40E+00	-1.43E+00	-1.41E+00
95.625	-1.36E+00	-1.40E+00	-1.44E+00	-1.44E+00
95.875	-1.34E+00	-1.40E+00	-1.41E+00	-1.44E+00
96.125	-1.33E+00	-1.40E+00	-1.39E+00	-1.43E+00
96.375	-1.40E+00	-1.41E+00	-1.39E+00	-1.35E+00
96.625	-1.50E+00	-1.41E+00	-1.38E+00	-1.23E+00

96.875	-1.40E+00	-1.36E+00	-1.34E+00	-1.29E+00
97.125	-1.43E+00	-1.41E+00	-1.30E+00	-1.35E+00
97.375	-1.54E+00	-1.48E+00	-1.26E+00	-1.37E+00
97.625	-1.40E+00	-1.39E+00	-1.22E+00	-1.30E+00
97.875	-1.39E+00	-1.36E+00	-1.24E+00	-1.32E+00
98.125	-1.41E+00	-1.33E+00	-1.27E+00	-1.37E+00

**A.3 Conversion exponents for converting backscatter ratio to extinction. These values are spilt for 3 monthly intervals and 5 km altitude resolution. Obtained from Juan Carlos Antuña Marrera from Jager and Deshler (2005).**

Year	TP-15 km	15-20 km	20-25 km	25-30 km
91.375	4.41E+01	4.94E+01	5.12E+01	4.11E+01
91.625	4.81E+01	5.22E+01	5.20E+01	4.45E+01
91.875	4.55E+01	4.70E+01	4.92E+01	5.14E+01
92.125	3.75E+01	3.87E+01	4.67E+01	5.48E+01
92.375	2.95E+01	3.07E+01	4.58E+01	5.17E+01
92.625	2.19E+01	2.63E+01	4.86E+01	5.34E+01
92.875	2.76E+01	3.35E+01	5.13E+01	5.51E+01
93.125	2.85E+01	3.75E+01	5.32E+01	5.31E+01
93.375	2.72E+01	3.39E+01	5.39E+01	4.81E+01
93.625	2.88E+01	3.23E+01	5.49E+01	5.17E+01
93.875	3.04E+01	3.71E+01	5.60E+01	5.35E+01
94.125	3.29E+01	4.20E+01	5.63E+01	5.37E+01
94.375	3.64E+01	4.19E+01	5.63E+01	5.07E+01
94.625	3.51E+01	4.28E+01	5.62E+01	4.75E+01
94.875	3.64E+01	4.78E+01	5.43E+01	4.62E+01

<b>95.125</b>	3.90E+01	5.02E+01	5.23E+01	4.63E+01
<b>95.375</b>	4.15E+01	4.75E+01	5.03E+01	4.50E+01
<b>95.625</b>	4.29E+01	4.57E+01	4.88E+01	4.40E+01
<b>95.875</b>	4.24E+01	4.45E+01	4.72E+01	4.45E+01
<b>96.125</b>	4.18E+01	4.33E+01	4.57E+01	4.51E+01
<b>96.375</b>	4.29E+01	4.21E+01	4.68E+01	4.75E+01
<b>96.625</b>	4.41E+01	4.08E+01	4.87E+01	5.08E+01
<b>96.875</b>	4.53E+01	4.68E+01	5.05E+01	4.76E+01
<b>97.125</b>	4.47E+01	5.09E+01	4.92E+01	4.10E+01
<b>97.375</b>	4.24E+01	4.51E+01	4.88E+01	3.89E+01
<b>97.625</b>	4.42E+01	5.03E+01	5.02E+01	3.87E+01
<b>97.875</b>	4.61E+01	5.08E+01	5.22E+01	4.02E+01
<b>98.125</b>	4.79E+01	5.03E+01	5.22E+01	4.18E+01

## **Appendix B Varying conversion factors vs blanket conversion of 40**

A comparison of the lidar extinction conversion factors was performed and shows the largest differences between the two backscatter to extinction methods within the layers. The upper parts of the layers have differences between 0.03-0.05, ~10 times larger than background values, with an average difference over time of 0.003. These values are significant, as values  $<0.001 \text{ km}^{-1}$  are generally considered as background values, therefore, differences consistently varying by 0.003 indicates the blanket conversion factor of 40 results in extinction values that differ by a factor of 3 in comparison to the size-dependent conversion. As the extinction values in are dependent on size-distributions, which vary greatly following a volcanic eruption, the extinction values in are used to compare with model simulations.

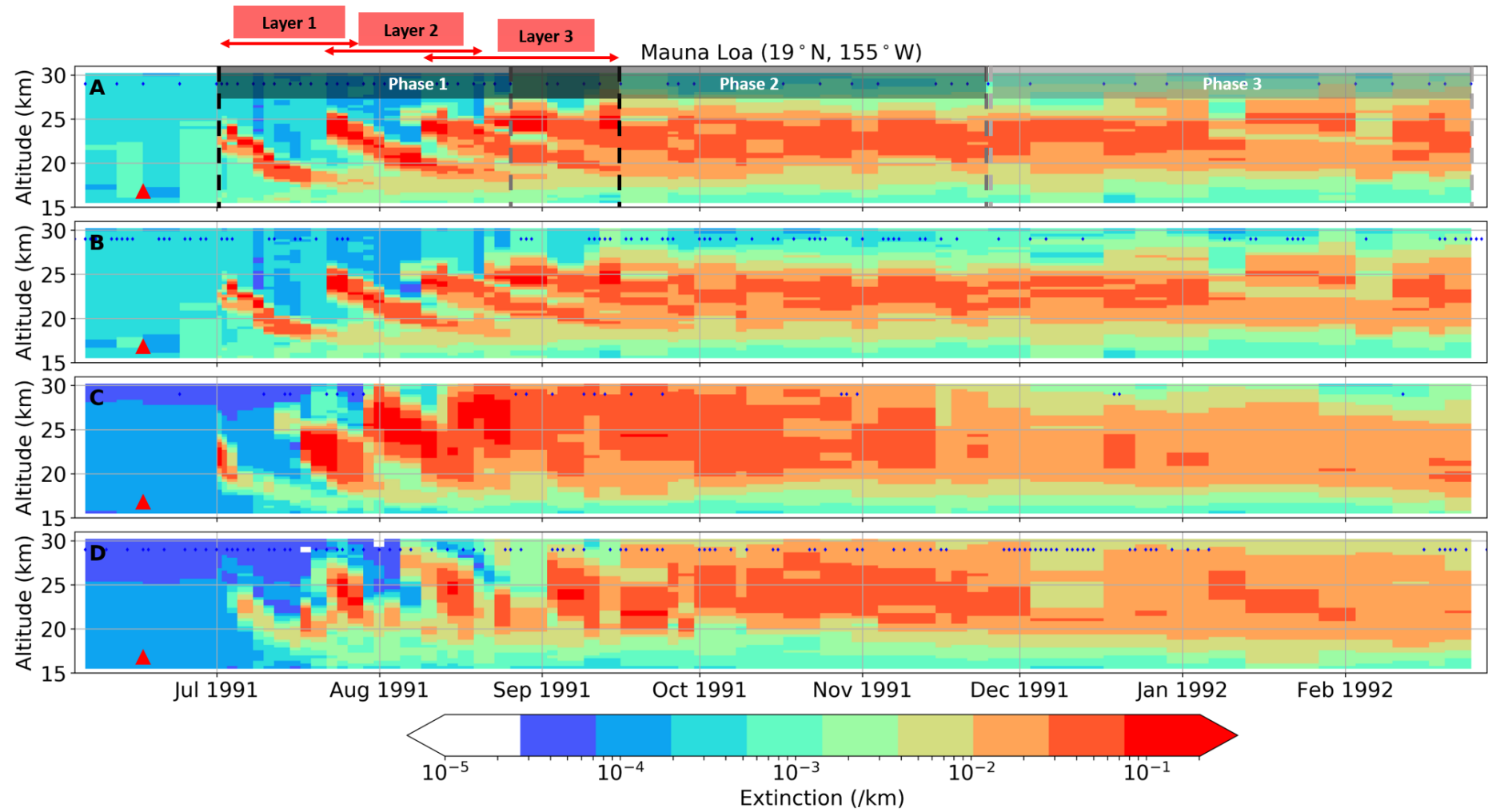


**Figure B-1** Extinction (/km) values for Mauna Loa (MLO) from June 1991 - February 1992. a) Lidar with varying BSR-EXT values over time, b) Lidar values with BSR-EXT value of 40, c) Model simulation with approximate-QBO, d) Model simulation with pre-nudged conditions.

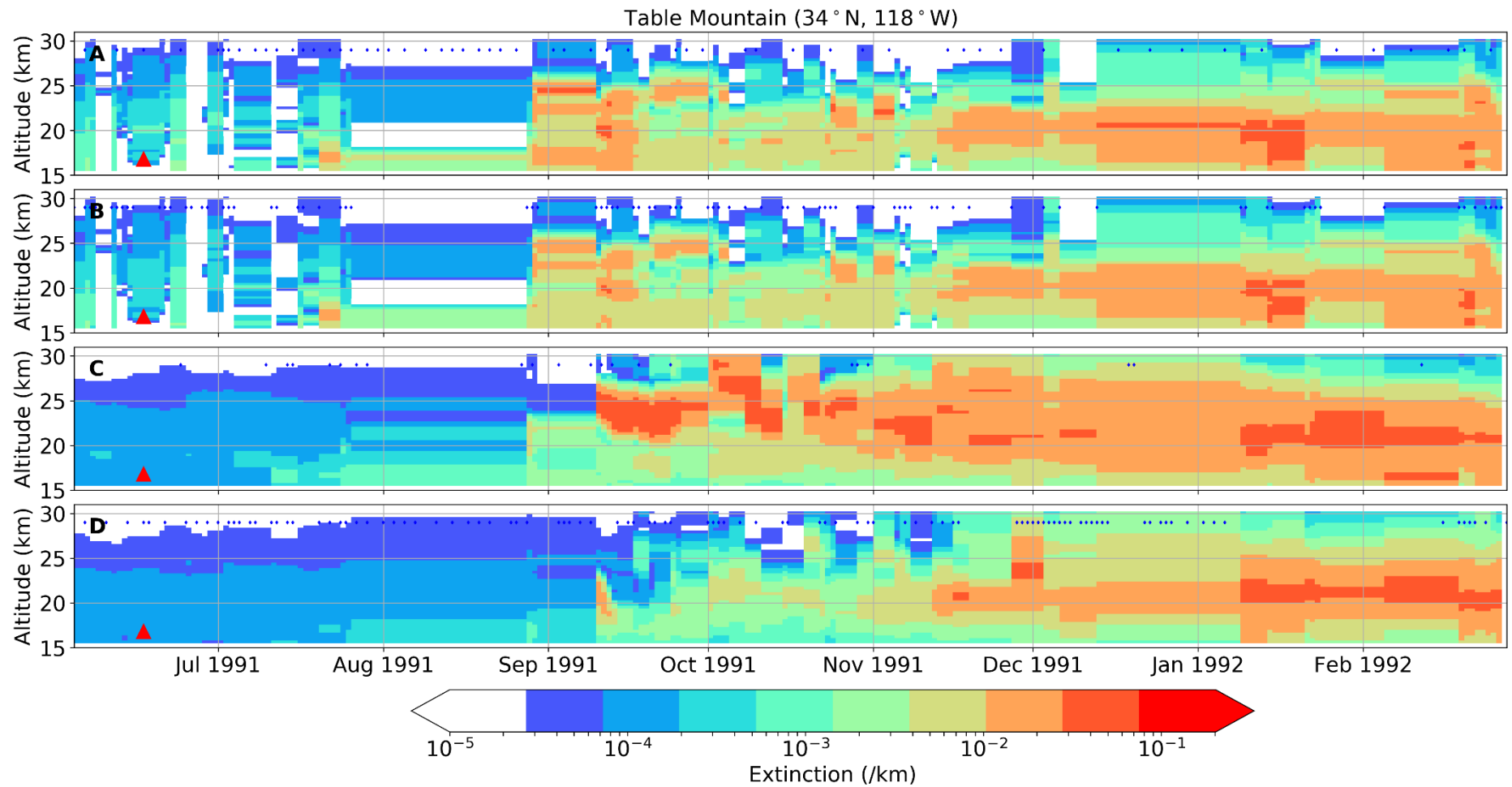


**Figure B-2** Extinction (/km) values for Table Mountain (TAB) from June 1991 - February 1992. a) Lidar with varying BSR-EXT values over time, b) Lidar values with BSR-EXT value of 40, c) Model simulation with approximate-QBO, d) Model simulation with pre-nudged conditions

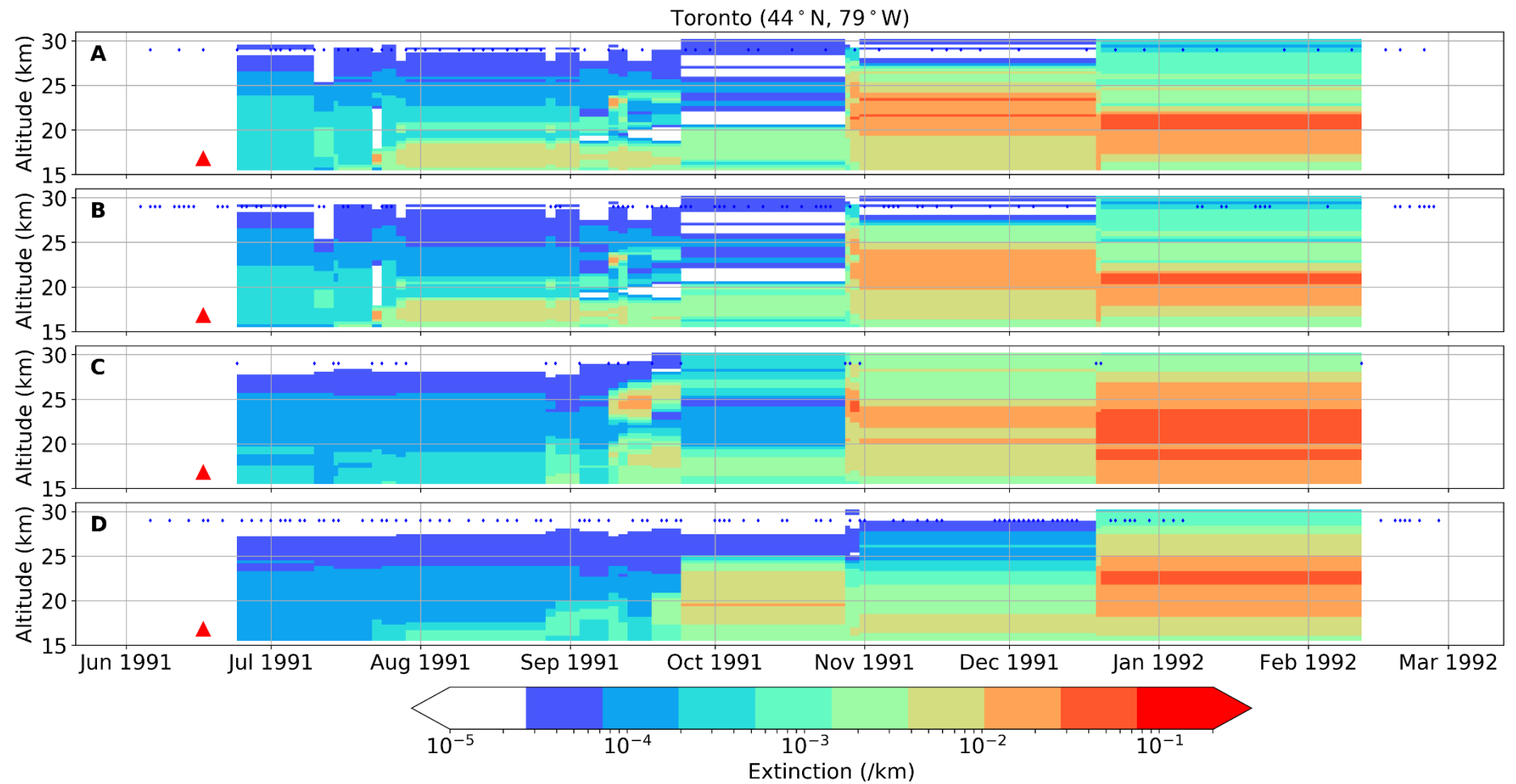


**Figure B-3** Extinction (/km) values for Toronto (TOR) from June 1991 - February 1992. a) Lidar with varying BSR-EXT values over time, b) Lidar values with BSR-EXT value of 40, c) Model simulation with approximate-QBO, d) Model simulation with pre-nudged conditions.

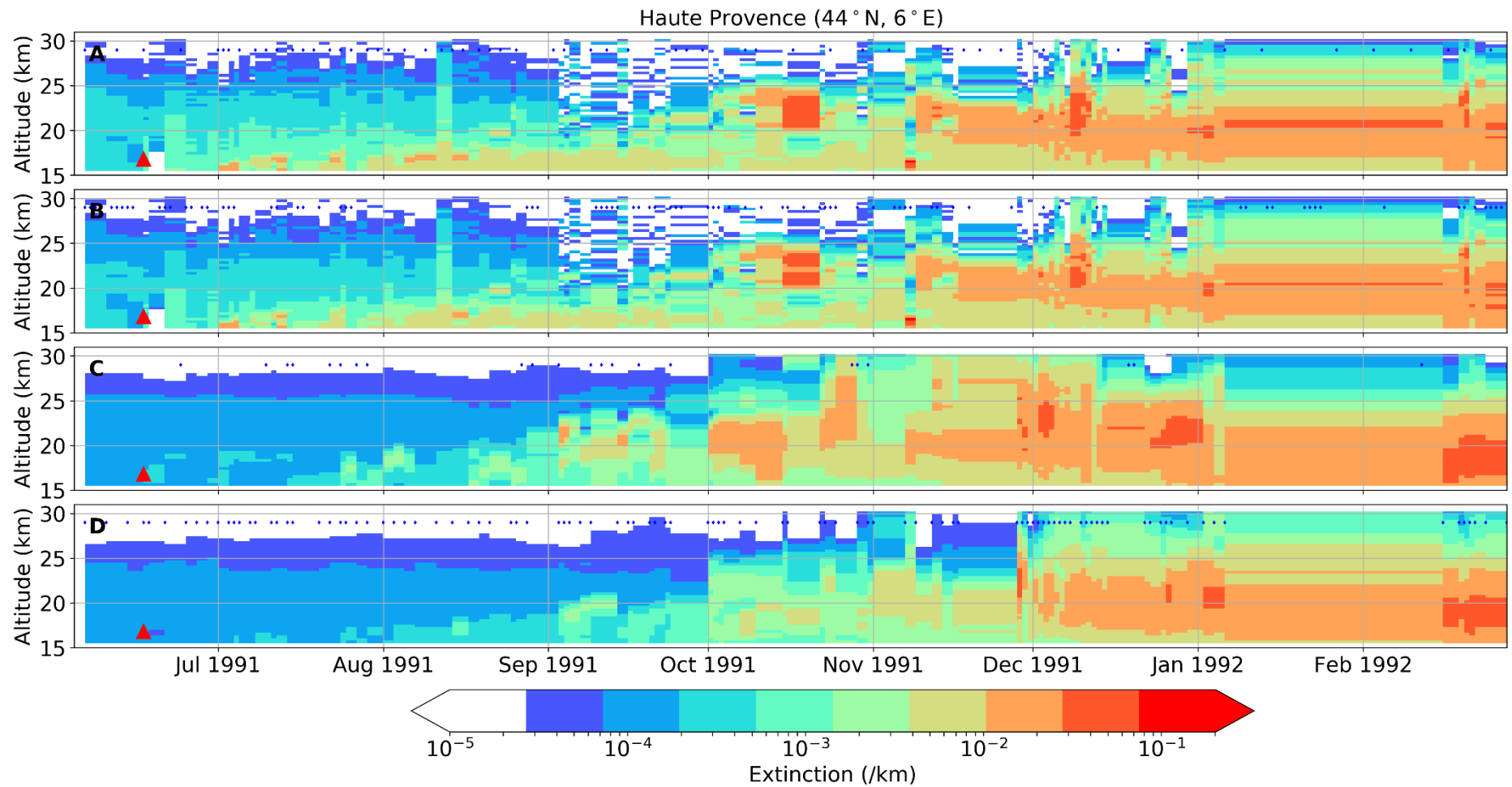


**Figure B-4** Extinction (/km) values for Haute Provence (OHP) from June 1991 - February 1992. a) Lidar with varying BSR-EXT values over time, b) Lidar values with BSR-EXT value of 40, c) Model simulation with approximate-QBO, d) Model simulation with pre-nudged conditions.

## Appendix C Chapter 5 Northern and southern hemisphere sulfate burden and SAOD

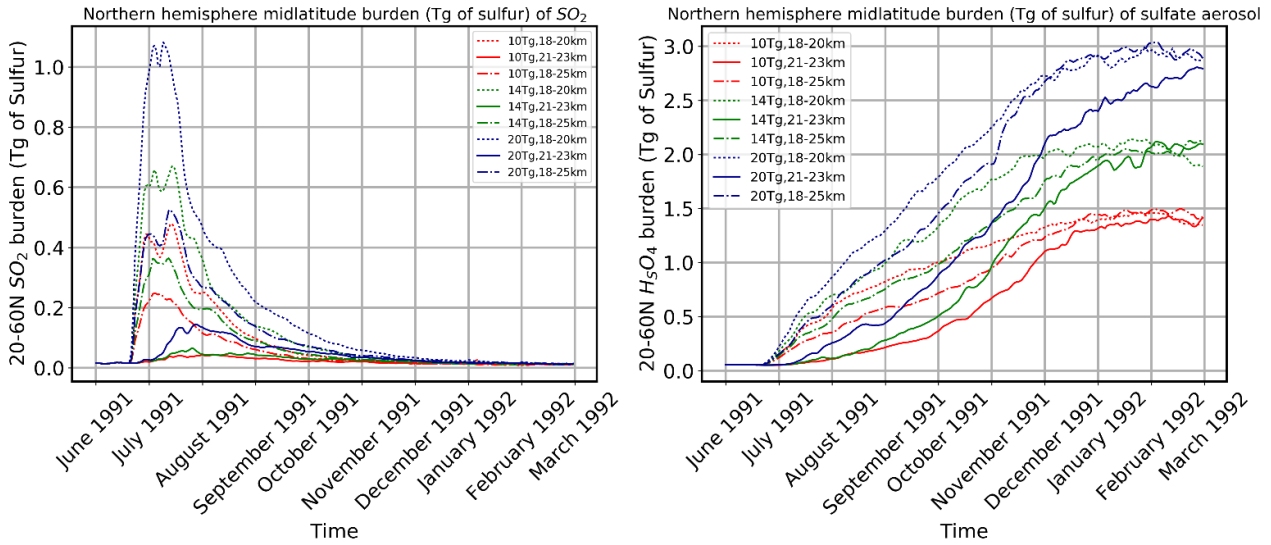


Figure C-1 Northern hemisphere (left) SO<sub>2</sub> sulfur burden and (right) SO<sub>4</sub> sulfur burden for each injection height and mass of SO<sub>2</sub>.

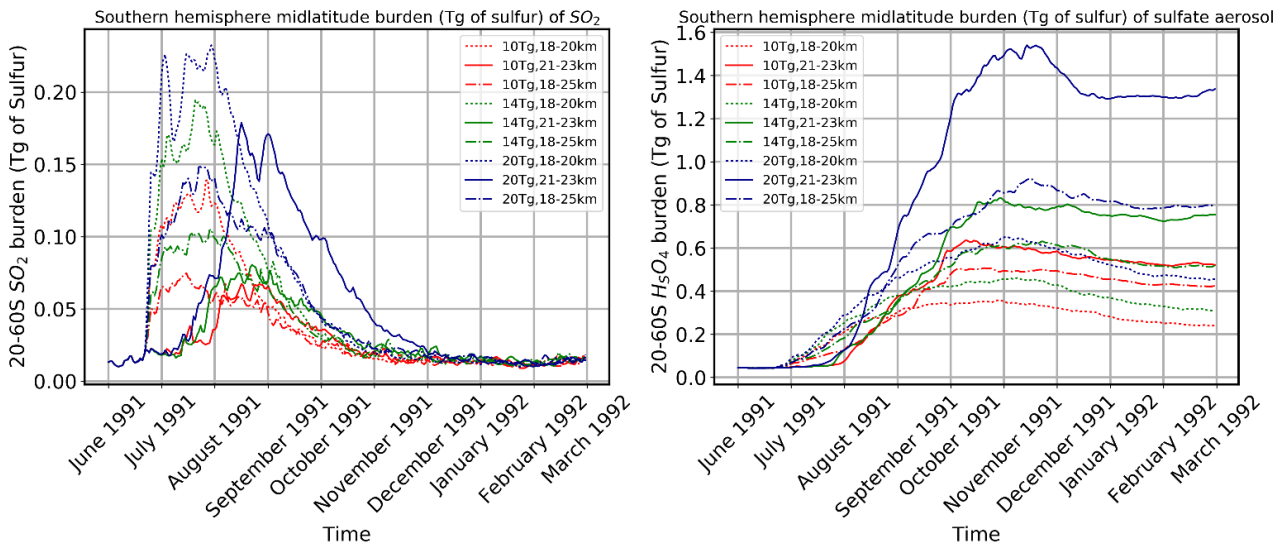
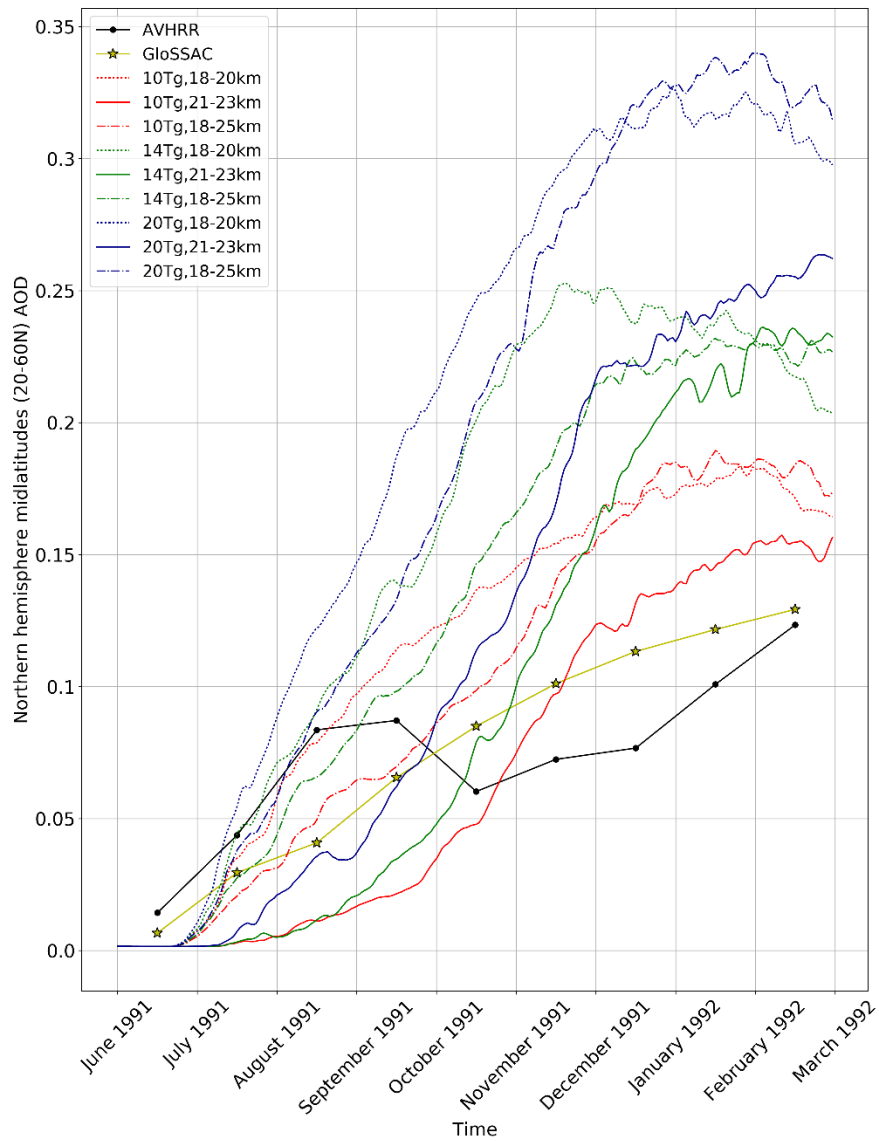
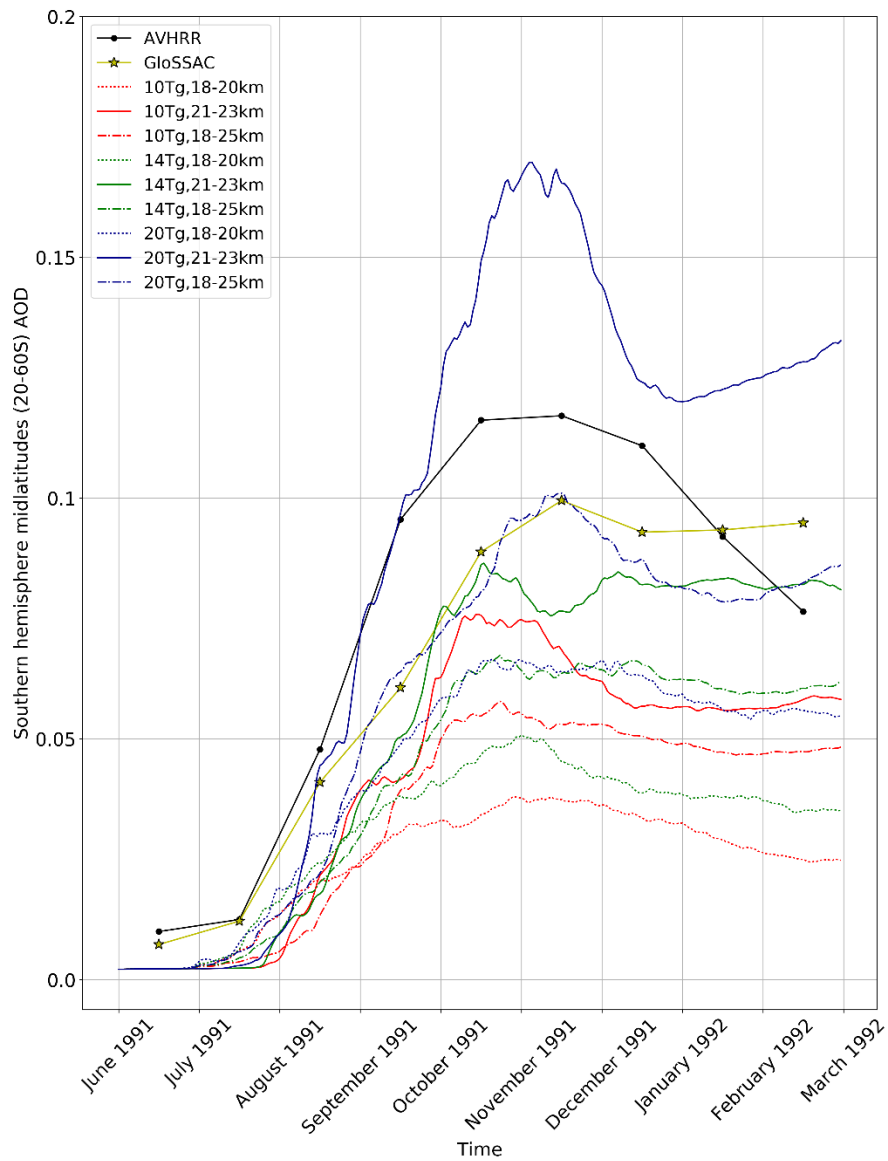


Figure C-2 Southern hemisphere (left) SO<sub>2</sub> sulfur burden and (right) SO<sub>4</sub> sulfur burden for each injection height and mass of SO<sub>2</sub>.



**Figure C-3 SAOD values for the northern hemisphere for each different injection height and mass of SO<sub>2</sub>. Red lines are 10 Tg, green lines are 14 Tg and blue lines are 20 Tg with different linestyles for each injection height.**



**Figure C-4 SAOD values for the southern hemisphere for each different injection height and mass of SO<sub>2</sub>. Red lines are 10 Tg, green lines are 14 Tg and blue lines are 20 Tg with different linestyles for each injection height.**

## Appendix D Chapter 6 sulfate and ash burden profiles

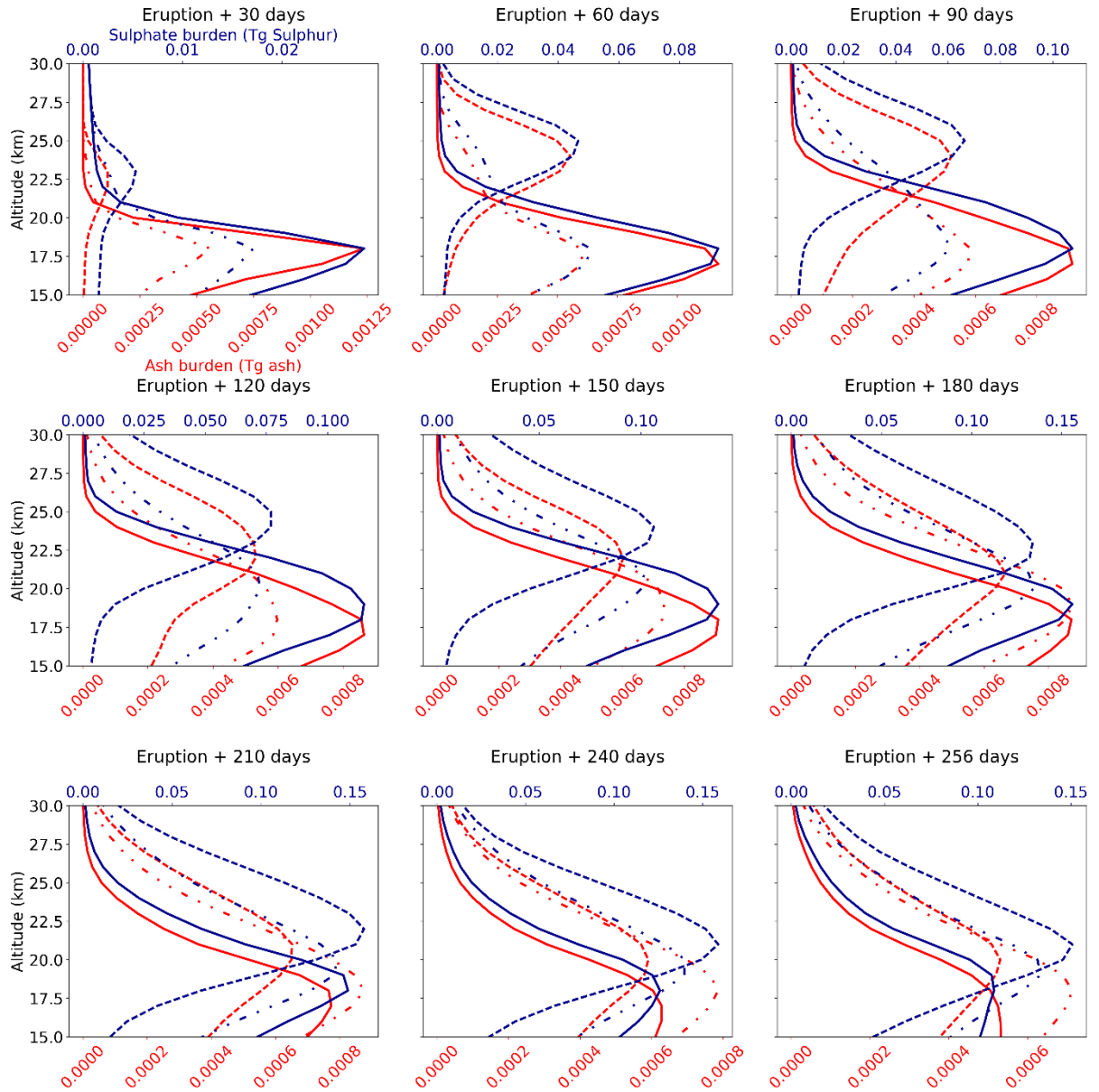


**Figure D-1** Monthly average ash (red) and sulfate (blue) burden for the northern mid-latitudes (20-60°N) for a 14 Tg SO<sub>2</sub> and 0.05 Tg ash injection mass at 18-20 km (solid lines), 21-23 km (dashed lines) and 18-25 km (dot-dashed line).

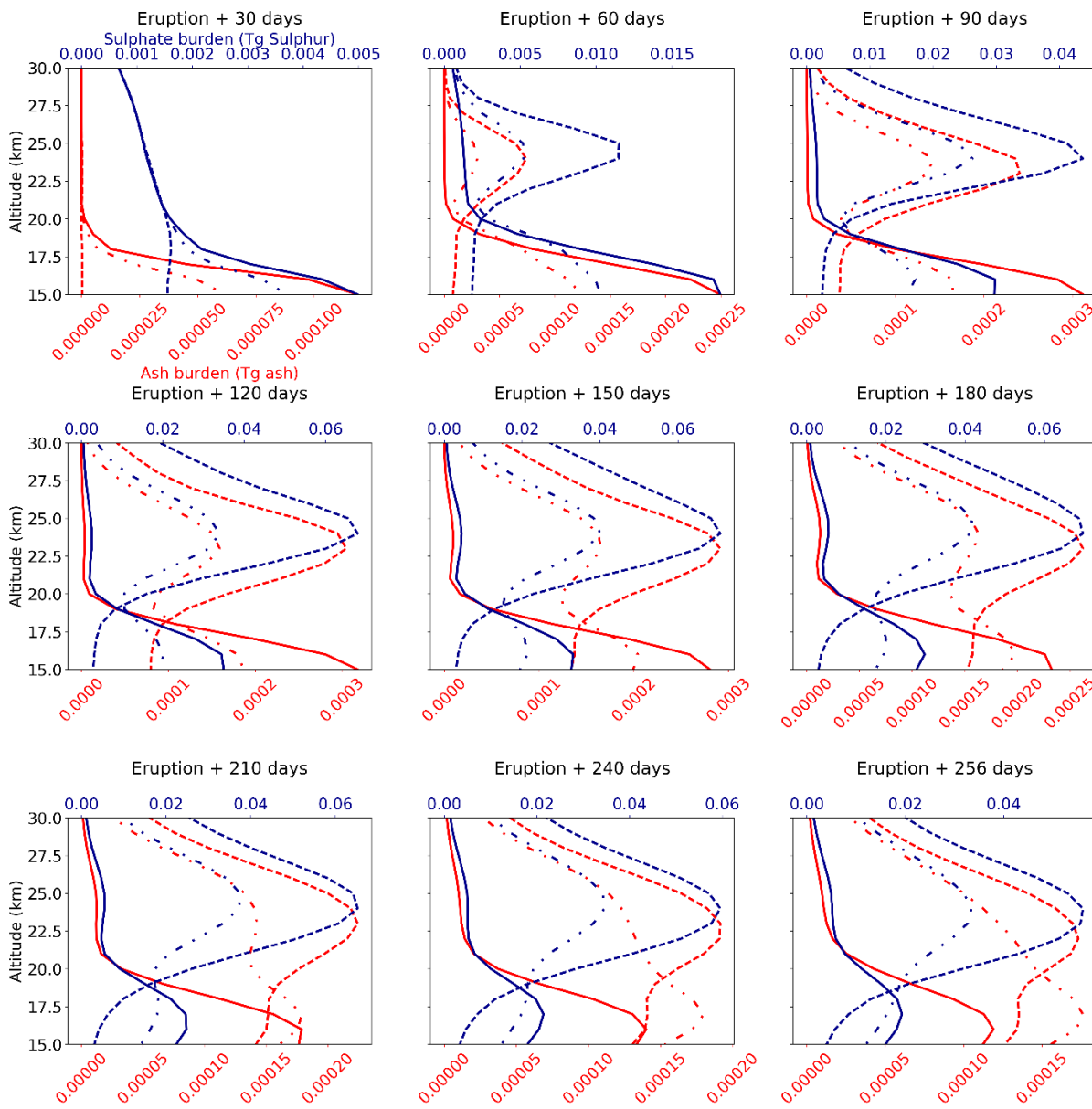


**Figure D-2 Monthly average ash (red) and sulfate (blue) burden for the northern mid-latitudes (20-60°S) for a 14 Tg SO<sub>2</sub> and 0.05 Tg ash injection mass at 18-20 km (solid lines), 21-23 km (dashed lines) and 18-25 km (dot-dashed line).**

## Appendix E Chapter 6 vertical extinction profiles for all lidar sites

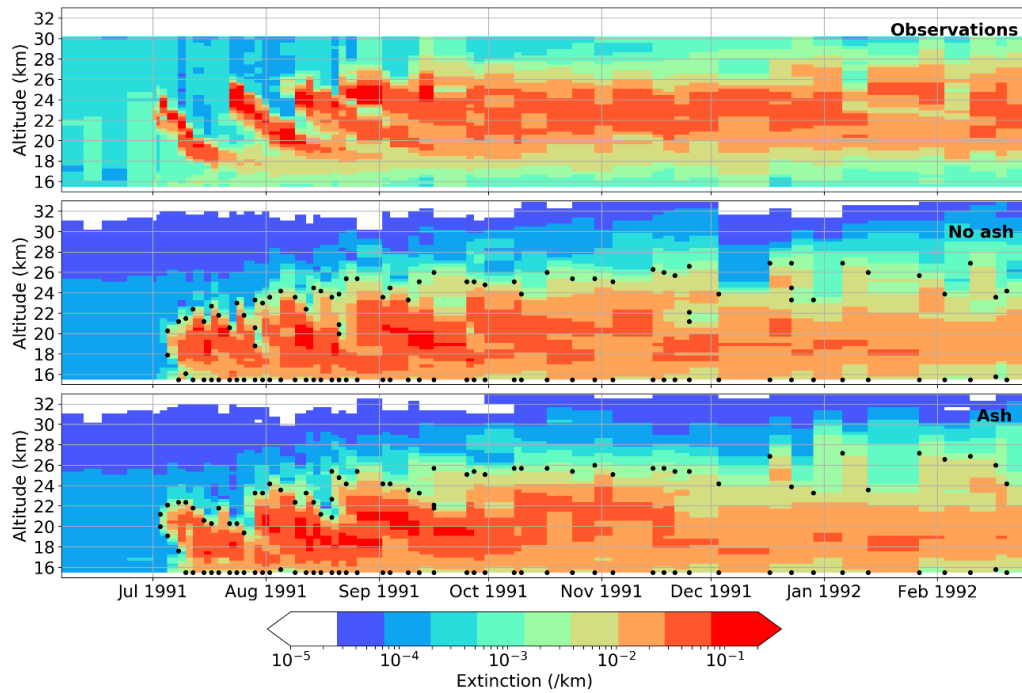


Figure E-1 Extinction plots for MLO with 10 Tg SO<sub>2</sub> and 18-20 km injection height. Plots show observations (top), no ash (middle) and with ash (bottom). Black dots denote where layers. .

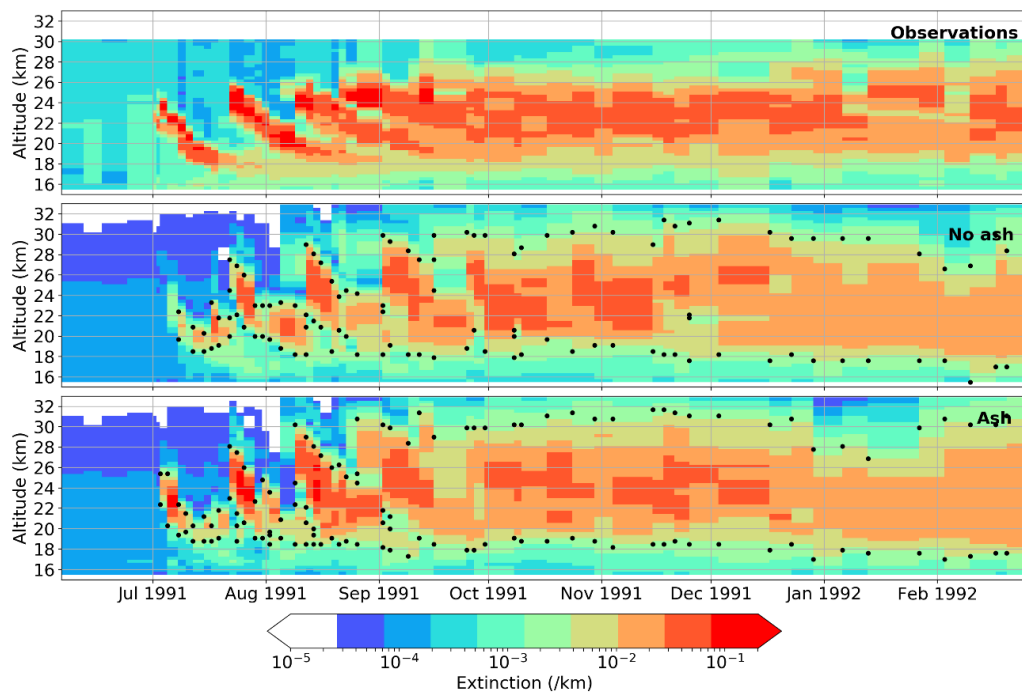
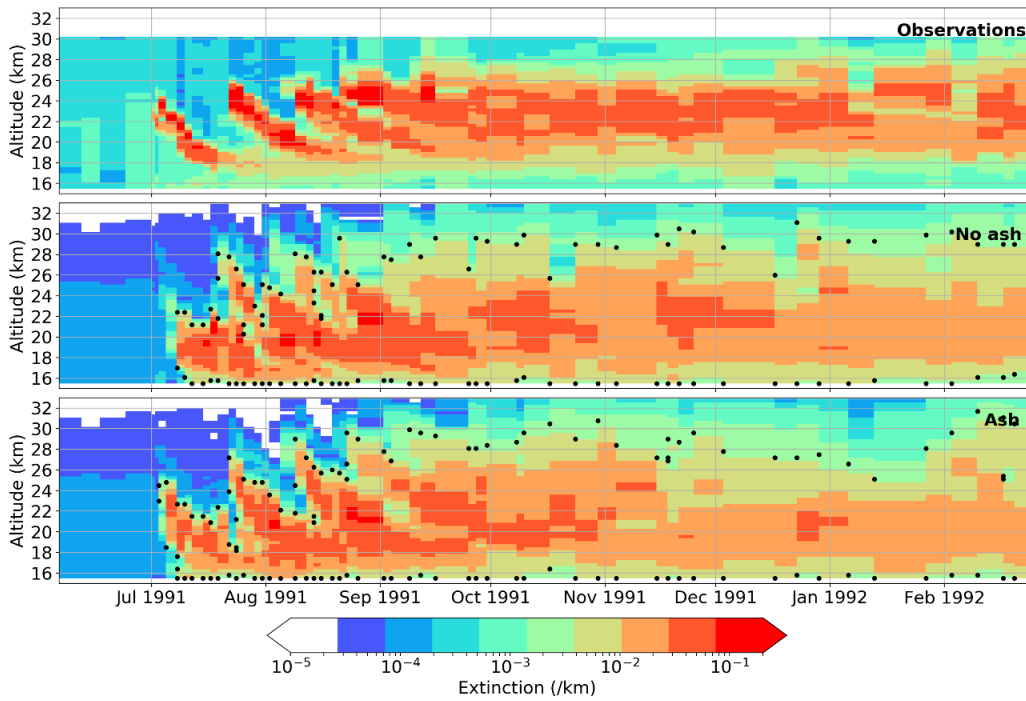
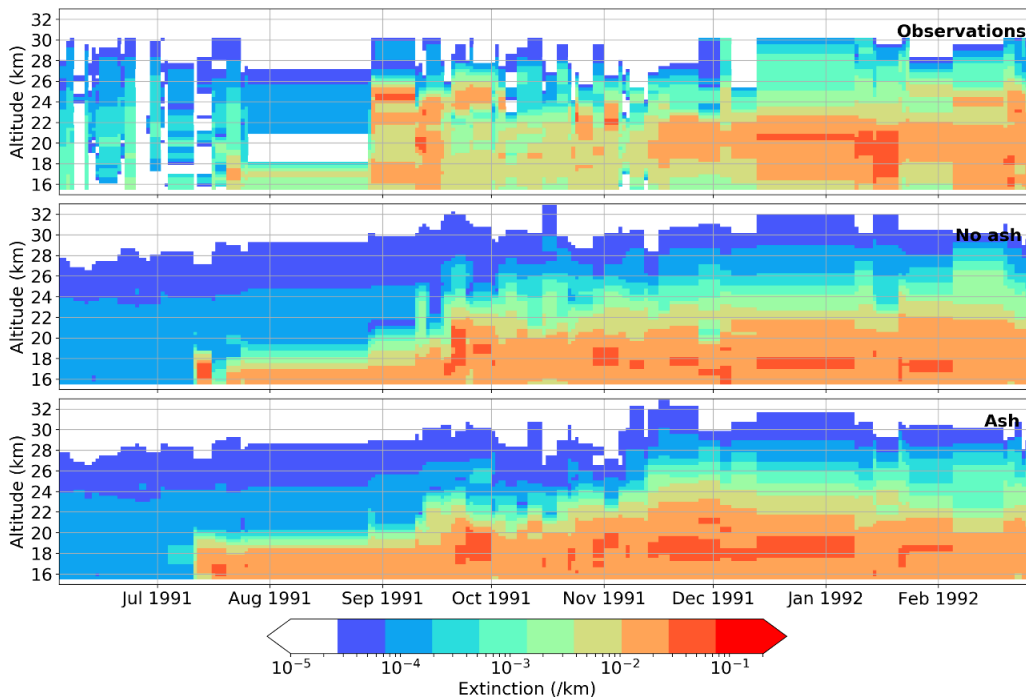


Figure E-2 Extinction plots for MLO with 10 Tg SO<sub>2</sub> and 21-23 km injection height. Plots show observations (top), no ash (middle) and with ash (bottom). Black dots denote layers.



**Figure E-3** Extinction plots for MLO with 10 Tg SO<sub>2</sub> and 18-25 km injection height. Plots show observations (top), no ash (middle) and with ash (bottom). Black dots denote layers.



**Figure E-4** Extinction plots for TAB with 10 Tg SO<sub>2</sub> and 18-20 km injection height. Plots show observations (top), no ash (middle) and with ash (bottom).

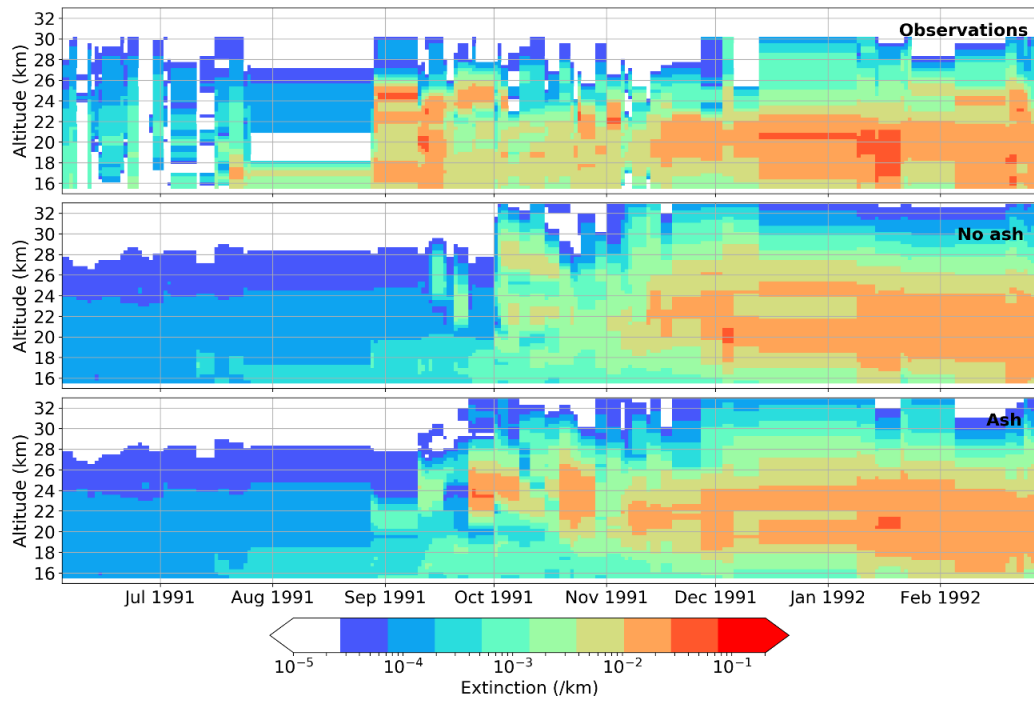


**Figure E-5** Extinction plots for TAB with 10 Tg SO<sub>2</sub> and 21-23 km injection height. Plots show observations (top), no ash (middle) and with ash (bottom).

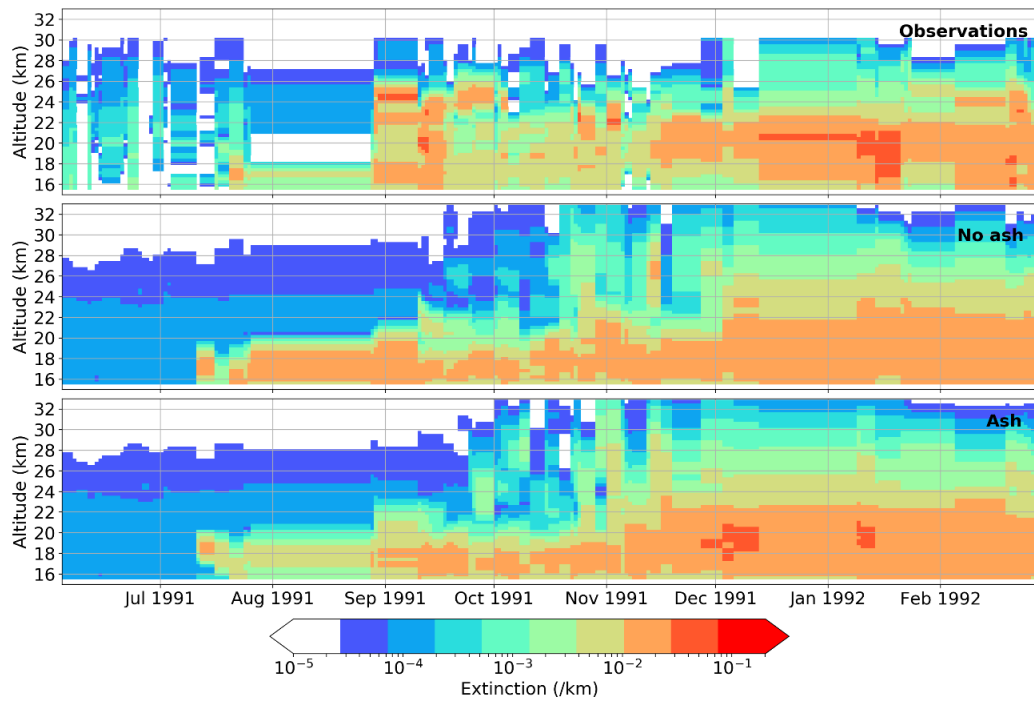


**Figure E-6** Extinction plots for TAB with 10 Tg SO<sub>2</sub> and 18-25 km injection height. Plots show observations (top), no ash (middle) and with ash (bottom).

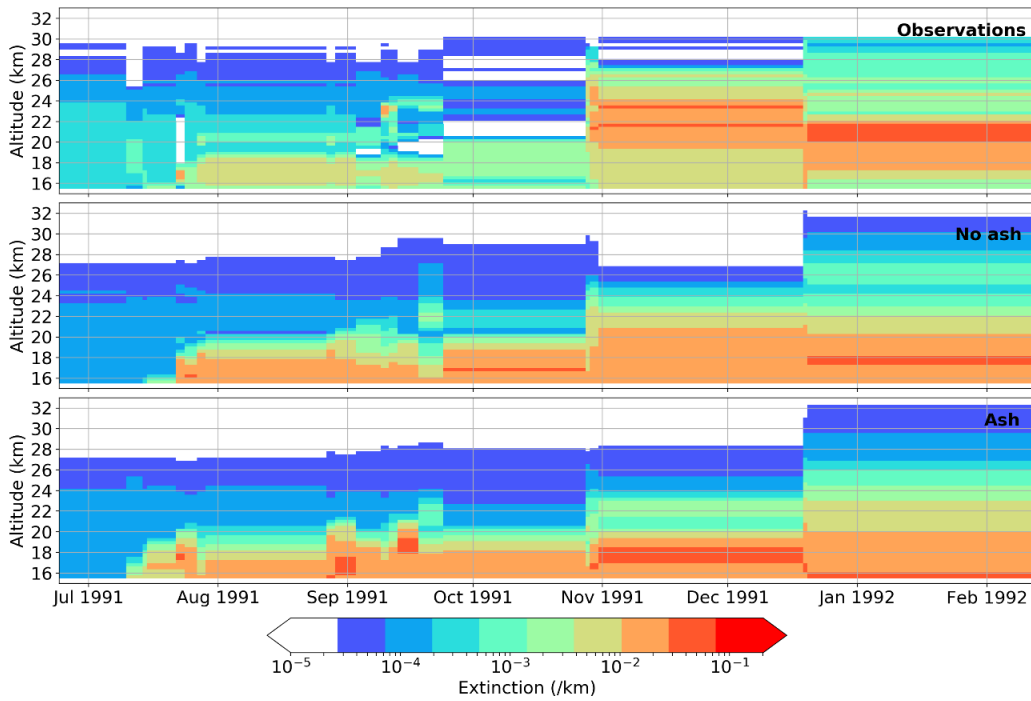


Figure E-7 Extinction plots for TOR with 10 Tg SO<sub>2</sub> and 18-20 km injection height. Plots show observations (top), no ash (middle) and with ash (bottom).

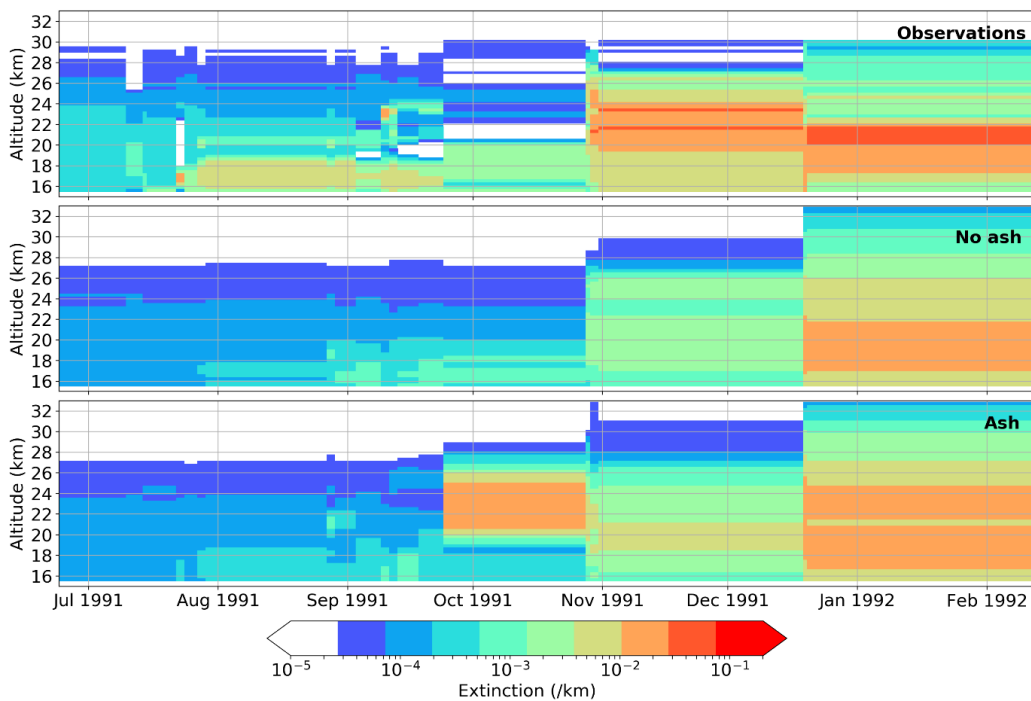
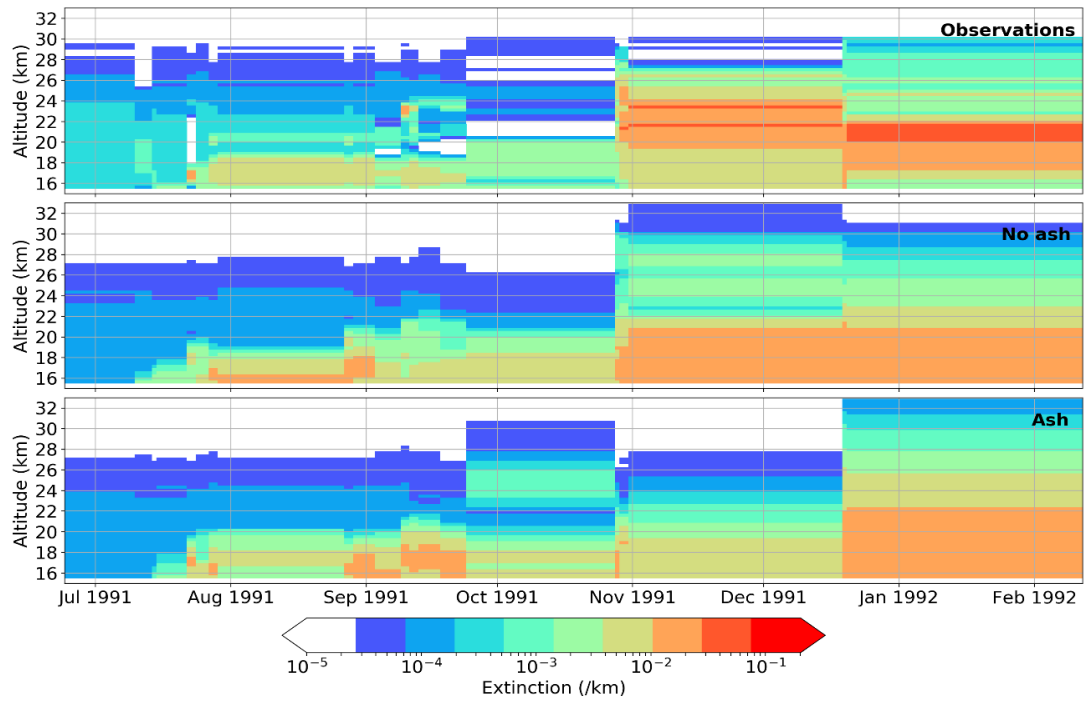
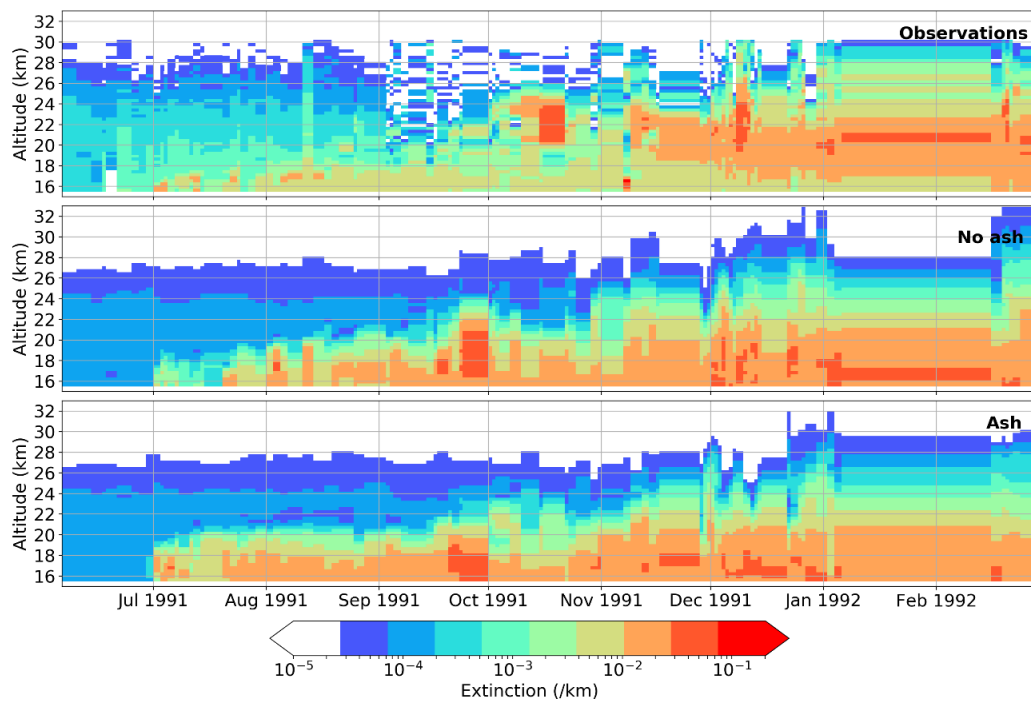


Figure E-8 Extinction plots for TOR with 10 Tg SO<sub>2</sub> and 21-23 km injection height. Plots show observations (top), no ash (middle) and with ash (bottom).



**Figure E-9** Extinction plots for TOR with 10 Tg SO<sub>2</sub> and 18-25 km injection height. Plots show observations (top), no ash (middle) and with ash (bottom).



**Figure E-10** Extinction plots for OHP with 10 Tg SO<sub>2</sub> and 18-20 km injection height. Plots show observations (top), no ash (middle) and with ash (bottom). Black dots denote where layers are picked out from the layer finding algorithm.

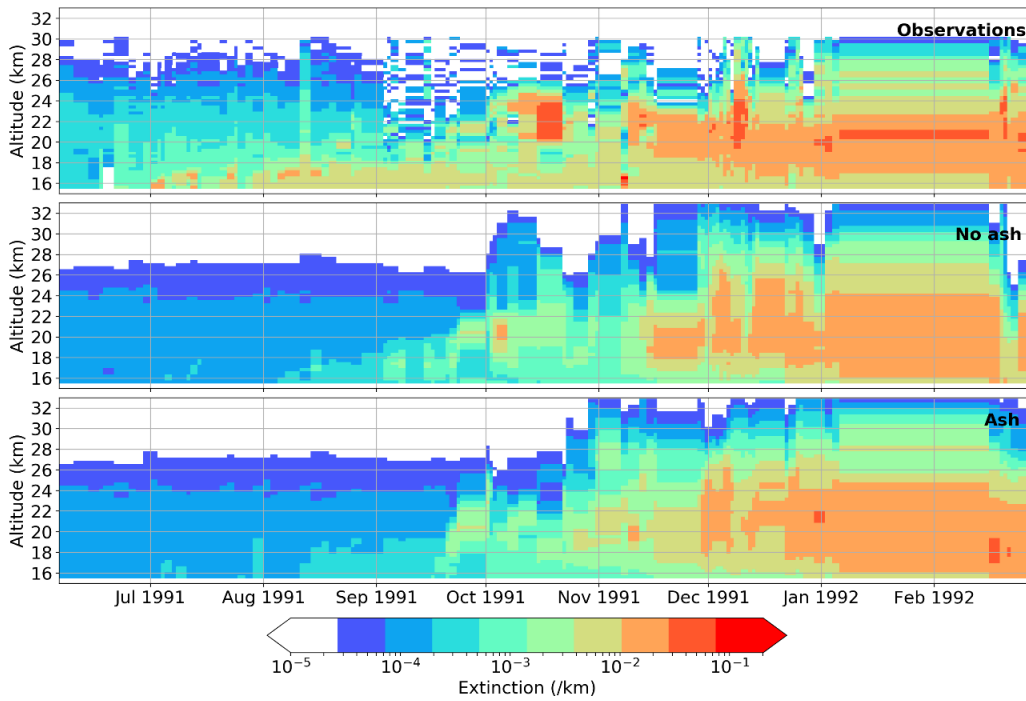


**Figure E-11** Extinction plots for OHP with 10 Tg SO<sub>2</sub> and 21-23 km injection height. Plots show observations (top), no ash (middle) and with ash (bottom).

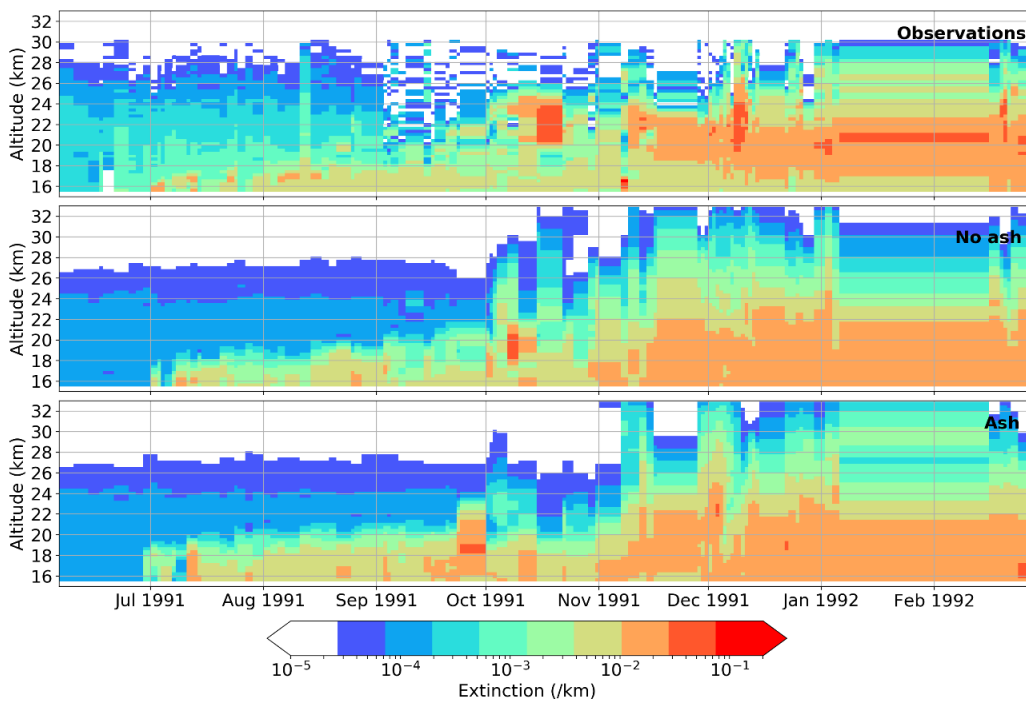


**Figure E-12** Extinction plots for OHP with 10 Tg SO<sub>2</sub> and 18-25 km injection height. Plots show observations (top), no ash (middle) and with ash (bottom).